IMPEDIMETRIC MONITORING OF
THREE-DIMENSIONAL TISSUE MODELS:
A CONSTRUCTION SET APPROACH

DISSERTATION

Zur Erlangung des Doktorgrades

der Naturwissenschaften (Dr. rer. nat.)

der Fakultät für Chemie und Pharmazie

der Universität Regensburg

vorgelegt von

Pierre Dominik Pütz

aus Ebersberg

2021

IMPEDIMETRIC MONITORING OF THREE-DIMENSIONAL TISSUE MODELS: A CONSTRUCTION SET APPROACH

DISSERTATION

Zur Erlangung des Doktorgrades

der Naturwissenschaften (Dr. rer. nat.)

der Fakultät für Chemie und Pharmazie

der Universität Regensburg

vorgelegt von

Pierre Dominik Pütz

aus Ebersberg

2021

This PhD thesis was written from April 2017 until July 2021 at the Institute of Analytical Chemistry, Chemo- and Biosensors of the Faculty of Chemistry and Pharmacy at the University of Regensburg.

The work was conducted under the supervision of Prof. Dr. Joachim Wegener.

PhD application submitted: _____

Date of the PhD colloquium: _____

Doctoral Commitee:

    Chairman: Prof. Dr. Hans-Heiner Gorris

    First examiner: Prof. Dr. Joachim Wegener

    Second examiner: Prof. Dr. Cornelia Kasper

    Third examiner: Prof. Dr. Rainer Müller

The mind is a beautiful thing.

OUTLINE

II

TABLE OF CONTENTS

I   ABSTRACT

In the development and preclinical testing of potential drugs, three-dimensional tissue models continuously keep gaining in importance for representing the *in vivo* conditions of living tissue far better than cell monolayers. Furthermore, a more realistic cell response is caused by certain stimuli in such more complex models. Although this type of artificially created, three-dimensional tissue models presents a valid imitation of real tissues, so far there are no adequate measurement methods available. The existing measurement methods are by and large endpoint assays and thus, no time-dependent information regarding the cell response is obtained. The concept of this PhD thesis is based on a layer-by-layer setup to create three-dimensional tissue models using thin, porous filter membranes with cell layers grown on each side. Additionally, these permeable supports are equipped with thin gold-film electrodes on each side on which the cells can directly adhere. When a low AC voltage is applied, the cells act as insulating particles and morphological changes upon a distinct stimulation are monitored via changes in the impedance. The unique layer-by-layer setup enables an individual addressing of each cell layer and as the permeable supports are brought in close proximity to each other, a physiological environment for all cells is guaranteed. Each cell layer can communicate with the one on the adjacent permeable support as well as through the pores of the filter membrane with the cell layer on the reverse side of the same permeable support. The ensuing three-dimensional tissue model can not only comprise a variable number of cell layers but also different cell types and therefore be used as a construction set for cell- and tissue culture.

II   INTRODUCTION

In pharmacological research in general and specifically in the screening for drug candidates, examinations of living, cultivated cells of the target tissue (cell-based assays) is a well-established experimental method to obtain information about the bioactivity and/or possible toxic side effects of such compounds in the early stages of the drug development process. On the long way from the initial discovery of a drug candidate to the introduction on the market, all early testing is done on cultivated cells before later on, it has to meet the expectations in animal testing. Normally, two-dimensional cell monolayers are used in cell-based assays which are grown on the bottom of petri dishes or multiwell plates. Inevitable animal testing is then followed by multiple phases of clinical testing during which the drug is administered to humans. Only after having gone successfully through every single stage and having been closely reviewed by the authorities, e.g. the Food and Drug Administration in the US or the European Medicines Agency in the EU, the drug candidate can finally be placed on the market[1]. Among the most controversial steps in the drug development process is the animal testing which should be reduced as much as possible. Animal testing is not only ethically questionable, but there are also considerable scientific problems to be addressed: (i) the complexity of an entire organism makes it hard to conduct mechanistical studies, (ii) animal testing usually goes hand in hand with a great variance and (iii) the applicability of results from animal testing on humans is limited due to species differences[2]. Furthermore, there still exists a wide-ranging gap between two-dimensional cell monolayers *in vitro* on the one hand, which are well-established and yield reproducible test results, and on the other hand testing on lab animals *in vivo* which is not only ethically controversial, but also scientifically due to the limited transferability of the results to the human species[3]. Due to this still wide-ranging gap, three-dimensional tissue models on an organ level for example, which allow for an interim evaluation, would be highly useful and a welcome step to improve the information content before the start of clinical studies.

II.1 Historic Development of *In Vitro* 3D Tissue Models

Particularly in this context it is obvious that a lot of effort has been made to develop reliable methods to test drug candidates on three-dimensional tissue models which represent the *in vivo* complexity far more accurately than cell monolayers[4,5]. Mankind has come a long way since the earliest attempts of culturing real animal organs outside of the body. Already in the 19th century, the English physiologist Sydney Ringer succeeded in mixing salt solutions from the chlorides of calcium, magnesium, potassium and sodium to maintain the beating of a heart taken out from an animal[6]. Still before the turn of the century, the German zoologist Wilhelm Roux was able to lay the groundwork for the principle of tissue culturing by removing part of the neural plate of an embryonic chicken and keeping it in a warm saline solution for a number of days[7]. Another milestone was achieved by the American biologist Ross Granville Harrison in 1907. Harrison used an already established bacteriology method to culture an isolated frog neuron in a hanging drop for as long as almost four weeks[8]. This achievement is widely accepted to represent the beginning of cell and tissue culture[9]. 5 years later, Alexis Carrel, a French surgeon and biologist, took up on these scientific achievements and was able to cultivate parts of an 18-day-old chicken embryo heart for three months[10,11]. This elegant work of passaging cardiomyocytes for 18 times while retaining the cardiac rhythm, granted him the honor of being the first person to propagate living cells *in vitro* and simultaneously initiating the art of histoculture as it is known nowadays. The first Nobel Prize in Physiology or Medicine for accomplishments using the underlying methodology of tissue culture was awarded in 1954 to John F. Enders, Thomas H. Weller and Frederick C. Robbins. The Nobel Prize Committee acknowledged "their discovery of the ability of poliomyelitis viruses to grow in cultures of various types of tissue" and in the presentation speech during the ceremony, Prof. Sven Gard of the Karolinska Institute referred to the field of tissue culture as "a cult… with Carrel as their high priest"[12]. Shortly before that time, the first human cell line was derived from a cervical cancer patient named Henrietta Lacks and therefore named HeLa cells. HeLa cells were found to be very robust and to proliferate quickly and still today this immortalized cell line is the most commonly used cell line[13]. From the 1950s on, cell culture and tissue culture have secured a firm place in helping to provide answers to many biomedical questions. Ever since, three-dimensional *in vitro* tissue models have tried to catch up with the well-established and reproducible cell culture in two dimensions.

In three-dimensional models, the natural tissue architecture is preserved and different types of cells can communicate with each other. The cells exhibit a differentiated cellular function and a co-culture of different cell types is possible. Moreover, the mass transport rates exhibit a higher similarity to the ones in normal living tissue and consequently yield more physiological results[14,15]. If the 3D tissue models are made from human cells, the aforementioned problems of the species differences can even be entirely circumvented. However, the close similarity with the *in vivo* situation is accompanied by the problematic nature of collecting analytical data from the inside of the 3D tissue model because initially only the cells on the surface are accessible for analysis. However, reliable ways of analyzing the reaction of the cells to an experimental stimulus are equally important for the successful application as the model itself. As of today, the problem persists that information from the inside of a 3D construct is only accessible by invasive means which only allow for end point assays without a time-dependent and continuous monitoring of the cell response. The most important three-dimensional tissue models as well as the established and well-known approaches to extract chemical or biological data from the inside of such a model will be discussed in detail in the following chapters.

II.2   Formation and Applications of 3D Tissue Models

In the recent past, different approaches have been established to mimic real three-dimensional tissue *in vitro* in order to be able to conduct measurements in a high throughput manner but simultaneously obtaining a more physiological cell response compared to standard two-dimensional cell culture. In these different models either only the cells themselves are used which group together and form three-dimensional structures (II.2.1) or a biocompatible supporting scaffold is provided where the cells can grow on (II.2.2 and II.2.3). Four of the most commonly used techniques to form 3D tissue models are presented in the following. General information on the formation and the application of the respective 3D tissue model will be given and the different tissue models compared to each other with respect to their advantages and disadvantages.

II.2.1 Generation of Scaffoldless 3D Cell Clusters

A prominent and widely used example are the so-called spheroids, i.e. spherical cell clusters consisting of some thousand cells which are used to create certain tissue types in order to investigate oxygen or nutrient gradients. These spheroids have initially been generated from one tumor cell type (multicellular tumor spheroids, MCTSs) and can be indicative for a first estimation of the chemosensitivity towards a given drug. The sizes of these MCTSs typically are around 500 µm and these small tumor models can help scientists to investigate and understand the microenvironments of an *in vivo* tumor. Especially in the field of tumor spheroids, combinations of two or three cell populations from different cell types are used to create one single spheroid in order to mimic real tumors even more precisely. However, not only tumor cells but also highly specialized, non-transformed cells like neurons (neuro spheroids) or cardiomyocytes (cardio spheroids) have already been successfully used to build three-dimensional tissue models for *in vitro* investigations. There are several ways and techniques described to generate spheroids[16]. Among the most widely used is the cultivation in hanging drops[17] where a small volume of cell suspension forms a drop on the underside of a substrate and the cells start to establish cell-cell contacts with each other because they are grouped close together and gravity prevents them from establishing contact with the substrate. Alternatively, spheroids can be generated using the liquid overlay method where cells are seeded in wells with a non-adhesive surface[18]. Oftentimes these cell culture receptacles with non-adhesive surfaces are additionally shaken to keep the cells in suspension. In both of these techniques the cells are not able to adhere to the surface and thus they will group together, aggregate and spontaneously form three-dimensional tissue constructs. Spheroids which have been generated this way are not interlaced with blood vessels and thus represent non-vascularized tissue. Exceeding a certain size, the center of the spheroid can no longer be sufficiently supplied because of the limitations of diffusive mass transport and a much-investigated central necrosis starts to occur due to a shortage of nutrients and oxygen[19]. The experimental investigations of the central necrosis shown in literature clearly demonstrate the complexity and difficulties in extracting chemical and biological information from the center of cell aggregates[20].

II.2.2   Tissue Engineering

A completely different form of creating three-dimensional tissue models is tissue engineering, which excels with spatially highly organized geometries and composition. In tissue engineering, cells first are cultivated and proliferated according to normal cell culture conditions. The cell suspension is then added to either synthetic or biological scaffolds, on which the cells can adhere and subsequently continue to proliferate under the influence of either growth factors or mechanical stimuli so that eventually a highly organized, three-dimensional tissue model is developed[21]. Generally speaking, tissue engineering comprises four elements: (i) living cells or tissue, (ii) a structural and biocompatible scaffold, (iii) signal transduction control of the living component (growth factors) and (iv) culture medium to provide nutrients. This principle is mostly applied in the field of regenerative medicine to regrow tissue and to be able to transplant it afterwards. With this approach, problems of transplant rejection can be limited by using autologous cells to regrow the target tissue[22].

Tissue engineering has already been successfully used to regrow cartilage tissue as this type of tissue consists of only one cell type (chondrocytes), nutrients *in vivo* are exclusively supplied by the articular fluid and cartilage tissue also uses a structure-providing scaffold from collagen fibers and proteoglycans[23]. To *in vitro* regrow other transplantable vital tissues from the body like kidney or liver parenchyma unfortunately is still a long way off as they are so complex in their construction that artificially creating viable organs has so far not been possible[24,25]. Even though a lot of progress has been made from the biological perspective, the analytical monitoring inside these tissue-engineered models is still extremely difficult and oftentimes not possible at all, although this would be indispensable for a controlled and reproducible tissue growth and to unfold their full potential in biomedicine.

II.2.3   Bioprinting

Closely related with the application of biological scaffoldings is the three-dimensional bioprinting, where, similar to a 3D printer, a mixture of nutrients, matrix elements, living cells and biocompatible scaffold-building blocks is used to create three-dimensional precursor structures which are then supposed to grow into independent tissues due to the proliferation of the cells[26]. Alternatively, cells can be suspended in a biocompatible gel made from proteins or other components present in the extracellular matrix. Examples for these components

which are normally used to fabricate the gels are collagen, fibrin, or hyaluronic acid. The cells suspended in the gels do not necessarily establish a direct physical contact with each other at first, but are able to communicate with their surroundings by signaling molecules, enabling biomedical investigations in a physiological microenvironment[27]. By mixing the respective cell type, the culture medium including all necessary nutrients and supplements as well as the scaffold-building material, unspecific three-dimensional tissue models can be formed in a short amount of time. The advantage of this method, however, lies in the possibility to reconstruct specific tissue pieces for later transplantation with high precision. In general, 3D bioprinting for the reconstruction of specific tissue parts can be divided into the following three steps:

(i) **Pre-Bioprinting:** In order to obtain the desired tissue substitute, a biopsy is needed from the biological point of view and a layer-by-layer image from the technical perspective. Suitable technologies to create such a model are *computed tomography* (CT) and *magnetic resonance imaging* (MRI). The multiplied target cells are then mixed with a viscous nutrient- and oxygen-providing culture medium to keep them alive and to prepare them for the printing process.

(ii) **Bioprinting:** The cell-medium mixture is filled in the bioprinter cartridge and each highly viscous layer deposited onto the next according to the medical scans. Solidifying processes of the individual layers can be accelerated by the use of crosslinking chemicals, heat or UV-light. The so-called pre-tissue is then transferred into an incubator which works at 37 °C and a humidified atmosphere to mature into the target tissue.

(iii) **Post-Bioprinting:** This maturation process is needed to adapt the tissue model to the conditions in the human body. The function as well as the mechanical stability are maintained and improved by chemical and mechanical stimulations to ensure excellent functioning in a constantly moving mammalian body.

There is a great variety of companies active in the field of bioprinting and applications range from the production of artificial blood vessels in vascular surgery to ideas of producing meat for the food industry or deceivingly real leather in the world of fashion[28]. Nevertheless, the problematic lack of analytical monitoring for these excellent biological models is not only valid for the tissue-engineered, but for the bioprinted tissue models alike.

II.2.4   Explantation

In surgical grafting, viable cells, cell clusters or even entire organs are taken from an organism. The so-called grafts can then be cultivated outside of the body until they are placed inside either the same or another organism. There are four graft types to be distinguished:

(i) **Autograft**, where a part of the body is relocated to another position as in skin graft after severe burns or when veins are taken from the leg to be used in heart surgery. Transplant rejection is nonexistent in this form since the body will recognize the cells as its own.

(ii) **Allograft** means the grafting between different individuals of the same species with their individual genotypes. Examples include the surgical transplantation of different organs like lung, kidney or heart. Transplant rejection needs to be taken into account and possibly suppressed with the help of immunosuppressants.

(iii) **Isograft** is the grafting between genetically similar organisms like identical twins. From the rejection perspective, this is highly favorable as the risk is minimal.
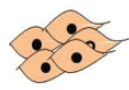
(iv) **Xenograft** is the process of transplanting between two individuals belonging to different species. An established example of this graft type is the replacement of human with porcine heart valves. The risk of graft rejection is substantial in this form and consequently immuno-suppressants are unavoidable.

Grafts from real organisms of course are medically indispensable but unquestionably inappropriate for high throughput drug research.

II.2.5   Hopes & Limits of 3D Tissue Models

It is highly complicated to decide which tissue model is better than the others as all of them have their "raison d'être". Spheroids of course are neither perfectly reproducible, nor do they win over with their phenotype similarity. But they are easily and rapidly made while being low cost and allow for quick testing at a high throughput level in the early stages of drug testing. Tissue engineering and bioprinting are a lot more complex processes and are therefore not used for rapid screening, but almost exclusively for medicinal purposes. The advantages and disadvantages of the different tissue types are compared to each other and to conventional two-dimensional cell culture in **Tab. 1**.

Tab. 1: Advantages and disadvantages of existing tissue models[29]. The table was adapted from Preethi et al. (2015). The characteristics reproducibility, drug penetration and similarity of the extracellular matrix (ECM) or the phenotype are compared to each other and to *in vivo* tissue (xenograft) with the help of plus and minus signs. Plus and minus signs signify better and worse representation of the individual characteristics, respectively, and the amount of signs shows the extent to which a physiological *in vivo* environment is imitated.

TISSUE MODEL	XENOGRAFT	TISSUE ENGINEERING	GEL EMBEDDING	SPHEROIDS	CELL MONOLAYER
REPRODUCIBILITY	+	+ +	−	−	+ + +
DRUG PENETRATION	+ + +	+ +	+ +	+ +	− − −
ECM SIMILARITY	+ +	+ + +	+	+	− − −
PHENOTYPE SIMILARITY	+ +	+ + +	+	− −	− − −

The main advantage of all three-dimensional tissue models compared with the two-dimensional equivalent is the ability to better represent the complexity of the tissue architecture and the mass transport rates of chemical substances in an *in vivo* sample. Cell-cell communication in a 2D model is very limited; every cell can only communicate and mechanically interact with the cells directly adjacent in the 2D tissue. In contrast to that, the cells in a three-dimensional model can additionally exchange signaling molecules with the cell layers above and below making the model more physiological. In addition, local concentrations as well as gradients of nutrients, oxygen and catabolic products reflect the reality better[30]. The extracellular matrix (ECM), which constitutes the filling material in between the cells and mediates a lot of chemical signals, is also fundamentally different in its organization in two and in three dimensions. Consequently, cell differentiation and polarization conditioned by the underlying ECM is also different and cell proliferation will reflect these differences when compared to *in vivo* conditions. Many studies have verified that the cell response in a three-dimensional tissue model comes closer to reality than in a two-dimensional one, especially when it comes to tissue-specific, physiological functions[31].

Recognizing the advantages mentioned above, three-dimensional tissue models are already widely used in preclinical studies to screen for novel, potentially active substances. Body-on-a-chip concepts are of special interest, as *in vitro* models of different organs are cultivated in a microfluidic chip and a flow of culture medium simultaneously provides oxygen and decreases levels of metabolic waste. The respective organ models and their microfluidic connections are arranged in a way that the organs are integrated in an entire, yet artificial

blood circulation process in which a series of different organ-specific metabolic reactions is mimicked. Thus, one tries to simulate the entire human body with all vital organ functions in the laboratory to be able to quantify the effects of active substances on the respective target tissue and simultaneously identify possible side effects on the target organ as well as on other organs in the organism[32]. This systemic approach of the body-on-a-chip models could help to further reduce the so far unavoidable animal testing which is still a mandatory part of the drug development process[33]. Especially relevant are these concepts in combination with human tissue models as they can favorably be obtained by differentiation of induced pluripotent stem cells (IPS cells). Using IPS cells for a systemic body-on-a-chip screening system renders the concern of potential species differences moot since the testing can be performed on an all-human test system.

II.3   Established Analytical Approaches for Monitoring 3D Tissue Models

Three-dimensional tissue models have experienced a great leap in development when it comes to the underlying structure and biology. The possibilities to chemically analyze and monitor the cells forming part of the 3D tissue after having been exposed to experimental noxae, however, are still trailing far behind. This of course is highly unfortunate because next to the biology itself, the analysis and the monitoring is the second crucial prerequisite to successful testing. In principle, there are three categories of analytical approaches to be distinguished which are introduced in the following.

II.3.1   Optical Analysis of Cells in the Periphery of the Tissue Model

Most analytical approaches can only investigate and monitor cell layers close to the surface of a tissue model. Predominantly, these are the very same techniques and assays used in the monitoring of two-dimensional cell monolayers. Typical examples of such analytical methods are the widely used metabolic assays which quantify the ability of a cell population to enzymatically reduce a dye precursor to a chromophore or a fluorophore. The resulting concentration of the chromo- or fluorophore after a certain incubation time directly reflects the metabolic activity of the cells and therefore their viability[34]. Examples are resazurin-based assays where the non-toxic blue precursor dye molecule resazurin (7-Hydroxy-3*H*-phenoxazin-3-one-10-oxide) is metabolically reduced by the NADH and $FADH_2$-dependent dehydrogenase to the pink-colored and fluorescing resorufin (7-Hydroxy-3*H*-phenoxazin-3-one) in living cells. The amount of resazurin being reduced to resorufin provides information on the viability of the cells. Similarly, tetrazolium salts can be reduced to the product formazan – a chromophore – with the help of dehydrogenases and reductases as enzyme classes in living cells. In these approaches, cells are first incubated with a specific substance of interest or otherwise pretreated prior to the addition of the viability reagent. This reagent is then converted to the fluorescing or colored product which can be read out at a specific wavelength. For the conversion of the precursor molecules into the detectable product, on the one hand they need to diffuse into the cytosol first and on the other hand the enzyme activity is another limiting factor. Consequently, an incubation step with the viability reagent is inevitable and no time-dependent information can be obtained[35].

Alternatively, the metabolic activity of a given cell population can be quantified by assessing the oxygen consumption rate during respiration. Cells in this particular approach are loaded with oxygen-sensitive nanoparticles (nano probes) whose luminescence can be determined after internalization into the cytoplasm to calculate the partial oxygen pressure[36]. Similarly, highly specific immunocytochemical and immunohistochemical stains can be applied in combination with microscopic analysis. However, there are two limiting factors for the microscopic approach to analyze tissue models: Firstly, mass transport rates from the periphery to the center of the spheroid are low and difficult to control if for example the conversion of a chemical substance is used as a readout system or a nano probe is supposed to be placed in the center of the spheroid. And secondly, the penetration depth of visible light for tissue models or tissue-like models is highly limited to approximately 300 μm, making only the topmost cell layers accessible for this method[37]. The reason for this phenomenon is that tissue models or human skin in particular contain a variety of chromophores which can absorb light and in addition, the incident light is scattered by organelles, granules and others in a wavelength-dependent manner[38]. A certain improvement concerning the penetration depth of an optical readout can be obtained by using techniques relying on near-infrared radiation (NIR), e.g. two-photon excitation microscopy (TPEF) or the use of upconverting nano-particles with which a penetration depth for the excitation light in the millimeter range is achievable[37] and furthermore, in the near-infrared range, no autofluorescence of the bio-molecules is triggered. However, the emitted luminescence which is needed for analysis is again in the visible wavelength range and therefore bound to the same basic conditions explained above. Current state-of-the-art methods to record time-dependent information for cells in the periphery of the tissue model for instance are genetically encoded fluorescent sensors which can be read out optically. Different sensor platforms for genetically encoded fluorescent sensors include e.g. *Förster resonance energy transfer* (FRET) or dimerization-based sensors[39]. These techniques generate a fluorescence signal after the two components either directly interact with each other or at least come into close contact with each other. The specificity of the genetically encoded sensors is excellent but the readout principle is again bound to the limits of the penetration depth. Apart from the genetically encoded fluorescent sensors, the aforementioned methods oftentimes only allow for endpoint determinations due to the (photo)toxicity of the needed markers and thus, no time-resolved observations of the cell response dynamics are possible.

II.3.2   Integral, Non-Invasive Analysis of Tissue Models

For an integral, non-invasive and label-free analysis of complex tissue models, the electrochemical impedance analysis has become firmly established. The application of a low AC voltage is able to non-invasively reach the inside of tissues or spheroids and yields information on the vitality and morphology of all cells along the current pathway by recording their dielectric properties. A variation of the measurement frequency allows for a separate monitoring of the extracellular way of the current around the cells and the intracellular way of the current directly through the cells. This way, changes in cell morphology which were elicited for example by a necrotic cell swelling or an apoptotic cell shrinking can be recorded quantitatively in a time-dependent way as well as for extended time periods[40]. There are basically three ways for the implementation of impedance spectroscopy on multicellular spheroids – being the most widely used tissue model – described in literature:

(i)   Hydrodynamic focusing of a spheroid at the opening of a central narrowing in a capillary with electrodes on both sides[40],

(ii)   Positioning of a spheroid on planar electrode structures[41],

(iii)   Lowering a spheroid into a cavity on a silicon chip with electrodes on the side walls of the cavity[42].

The undisputed advantage of an impedance-based dielectric analysis of tissue models is the non-invasive nature to monitor the spheroid or any other tissue model in its entirety. Measurement setups akin to the latter have already been successfully used to quantitatively test chemotherapeutic agents on multicellular tumor spheroids (MCTS) to get an estimation of chemosensitivity[42].

Another technique pertaining to this category is the digital holographic microscopy (DHM) which can depict the three-dimensional outer form of a spheroid and its change over time with high precision and accuracy without the need for a label. In this technique, an interference pattern (the hologram) is created with the help of coherent, monochromatic light being first split in two beams – the object beam and a reference beam – to be recombined behind the sample and thus create a unique interference pattern. DHM with a laser wavelength of 840 nm and a CCD camera at the Fourier plane of the object has a substantial penetration depth of more than a millimeter to offer[43] with the main drawback being the impossibility to label a specific feature of the sample and the occurrence of coherent noise as well as other disturbances based on reflections in the experimental setup[44]. Next to the DHM, phase

contrast microscopy (see chapter III.2.1) also qualifies for an integral and non-invasive depiction of the outer morphology of e.g. spheroids. However, from the three-dimensional geometry of the respective tissue model, only the outline can be projected to a two-dimensional image with the help of this technique. Due to the easy handling, phase contrast microscopy is often used for routine control during spheroid formation.

A new method for the monitoring of the respiration of spheroids has recently been established at the University of Regensburg (PhD thesis Carina Schmittlein, 2017). With this technique, it is possible to get a non-invasive but nonetheless spatially resolved analysis of the oxygen consumption. Fully grown spheroids are deposited on a culture substrate which is coated with a functional layer consisting of an oxygen-permeable polymer doped with two fluorophores. One of those fluorophores exhibits an oxygen-sensitive emission due to quenching processes in the presence of higher levels of oxygen, while the other one serves as an oxygen-insensitive reference. With the help of a previous calibration, the ratiometric fluorescence signal from both fluorophores can be used to quantitatively calculate local oxygen concentrations. As soon as the spheroids establish contact with the sensor foil, the cells start to adhere and to spread on the surface until the initially round structure has eventually flattened to yield a semi-spherical geometry. Taking these underlying conditions into consideration, one can depict the local oxygen distribution underneath the spheroids from the ratiometric imaging.

II.3.3   Spatially Resolved, Destructive Analysis of Tissue Models

Apart from the analysis methods mentioned above which monitor the whole, intact tissue model, it is also possible to measure metabolite gradients within three-dimensional tissue models by inserting analyte-sensitive microelectrodes into the sample. This way, e.g. oxygen tensions were measured along the diameter of mesenchymal stem cell spheroids with the help of an invasive 10-µm micro electrode[45]. A two-dimensional analysis of a target molecule can be achieved by rapidly freezing the biological sample and afterwards slicing it into thin layers in a thickness range typically between 10 µm to 20 µm[46] or even less[47]. Within these individual layers, the lateral distribution of metabolites or other molecules of interest can then be determined. Thus, the complexity of a three-dimensional distribution is simplified to a two-dimensional problem. Analysis can for instance be performed with matrix-assisted laser desorption/ionization mass spectrometry (MALDI). MALDI appeals with a lateral resolution of less than 100 µm and yields complete mass spectra of the investigated volume element[48].

Knowing the metabolites' distribution in each slice makes a three-dimensional mapping of the entire sample accessible via computer-assisted reconstruction. Due to the high analytical information content of the mass spectra, the three-dimensional distribution of an abundance of interesting analytes is available at the same time. Similar approaches have been attempted on the basis of highly specific bioluminescence staining coupled with optical microscopy[49]. Immunohistochemical and immunocytochemical stainings of such cryosections enable a detailed structural analysis of spheroids and other three-dimensional tissue models with molecular specificity. The drawbacks of these approaches are not far to seek: they are all endpoint assays lacking any information about the time-dependent change in metabolite concentration under the influence of an experimental model substance. Apart from the lack of time-dependent information, the spheroids have to undergo complicated and highly invasive preparation steps to end up as cryosections.

The last example constitutes a technique of maximal invasiveness: the spheroid as the tissue model is completely disassembled into single cells in order to be able to conduct an analysis of genomics and proteomics. Having separated all the cells from each other enables flow cytometry and also fluorescence-activated cell sorting (FACS) to count the cells and to sort them according to physical or molecular properties with the help of fluorescently-labelled antibodies, viability dyes, fluorescent expression proteins and many more[50]. This way, distinct properties of a whole cell population can be documented on a single cell basis. The information depth is unparalleled but at the same time so is the degree of invasiveness.

II.4   Objectives

This project shall attempt to create a completely new technological approach to fundamentally improve and to advance the sensoric monitoring of 3D tissue and organ models. Instead of retrofitting a 3D tissue model with sensoric functionality, e.g. microelectrodes or nanoprobes, or to slice the model up at the time of the measurement to extract spatially resolved chemical or physical information from the inside, the tissue models should be composed of a distinct number of two-dimensional layers already equipped with the required electrochemical sensoric elements. Therefore, 2D cell monolayers shall separately be cultivated on both sides of permeable supports, with the porosity ensuring mass transfer and cellular communication in all three dimensions. Those already integrated sensoric elements on each side of the permeable supports will allow for individual addressing and analyzing of every single cell layer in this artificial tissue model. Later on, several of these permeable supports with a fully differentiated cell layer on both sides shall be stacked together in a measurement cell with the close proximity of the individual layers ensuring a physiological environment for the cells. This way, a partial mechanical contact can be realized through the filter membrane and chemical communication is possible via diffusion processes. These final 3D hybrid models could comprise either only cell layers of the same type or, in a kind of modular construction system, they could be composed of different cell types. The system could also be used with induced pluripotent stem cells which have become increasingly important in regenerative medicine. In the long run, human organ models could be envisioned in which every single tissue would be individually addressable thanks to the integrated sensors.

For the implementation, permeable polycarbonate membranes should be equipped on both sides with thin planar gold-film electrodes so that on each side cells will be able to grow directly on the electrodes and therefore be monitored impedimetrically. Impedance spectroscopy on two-dimensional cell layers has been established in the recent past as a versatilely applicable method to quantitatively analyze the dynamic properties of cells adhering to the electrodes. It shall now be used to individually monitor the cell layers which will be stacked closely together in the novel three-dimensional tissue model. **Fig. 1** shows the original project idea as an exploded assembly drawing like it was submitted in the exposé of the application process for a PhD scholarship by the "Studienstiftung des deutschen Volkes".
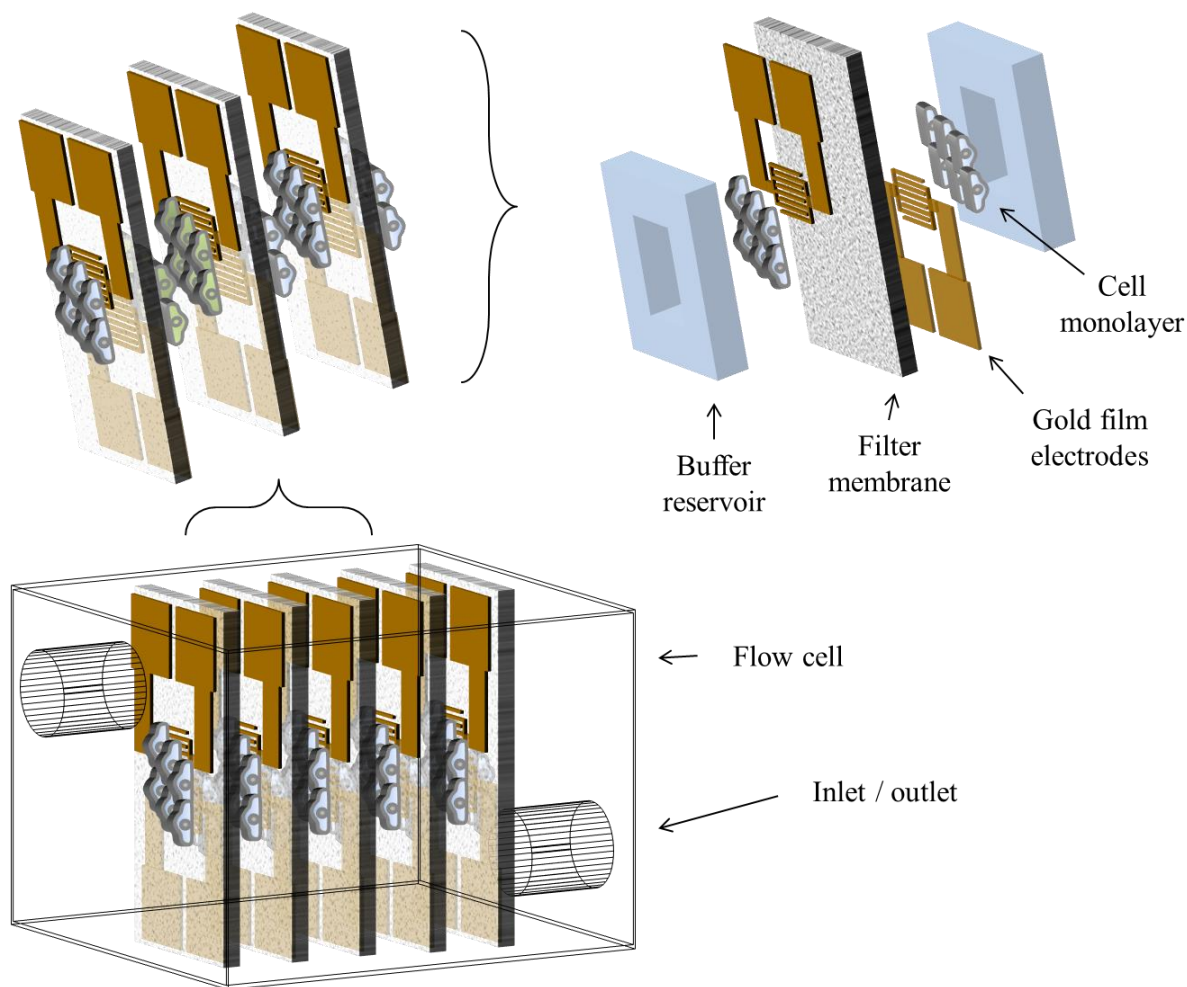
Fig. 1: Schematic exploded drawing of the impedimetric sensors for 3D tissue models in a modular construction system as submitted in the application for a PhD scholarship by the "Studienstiftung des deutschen Volkes".

Possible applications for the final tissue model assays could for instance include:

- Determination of the cell viability,
- Monitoring of the activation of signal cascades after stimulation,
- Analysis of metabolically-driven micromotions.

Thanks to the layer-by-layer setup, analytical information from the inside of the tissue model will be made accessible and obtained in real time, non-invasively and label-free which has previously not been possible.

All in all, this project aims to yield a contribution to bridge or at least narrow the yawning gap between the far-developed biological tissue models and the still lagging ways to extract analytical information out from the inside.

III   METHODS

The following chapter will provide background information on the most important experimental techniques used in this PhD thesis. The main focus lies on impedance spectroscopy and the application *Electric Cell-Substrate Impedance Sensing* because it is the core concept of the developed tissue model. Other techniques implemented in this thesis are also discussed, however not as detailed.

III.1   Impedance Spectroscopy

III.1.1   Theoretical Background

Impedance spectroscopy is built on a foundation that was already laid in 1825 and 1826 by the German physicist and mathematician Georg Ohm. It starts with Ohm's law that was published in 1827:

$$U = R \cdot I \tag{1}$$

The direct current (DC) voltage (U) equals the product of an Ohmic resistor (R) and the resulting current (I). However, Ohm's law can also be applied in the case of alternating current (AC) with slight modifications. Since an AC voltage is not constant in time but exhibits a harmonic oscillation, it can mathematically be described as the complex voltage:

$$U(t) = |U| \cdot (\cos(\omega t + \varphi_U) + i \sin(\omega t + \varphi_U)) \tag{2}$$

|U| is the amplitude of the complex voltage and ω in the arguments is the angular frequency. The angular frequency equals $\omega = 2\pi f$ which renders the voltage frequency-dependent. φ_U is the voltage phase shift and i is the imaginary unit ($i^2 = -1$). In response to an applied complex AC voltage, a corresponding complex alternating current is induced in the system under study with the amplitude |I| at the same frequency. However, dependent on the system, the resulting current I(t) can be shifted in phase φ_I between +90° and –90° with regard to U(t).

$$I(t) = |I| \cdot (\cos(\omega t + \varphi_I) + i \sin(\omega t + \varphi_I)) \tag{3}$$

This phase shift occurs in the presence of storage elements in the circuit (e.g. capacitive or inductive elements). In an ideal capacitor, the voltage trails the current at exactly 90° and per

definition this equals a phase shift of –90°. The frequency-independent voltage and current expressions in equation (1) can now be substituted with equations (2) and (3) which yields the impedance Z as the AC equivalent for the resistance R under DC conditions:

$$Z = \frac{U(t)}{I(t)} = \frac{|U| \cdot (\cos(\omega t + \varphi_U) + i\sin(\omega t + \varphi_U))}{|I| \cdot (\cos(\omega t + \varphi_I) + i\sin(\omega t + \varphi_I))} \tag{4}$$

The term is favorably expressed using an exponential representation via Euler's formula:

$$e^{ix} = \cos(x) + i \cdot \sin(x) \tag{5}$$

With Euler's formula (eq. (5)), equation (4) can be simplified to:

$$Z = \frac{|U| \cdot e^{i(\omega t + \varphi_U)}}{|I| \cdot e^{i(\omega t + \varphi_I)}} = |Z| \cdot e^{i(\varphi_U - \varphi_I)} = |Z| \cdot e^{i\varphi} \tag{6}$$

The ratio of a complex sinusoidal voltage and the respective complex current equals the impedance with the magnitude $|Z|$ and the corresponding phase angle difference φ ($\varphi_U - \varphi_I$) which can be expressed either in polar coordinates or in a Cartesian complex plane representation (*Nyquist plot*) where the complex impedance is divided into the real part Z' (resistance, R) on the x-axis and the imaginary part Z'' (reactance, X) on the y-axis:

$$Z = Z' + i \cdot Z'' = R + i \cdot X \tag{7}$$

In these *Nyquist plots*, in which the complex impedance is split in its real and imaginary part and the imaginary reactance is plotted against the real resistance, the impedance at each distinct frequency yields one single point in the plot. Identical scaling of both axes allows for characteristic shapes and to quickly assess the dielectric structure of the system and to identify individual impedance elements. However, it is not possible to extract frequency dependencies from *Nyquist plots*. Alternatively, one can use *Bode plots* where log$|Z|$ and φ are plotted against log(f), yielding the impedance spectra $|\mathbf{Z}|(\mathbf{f})$ and the phase spectra $\boldsymbol{\varphi}(\mathbf{f})$. In this thesis, exclusively *Bode plots* were used as frequency dependencies have been essential during the development of the measurement system.

A commercially available Impedance/Gain-Phase analyzer (SI 1260A, Ametek Scientific Instruments, US) measures the oscillating current amplitude and the respective phase shift at a pre-set 50-mV root mean square (RMS) voltage amplitude. According to equation (4), this directly yields the magnitude of impedance which, together with the phase shift, can be used to calculate the resistive real part and the reactive imaginary part according to the following equations:

$$|Z| = \sqrt{R^2 + X^2} \tag{8}$$

and

$$\varphi = arctan\left(\frac{X}{R}\right) \tag{9}$$

Knowing the reactance allows for a transformation into the equivalent capacitance C:

$$C = \frac{1}{2\pi f \cdot X} \tag{10}$$

The resistance and the capacitance can, similar to the *Bode plots*, also be plotted against the frequency in a log-log plot, yielding **R(f)** and **C(f)**.

III.1.2 Electrical Cell-Substrate Impedance Sensing

Taking up on the principle of impedance spectroscopy, the technique of *Electric Cell-Substrate Impedance Sensing (ECIS®)* was developed in the 1980s by Drs. Ivar Giaever and Charles Keese at *General Electric Corporate Research and Development*. In 1984, Giaever and Keese baptized their first publication using that technique "Monitoring fibroblast behavior in tissue culture with an applied electric field"[51]. The basic principle is to grow cells on a thin electrode, apply a low, non-invasive AC voltage and to measure the resulting current as the cells provide an additional impedance. Advantages of this technique include the non-invasive and label-free character and therefore the ability to continuously collect data for extended periods of time[52,53]. ECIS® has evolved into a versatile and well-established tool for cell monitoring in bioanalysis. The electrode material is typically non-cytotoxic gold in a layer thickness of 50 – 100 nm which is thick enough to provide excellent conductivity and at the same time thin enough to be optically semi-transparent. Two electrodes as well as an electrolyte are needed for the electric circuit to be closed and thus, a simple equivalent circuit can be used to describe the cell-free system. In this equivalent circuit, there is a resistor and a capacitor connected in series; the resistor representing the frequency-independent resistance of the leads, the electrolyte as well as the constriction resistance for smaller electrodes (the contributions are grouped together as R_{bulk}) and the frequency-dependent electrode-electrolyte interface is represented by the capacitor. According to equation (8) in the previous chapter, the magnitude of impedance can be calculated by the square root of the sum of the squared resistance and reactance values. According to equation (9), the reactance can be expressed as

$X = 1/(2\pi f \cdot C)$. The purely resistive part R_{bulk} dominates at high frequencies resulting in a horizontal line in the impedance spectra and a corresponding phase shift of 0°. The electrode-electrolyte interface on the other hand behaves almost like an ideal capacitor and this capacitive part becomes the more important the lower the frequency gets. This is due to the fact that at low frequencies the capacitor is fully charged before the AC voltage is reversed and thereby the diffusion of ions as charge carriers is inhibited. Mathematically speaking, at high frequencies the reactance can be neglected due to the frequency position in the denominator, whereas at low frequencies the reactance outweighs the resistance. In double-logarithmic presentation, this capacitive element is displayed by a straight line with a slope close to (–1) and a corresponding phase shift of –90°. The fact that the interface impedance of noble metal electrodes immersed in physiological buffers deviates slightly from that of an ideal capacitor ($Z_C = (i\omega C)^{-1}$) is well-known[54] and is therefore better described by the empirical impedance of a *constant-phase element* ($Z_{CPE} = (i\omega)^{-n} \cdot A^{-1}$) that accounts for the non-ideality by the introduction of the parameters n_{CPE} and A_{CPE}. The first parameter indicates the ideality of the capacitor in the range of $0 \leq n_{CPE} \leq 1$ with $n_{CPE} = 0$ meaning it is purely resistive ($\rightarrow 1/A_{CPE} = R$) and $n_{CPE} = 1$ showing ideal capacitive properties ($\rightarrow A_{CPE} = C$).

There exists a broad variety of electrode layouts but the most widespread are the 8-well-1-electrode (8W1E) and the 8-well-10-electrode (8W10E) versions, where a large electrode serves as counter electrode (CE) for all eight wells and each of the eight wells contains either one or ten small circular working electrodes (WE, diameter of 250 µm). The working electrodes from each well are measured sequentially against the substantially larger counter electrode. By choosing a ten to a hundred times larger counter electrode, the capacitance of the counter electrode can be neglected as capacitances connected in series mathematically need to be added in a reciprocal way:

$$\frac{1}{C_{total}} = \frac{1}{C_{WE}} + \frac{1}{C_{CE}} \qquad (11)$$

The size ratio of the two electrodes focusses the measurement on the smaller electrode as it has an impact on the resistive and the capacitive contributions alike and thus, only the 50 – 100 cells on the working electrode contribute to the signal in an 8W1E array and ensure maximum sensitivity for migration and micromotion studies. Consequently, in the case of 8W10E arrays 500 – 1000 cells can adhere to the area of the working electrode which on the one hand reduces the sensitivity but on the other hand provides a fair average of the whole cell population. Typical assay formats for this array type include cell adhesion and

cytotoxicity studies. Whereas the impedance spectrum of a cell-free electrode can be easily described by an equivalent circuit as already mentioned above, cells growing on the electrode make things a lot more complicated. As a first approach, a resistor ($R_{cell\ layer,\ cl}$) and a capacitor ($C_{cell\ layer,\ cl}$) can be added which are connected in parallel and inserted between the bulk resistance and the electrode-electrolyte interface. R_{cl} takes into account the intercellular resistance for the current flowing beneath the cells as well as through the cell-cell contacts and C_{cl} corresponds to the capacitive properties of the lipid bilayer making up the cell membrane. With a confluent cell monolayer growing on the electrode surface, the current has two options to pass the cell layer in order to reach the counter electrode as shown in **Fig. 2**: it can either flow extracellularly underneath the cell and then through the cell-cell contacts (mainly tight junctions, depicted in red) or take the direct transcellular route (depicted in green). The first alternative is the way of choice at lower frequencies and the latter at higher frequencies which can once more be explained by the parallel connection of the resistive paracellular element and the capacitive transcellular element. At low frequencies, the capacitive route is of high impedance which is why the resistive way is preferred and vice versa.
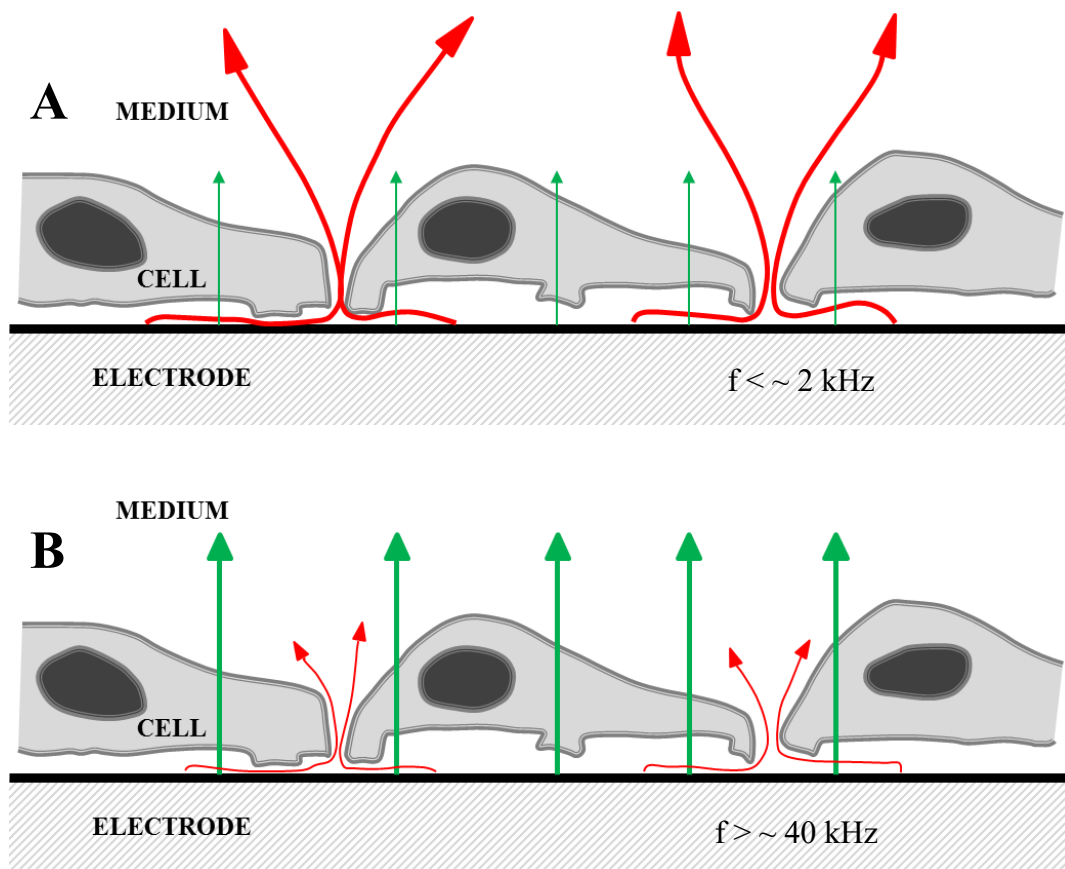
Fig. 2: Schematic image of alternative routes of the current through a confluent cell layer. (**A**) depicts the mostly extracellular way at frequencies lower than ~ 2 kHz and (**B**) corresponds to the primarily transcellular way at frequencies higher than ~ 40 kHz. The frequencies only serve as guidelines as they depend on electrode geometry and cell type. The figure has been adapted from the homepage of Applied BioPhysics, Inc. founded by Drs. Giaever and Keese in 1991.

The resulting equivalent circuit is an acceptable first estimate; however, it cannot discriminate between the part of the current flowing in the narrow cleft between the cells and the substrate and the part flowing through the cell-cell contacts. These two contributions are taken together as R_{cl}. To take these different pathways into consideration and to be able to discriminate between them, Giaever and Keese developed a model[52] that shall be discussed in the following. The model was originally published in 1991 and introduces three cell-related parameters that can be extracted from an experimental spectrum and can therefore be used to distinguish between different cell types according to the spectra of the cell-covered electrode. **Fig. 3** illustrates the assumptions made for the development of the ECIS® model.
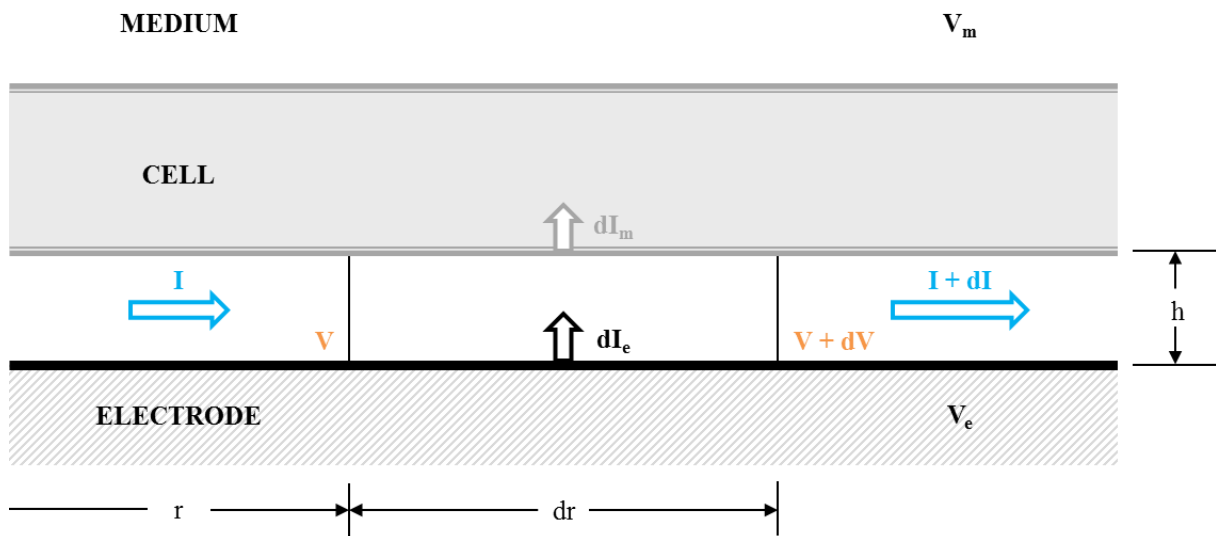
Fig. 3: Depiction of the cleft between the cell and the electrode and the radial current flow within. This figure was adapted from the original publication by the Drs. Giaever & Keese in 1991 in which the cells are assumed to be circularly shaped discs. Different potentials of the electrode and the culture medium are denoted V_e and V_m, respectively. h is the height of the space between the cell and the electrode, r is the radius of an arbitrary area, dr is an infinitesimally small extension of the radius, dI_e and dI_m are the contributions of the current flowing from the electrode into the subcellular cleft and from the cleft into the cells.

For the development of the model, the area under the cells is divided into infinitesimally small elements. Furthermore, **Fig. 3** as well as equation (4) and the definition of the resistance R (compare equation (12)) are needed. In (12), ρ equals the specific resistance, L is the length of the resistive element and A is the cross section of the resistive element. Thus, the current routes in the channel, from the electrode and through the cell are expressed as stated in the following equations:

$$R = \frac{\rho \cdot L}{A} \tag{12}$$

(Current in channel) $\qquad V - (V + dV) = I \cdot \dfrac{\rho dr}{2\pi r \cdot h} \tag{13}$

(Current from electrode) $\qquad V_e - V = \dfrac{Z_e}{2\pi r dr} \cdot dI_e \tag{14}$

(Current through cell) $\qquad V - V_m = \dfrac{Z_m}{2\pi r dr} \cdot dI_m \tag{15}$

Z_e (f) is the frequency-dependent impedance of the electrode-electrolyte interface and Z_m (f) is the frequency-dependent integral membrane impedance of the cells (apical and basolateral membranes connected in series). The part of the current having entered the subcellular cleft but not entered the cell equals the part flowing radially underneath the cell:

$$dI = dI_e - dI_m \tag{16}$$

Solving equation (13) for I and taking the derivative on both sides yields an expression for dI which, together with the equations (14) and (15) solved for dI_e and dI_m, can substitute the three terms in equation (16) after having divided the whole equation by dr. That leaves an expression depending only on the potential in the form of equation (17) with equations (18) and (19) as simplifying substitutions.

$$\frac{d^2V}{dr^2} + \frac{1}{r} \cdot \frac{dV}{dr} - \gamma^2 \cdot V + \beta = 0 \tag{17}$$

$$\gamma^2 = \frac{\rho}{h} \cdot \left(\frac{1}{Z_e} + \frac{1}{Z_m} \right) \tag{18}$$

$$\beta = \frac{\rho}{h} \cdot \left(\frac{V_e}{Z_e} + \frac{V_m}{Z_m} \right) \tag{19}$$

This differential equation can be solved with the help of Bessel functions because the prerequisite of cylindrical coordinates are given in this problem. The final solution can be seen in equation (20) with equation (21) showing the involvement of the subcellular cleft height in the total impedance of the cell-covered electrode.

$$\frac{1}{Z_{cl}} = \frac{1}{Z_e} \cdot \left(\frac{Z_e}{Z_e + Z_m} + \frac{\dfrac{Z_m}{Z_e + Z_m}}{\dfrac{\gamma r_c}{2} \cdot \dfrac{I_0 \cdot (\gamma r_c)}{I_1 \cdot (\gamma r_c)} + R_b \cdot \left(\dfrac{1}{Z_e} + \dfrac{1}{Z_m} \right)} \right) \qquad (20)$$

$$\gamma r_c = r_c \sqrt{\frac{\rho}{h} \cdot \left(\frac{1}{Z_e} + \frac{1}{Z_m} \right)} = \alpha \cdot \sqrt{\frac{1}{Z_e} + \frac{1}{Z_m}} \qquad (21)$$

In Equation (20), Z_{cl} is the total impedance of a confluent cell layer growing on an electrode, r_c is the average radius of the cells and I_0 and I_1 are modified first and second kind Bessel functions. Equation (20) also displays the first ECIS® parameter **R_b** which corresponds to the resistance between the cells. The second parameter **α**, which describes the impedance of the subcellular cleft, is hidden in the term γr_c as shown in equation (21). The last cell-related parameter **C_m** can be extracted from Z_m according to equations (8) and (10) as the membrane capacitance is purely capacitive which makes the impedance equal to the reactance and therefore $Z_m = X_m = 1/(\pi \cdot f \cdot C_m)$. The three cell-related parameters, their origins, units and the visibility in the impedance spectrum are listed in the following table. The cell-independent parameters of the electrode-electrolyte interface n_{CPE} and A_{CPE} as well as the resistance of the electrolyte R_{bulk} are also included.

Tab. 2: Extractable parameters from the ECIS® model. Parameters α, R_b and C_m are cell-related whereas n_{CPE}, A_{CPE} and R_{bulk} stem from the electrode-electrolyte system alone.

	Parameter	Origin	Unit	Visibility
Cell parameter	α	Impedance from cell adhesion sites	$\sqrt{\Omega} \cdot cm$	Plateau slope
	R_b	Resistance between cells	$\Omega \cdot cm^2$	Plateau height
	C_m	Membrane capacitance	$\mu F / cm^2$	Distance electrode & cell dispersion
System parameter	n_{CPE}	Ideality of capacitor	dimensionless	Slope of electrode dispersion
	A_{CPE}	Roughness of electrode surface	$\mu F \cdot s^{(n-1)} / cm^2$	Position of electrode dispersion
	R_{bulk}	Resistance of electrolyte	Ω	Frequency-independent impedance at high frequencies

To better visualize the influence of the different parameters, *Bode plots* for three different cell types (*normal rat kidney cells – **NRK*** and *Madin-Darby canine kidney cells – MDCK* in a high resistant strain (**MDCK-I**) and a low resistant strain (**MDCK-II**)) are simulated in **Fig. 4**. The electrode layout was chosen to be similar to the commercially available 8W10E ECIS® array from Applied BioPhysics, Inc. This includes values for $A_{CPE} = 15\ \mu F \cdot s^{(n-1)}/cm^2$

26

and $n_{CPE} = 0.95$. The bulk resistance was set to be $R_{bulk} = 250\,\Omega$. NRK cells are leaky epithelial-like cells, MDCK-II cells are moderately tight epithelial cells and MDCK-I cells are extremely tight epithelial cells (compare chapter IV.2). Because of these differences due to the number and nature of cell-cell contacts, the three cell lines show very distinct and distinguishable impedance spectra. The most striking difference is in the parameter R_b as it directly reflects the resistance of the cells. The experimentally determined parameter values for α, R_b and C_m from Reiss et al. (2015), which were used to simulate the spectra, are listed in **Tab. 3**. Extracting the parameters from experimental spectra as well as simulating the spectra in **Fig. 4** was done with a LabVIEW™ software written by Prof. Dr. Joachim Wegener (ECIS_fit_cir_V2019-01 & ECIS-simulation-2017-V2-0, respectively) according to the ECIS® model explained above.

Tab. 3: Extracted ECIS® model parameters from a collection of experimental data for three different cell types. NRK cells are considered to be epithelial-like, MDCK-II cells are moderately tight epithelial cells and MDCK-I cells are very tight epithelial cells. Simulations were done with a LabVIEW™ software written by Prof. Dr. Wegener according to the ECIS® model described above. Published data incl. the error margin by Reiss et al. (2015) is shown.

Cell type	$\alpha\,/\,\sqrt{\Omega}\cdot cm$	$R_b\,/\,\Omega\cdot cm^2$	$C_m\,/\,\mu F\cdot cm^{-2}$
NRK	7.9 ± 0.3	9.3 ± 0.8	1.20 ± 0.08
MDCK-II	16 ± 0.6	88 ± 4	3.03 ± 0.03
MDCK-I	117 ± 3	2870 ± 240	1.91 ± 0.03
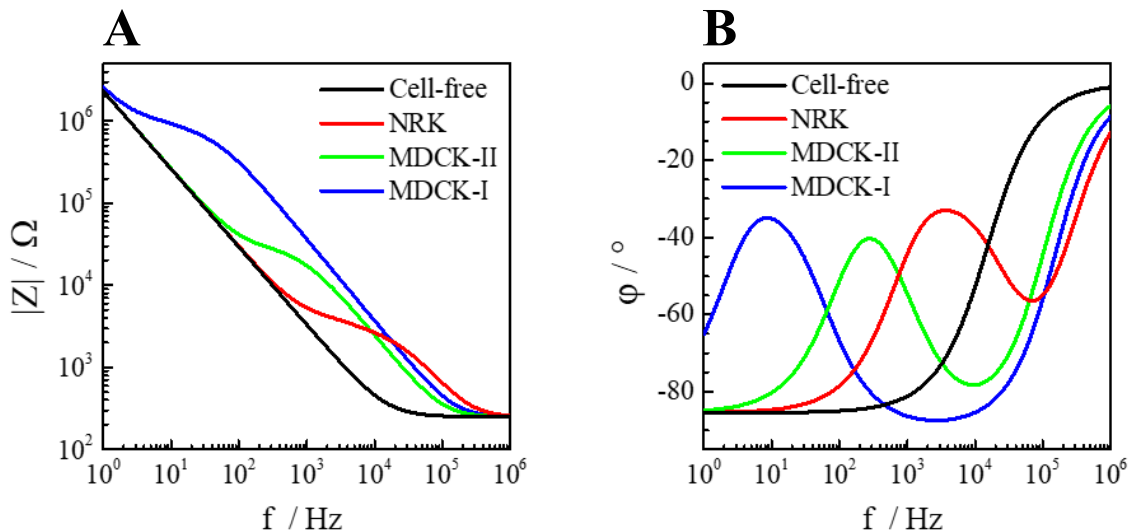
Fig. 4: Bode plots of a cell-free electrode (**black**) in the typical 8W10E layout with an electrode area of $5\cdot10^{-3}$ cm². $R_{bulk} = 250\,\Omega$, $A_{CPE} = 15\,\mu F\cdot s^{(n-1)}/cm^2$, $n_{CPE} = 0.95$. The impedance spectrum (**A**) and the corresponding phase spectrum (**B**) of the same electrode were simulated according to the ECIS® model when covered by a confluent epithelial-like NRK cell layer (**red**), a confluent moderately tight epithelial MDCK-II cell layer (**green**) and a confluent very tight epithelial MDCK-I cell layer (**blue**). Values of the cell-related parameters as used in the simulation are given in **Tab. 3**.

As stated in chapter III.1.1, an ideal resistive element displays a horizontal line in the impedance spectrum and a phase shift of 0°. An ideal capacitive element is reflected by a straight line with a slope of (–1) in the impedance spectrum and a phase shift of –90°. This is also true for the cell contributions, although ideal values are of course not reached. **Fig. 4** shows that the impedance spectrum of a cell-covered 8W10E electrode exhibits two horizontal frequency regions as well as two regions with a slope close to minus one. At low frequencies, this is due to the capacitive electrode-electrolyte interface and at high frequencies the resistive influence of the electrolyte resistance is the dominating factor. In the mid-frequency region, the cell influence is visible with the resistive and capacitive contributions at lower and higher frequencies, respectively. The more cell-cell contacts a cell type expresses, the higher is the impedance value in the mid-frequency spectrum which corresponds to a high R_b value. The increasing height of the plateau is also accompanied by the occurrence at lower frequencies. Thus MDCK-I cells exhibit a plateau at approximately $1\,M\Omega$ and $10\,Hz$, MDCK-II cells at around $30\,k\Omega$ and $500\,Hz$ and NRK cells at only $4\,k\Omega$ and $10\,kHz$. Each horizontal stretch in the impedance spectrum is accompanied by a maximum in the phase spectrum whereas every region exhibiting a straight line with a slope close to (–1) in the impedance spectrum entails a minimum in the phase spectrum. Local maxima in the phase shifts are therefore observed at $10\,Hz$, $500\,Hz$ and $10\,kHz$ for MDCK-I cells, MDCK-II cells and NRK cells, respectively.

The slope of the plateau directly reflects the value of α because the slope is steeper for higher α values. Thus, the plateau slope is steepest for the MDCK-I cells and only falling gently in the case of the NRK cells, indicating higher α values for MDCK-I cells. The last parameter C_m is observable in the spectrum by comparing the fixed position of the capacitive dispersion of the electrode-electroyte interface and the C_m-dependent position of the capacitive cell dispersion on the frequency axis because both are flanking the cell-specific plateau. If different C_m values are compared on the same electrode layout, the cell-specific dispersion for lower C_m values is observed at higher frequencies (entailing a broader plateau) and the capacitive dispersion for higher C_m values is found at lower frequencies (narrower plateau). In the spectra in **Fig. 4**, the cell dispersion at the lowest frequency corresponds to the MDCK-II cells (highest C_m value) and the one at the highest frequency to the NRK cells (lowest C_m value).

III.2 Optical Imaging Techniques

In the following, all microscopic imaging techniques that were used in this thesis will be discussed. As the focus lay on the electrochemical aspect and microscopy was only used for characterizational purposes, the descriptions are not as detailed as in chapter III.1.

III.2.1 Phase Contrast Microscopy

Phase contrast microscopy is an optical light microscopy technique that is oftentimes used in cell culture labs for optical routine controls. Visible light ($380\ nm < \lambda < 740\ nm$) is a form of electromagnetic radiation and thereby exhibits a characteristic amplitude and phase. Whenever light interacts with anything that is not a perfect vacuum, the trespassed medium causes changes in the amplitude as well as the phase of the light. Changes in the amplitude are perceptible for the human eye as brightness differences and are due to the scattering and absorption of visible light. Furthermore, light scattering and absorption processes are oftentimes wavelength-dependent and are the reason for colorfulness. However, the human eye as well as photographic equipment is only sensitive to changes in the amplitude with phase changes going unnoticed without additional arrangements. To get access to the information content of phase changes, phase contrast microscopy was developed in the 1930s by the Dutch physicist Frits Zernike who was awarded the Nobel Prize in Physics in 1953[55]. Zernike made it possible to separate the illuminating light into a fraction that interacts with the specimen and a fraction not influenced by the sample. **Fig. 5** depicts the setup and the optical path of the light from the light source through the specimen and to the human eye.
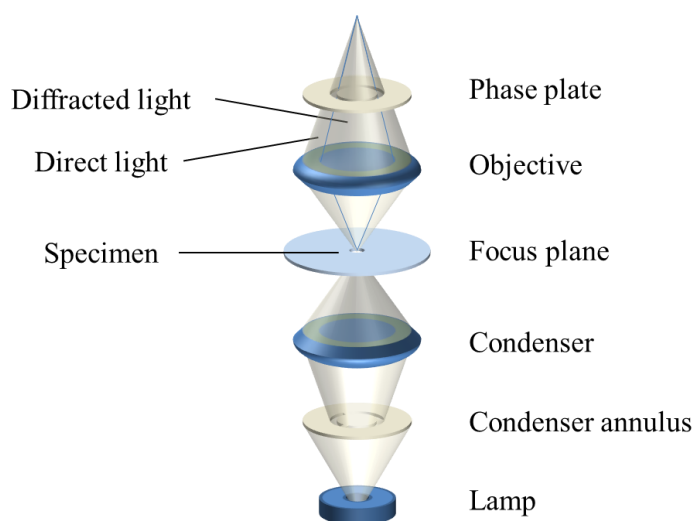
Fig. 5: Schematic depiction of the optical pathway and the different elements needed in phase contrast microscopy. The picture was adapted from Encyclopædia Britannica, Inc.

A lamp sends out visible light that first passes a condenser annulus. The part of defocused, parallel light wave fronts having passed the condenser annulus is afterwards focused on the specimen with the help of a condenser. As the specimen is at the very least partly transparent, the light is subsequently collected by an objective and passed on through a phase plate to the eye or a camera. The condenser annulus restricts the incident light reaching the specimen to a specific angle. If no specimen is present, the entire incident light (direct light) reaches the phase plate which (i) dims the light and (ii) shifts the phase of the light by +90°. If a specimen is now placed under the microscope, part of the incident light is diffracted and phase-shifted by –90° due to the optical path difference (difference of the refractive indices multiplied by the sample thickness corresponding to a phase shift of $\lambda/4$). However, this part of the light is unaffected by the phase ring because the angle of incidence changed after diffraction. The direct light (+90° phase-shifted by the phase ring) and the diffracted light (–90° phase-shifted due to the physical properties) create a special interference pattern which is made visible by the light-dark contrast. To maximize this contrast, the phase-shifted incident light needs to destructively interfere with the diffracted light as much as possible which results in a dark object before a brighter background. This form of phase contrast microscopy with destructive interference is called *positive phase contrast.* Alternatively, the incident light can also be phase-shifted –90° meaning that the direct light and the diffracted light are aligned in their phases which leads to constructive interference. In this *negative phase contrast* objects appear to be brighter than the background which can additionally be dimmed by a gray filter to maximize the contrast[56]. Phase contrast microscopy can reach magnifications of up to 1000x.

The phase contrast microscope used for routine control during cell culture procedures as well as cell counting and other optical documentation was a Nikon Diaphot (Nikon GmbH, Düsseldorf, Germany) which was additionally equipped with a Nikon D5000 digital camera (Nikon GmbH, Düsseldorf, Germany).

III.2.2 Stereo Microscopy

Stereo microscopy is another form of light microscopy with the distinct feature of two separate optical paths, one for each eye. The two optical paths enclose an angle of $11 - 16°$, which represents the angle of convergence for the near point accommodation of the human eye (at 25 cm distance from the object). Thereby, the two optical pathways allow for an

examination from slightly different points of view and create a three-dimensional *stereo effect*. The optics of a conventional stereo microscope are shown in **Fig. 6**[57].

Eyepieces
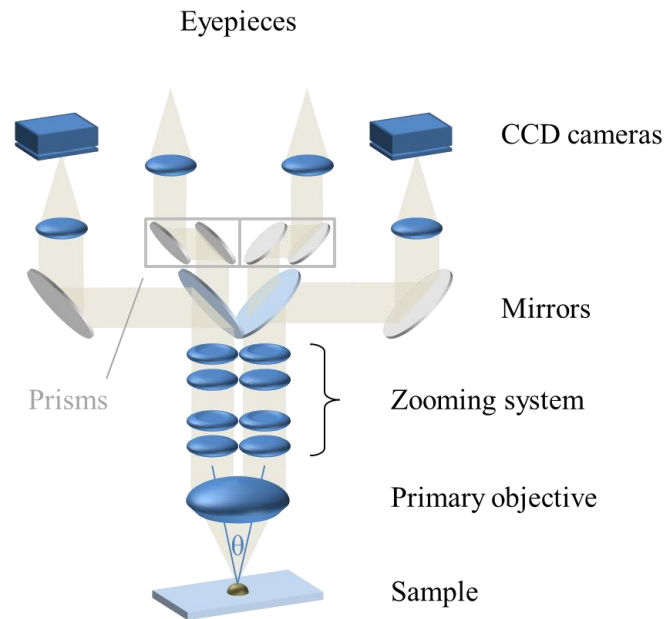
Fig. 6: Depiction of the optical pathway and the necessary elements in stereo microscopy. The two optical pathways enclose an angle θ of 11 – 16°. The picture was adapted from Kwon et al. (2010).

While phase contrast microscopy is ideal for transparent samples, stereo microscopy in general can work with either transparent or solid samples by using transmitted light or external light sources, respectively. The sample can therefore also be illuminated by an external light source which ensures even lighting of the object. The scattered light then passes the primary objective and a subsequent set of lenses which can be adjusted to deliver the desirable magnification. Each optical path can then be split between a camera system and an eyepiece. For a human to be able to see each of the two independent optical paths with one eye each, the two optical pathways need to be farther apart which is achieved by the implementation of two prisms. A prism is preferable over mirrors because mirrors can only reflect approximately 95 % of what prisms are able to reflect if the *total internal reflection angle* is used. The working magnifying range for stereo microscopy is below 100x since at higher resolutions the depth of field is rapidly decreasing which in turn means that the three-dimensional effect is lost.

The stereo microscope used in this thesis was a Nikon SMZ 1500 C-W10xB/22 stereo microscope (Nikon GmbH, Düsseldorf, Germany) equipped with a Nikon Coolpix 990 digital camera and a COOLPIX MCD Lens (Nikon GmbH, Düsseldorf, Germany).

III.2.3 Confocal Laser-Scanning Microscopy

In a confocal laser-scanning microscope (CLSM) not the full visible light spectrum but only monochromatic laser light is used as the underlying principle is not light absorption or scattering, but the excitation of fluorophores. After having been excited, fluorophores possess the ability to relax to a lower energy state by re-emitting photons with the same electron spin[58]. According to Stokes' Law, the emission of light is shifted to longer wavelengths. As only distinct wavelengths occur for the excitation and emission, a dichroic mirror is used for a CLSM in order to selectively deflect only one of the two wavelengths. Dichroic mirrors exist in short- and longpass versions and a shortpass dichroic mirror deflects higher wavelengths whereas shorter wavelengths are able to pass the mirror. **Fig. 7** illustrates the optical pathway in a CLSM.
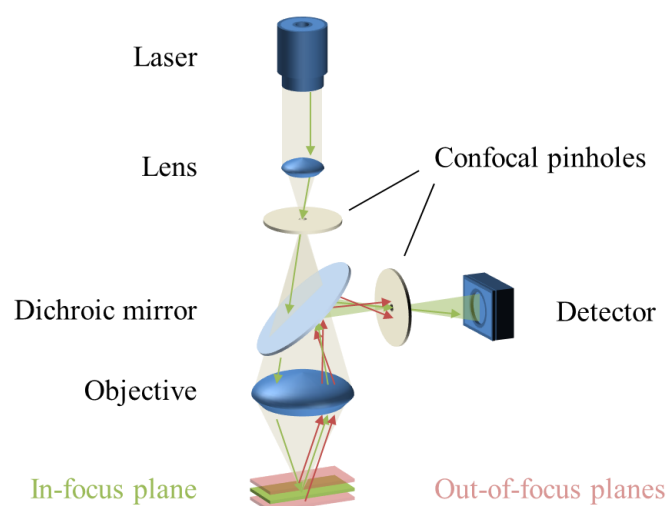
Fig. 7: Schematically depicted optical pathway and general setup of a confocal laser-scanning microscope. The picture was adapted from Encyclopædia Britannica, Inc.

The CLSM optical pathway begins with a laser beam which is focused on a pinhole with the help of a lens. This way, it can first pass the pinhole and then the dichroic mirror which lets the laser light with the initial wavelength pass. An objective subsequently focuses the light on the sample where it can excite the fluorophores. The fluorophores in turn send out stokes-shifted light which is collected by the objective and passed on to the dichroic mirror where it is deflected. The dichroic mirror lets the incident light pass and selectively deflects fluorescent light due to the red-shifted wavelength. After the dichroic mirror, a second pinhole is passed before the light reaches the detector which is oftentimes a photo multiplier tube (PMT). The second pinhole is optically conjugated with the in-focus plane of the sample and the first pinhole in the path of the incident light, meaning that only light emitted from that

32

very plane can pass the optically conjugated pinhole to reach the detector whereas light emitted from out of focus planes is held back at the pinhole. This feature provides axial resolution as background fluorescence is reduced. The sample is located on an adjustable stage for manual movement in the in-focus plane and laser scanning in x-y-direction is performed via movable mirros in the optical path. The stage can also be moved automatically in the z-direction in order to virtually reconstruct a sample.

Microscopic images of fluorescently labeled cells were recorded with the upright fluorescence microscope Eclipse 90i and the corresponding laser scanning unit CS1 (Nikon GmbH, Düsseldorf, Germany). Three different laser diodes in the wavelengths of $400 - 405$ nm (< 500 mW), 488 nm (< 50 mW) and 543 nm (< 5 mW) were available for excitation as well as three matching detectors with the default settings for blue: $435 - 450$ nm, green: $515 - 530$ nm and red: 650 nm long pass. The software Nikon EZ-C1 allows for changing between four different pinhole sizes (small: 30 µm, medium: 60 µm, large: 100 µm and open: 150 µm) as well as multiple objectives with different magnifications including a 60x immersion objective with a numerical aperture NA = 1.00.

III.2.4 Scanning Electron Microscopy

Scanning electron microscopy (SEM) is a technique using electrons instead of electromagnetic waves. The electrons interact with the sample and a topographical picture of the object surface with a high depth of field is received. The resolution for diffraction-limited microscopy techniques using visible light ($\lambda > 400$ nm) is approximately 200 nm according to Abbe's Law. It states that the distance (d) of two distinguishable points in the specimen for a setup with an objective and a condenser with the same numerical aperture is $d = \lambda/(2 \cdot NA)$. As SEM is using electrons and the associated DeBroglie wavelength[59] is in the single digit nanometer range, this technique, according to Abbe's Law, reaches a resolution as low as 1 nm which corresponds to a 10^6x magnification. The entire process of scanning an object with an electron beam is done in vacuum to avoid interactions of the electrons with air molecules. This entails the first of two prerequisites when it comes to sample preparation: the sample needs to be stable under vacuum. The second prerequisite is the suppression of charging effects of the sample. Isolating materials of interest are commonly coated with a very thin layer (a few nanometers) of a conductive material, e.g. gold, platinum or chromium. **Fig. 8** portrays the working principle of an SEM and the critical parts.
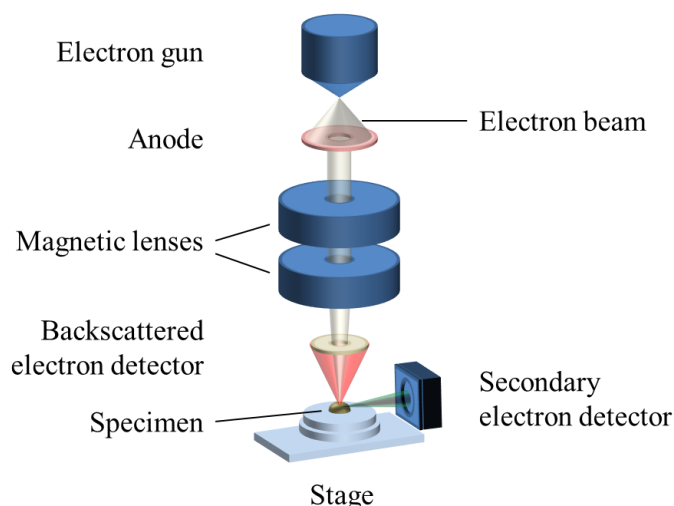
Fig. 8: Schematic drawing of a scanning electron microscopy setup with the critical components. The picture was adapted from Encyclopædia Britannica, Inc.

The electron source can be a hot tungsten or lanthanum hexaboride wire (hot cathode) which emits electrons that are subsequently accelerated in an electrical field with a voltage of up to 30 kV[60]. The German physicist Hans Busch was 1925 the first to be able to use a magnetic field as an electron lens similar to a glass lens with respect to electromagnetic radiation. The electron beam in SEM is then focused on the sample with the help of two electromagnets. Upon reaching the specimen, the electron beam generates secondary electrons (**Fig. 8**, depicted in green) with the energy of a few electron volts that can be detected by an *Everhart-Thornley detector*[61]. Due to their lower energy after inelastic interactions of the electron beam with the sample, they stem from layers close to the surface and therefore image the topography of the specimen. Any backscattered primary electrons (depicted in red) are collected by an additional electron detector.

The SEM technique can, besides the high-resolution imaging ability, also be used for material characterization in the form of *energy-dispersive X-ray spectroscopy* (EDX). With EDX, an elemental analysis or a chemical characterization of the sample can be performed when atoms are hit by the electron beam and an electron from the layer close to the nucleus (K shell) is ejected. This electron vacancy is then filled by an electron from a higher-energy shell (L or M shell) and the energy difference is released in the form of element-specific X-radiation (e.g. Au: 9.712 keV and 2.120 keV for the L and M shell, respectively). The general setup is very similar, with the sole difference consisting in the collection of the X-radiation by a semiconductor detector instead of the secondary electrons being collected by the combination of a scintillator and a PMT. SEM pictures shown in this thesis were kindly provided by Dr. Marcel Simsek (Prof. Dr. Bäumner's lab) and the company nanoAnalytics GmbH (Münster, DE).

IV   MATERIALS & PROTOCOLS

IV.1   Fabrication Processes of Measurement Devices

As many electrode arrays as well as the final permeable supports have been manufactured in the lab and are not commercially available, important manufacturing steps will be explained in this chapter. Furthermore, the focus in this chapter lies on the geometry and exact dimensions of electrode layouts and chambers. Cartoons have been sketched with Powerpoint 2019 (Microsoft Corp., Redmond, US), electrode layouts with CorelDRAW Graphics Suite 2017 (Corel Corporation, Ottawa, CA) and technical drawings as well as dimensioned layouts have been performed with AutoCAD 2019 (Autodesk, Inc., San Rafael, US).

IV.1.1   Relevant Techniques

IV.1.1.1 *Physical Vapor Deposition of Gold-Film Electrodes*

Preparation of gold-film electrodes was done by a *physical vapor deposition* (PVD) / sputter deposition process using the sputter coater SCD 050 (Bal-Tec AG, Balzers, LI) and a corresponding vacuum unit DCU (Pfeiffer Vacuum GmbH, Aßlar, DE). In the process, a high voltage is applied to the gold target (cathode) under argon atmosphere, establishing a high voltage field between the target and the substrate table (anode). Free electrons collide with argon atoms which are ionized and accelerated towards the cathode. The cascading process causes the ignition of a glow discharge and the impact of the argon atoms in turn causes a vaporization of the gold atoms and a subsequent condensation on the substrate. Suitable substrates range from solid polycarbonate or polyethylene terephthalate sheets over permeable filter membranes to three-dimensional objects that need to be covered with a very thin conductive layer for scanning electron microscopy (compare III.2.4). For this work, gold-film electrodes were deposited on impermeable as well as permeable substrates. Transparent polycarbonate sheets (Lexan®, GE, München, DE) in a thickness of 500 µm were used as impermeable substrates and polycarbonate filter membranes (HTTP09030, Merck Group, Darmstadt, DE) in a thickness of 10 µm, a pore diameter of 400 nm and a density of 10^8 pores per square centimeter were used as permeable substrates. The object to be sputtered with gold was placed on the table inside the vacuum chamber directly underneath the gold target. The substrate could either be covered fully with gold, or electrode geometries on a millimeter

scale could directly be defined with a metal shadow mask that was placed on top of the substrate. Evacuation of the chamber and repeated rinsing with argon ensured optimal sputtering conditions. Subsequently the sputter process was started (600 s, $4 \cdot 10^{-2}$ mbar, 47 mA) to produce a 100-nm-thick gold layer or the sputtering time shortened (12 s, 47 mA, $4 \cdot 10^{-2}$ mbar) to coat objects only with a 2-nm layer in preparation of SEM measurements.

IV.1.1.2 Photolithographic Patterning of Electrode Structures

The generation of intricate electrode structures on a sub-millimeter scale, which were too small for a metal mask, required a photolithographic fabrication process. Photolithography enables rapid prototyping as a variety of electrode layouts can be designed using a graphic design software. The self-designed electrode geometry is printed on a transparent film and thus the black ink protects the underlying photopolymer during UV illumination. The exposed parts of the photopolymer can afterwards easily be removed to uncover the conductive material underneath which can subsequently also be removed to yield the desired electrode layout. The standard photolithography process is shown in **Fig. 9**.

Lexan®	Transparent polycarbonate sheet, 500 µm thickness
AZ® ECI3027	Positive photoresist spin-coated on substrate
Gold	Elemental gold, 100 nm thickness
Mask	Printed on transparent films with ink jet technology
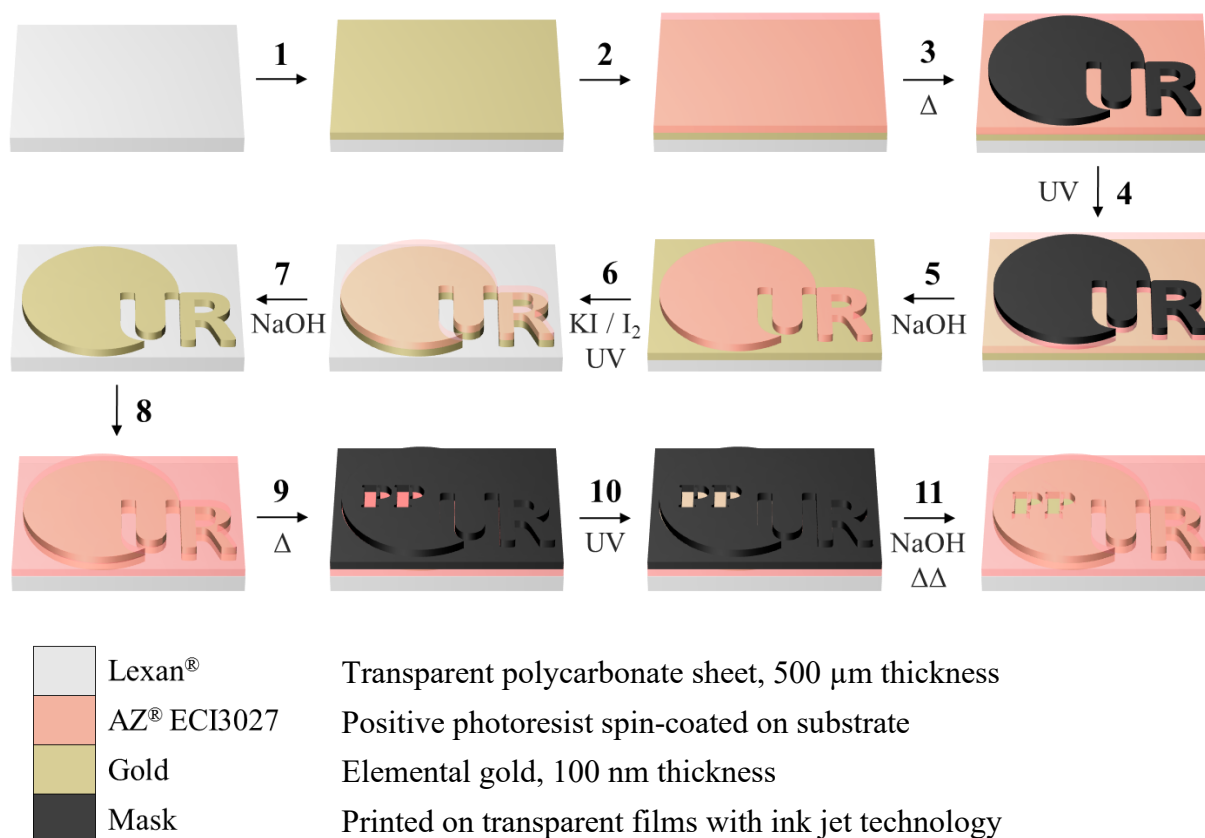
Fig. 9: Description of the different steps forming the standard photolithography process. Concentrations, temperatures and exposure times are described in detail in the text below.

Transparent polycarbonate sheets (Lexan®, GE, Munich, DE) served as substrate and were coated completely with a 100-nm-thin gold layer (step **1**, compare IV.1.1.1). A subsequent even coating with the positive photoresist AZ® ECI3027 (Microchemicals, Ulm, DE) was achieved by spin coating (3000 rpm, 1 min, N_2 atmosphere) using the spin coater WS-650-23B (Laurell Technologies Corp., North Wales, US, step **2**). The photoresist was stabilized in a drying oven SLE 500 (Memmert, Schwabach, DE) for 30 min at 100 °C (step **3**). Then the three-layered setup was placed inside a UV exposure unit BEL14017 (ISEL Germany AG, Eichenzell, DE), and covered with an electrode layout mask which was printed with an ink jet printer SC-P600 (Epson, Suwa, JP) on commercially available transparent X-10 A4 ink jet films (Folex Coating GmbH, Cologne, DE). Illumination was performed for 2 min at 60 W (step **4**). Since AZ® ECI3027 is a positive photoresist meaning that light-exposed areas become soluble to a developer, these areas were subsequently removed in a sodium hydroxide solution ($\beta = 7$ g/L, 20 s) before washing with distilled water (step **5**). Removal of the photoresist exposed the gold layer beneath which was etched away using an aqueous iodine / potassium iodide solution (30 s, $c(I_2) = 0.265$ mol/L, $c(KI) = 0.499$ mol/L) followed by a washing step with distilled water and again a UV exposure (step **6**). The second UV exposure weakened the photoresist still covering the electrode which was then removed in the NaOH solution according to step 5 (step **7**). This yielded a ready-to-use gold electrode layout on Lexan®. Steps 8 – 11 were optional if, for instance, the feed lines were supposed to be insulated or if multiple small working electrodes were supposed to be defined on that larger electrode generated so far. Therefore, the Lexan® with the defined electrode structure was completely covered with the AZ® ECI3027 photoresist according to step 2 (step **8**). As already explained in step 3, the photopolymer was first dried and then the array was placed in the UV exposure unit covered with a second mask defining the final bare electrode area (step **9**). UV exposure was performed similar to steps 4 and 6 to weaken the photoresist only where the electrode was supposed to be uncovered (step **10**). The mask was removed, the light-exposed photopolymer washed away in the NaOH solution from steps 5 and 7 and the electrode array was finally hardened in the drying oven SLE 500 (Memmert, Schwabach, DE) for 2 h at 118 °C (step **11**).

IV.1.1.3 Generation of Laser-Scribed Graphene

The following preparation protocol for the generation of LSG electrodes was adapted from the publication "Laser-scribed graphene (LSG) as new electrode material for impedance-based cellular assays" by P. Pütz, A. Behrent, A.J. Bäumner and J. Wegener published 2020 in Sensors and Actuators B: Chemical[62]: The LSG electrodes were prepared by laser-induced carbonization of polyimide as precursor material using 125-μm-thick polyimide sheets (Kapton®, DuPont, Wilmington, US). The Kapton® foil was first cleaned with isopropyl alcohol and then placed inside a commercial laser cutting platform (VLS2.30, Universal Laser Systems, Inc., Scottsdale, US). The VLS2.30 was equipped with a 30 W CO_2 laser emitting at a wavelength of 10.6 μm. The LSG electrodes were prepared using a 2.0" lense (parameters of the lens include a focal length corresponding to the distance between the lens and the focal plane of 2.0 inches, a focal spot size of 0.005 inches and a depth of focus which describes the tolerance of the lens to focal plane deviations of 0.1 inches) and the following laser settings: 0.3 W laser power (1 %), 12.7 cm/s scan speed of the laser (10 %) and an image density of 7 corresponding to 1000 laser pulses per inch in x-direction and 2000 pulses per inch in y-direction. The electrodes were produced at ambient temperature and pressure. Electrode layouts were designed with CorelDRAW Graphics Suite 2017 (Corel Corporation, Ottawa, CA) and saved in the 18.0 version due to compatibility with the software of the laser cutting software. Prior to all cell experiments, the LSG electrodes were cleaned and sterilized for 30 s using an argon plasma (PDC 32G-2, Harrick Plasma, New York, US). A polydimethyl-siloxane (PDMS) chamber (Sylgard® 184, Dow Chemical Company, Midland, US) with a cell growth area of 0.56 cm^2 was glued with silicon glue (RS Components, Corby, UK) upon the Kapton® substrates carrying the LSG electrodes. The electrodes were patterned such that each measurement chamber held two pairs of equally large, rectangular electrodes with a surface area of 3 mm² each (compare chapter IV.1.2.1.1). After sterilization the electrode surface was coated with fibronectin (20 μg/mL, 10 min, RT) and washed twice with serum-containing culture medium before the baseline impedance was recorded for at least 1 h. Cells were seeded in a density of $5 \cdot 10^5$ cells/cm^2 and the medium was exchanged 24 h and 72 h after cell inoculation.

IV.1.2   Design & Development of Permeable Supports

During the course of development, the final and stackable layout of the permeable supports, different electrode geometries and chamber models have been investigated. In principle, three different electrode layouts as well as three different three-dimensional chamber types were employed and the following chapter will provide detailed information on electrode geometries, the final version of the permeable supports as well as chamber materials and dimensions. Technical drawings are true to scale and have been performed with AutoCAD 2019 (Autodesk, Inc., San Rafael, US).

IV.1.2.1 Electrode Layouts

IV.1.2.1.1   Rectangular, Equally-Sized Electrodes
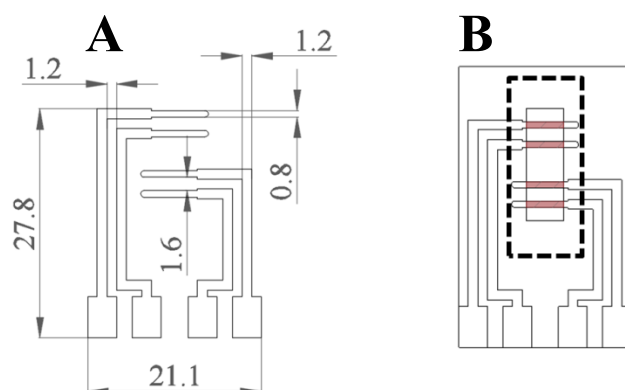
Fig. 10: (**A**) Dimensioned drawing of the rectangular, equally-sized electrode (REE) layout. All sizes are given in mm. (**B**) Active electrode area (highlighted in red) for each of the four electrodes is 2.8 mm^2 after placing a PDMS chamber (Sylgard® 184, dashed black line) on the substrate forming a central cell culture dish (straight black line).

The rectangular, equally-sized electrode (REE) layout was used for gold as electrode material on Lexan® as well as LSG as alternative electrode material made from Kapton®. In the case of the gold-film electrodes, the geometry was defined by a metal mask during the sputtering process and in the case of LSG the laser cutting platform was fed with a CorelDraw drawing exhibiting the same electrode dimensions to yield a comparable LSG electrode layout. The electrodes were patterned according to **Fig. 10**. They were subsequently cleaned and sterilized for 30 s using an argon plasma (PDC 32G-2, Harrick Plasma, New York, US) before a cell growth area of 0.56 cm^2 with a volume capacity of 300 µL was defined by a PDMS chamber (Sylgard® 184, Dow Chemical Company, Midland, US) which was glued onto the substrate with silicon glue.

The PDMS chamber yields two pairs of equally large, rectangular electrodes with a surface area of 2.8 mm² each. After a second sterilization step, the electrode surface was coated with fibronectin (20 µg/mL, 10 min, RT) and washed twice with serum-containing culture medium before the measurement.

IV.1.2.1.2 Interdigitated Finger Electrodes
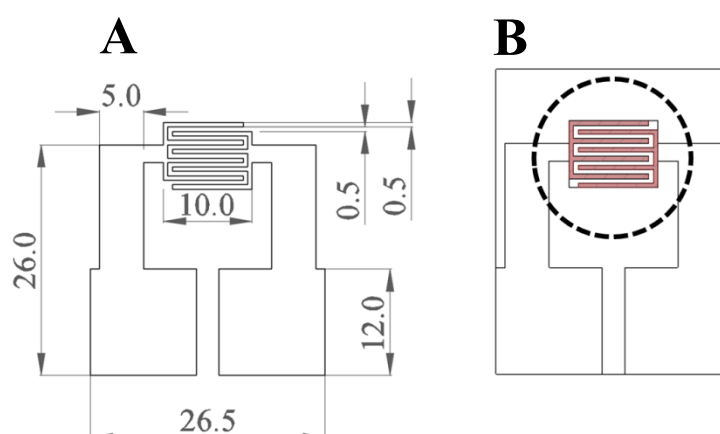
Fig. 11: (**A**) Dimensioned drawing of the interdigitated finger (IDF) electrode layout. All sizes are given in mm. Width of the electrode fingers and the distance between the fingers were 500 µm each, yielding a pitch of 1 mm. (**B**) Active electrode area defined by photolithography for the equally sized working and the counter electrode was 20.25 mm² (shown in red). The dashed black line indicates a glass ring defining the cell growth area.

An interdigitated finger (IDF) electrode layout was manufactured using a photolithographic patterning process on a commercial Lexan® substrate. The final definition of the bare gold electrodes yielded an active electrode area of 20.25 mm² for the working and the counter electrode alike. The width of the electrode fingers as well as the distance between them was 500 µm yielding a 1-mm pitch (cumulative width of electrode finger and distance between interdigitated fingers) in total. As the photoresist already defined the active electrode area, the cell growth area could be chosen freely. Therefore, the Lexan® substrate with the final electrode layout was sterilized for 30 s using an argon plasma (PDC 32G-2, Harrick Plasma, New York, US). Subsequently, a glass ring with an inner diameter of 1.8 cm was glued on top with silicon glue, resulting in a cell growth area of 2.54 cm² and a volume capacity of 1.5 mL. The electrode array was again sterilized and subsequently coated with fibronectin (20 µg/mL, 10 min, RT) and washed twice with serum-supplemented culture medium before the measurement.

40

IV.1.2.1.3 Horse Shoe Electrode Layouts
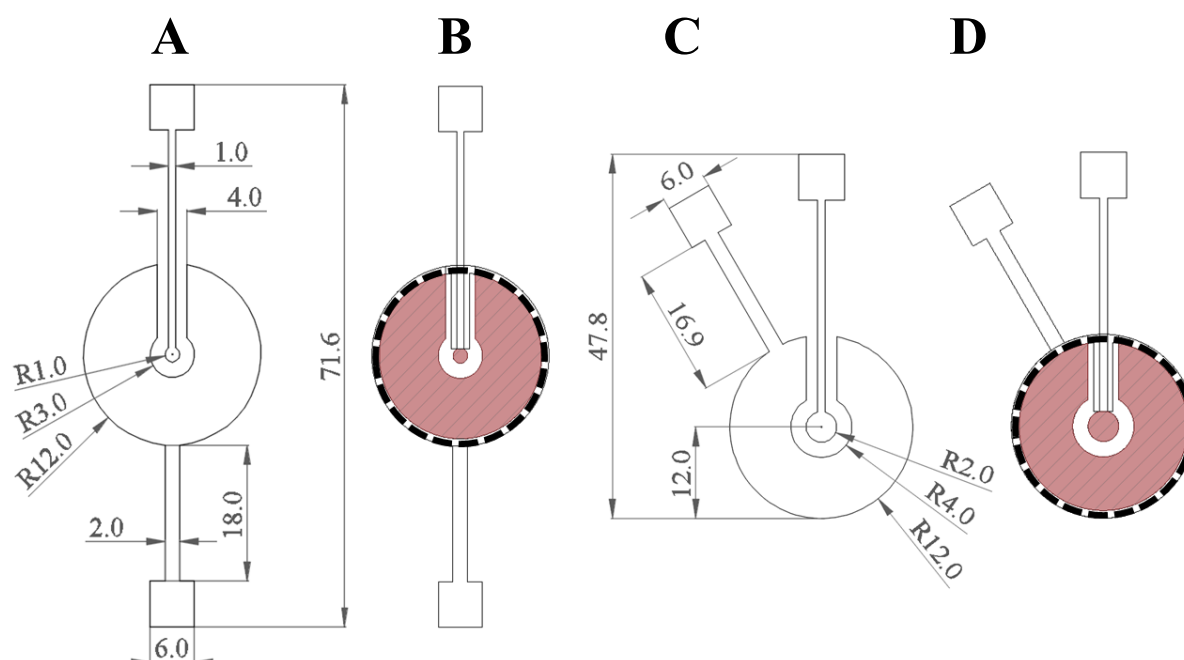
Fig. 12: (**A, C**) Dimensioned drawings of two types of horse shoe electrode (HSE) layouts with a 2-mm and a 4-mm diameter of the central working electrode. All sizes are given in mm. (**B, D**) Total active electrode areas (in red) of working and counter electrode defined by a glass ring glued to the substrate (dashed black line). Areas of the working electrodes amount to 3.05 mm^2 and 12.53 mm^2 for B and D, respectively. The feed lines to the electrode inside the glass ring were insulated.

Two different horse shoe electrode (HSE) layouts have been used throughout this thesis (**Fig. 12**). In both cases, the counter electrode with a diameter of 2.4 cm was significantly larger than the working electrode. The first layout (**Fig. 12A** & **B**) exhibited a working electrode of 2 mm in diameter whereas in the second layout the diameter was 4 mm (**Fig. 12C** & **D**). For the layouts A & B and C & D this resulted in active working electrode areas of 3.05 mm^2 and 12.53 mm^2, respectively. The corresponding electrode area of the counter electrode amounted to 3.19 cm^2 for the first layout and 3.01 cm^2 for the second layout. After the substrate was cleaned and sterilized for 30 s using an argon plasma (PDC 32G-2, Harrick Plasma, New York, US), a glass ring with an inner diameter of 2.2 cm was glued with silicon glue onto the Lexan$^®$ substrate with the final electrode layout resulting in a cell growth area of 3.8 cm^2 and a volume capacity of 2 mL. The feed line to the working electrode located inside the glass ring was insulated with silicon glue. The thus fabricated electrode array was again sterilized and subsequently coated with fibronectin (20 µg/mL, 10 min, RT) and washed twice with serum-supplemented culture medium before the measurement.

IV.1.2.2 IDE Sensor Arrays with Suspendable Filter Inserts

To bridge the gap between impedance-based cell monitoring on impermeable substrates and the development of stackable permeable substrates, the following measurement setup was created. The setup included the interdigitated finger electrode layout from chapter IV.1.2.1.2 which was patterned using photolithography. Three pairs of interdigitated fingers sharing one mutual counter electrode were aligned on a Lexan® substrate of the same footprint than regular ECIS® electrode arrays. The photolithographic patterning was performed according to the protocol given in chapter IV.1.1.2 and the individual illumination masks are depicted in **Fig. 13**.
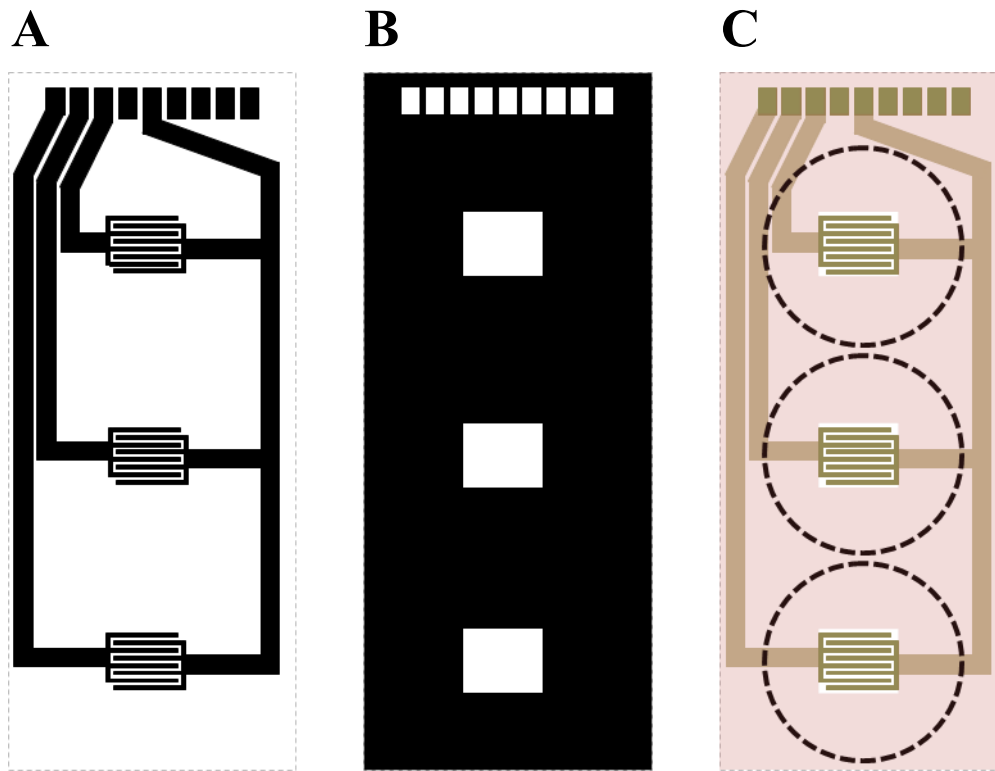
Fig. 13: Manufacturing of the IDE sensor arrays using photolithography. (**A**) Mask to define the gold electrode structure. The electrode layout was adapted from chapter IV.1.2.1.2. Width of the electrode fingers and the distance between the fingers were 500 µm each, yielding a pitch of 1 mm. (**B**) Second mask defining the active electrode area and exposing the contacting pads. (**C**) Ready-to-use array in which all but the active electrode areas and the contacting pads were covered by the positive photoresist. The dashed lines indicate glass rings defining the cell growth area.

The three IDF electrode layouts were patterned on commercial Lexan® substrates (3.8 cm x 9.2 cm) according to **Fig. 13A**. After the gold areas unprotected by the positive photoresist had been etched away, the whole substrate was once again covered with photopolymer and subsequently illuminated, using the mask shown in **Fig. 13B** to define the active electrode area as well as the contact pads. The final definition of each of the three IDF

pairs yielded an active electrode area of 20.25 mm^2 for the working and the counter electrode alike. The width of the electrode fingers as well as the distance between them was 500 µm yielding a 1-mm pitch (cumulative width of electrode finger and distance between interdigitated fingers) in total. As the photoresist already defined the active electrode area, the cell growth area could be chosen freely. The substrate was sterilized for 30 s using an argon plasma (PDC 32G-2, Harrick Plasma, New York, US). Subsequently, three glass rings with an inner diameter of 2.2 cm were glued with silicon glue onto the Lexan® substrate with the final electrode layout resulting in a cell growth area of 3.8 cm^2 and a culture medium capacity of 1.5 mL per well as indicated in **Fig. 13C**. The glass rings were chosen in the aforementioned diameter and a height of 18 mm so that commercially available Transwell® filter inserts (Corning Inc., New York, US) exhibiting a growth area of 1.12 cm^2 and a polystyrene scaffold for suspension could be suspended in a 1-mm distance to the IDE layout. The final electrode array was again sterilized, subsequently coated with fibronectin (20 µg/mL, 10 min, RT) and washed twice with serum-supplemented culture medium before the measurement.

IV.1.2.3 Permeable Support Manufacturing

This chapter provides a detailed manufacturing protocol for the permeable supports in the final layout as well as all necessary dimensions.
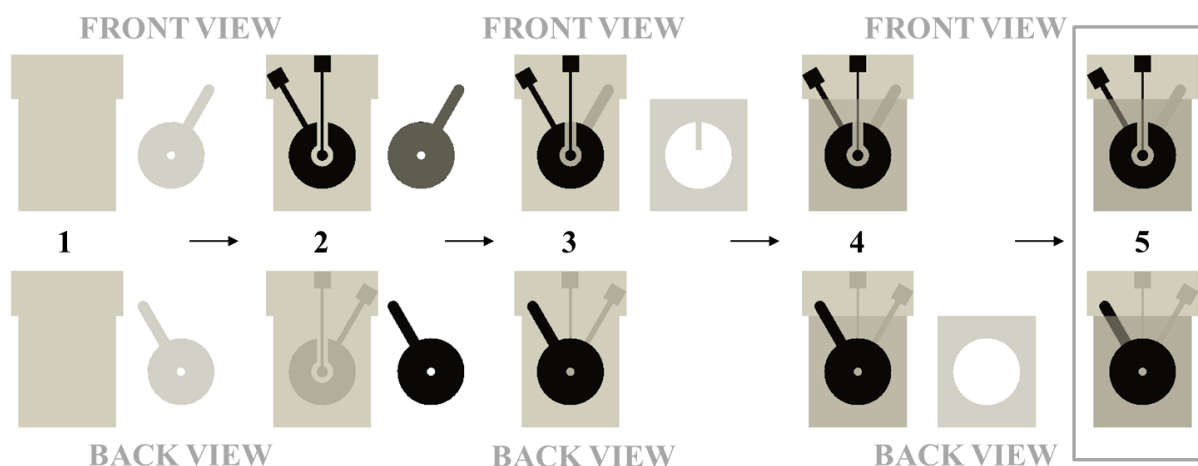
Fig. 14: Schematic illustration of the manufacturing process of the permeable supports. Highlighted in the grey box is the final permeable support. The process is shown from the front side (upper row) and the back side (lower row). (**1**) Pristine filter membrane (left) and lamination foil (right), (**2**) filter membrane and lamination foil after gold sputtering using individual masks, (**3**) gold-sputtered lamination foil glued to the reverse side (left) and lamination foil frame (right), (**4**) lamination foil frame glued to the front side (left) and Lexan® frame (right). (**5**) Stabilizing Lexan® frame glued to the reverse side yields the final permeable support.

Fig. 14 illustrates the manufacturing process of the permeable supports, starting with a polycarbonate filter membrane (HTTP09030, Merck Group, Darmstadt, DE) in a thickness of 10 µm with a pore diameter of 400 nm and a density of 10^8 pores per square centimeter, as well as a self-adhesive lamination foil (KN2120, Fraunhofer EMFT, Munich, DE) in a thickness of 190 µm and a central opening in a diameter of 3 mm (state **1**). The central hole and the contour of the lamination foil were cut with a commercially available laser scriber (Universal Laser Systems, Inc., Scottsdale, US) using a *high power density focusing optics* lens and the settings set to 50 % power, 70 % speed and 200 pulses per inch. The filter membrane was covered with a metal mask defining the electrode structure from **Fig. 12C** whereas the lamination foil was sputtered entirely with a 100-nm-thick gold layer (state **2**). The protective layer of the gold-coated lamination foil was then removed and the lamination foil glued to the reverse side of the filter membrane so that the central opening and the working electrode were aligned. The feed lines for the two counter electrodes included an angle of 30° with the WE feed line (state **3**). Soft and even pressure needed to be exerted on every part of the lamination foil for it to adhere permanently to the filter membrane. A frame also made from the same

lamination foil KN2120 (state **3**, right-hand side) was used to stabilize the permeable support on the front side as well as to simultaneously insulate the part of the working electrode feed line (state **4**). The gold-coated lamination foil on the reverse side in turn was framed by a stabilizing 500-µm-thick Lexan® mount exhibiting a 24-mm diameter hole. Therefore, the state 4 permeable supports and the Lexan® frame were sterilized for 30 s using an argon plasma (PDC 32G-2, Harrick Plasma, New York, US) before the Lexan® frame was sterilely glued to the back side with silicon glue (RS Components, Corby, UK). After a 24-h drying period inside the flow hood, the inner edges of the lamination and Lexan® frames were sealed with silicon glue and left to dry for another 24 h (state **5**). The filter supports were stored in a cool and dark place and again sterilized for 30 s before cell seeding. All dimensions, distances and angles of the permeable supports on both sides are shown in **Fig. 15**.
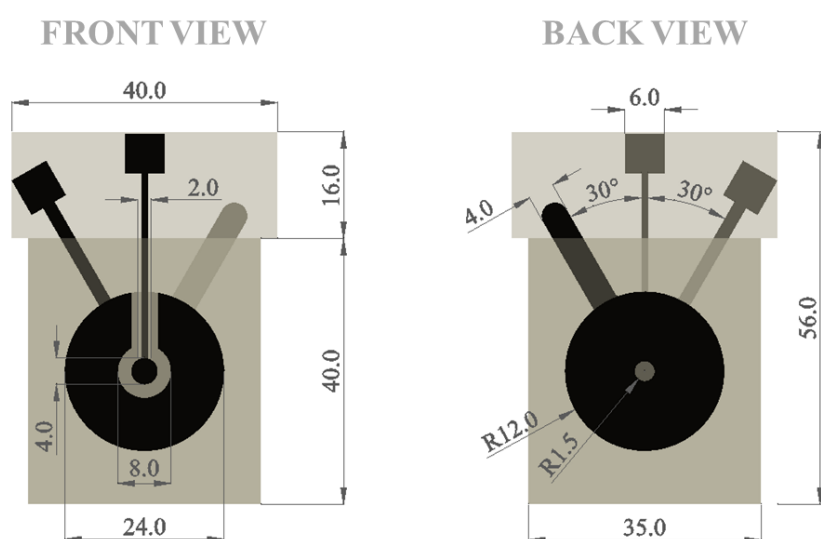
Fig. 15: Dimensioned drawing of one permeable support depicted faceup (left-hand side) and facedown (right-hand side).

Due to the insulation of the feed line of the working electrode on the front side of the filter, the area of the working electrode was 12.53 mm^2. The area on the back side of the working electrode left free by the lamination foil was only 7.07 mm^2 as the central hole in the lamination foil was not 4 mm in diameter but just 3 mm. The total material thickness of the permeable supports including the filter membrane, the additional counter electrode on the reverse side as well as the KN2120 and Lexan® frames was 890 µm, but considering that the silicon glue for the Lexan® frame is manually applied, the final product had a thickness of approximately 1 mm. Stabilizing both sides with the KN2120 and Lexan® frames signify-cantly increased the durability of the permeable supports so that they could be re-used multiple times for sustainability reasons and to save production costs and time.

IV.1.2.4 Chamber Construction

During the development of the final permeable support layout, three different chamber types have been designed and tested. Two different chamber prototypes have represented essential milestones on the path of developing the construction set for the impedimetric monitoring of three-dimensional tissue models and will therefore be introduced in the following chapter. Overcoming handling issues and other unforeseen problems while working with these prototypes eventually led to the final cultivation chamber (IV.1.2.4.2) and the corresponding measurement chamber (IV.1.2.4.3).

IV.1.2.4.1   Prototypes

A three-dimensional drawing of the first generation of the prototype can be seen in **Fig. 16**.
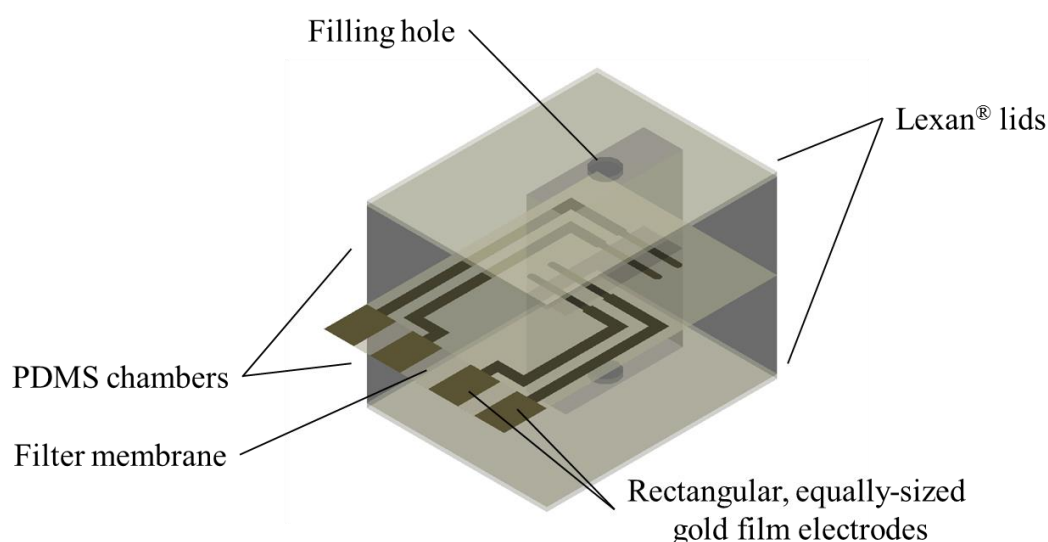
Fig. 16: Schematic representation of the first-generation prototype. The electrode layout from chapter IV.1.2.1.1 was sputtered on the polycarbonate filter membrane (HTTP09030) and clamped between two PDMS chambers as buffer reservoirs.

A metal mask was used to pattern the rectangular, equally-sized electrode layout from chapter IV.1.2.1.1 on one side of the polycarbonate filter membrane (HTTP09030). Two PDMS chambers (Sylgard® 184, Dow Chemical Company, Midland, US) were prepared in a height of 1 cm and a curing agent to base ratio of 1:10. The PDMS chambers exhibited a rectangular hole with an area of 0.56 cm^2 that was placed over the electrode fingers in order to define (i) the cell growth area and (ii) the active electrode area of 2.8 mm^2 for each of the four individual electrodes. The chambers could then be sealed with two Lexan lids each equipped

46

with a small hole to fill in the cell suspension with the help of a syringe and to be closed afterwards with sterile and cell-compatible Blu Tack (Bostik, Inc., Milwaukee, US). Prior to assembling the individual parts, they were sterilized for 30 s using an argon plasma. The individual parts were then arranged, pressed together and fixated with two elastic bands.

For the second-generation prototype, the horse shoe electrode layout (**Fig. 12A**) was sputter-deposited on the polycarbonate filter membrane (HTTP09030). The lamination foil (KN2120) introduced in chapter IV.1.2.3 was evenly gold-coated and glued to the reverse side of the filter membrane. **Fig. 17** depicts the complete setup of the second-generation prototype.
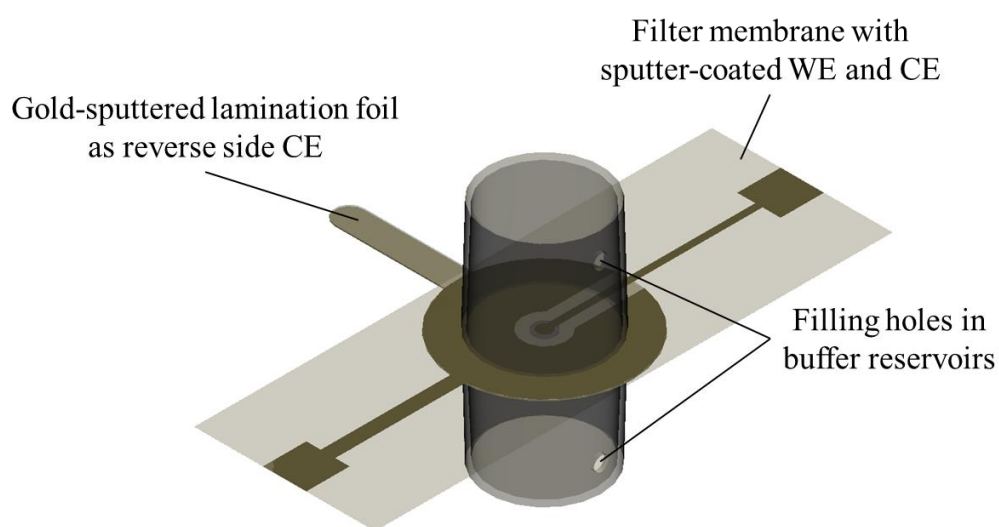
Fig. 17: Schematic representation of the second-generation prototype. The electrode layout from **Fig. 12A** was sputtered on the polycarbonate filter membrane (HTTP09030) and the lamination foil (KN2120) from chapter IV.1.2.3 was equally coated with gold and glued to the reverse side. Buffer reservoirs with filling holes were glued to each side of the three-electrode setup.

The protective layer of the gold-coated lamination foil with the central opening was removed and the self-adhesive part placed on the reverse side of the filter membrane with the central opening aligned with the WE. The individual feed lines were oriented in a 90°-angle for convenient connection to the hardware. A transparent buffer reservoir with a filling hole (typical 24-well plate dimensions with a growth area of 1.91 cm^2 and a height of 1.54 cm amounting to a volume of approximately 3 mL) was glued with silicon glue (RS Components, Corby, UK) on both sides of the three-electrode setup after all parts had been sterilized for 30 s in an argon plasma. Similar to the first-generation prototype, the filling holes could be sealed airtight with sterile and cell-compatible Blu Tack (Bostik, Inc., Milwaukee, US). With this setup, cells on both sides could be seeded directly on the electrodes and the buffer reservoirs filled air-bubble free.

IV.1.2.4.2   Cultivation Chamber

In order to be able to establish a confluent cell monolayer on the permeable supports from chapter IV.1.2.3, a chamber had to be developed where cells could be seeded and cultivated on both sides until they were needed for an actual measurement. The final version consisted of two half pieces, where a neodymium magnet was embedded at every corner and a torus-shaped rubber gasket was countersunk into an indentation around the cylindrically shaped cavity. That way the permeable support could be jammed between the two parts and the assembled and sealed chamber could be turned in every direction without the culture medium leaking from the chamber. The cultivation chamber is depicted in **Fig. 18**.
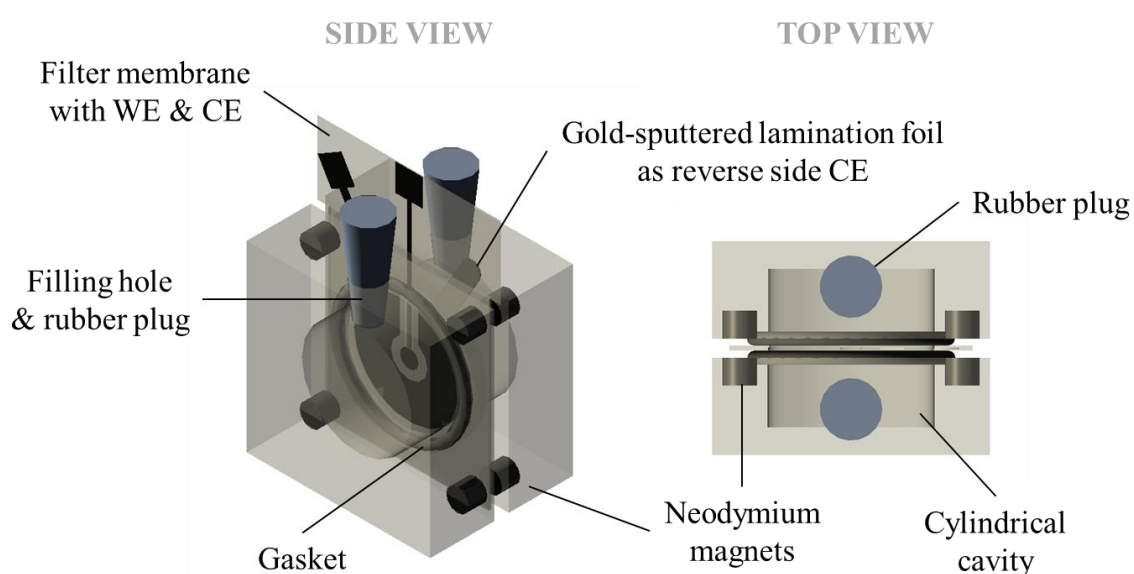
Fig. 18: Depiction of the designed and assembled cell cultivation chamber with the permeable support jammed between the two magnetic half pieces in side view (left-hand side) and top view (right-hand side). The maximum volume for the cylindrical cavity was 5 mL and the filling holes could be sealed with fitting rubber plugs.

The novelty of this cultivation chamber consisted in the easy and rapid assembling and disassembling due to the magnetic connectors. The strong neodymium magnets were permanently embedded in the polycarbonate material and guaranteed firm but even pressure on the permeable support. For cleaning and sterility issues, the two rubber gaskets were removable. The torus-shaped rubber gasket was 2 mm thick and had an inner diameter of 26 mm allowing for the full area of the counter electrode on the filter and the additional gold-film counter electrode on the lamination foil to be populated by the cells. The cylindrical cavity offered a maximum volume capacity of 5 mL to ensure sufficient nutrient supply for the cells. The total size of the cultivation chamber including the permeable support as depicted in **Fig. 18** on the left was 5.6 cm in height, 4.0 cm in width and 3.1 cm in depth.

Prior to any measurement, the two chamber halves as well as the pair of rubber gaskets and plugs were first cleaned with ethanol (70 % (v/v)), left to dry under the flow hood and afterwards washed with sterile, distilled water before assembly.

IV.1.2.4.3   Measurement Chamber

The stacking of multiple cell-populated permeable supports was possible with a correspondingly designed measurement chamber. The whole chamber including all assembled parts is shown in **Fig. 19**.
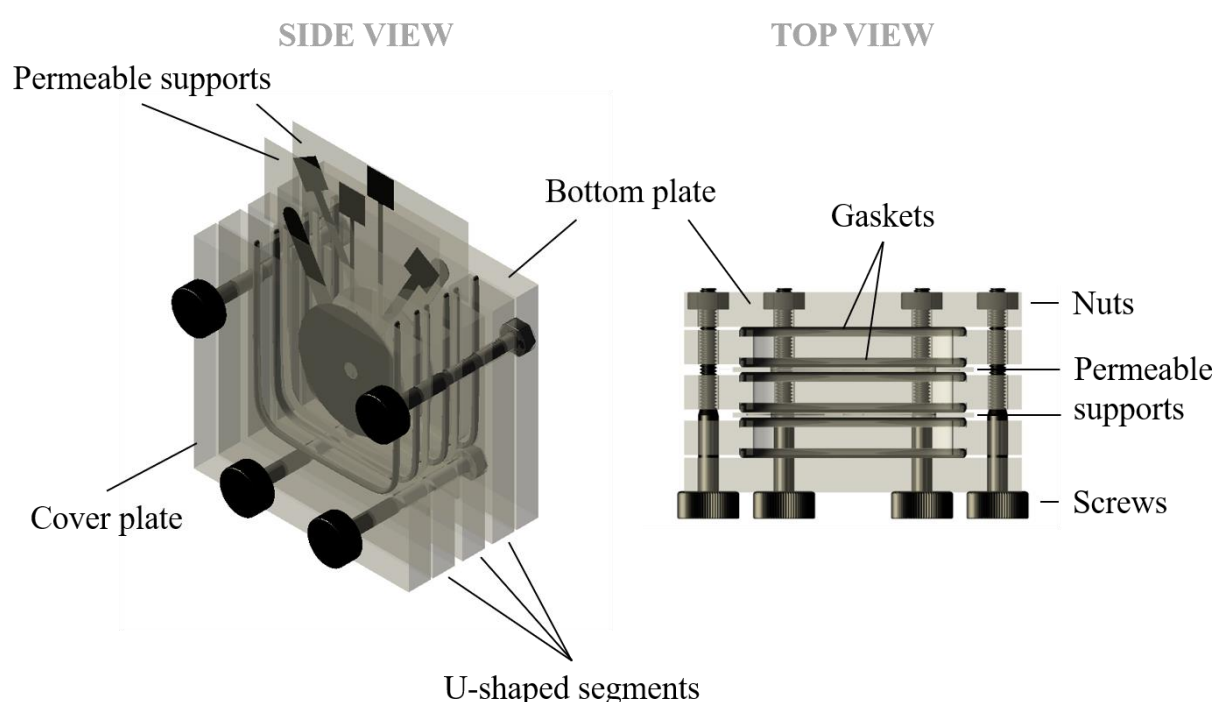
Fig. 19: Depiction of the measurement chamber holding two permeable supports and tightened with screws and nuts. The maximum volume capacity for each of the U-shaped segments is 4.5 mL allowing for the addition of model substances from above.

The chamber was made of tempered polycarbonate that could withstand the local pressure applied by the screws. It consisted of a cover and a bottom plate enclosing three U-shaped segments where a 1-mm-thick rubber gasket could be half-embedded on every side in 500-μm-deep grooves. If the permeable supports were stacked inside the chamber, they only made contact with the gaskets and by tightening the screws the whole chamber became leak-proof. In the assembled state, each U-shaped segment offered a volume capacity of 4.5 mL. The total dimensions as seen in **Fig. 19** on the left-hand side including the two permeable supports were 6.2 cm in height, 4.9 cm in width and 3.4 cm in depth.

IV.1.3 Experimental Setup for Impedance-Based Analysis

All impedance-based investigations were performed under normal cell culture conditions and in the same experimental setup that will be described in the following:

Experiments were conducted in a cell culture incubator (CO2cell 190, MMM Group, Planegg, DE) working at 37 °C, 5 % CO_2 and humidified atmosphere. Inside the incubator, an ECIS®-compatible array holder offered the possibility to either directly contact commercially available ECIS® arrays or alternatively the self-made electrode layouts introduced in chapter IV.1.2.1. The latter were contacted by interposing a circuit board ending in a 9-pin RS232 connector (made by the electronics workshop of the University of Regensburg) to be able to connect a measurement table with adjustable contacting pins. A relay outside of the incubator could switch between the different electrode pairs as an impedance analyzer with a built-in oscillator (SI-1260, Solartron Instruments, Farnborough, UK) generated a sinusoidal 50-mV RMS voltage amplitude signal and recorded the resulting current and phase angle. The known amplitudes of the voltage and the current as well as the value of the phase angle were then used to calculate the magnitude of impedance as well as the resistance and the capacitance according to chapter III.1.1. The relay and the impedance analyzer were both connected to a normal personal computer. The entire experimental setup is shown in a simplified way in **Fig. 20**.
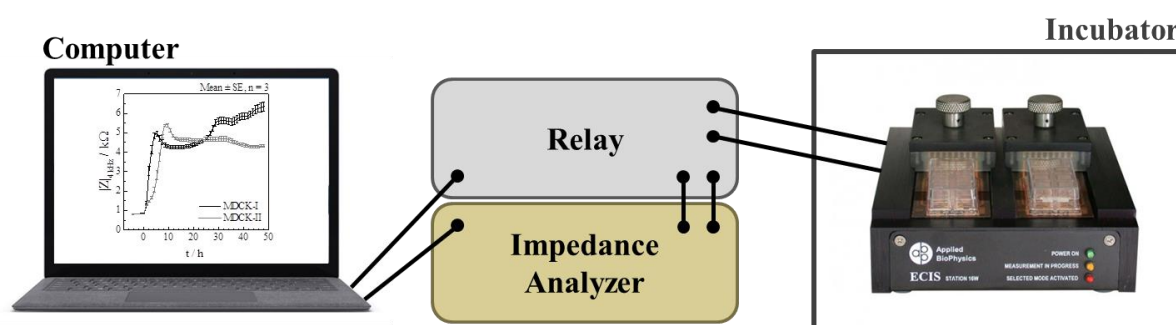
Fig. 20: Schematic depiction of the experimental setup for impedance-based analysis. The picture of the ECIS® holder was taken from the homepage of ibidi GmbH (Gräfelfing, DE).

Data was collected in a frequency range from 1 Hz to 1 MHz (61 individual frequencies spread evenly across a logarithmic scale) and was processed with a LabVIEW™ software (National Instruments, Austin, US) written by Prof. Dr. Wegener (University of Regensburg). Data analysis and presentation was done exclusively with OriginPro 2016 (OriginLab Corp., Northampton, US).

IV.2　Cell Culture Techniques

As of today, there exist more than 3600 cell lines from over 150 species[63]. In this thesis however, the focus was placed on three different model cell lines. All three cell lines were adherently growing cells derived from mammalian kidney and obtained from the Leibniz Institute DSMZ (German Collection of Microorganisms and Cell Cultures GmbH, Braunschweig, DE).

The heterogeneous parent cell line *Madin-Darby Canine Kidney (MDCK)* cells has been used in the form of two different strains. The biological source of these cells is the kidney of a cocker spaniel (*canis familiaris*). The two subtypes are equally derived from the parental strain "NBL-2" and henceforth designated MDCK type I and MDCK type II. In contrast to MDCK-II cells, which have been isolated at higher passages, MDCK-I cells have been isolated from the parental strain at low passages. MDCK-I cells exhibit very high transepithelial electrical resistance (TER) values exceeding 4000 $\Omega \cdot cm^2$ classifying these cells as tight whereas MDCK-II cells exhibit much lower TER values of around 300 $\Omega \cdot cm^2$ or less[64] and are therefore classified as only moderately tight.

The third cell line used in this thesis is derived from the kidney of a rat (*rattus norvegicus*) and called *normal rat kidney (clone 52E) (NRK)* cells. NRK cells are widely used as a model cell line and are well-characterized in their behavior. This cell line exhibits an epithelial-like morphology and corresponding TER values of only 10 $\Omega \cdot cm^2$ are described in literature[65] which is why NRK cells are classified as a leaky cell line with low barrier function.

IV.2.1　General Cell Culture Conditions

All work associated with cell culture was performed under sterile conditions in a laminar flow hood (HERAsafe, Thermo Fisher Scientific Inc., Waltham, US). All receptacles and consumable items like pipettes or pipette tips in contact to the cells were autoclaved for 20 min at 120 °C (DX-45, Systec GmbH, Nürnberg, DE) if not packaged sterilely. Cell culture media and model analyte solutions were prepared under sterile conditions and if necessary, sterile-filtered using a 0.22 µm polysulfonate syringe filter (Techno Plastic Products AG, Trasadingen, CH). Cells were cultivated in cell culture flasks with a growth area of 25 cm^2 and a supernatant volume of 4 mL (Greiner Bio-One, Kremsmünster, AT) and

stored in a cell incubator (Heraeus Function Line BB15, Thermo Fisher Scientific Inc., Waltham, US) at 37 °C, 5 % CO_2 and humidified atmosphere. Cell culture medium was exchanged every three days.

IV.2.2   Cultivation & Subcultivation of Adherent Cell Lines

The three cell lines NRK, MDCK-I and MDCK-II were subcultured once a week according to the following standard protocol with the exact compositions, concentrations, volumes and incubation times listed in **Tab. 4** and **Tab. 5**. PBS⁻, EDTA, trypsin and culture medium have been purchased (Sigma Aldrich, St. Louis, US) and warmed to 37 °C prior to cell contact. All incubation steps have been performed at 37 °C, 5 % CO_2 and humidified atmosphere.

Tab. 4: Composition of buffers and culture media used in the subcultivation process.

	Composition	
Dulbecco's phosphate buffered saline (PBS⁻)	0.2 g/L KCl, 0.2 g/L KH_2PO_4, 8.0 g/L NaCl, 1.15 g/L Na_2HPO_4	
Ethylenediaminetetraacetic acid (EDTA)	1 mM EDTA in PBS⁻	
Culture medium	Dulbecco's Modified Eagle Medium (DMEM)	Minimum Essential Medium Eagle (MEME)
incl. glucose	4.5 g/L	1.0 g/L
+ fetal bovine serum (FBS)	5 % (v/v)	5 % (v/v)
+ penicillin	100 µg/mL	100 µg/mL
+ streptomycin	100 µg/mL	100 µg/mL
+ L-glutamine	2 mM	4 mM

Tab. 5: Cell line-specific subculturing information. Incubation (inc.) was done at 37 °C, 5 % CO_2 and humidified atmosphere.

	NRK	MDCK-II	MDCK-I
PBS⁻	2.5 mL, 2x washing		
EDTA	4 mL, 8 min inc., 1x		4 mL, 10 min inc., 2x
Trypsin	0.05 % (w/v), 10 min inc.		0.25 % (w/v), 12 min inc.
Culture medium	DMEM		MEME

For subcultivation, the culture medium covering the confluent monolayer of cells was first aspirated and the cells were washed two times with PBS⁻⁻ (2.5 mL) to remove medium residues as well as dead cells. The cells were then incubated with a solution of EDTA in PBS⁻⁻ (4 mL) to complex divalent calcium and magnesium ions which are of crucial importance for the formation and maintenance of cell-substrate contacts. Next, the EDTA was replaced with a solution of trypsin (1 mL) to digest cell-cell and cell-substrate contacts. Trypsin is a serin protease hydrolyzing cell surface proteins leading to the detachment of the cells from the plastic bottom of the cell culture flask and the dissociation of the cells from each other. The enzymatic activity of cleaving cell-cell and cell-substrate contacts was stopped by the addition of serum-containing culture medium (9 mL) followed by the transfer into a Falcon® tube (Sarstedt AG & Co. KG, Nümbrecht, DE) and a centrifugation step (110 x g, 10 min, Heraeus Multifuge 1S-R, Thermo Fisher Scientific Inc., Waltham, US). The supernatant medium was aspirated; the cell pellet resuspended in fresh culture medium (4 mL) and subsequently 5 % of the cells in suspension reseeded in new culture flasks containing fresh culture medium (4 mL). The different morphologies of the three cell lines in a confluent cell monolayer are shown in **Fig. 21**.
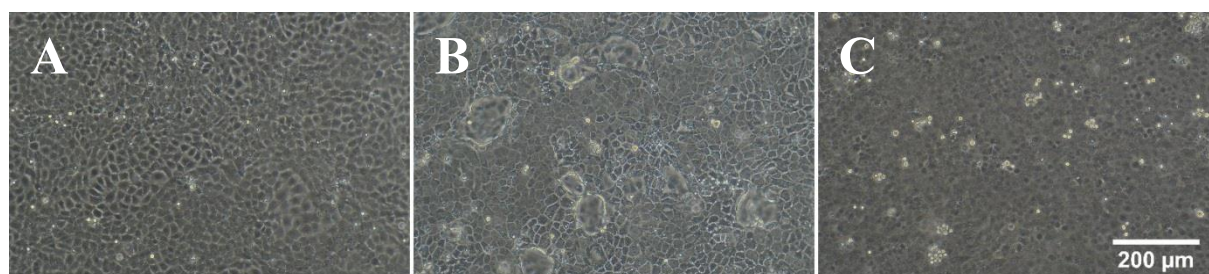
Fig. 21: Phase contrast micrographs of the three epithelial kidney cell types NRK (**A**), MDCK-II (**B**) & MDCK-I (**C**) in a confluent state. Pictures were taken with phase contrast microscope (Diaphot, Nikon GmbH, Düsseldorf, DE) in a 4x magnification. Scale bar depicts 200 µm.

The three cell lines mostly differ in the amount and tightness of their cell-cell contacts as already explained in chapter III.1.2. NRK cells typically exhibit very regular cobblestone morphology as displayed in **Fig. 21A**. The aspect of MDCK-II cells in general is very similar to the one of NRK cells with the only difference that this cell type forms blisters which are intact parts of the cell layer, being lifted off the substrate surface and therefore evading the focal plane (**Fig. 21B**). The cell type with the most cell-cell contacts in this thesis were MDCK-I cells (**Fig. 21C**) and in contrast to the morphology of the other two cell lines, the appearance is less regular and more densely packed.

IV.2.3 Cryopreservation

<u>Cell freezing</u>

For the long-term storage of adherently growing cells, the cells were detached from the bottom of the cell culture flask according to the subcultivating protocol in chapter IV.2.2 and after the centrifugation step (110 x g, 10 min, Heraeus Multifuge 1S-R, Thermo Fisher Scientific Inc., Waltham, US), the cell pellet was resuspended in culture medium suitable for cryopreservation (1.8 mL total culture medium volume, 10 % (v/v) dimethyl sulfoxide (DMSO, Carl Roth GmbH & Co KG, Karlsruhe, DE) in FBS (Sigma Aldrich, St. Louis, US)) and transferred into a cryo vial (Techno Plastic Products AG, Trasadingen, CH). The vials were first cooled slowly to $-70\,°C$ ($1\,°C/min$) with an isopropanol bath (Mr. Frosty^{TM}, Thermo Fisher Scientific Inc., Waltham, US) inside an ultra-deep freezer (B 30-85, Fryka-Kältetechnik GmbH, Esslingen am Neckar, DE) before the cells were finally transferred into a liquid nitrogen tank (German Cryo GC-BR2150 M, Jutta Ohst german-cryo GmbH, Jüchen, DE) for long-term storage at $-196\,°C$.

<u>Cell thawing</u>

The re-cultivation of frozen cells started with the removal from the liquid nitrogen tank and subsequent storage for $1-2$ h at $-20\,°C$. The still frozen cryo vial was then warmed in a waterbath (TW12, Julabo GmbH, Seelbach, DE) until two thirds of the content were thawed. The cell suspension was then transferred sterilely into a Falcon$^®$ tube (50 mL, Sarstedt AG & Co. KG, Nümbrecht, DE) and pre-warmed culture medium (20 mL) was added dropwise. After a cell-specific centrifugation step according to the protocol in chapter IV.2.2, the supernatant culture medium still containing the DMSO was aspirated and the cells resuspended in fresh culture medium (7 mL). Volumes of 1 mL, 2 mL and 4 mL of the cell suspension were then transferred to standard T-25 cell culture flasks (Greiner Bio-One, Kremsmünster, AT) and complemented with standard culture medium to yield a final volume of 4 mL. After an initial adhesion phase of 24 h, the cells were washed with PBS^{--} and the culture medium was exchanged before the established cultivation and subcultivation protocols were applied.

IV.2.4 Cell Culture on Impermeable Substrates

All impermeable substrates (e.g. commercial ECIS® arrays (Applied BioPhysics, Inc., Troy, US), self-made Kapton® or Lexan® substrates with patterned electrode structures) were sterilized for 30 s in an argon plasma (PDC 32G-2, Harrick Plasma, New York, US) before cells were inoculated after the standard subculturing process in a seeding density of $5 \cdot 10^5$ cells/cm^2. Cell seeding on the substrates and the subsequent measurements were performed according to general cell culture conditions and the culture medium was exchanged 24 h after cell inoculation and again 48 h later depending on the length of the measurement. Impermeable substrates were re-used multiple times after a standard regeneration process. Therefore, the arrays were regenerated by first washing the cell layer two times with PBS^{--} followed by an EDTA incubation step (20 min, 37 °C). The EDTA solution was then replaced by trypsin (concentration varying according to the cell type, 20 min, 37 °C). The trypsin solution was aspirated and the cell-free electrodes washed multiple times with distilled water to prevent salt residues from corroding the electrode surface during storage. The clean and dry electrode arrays were kept under the exclusion of sunlight at room temperature.

IV.2.5 Cell Culture on Permeable Substrates

Two different types of permeable cell culture substrates have been used in this thesis; both using the same polycarbonate filter membrane (HTTP09030, Merck Group, Darmstadt, DE) in a thickness of 10 μm, having a pore diameter of 400 nm and a density of 10^8 pores per square centimeter as cell growth substrate.

Transwell® filter inserts

The first permeable substrates were commercially available Transwell® filter inserts (Corning Inc., New York, US) exhibiting a growth area of 1.12 cm^2 and a polystyrene scaffold for suspension. The pre-sterilized filter inserts were delivered in a standard 12-well plate (Corning Inc., New York, US) forming a basolateral compartment (well working volume) and an apical compartment (filter insert). To cultivate cells on such an insert, the well holding the sterile filter insert was filled with pre-warmed culture medium (1.5 mL) before the cell suspension (0.5 mL) was added to the apical compartment on top of the filter.

Equal to cell seeding on impermeable substrates, the cell seeding density was $5 \cdot 10^5$ cells/cm^2. 24 h or 48 h after cell inoculation, depending on the cell type, the filter insert was taken from the 12-well culturing plate and suspended either inside the plasma-sterilized glass rings of the IDE sensor array (see IV.1.2.2) or the previously autoclaved (DX-45, Systec GmbH, Nürnberg, DE) and pre-warmed stainless steel measurement wells pertaining to the cellZscope (nanoAnalytics GmbH, Münster, DE). After the Transwell® filter inserts had been suspended inside the cellZscope measurement wells, the two separate compartments were connected only via the polycarbonate membrane and the adhering cell layer on top. Both the basolateral compartment (1.5 mL for the glass rings and 1.65 mL in the cellZscope) and the apical compartment (500 µL and 760 µL for glass rings and cellZscope, respectively) were subsequently filled with cell culture medium and cellZscope measurements performed in a frequency range from 1 Hz to 100 kHz at an RMS voltage amplitude of 35 mV. The measurement settings for the IDE sensor arrays are given in chapter IV.1.3. Regeneration of the filter inserts was performed in a 12-well culture plate according to IV.2.4 (in the apical compartment) and throughout the regeneration process, the basolateral compartment was filled with EDTA solution to prevent the cells from making air contact from below. After the regeneration process was completed, both compartments were washed with distilled water and stored in a cool, dark and dry place. Prior to the next cell seeding, the filter inserts were again sterilized for 30 s in an argon plasma and could thus be used multiple times.

Self-made permeable supports

The second type of permeable substrates was the permeable support described in chapter IV.1.2.3. Depending on the measurement, between one and two permeable supports were argon plasma-sterilized for 30 s while the cultivation chamber halves (compare chapter IV.1.2.4.2) as well as the rubber gaskets and plugs were first cleaned with ethanol (70 % (v/v)), left to dry under the flow hood and then the cylindrically-shaped reservoirs were washed with sterile, distilled water to prevent osmolality changes. The full cell inoculation process on both sides of one permeable support is shown in **Fig. 22**. The cell seeding on the reverse side is depicted in the upper row and the cell seeding on the front side of the permeable support is shown in the lower row. Different steps in the cell seeding process have been assigned numbers from one to ten which are referenced in the description text by the numbers in brackets.
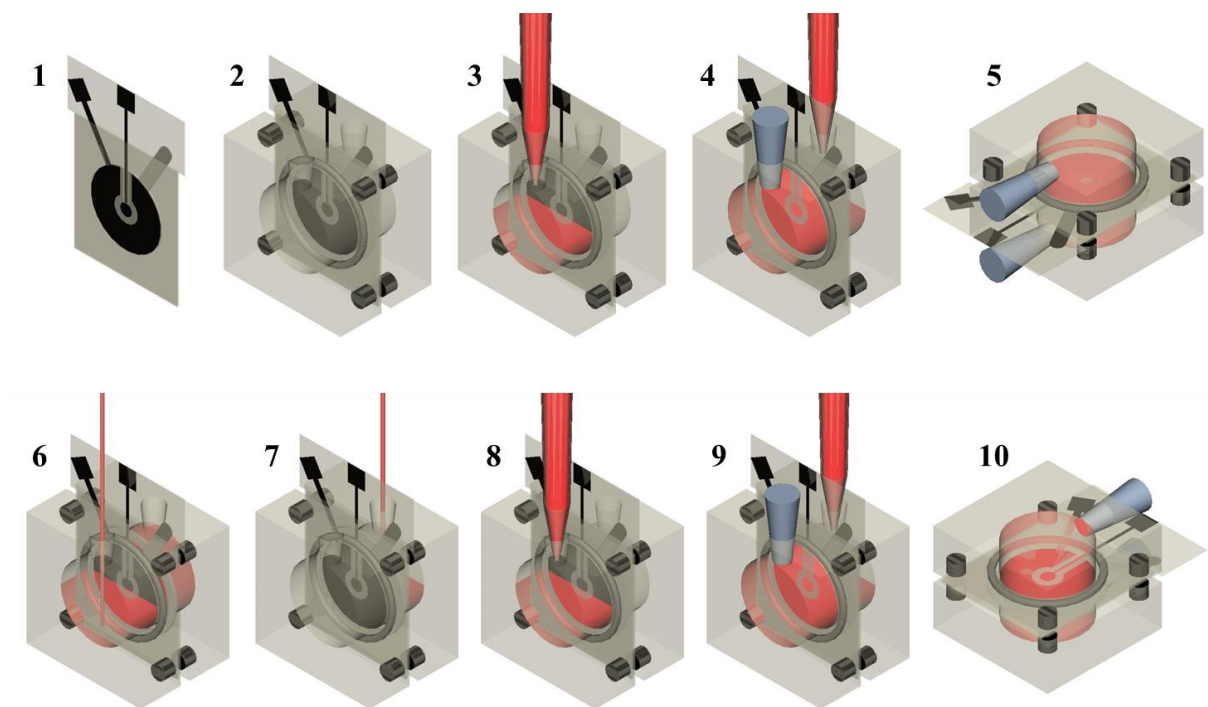
Fig. 22: Cell cultivation process on both sides of one permeable support. The process is shown in the correct chronological order and in this case, cell inoculation is performed first on the reverse side of the permeable support (upper row) and subsequently on the front side of the same permeable support (lower row). The numbers represent different steps in the cultivation process and are referenced in the detailed description below.

Once the sterilizing ethanol had evaporated, the rubber gaskets were put in place and the two chamber halves positioned on each side of the permeable support so that, due to the magnetic properties, the cultivation chamber turned leak-proof (**Fig. 22**, step **2**). Through the filling hole, the compartment on the front side of the permeable support was filled with pre-warmed culture medium supplemented with HEPES (20 mM, 2-[4-(2-hydroxyethyl)piperazin-1-yl] ethanesulfonic acid, Carl Roth GmbH & Co KG, Karlsruhe, DE) (**Fig. 22**, step **3**). The cell suspension was added to the other side (2 mL, cell number was chosen with respect to a seeding density of $5 \cdot 10^5$ cells/cm^2) and the remaining 3 mL of the same compartment were filled with the same HEPES-supplemented culture medium (**Fig. 22**, step **4**). The filling holes were carefully closed air bubble-free with the rubber plugs and the whole cultivation chamber tilted 90° to the side with the freshly seeded side of the permeable support facing upwards (**Fig. 22**, step **5**). A 200 µL pipette tip inside the lid of a petri dish was used to provide a minimal incline in order for potentially emerging bubbles to be caught on the sides and not linger directly below the working electrode. An actual photograph of four permeable supports during the cell adhesion process can be seen in **Fig. 23**.
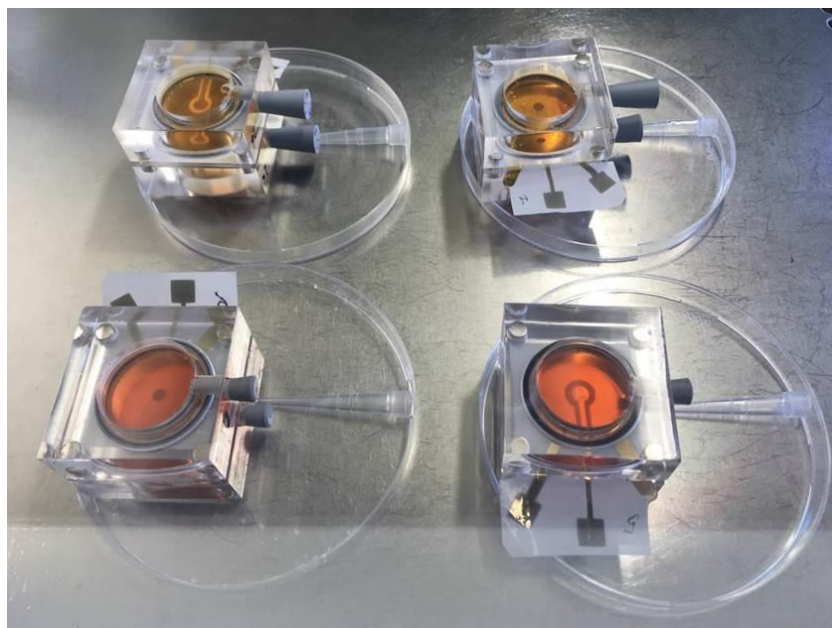
Fig. 23: Cell adhesion on permeable supports inside the cultivation chamber. Cells have been freshly seeded in the two chambers in the foreground whereas in the two chambers in the background, cells have had time to adhere for 24 h.

Owing to the HEPES supplementation, cell adhesion could occur either with or without CO_2 atmosphere. Nevertheless, a complete medium exchange was necessary after 24 h due to the cellular respiration and the ensuing acidification of the culture medium as can be seen in **Fig. 23** (color change from red (foreground) to yellow (background), indicating a change from physiological pH values to more acidic ones). Thus, after 24 h of adhesion time, the cultivation chambers were carefully uncorked, the culture medium on both sides aspirated (**Fig. 22**, steps **6** and **7**) and the cell seeding procedure repeated for the so far cell-free front side of the permeable support (**Fig. 22**, step **8**) while the other compartment was only filled with the HEPES-supplemented culture medium to provide fresh nutrients at a physiological pH (**Fig. 22**, step **9**). Again, the cultivation chamber was tilted 90° to the side, this time with the front side of the permeable support facing upwards so that the cells could adhere to the surface of the electrode (**Fig. 22**, step **10**). During the second cell adhesion, the cultivation chamber was again placed inside the petri dish lid on the pipette tip to achieve the slight incline in order for potentially emerging bubbles to be caught on the sides. With a confluent cell monolayer established on both sides of one permeable support after 48 h, two such permeable supports with a total of four cell layers were stacked inside a corresponding measurement chamber (compare chapter IV.1.2.4.3). The process of transferring two permeable supports with confluent cell monolayers on each side into the measurement chamber is depicted in **Fig. 24**. Different steps in the process are again assigned numbers which are referenced in the description below.

58
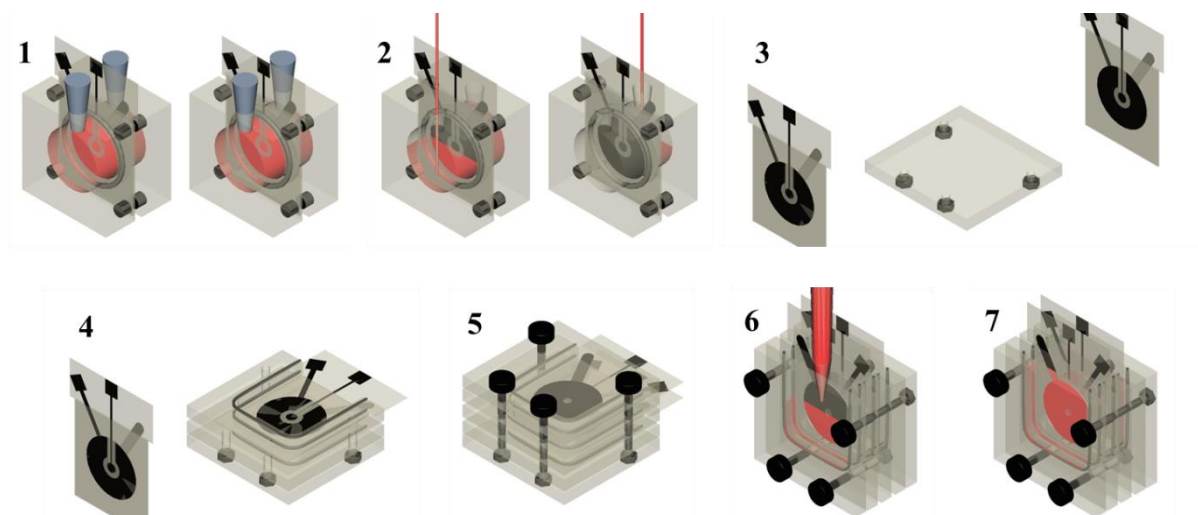
Fig. 24: Process of stacking two permeable supports with confluent cell monolayers on each side inside a measurement chamber. The process is shown in the correct chronological order and the numbers, which represent different steps, are referenced in the detailed description below.

In order to stack two permeable supports (**Fig. 24**, step **1**) inside the measurement chamber, the rubber plugs were carefully removed, the culture medium aspirated (**Fig. 24**, step **2**) and the two permeable supports transferred to one measurement chamber which had previously been sterilized with ethanol (70 % (v/v)) and was already equipped with rubber gaskets (**Fig. 24**, steps **3** and **4**). The permeable supports were stacked with the two gold-sputtered lamination foils facing outwards for convenient connection to the hardware (**Fig. 24**, step **5**) and each of the three compartments was filled with pre-warmed culture medium or L-15 (4.5 mL, compare **Fig. 24**, step **6**). Step **7** of **Fig. 24** shows the completely assembled and culture medium-filled measurement chamber holding two permeable supports and thus four confluent cell layers in close proximity to each other.

At the end of the experiment, the permeable supports were regenerated by a re-transfer to the cultivation chamber, filling both sides entirely with an EDTA solution (5 mL, 1 h, 37 °C) before the EDTA on the side facing up was substituted with a solution of trypsin (500 µL, 1 h, 37 °C). After the 1-h incubation time, the side holding the trypsin solution was filled up with a solution of EDTA, the chamber turned upside-down and the EDTA on the side then facing upwards also replaced with a solution of trypsin (500 µL, 1 h, 37 °C). Eventually, both sides were rinsed multiple times with distilled water before the chambers were disassembled and the permeable supports stored in a cool, dark and dry place.

After every cell contact, all parts of the cultivation and measurement chambers were first sterilized with ethanol (70 % (v/v)), then cleaned with a detergent and finally rinsed with distilled water.

IV.2.6   Cell Staining

The staining of the actin cytoskeleton and the cell's nuclei was performed according to the following staining protocol which was cell-type unspecific:

Cellular protein was crosslinked with PFA (4 % (w/v) in PBS^{++}, 10 min, RT) and subsequently the cell membranes lysed with Triton-X-100 (0.5 % (v/v) in PBS^{++}, 10 min, RT). After two washing steps with PBS^{++}, the actin cytoskeleton was stained with tetramethylrhodamine-isothiocyanate phalloidin (TRITC phalloidin, 3 µg/mL in PBS^{++}, 40 min, 37 °C) and the cell nuclei were subsequently stained with 4',6-diamidino-2-phenylindole (DAPI, 10 ng/mL in PBS^{++}, 2 min, RT). A final washing step with PBS^{++} was performed prior to microscopic examination. Confocal laser scanning microscopic images were collected using a fluorescence microscope with a corresponding laser scanning unit (Eclipse 90i, Nikon GmbH, Tokyo, JP). The DAPI dye was excited with a laser diode of the wavelength 400 – 405 nm and detected in the range between 435 – 450 nm. The TRITC phalloidin fluorophore was excited at 543 nm and detected with a 650 nm long pass detector. All images were taken using a 60x immersion objective (NA 1.00) with PBS^{++} as immersion medium.

IV.2.7   Buffer & Solution Composition

All buffers and model analytes used in this thesis are listed in the tables below. Cysteine, 2-[4-(2-hydroxyethyl)piperazin-1-yl]ethanesulfonic acid (HEPES), ferro- and ferricyanide as well as paraformaldehyde (PFA) are solids and were weighed in to yield a stock solution from which the final concentrations in **Tab. 6** were prepared by dilution with the respective solvent. Cytochalasin D, tert-butyl hydroperoxide (tBHP), tetramethylrhodamine-isothio-cyanate (TRITC) phalloidin, 4',6-diamidino-2-phenylindole (DAPI), carbol fuchsin (according to Ziehl-Neelsen) and 2-[4-(2,4,4-trimethylpentan-2-yl)phenoxy]ethanol (Triton X-100) were purchased as stock solutions and further diluted.

Tab. 6: Formulas, functions and concentrations of buffers, model analytes and dyes.

	Formula	Function	Concentration	Solvent
Cysteine	$C_3H_7NO_2S$	Adsorption promotor*	10 mM	H_2O (+ 150 mM NaCl)
HEPES	$C_8H_{18}N_2O_4S$	Buffer solution	10 – 20 mM	Culture medium

Cytochalasin D[**]	$C_{30}H_{37}NO_6$	Mycotoxin	0.1 µM – 5 µM	Culture medium
tBHP	$C_4H_{10}O_2$	Oxidizing agent	10 µM – 2 mM	Culture medium
Ferrocyanide	$K_4[Fe(CN)_6]$	Redox probe	0.25 mM – 1 mM	PBS[++]
Ferricyanide	$K_3[Fe(CN)_6]$			
TRITC phalloidin	$C_{62}H_{72}N_{12}O_{12}S_4$	Cytoskeleton dye	3 µg/mL	PBS[++]
DAPI	$C_{16}H_{15}N_5$	Cell nucleus dye	10 ng/mL	PBS[++]
Carbol fuchsin	$C_{21}H_{22}ClN_3$	Protein stain	0.2 % (w/v)	H_2O
PFA	$OH(CH_2O)_nH$ (n = 8 - 100)	Fixation agent	4 % (w/v)	PBS[++]
Triton X-100	$C_{14}H_{22}O(C_2H_4O)_n$ (n = 9 - 10)	Surfactant	0.5 % (v/v)	PBS[++]

(*) Full function: stabilization of interface impedance of gold electrodes and hydrophilization of the surface for protein adsorption.

(**) dissolved in DMSO.

In addition to the buffers and model analytes in **Tab. 6**, two isoosmolar solutions with different conductivities were prepared. The first solution was pure Leibovitz medium (L-15, Sigma Aldrich, St. Louis, US) which has originally been developed as culture medium in a CO_2-free environment. In contrast to normal culture medium, L-15 is buffered by free basic amino acids as well as phosphate buffers and contains higher amounts of sodium pyruvate and galactose. Thus, a physiological pH value is maintained without the usual 5 % CO_2. The second solution was a 50:50 mixture of L-15 and distilled water (50 mL) which was supplemented with sucrose (2.25 g) to establish isoosmolar conditions and traces of sodium chloride to yield approximately half the conductivity of pure L-15. The osmolality was determined with a cryoscopic osmometer (Osmomat030, Gonotec GmbH, Berlin, DE) which reads the freezing point of the solution of interest and returns the corresponding osmolality. The conductivity was measured with an electrical conductivity meter (Multi 720, WTW[TM], Weilheim, DE). A laboratory conductivity meter determines the conductivity of a solution via a four-electrode-setup by applying an alternating current between the outer two electrodes and measuring the resulting voltage between the inner ones. **Tab. 7** summarizes the component ratios as well as the measured osmolalities and conductivities.

Tab. 7: Ratios of L-15 medium to distilled water as well as determined osmolality & conductivity values for the isoosmolar solutions with full and half conductivity.

	L-15	**dest. H_2O**	**Osmolality**	**Conductivity**
Full conductivity	100 %	0 %	0.324 Osmol/kg	15.68 mS/cm
Half conductivity	50 %	50 %	0.306 Osmol/kg	7.79 mS/cm

V RESULTS & DISCUSSION

V.1 Permeable Support with Integrated Sensors for Adherent Cells

The following chapters will provide detailed information and insight on the development process of the permeable supports for adherent cells with integrated sensors. The road leading to the final design included an initial testing of different electrode layouts which will be compared to each other.

V.1.1 Comparison of Different Electrode Layouts

From the entirety of the electrode layouts under test, three distinct ones will be compared in the following. Dimensioned drawings of all layouts can be found in chapter IV.1.2.1.
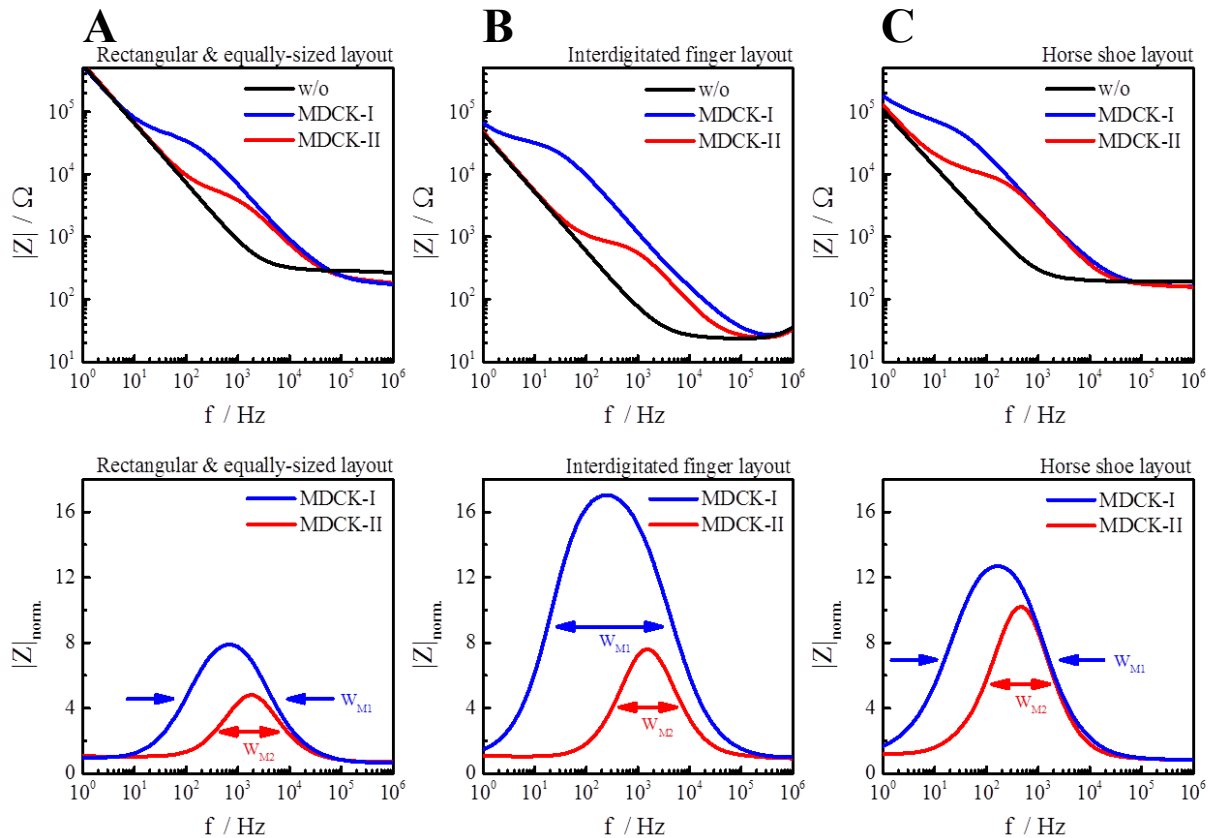
Fig. 25: Comparison of three distinct electrode layouts with an electrode thickness of 100 nm on Lexan®. Representative single spectra for confluent cell monolayers in serum-containing culture medium are shown (T = 37 °C, 5 % CO_2). (**A**) Represents the REE layout (IV.1.2.1.1), (**B**) the IDF layout (IV.1.2.1.2) and (**C**) the first generation HSE layout (IV.1.2.1.3). In the upper row, impedance spectra are shown for MDCK-II cells in red and for MDCK-I cells in blue. The lower row depicts the normalized impedance spectra which were calculated by dividing $|Z|_{cell\text{-}covered}(f)$ by $|Z|_{cell\text{-}free}(f)$ as well as the bandwidth W (full width at half maximum).

Fig. 25 depicts the frequency-resolved impedance spectra for the three individual gold electrode layouts. MDCK-II cells serve as a model for moderately tight epithelial cells and the corresponding spectra are shown in the upper row, depicted in red. The spectra of the cell-covered electrodes were recorded 48 h after cell inoculation. Depicted in blue, impedance spectra for MDCK-I cells – a model for very tight epithelial cells – are shown. Data for the MDCK-I cell-covered electrode was collected after 72 h as MDCK-I cells need a prolonged period of time to fully develop their tight cell-cell contacts[66]. The impedance spectra $|Z|(f)$ of the cell-free electrodes exhibited the typical shape with the frequency-independent impedance of the electrolyte resistance (bulk resistance) at high frequencies forming a horizontal line and the frequency-dependent impedance of the electrode-electrolyte interface at low frequencies forming a slanted line with a slope close to (–1). The active electrode area in the REE layout was approx. twice as large (6 mm^2, both equally-sized rectangular electrodes connected in series) compared to the WE of the HSE layout (3 mm^2). The bulk resistance (R_{bulk}, horizontal part at high frequencies) is generally determined by the resistivity of the electrolyte, the constriction resistance ($\sim 1/r$) as well as the resistance of the leads and contact pads and exhibited similar values of around 200 Ω for **A** and **C**. The active electrode area of the interdigitated layout in contrast was almost sevenfold higher, which, due to broader leads, lower constriction resistance and a shorter distance in the electrolyte, corresponded to a lower R_{bulk} of approximately 25 Ω (see **Fig. 25B**). The impedance values at the lower frequency end (1 Hz) were determined to be approximately 500 kΩ, 40 kΩ and 200 kΩ for the REE layout, the IDF electrode layout and the HSE layout, respectively. The cellular influence on the spectrum was found in the mid-frequency range with the resistive contribution of the cell-cell contacts at lower frequencies and the capacitive contribution of the cell membrane at higher frequencies (compare III.1.2).

The lower row in **Fig. 25** shows the normalized impedance which was calculated by dividing the impedance values of the cell-covered electrode by the values of the cell-free electrode. The sensitive frequency could be read from the resulting Gaussian-like curve at the maximum value. This frequency of maximal impedance change was chosen for monitoring the adhesion and proliferation behavior or the effect of toxins to a confluent cell layer with maximum sensitivity. If the magnitude of impedance is followed in a time-dependent manner at the most sensitive frequency, it serves as an integral descriptor of cell attachment and spreading as well as cell differentiation including barrier formation. In general, the most sensitive frequency strongly depends on the electrode layout (electrode-electrolyte interface) and the cell type (barrier properties). MDCK-I cells with their high-resistant tight junctions are oftentimes

monitored at lower frequencies than MDCK-II cells. Thus, the obtained most sensitive frequencies for the impedance data were determined to be 800 Hz and 2 kHz for MDCK-I and MDCK-II, respectively, when grown on the rectangular, equally-sized electrode layout; 250 Hz and 1.5 kHz on the interdigitated finger layout and 150 Hz and 500 Hz for MDCK-I and MDCK-II, respectively, on the horse shoe electrode layout (compare **Fig. 25**). The bell-shaped spectra of the normalized impedance not only differed in their height, but also in the bandwidth W (full width at half maximum). The value of W was at least one order of magnitude larger for MDCK-I cells in comparison to MDCK-II cells. Although the frequency region suitable to follow MDCK-I cell behavior was larger, the most sensitive frequency was determined prior to every experiment.

The spectra in **Fig. 25** have been fitted with a LabVIEW^{TM} software based on the ECIS$^{®}$ model (compare chapter III.1.2) to yield the parameters **α**, **R$_b$** and **C$_m$**. The full set of parameters, including the bulk resistance R$_{bulk}$, the parameters A$_{CPE}$ and n$_{CPE}$ of the electrode-electrolyte interface and the full width at half maximum W, is listed in **Tab. 8**.

Tab. 8: Parameters obtained by fitting the single spectra from **Fig. 25** of the MDCK cell-covered electrodes in different electrode layouts.

Layout	WE / mm^2	Cell type	R$_b$ / $\Omega \cdot cm^2$	α / $\sqrt{\Omega} \cdot cm$	C$_m$ / $\mu F \cdot cm^{-2}$	A / $\mu F \cdot s^{(n-1)} \cdot cm^{-2}$	n / a.u.	R$_{bulk}$ / Ω	W / Hz
REE	2.8	M2	28	17	3.3	2.14E-5	0.94	207	7543
		M1	209	46	4.1	3.74E-5	0.94	173	4912
IDF	20.25	M2	54	14	4.0	3.63E-5	0.95	25	7627
		M1	1764	133	2.6	3.62E-5	0.95	28	4994
HSE	3.05	M2	188	38	3.8	4.70E-5	0.93	166	1895
		M1	874	135	3.9	4.70E-5	0.93	168	1569

The area of the working electrode (WE) and the size ratio between working and counter electrode was taken into account for the determination of the parameters: for the REE and the IDF layout, the sizes of working and counter electrode are similar which means that the active electrode area amounts to the combined area of WE and CE as they are connected in series. For the HSE layout, the measurement is focused on the significantly smaller working electrode meaning the active electrode area is similar to the area of the WE. R$_b$ values, which indicate the electrical tightness of cell-cell contacts, ranged from 28 $\Omega \cdot cm^2$ to 188 $\Omega \cdot cm^2$ for MDCK-II cells (M2) whereas MDCK-I cells (M1) exhibited significantly higher values between 209 $\Omega \cdot cm^2$ and 1764 $\Omega \cdot cm^2$. These values concurred very well with data given in literature for MDCK-II cells (88 $\Omega \cdot cm^2$) and were lower but still in the same magnitude for

MDCK-I cells (2870 $\Omega \cdot cm^2$)[67]. The averaged value of the parameter α, indicating the resistance of the subcellular cleft, was also at least four times higher for MDCK-I cells (105 $\Omega^{0.5} \cdot cm$) than for MDCK-II (23 $\Omega^{0.5} \cdot cm$) cells indicating stronger substrate contact. Literature confirmed this data with values of 117 $\Omega^{0.5} \cdot cm$ and 16 $\Omega^{0.5} \cdot cm$ for MDCK-I and MDCK-II, respectively[67]. The third parameter C_m – providing information about the capacitive properties of the cell membranes – was determined to be 3.7 $\mu F \cdot cm^{-2}$ on average for MDCK-II cells, which was only slightly higher than the value 3.03 $\mu F \cdot cm^{-2}$ given in literature[67] in contrast to MDCK-I cells, where the average value was determined to be 3.5 $\mu F \cdot cm^{-2}$ and the value given in literature[67] is only 1.91 $\mu F \cdot cm^{-2}$. The higher values for the full width at half maximum W for MDCK-II cells compared to MDCK-I cells in **Tab. 8** are due to the logarithmic presentation on the frequency scale.

Comparing the three different electrode layouts with each other, an unequivocal distinction between the two cell types with respect to the impedance spectra of the cell-covered electrodes was clearly possible in all cases. The ECIS® parameters averaged for all three electrode layouts were confirmed by literature data and the individual layouts came with distinct advantages and disadvantages. The interdigitated electrodes for example yielded the values closest to literature, especially in the case of the MDCK-I cells, but also required the most cell suspension as the active electrode area was by far the largest. The ECIS® parameters determined on the rectangular and equally-sized electrode layout deviated most from the literature ones which could be due to the size of the active electrode area varying with the manual positioning of the PDMS cell culture dish. Slight differences in the amount of silicon glue had a direct impact on the size of the WE and therefore on the amount of cells under study. Nevertheless, the REE layout was ideally suited for rapid prototyping as the electrode leads were designed to be most material-efficient. Furthermore, solely in the case of the horse shoe electrode layout, it was possible to effectively insulate the counter electrode because of the centrosymmetrical geometry, which played a crucial role in the permeable support development process.

Differences were also observed in the capacitance spectra which are shown in **Fig. 26** for all three electrode layouts. In the upper row, spectra of electrodes covered with a confluent MDCK-I cell layer are depicted in **blue**, whereas spectra of MDCK-II cell-covered electrodes are depicted in **red**. The lower row shows the normalized capacitance spectra which were derived from the upper row by dividing the capacitance spectrum of the cell-covered electrode by the one of the cell-free electrode.
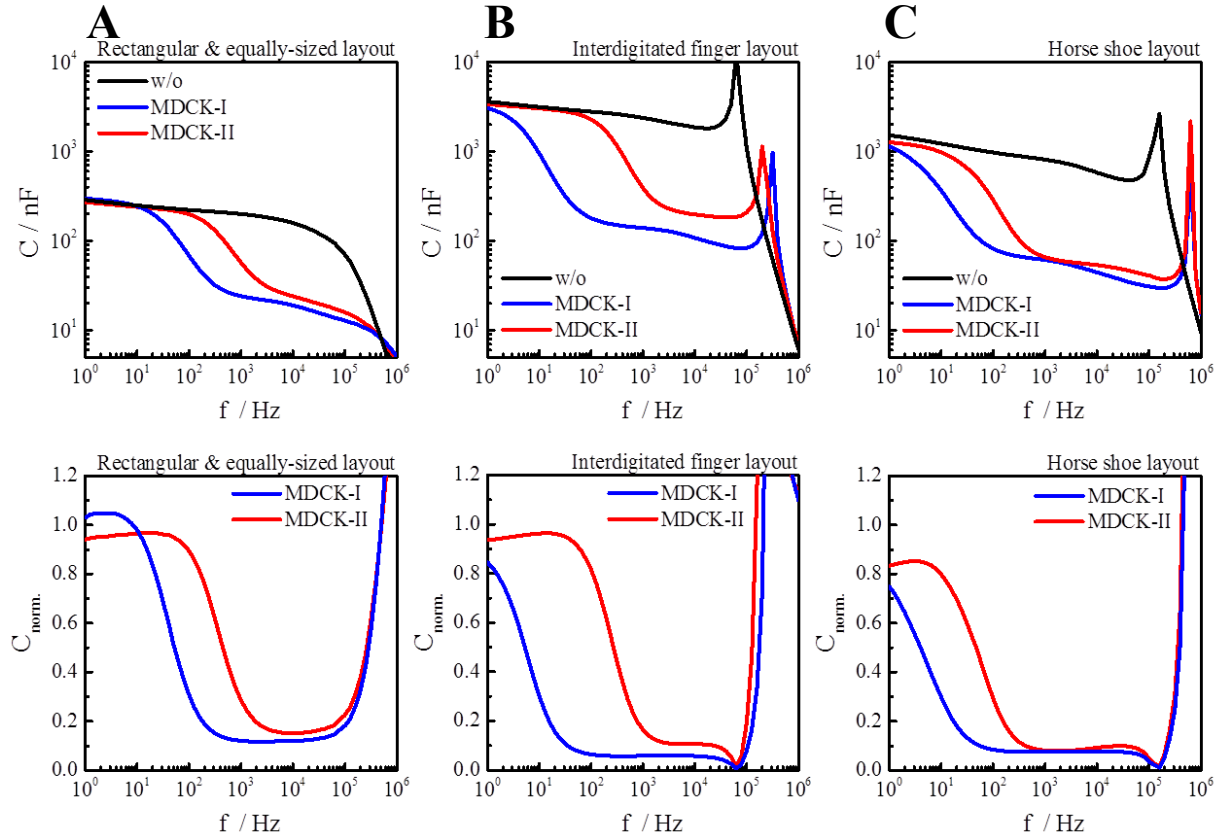
Fig. 26: Comparison of three distinct 100-nm-thick gold electrode layouts sputtered on Lexan®. (**A**) Represents the REE layout (IV.1.2.1.1), (**B**) the IDF layout (IV.1.2.1.2) and (**C**) the first generation HSE layout (IV.1.2.1.3). In the upper row, capacitance spectra are shown for moderately tight epithelial cells (MDCK-II, **red**) and for extremely tight epithelial cells (MDCK-I, **blue**). The lower row depicts the normalized capacitance spectra which were derived from the upper row by dividing $C_{cell\text{-}covered}(f)$ by $C_{cell\text{-}free}(f)$.

A high electrode-electrolyte capacitance at low frequencies always corresponds with a low interface impedance due to the reciprocal relation of the two parameters (compare equations (8) and (10)). Thus, the interdigitated finger electrode layout with the largest active electrode area displayed the highest capacitance of the cell-free electrode of around 3 µF followed by the horse shoe electrode layout (approximately 1 µF) and the rectangular and equally-sized one (300 nF). All three cell-free electrode layouts exhibited the typical capacitance spectra $C(f)$ of constant capacitance values at the lower frequency end from 1 Hz to 10^4 Hz due to the capacitive electrode-electrolyte interface. The slightly falling capacitances from 1 Hz to 10^4 Hz stemmed from the only almost ideal capacitive behavior of the electrode material ($n_{CPE} = 0.93 - 0.95$). Deviations from an ideal spectrum were seen for frequencies higher than 10^4 Hz where the capacitance began to decrease steeply which was caused by a setup-related parasitic parallel capacitance originating from the sum of the contacts, the wiring and the relay. In addition, in **Fig. 26B** & **C** local maxima were observed in the cell-free as well as the

cell-covered capacitance spectra in the range between 10^5 - 10^6 Hz. These peaks could also be attributed to parasitic contributions of the measurement setup; this time mainly inductive influences supposedly from the broadband cables connecting the ECIS® holders with the relay. In **Fig. 26A**, this additional parasitic inductive contribution was not observed as the rectangular and equally-sized electrode layouts were contacted in a special holder which was connected directly to the relay instead of interposing a circuit board which itself was connected via the ECIS® holders inside the incubator. Similar to the impedance spectra, the useful frequency range significantly increased by using a confluent MDCK-I monolayer. This frequency window in the capacitance spectra was flanked by the resistive contribution of the cells in |Z|(f) and the part where the capacitance was decreasing sharply due to the unwanted parallel capacitance. Given that this parallel capacitance was exclusively setup-related and therefore independent of the cell type and the cell type-specific resistive influence of MDCK-I cells was found at lower frequencies in |Z|(f), a broader range of constant values resulted for the MDCK-I cells in the capacitance spectra $C_{cell-covered}$(f) (compare **Fig. 26**, upper row).

Dividing the capacitance spectrum of the cell-covered electrode by the spectrum of the same cell-free electrode yielded the normalized capacitance (**Fig. 26**, lower row). With a confluent cell layer being present on the electrode surface, the normalized capacitance for all three electrode layouts was found to be close to 1.0 at low frequencies and displayed a value around 0.1 in the mid-frequency range before rising steeply at high frequencies from 10^5 to 10^6 Hz. The fact that the normalized capacitance did continue to measure the low values from the mid-frequency region but kept rising further could once again be attributed to the parasitic parallel capacitance mentioned above which originated from the contacting of the arrays. Confirming the observations from the impedance data, the low-frequency inflection point of $C_{norm.}$ was shifted one order of magnitude to lower frequencies for MDCK-I cells compared to MDCK-II cells when they were grown to confluence on the rectangular and equally-sized electrode layout as well as on the horse shoe electrode layout. In the case of the interdigitated finger electrode layout, the difference in the positions of the inflection points on the frequency axis for MDCK-I and MDCK-II cells was two orders of magnitude and thus even larger. Nevertheless, as the major signal difference between the spectrum of the cell-free electrode and the spectrum of the cell-covered electrode after 48 h and 72 h in the case of MDCK-II and MDCK-I cells, respectively, was observed at a frequency of 10^4 Hz for both cell types on all three electrode layouts, this most sensitive frequency was kept constant for all time-resolved capacitance measurements. Furthermore, a sensitive frequency of 10^4 Hz ensured that no setup-related artefacts could incorrectly be interpreted as a cell signal.

V.1.2 Independent Monitoring of Co-Cultures

As previously described in chapter II.3, an independent monitoring of stratified cell layers using an impedance-based approach with coplanar gold electrodes has so far not been reported in literature. The groundwork for the establishment of the novel measurement system has been laid at the University of Regensburg (PhD thesis Kathrin Hayek, 2016) where commercially available Transwell® filter inserts (Corning Inc., New York, US) were sputtered on the reverse side with a 100-nm-thick gold layer which could then be used as an additional electrode when contacted via an insulated copper wire. The other electrodes consisted of (i) the stainless-steel bottom plate of the well holding the filter insert and (ii) a stainless-steel dipping electrode which was suspended above the filter insert. Cells were afterwards co-cultured on both sides of the filter insert – the pristine polycarbonate membrane on the upper side and the gold-covered membrane on the lower side – to create a physiological environment for both cell layers in which they could communicate with each other through the porous membrane due to the physical proximity[68]. Different electrode combinations yielded different information: integration across both cell layers was obtained by measuring the steel bottom plate against the steel dipping electrode. In contrast to that, individual signals of the two cell layers were obtained either by a combination of the porous gold layer with the bottom plate to monitor the cell layer on the reverse side or measuring the dipping electrode against the porous gold layer in order to monitor the cells on the upper side. This way, the transepithelial electrical resistance (TER) as well as the cell layer capacitance could be determined either for the whole co-cultured model or the individual contributions of each cell layer using equivalent circuit modelling. The proof-of-concept measurements had been successful; however, a stacking of more than the two cell-layers remained inconceivable as the dipping electrode and the bottom plate were bulky and impermeable and it would have been impossible to address all of the cell layers individually and independently except for the topmost and the bottommost layers, which nipped ideas of stacking multiple filter inserts in the bud.

Thus, the aim of this thesis was to build on these preliminary findings and to develop a type of permeable support which equally enabled the independent addressing of the two co-cultured cell layers on both sides but at the same time allowed for a stacking of multiple supports inside a measurement chamber. The most important steps and pioneering measurements will be discussed in the following three chapters leading to the final version of the permeable supports.

V.1.2.1 Reverse Side Electrolyte Impact

In this chapter, the influence of the substrate (permeable or impermeable) as well as the influence of buffer solution being present on both sides of the filter membrane shall be examined. The studies have been performed with two equally large gold-film electrodes and a centrosymmetrical electrode layout exhibiting a similar active electrode area (compare chapter IV.1.2.1). All studies have been performed with MDCK-I cells during the initial phase of the development process to obtain a maximum signal. Spectra of the cell-covered electrodes have been recorded after a confluent cell monolayer was established and the cells were given enough time to fully differentiate. **Fig. 27** shows *Bode plots* of the rectangular and equally-sized electrode layout (chapter IV.1.2.1.1) patterned on Lexan® as an impermeable substrate (**A**) and on the permeable polycarbonate filter (catalogue number: HTTP09030, Merck Group, Darmstadt, DE) either insulated with highly adhesive PDMS from below (**B**) or suspended between two buffer compartments (**C**).

Fig. 27: Rectangular and equally-sized electrode layout (chapter IV.1.2.1.1) patterned on Lexan® (**A**) or a permeable polycarbonate filter membrane (**B&C**). The polycarbonate filter membrane was either insulated from below with an adhesive layer of PDMS (**B**) or freely suspended in between two buffer reservoirs (**C**). Spectra of the cell-free electrodes are color-coded **black** and spectra of a confluent MDCK-I cell layer are depicted in **blue** in the *Bode plots* with the impedance spectra |Z|(f) shown in the upper row and the corresponding phase angle φ(f) in the lower row. Representative single spectra were recorded at T = 37 °C and 5 % CO_2.

In **Fig. 27**, the impedance spectra |Z|(f) are shown in the upper and the corresponding phase angle φ(f) in the lower row. The impedance spectra of the cell-free electrodes were similar regardless of the substrate and its insulation. The bulk resistance at high frequencies consistently displayed values around 200 – 300 Ω which, in a range from 1 – 10 kHz, merged into the CPE element exhibiting 200 kΩ at the lower frequency end. Solely in the case of the permeable substrate suspended in buffer, there were obviously resistive influences present at low frequencies, as the phase shift was slightly elevated, displaying –65° instead of the expected –90°. The underlying reason is most certainly setup-related, as (i) the porosity of the electrode offered an alternative current pathway and (ii) the PDMS masks from **Fig. 16** have not been entirely planar and a lot of external pressure had to be applied to keep the culture medium from leaking from the setup. A clear cell signal was observed in the case of the impermeable Lexan® substrate as well as the permeable, PDMS-insulated filter membrane but not for the filter membrane suspended in buffer. In this case, a fully developed and differentiated MDCK-I cell layer was invisible for the impedance-based detection method as the alternating current was not forced to pass the cell layer in order to reach the other electrode, but could flow through the permeable substrate to the other side and overcome the distance with the help of the electrolyte on the other side. This phenomenon has also been encountered in some studies in literature, however, it has not always been noticed and resolved. An example of such a study, in which the setup is similar to the one under development in this thesis, is Ramiah Rajasekaran et al. (2020)[69]. Herein, a coplanar gold-film electrode layout was sputtered on a permeable substrate which was suspended between two buffer compartments. The authors of the mentioned publication claimed to be able to detect a cell signal with their setup which, effectively, was only a shift of the electrode-electrolyte interface-related contribution to the overall impedance at low frequencies. A cell-related influence in contrast, was not discernible. As unfortunate as the publication of this misleading study is in itself, it also showed that the problem of the reverse side electrolyte current has been experienced by others as well and that a suitable solution to that problem is needed. **Fig. 27C** already implied that the only possible solution to this problem would be a strategy to prevent the alternating current from reaching the counter electrode without having to pass the cell layer growing on top of the filter membrane. Due to practical reasons, the implementation entailed a shift from a pair of equally-sized electrodes to a centrosymmetrical electrode layout. **Fig. 28** shows the same measurement conditions using the HSE layout (first layout in IV.1.2.1.3): on Lexan® as an impermeable substrate (**A**) and on a permeable polycarbonate filter either insulated with highly adhesive PDMS from below (**B**) or suspended between two buffer compartments (**C**).
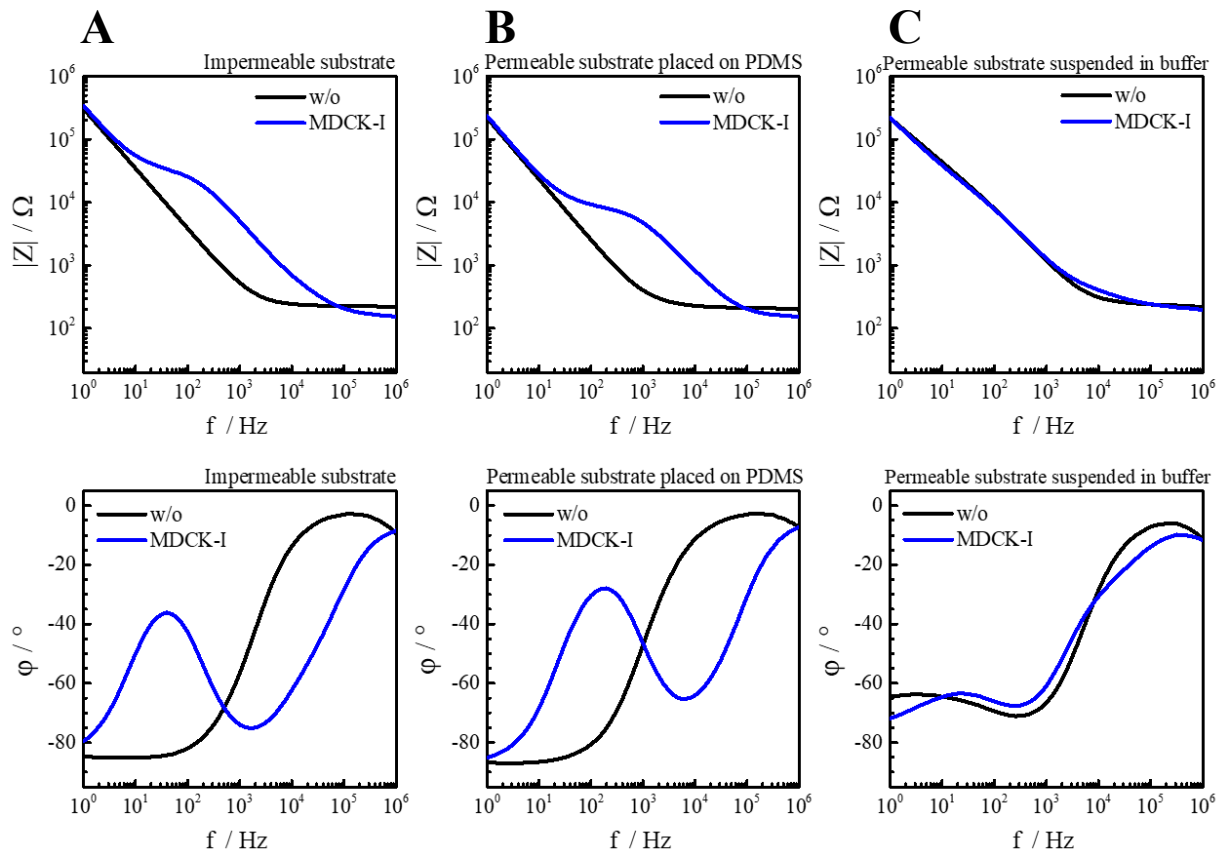
Fig. 28: Horse shoe gold electrode layout (first layout, chapter IV.1.2.1.3) patterned on Lexan® (**A**) or a permeable polycarbonate filter membrane (**B&C**). The filter membrane was either insulated from below with an adhesive layer of PDMS (**B**) or freely suspended in buffer (**C**). Spectra of the cell-free electrodes are color-coded **black** and spectra of a confluent MDCK-I cell layer are depicted in **blue** in the *Bode plots* with the impedance spectra $|Z|(f)$ shown in the upper row and the corresponding phase angle $\varphi(f)$ in the lower row. T = 37 °C, 5 % CO_2.

The values of the bulk resistance were determined to be between $100 - 300\ \Omega$ and, at a frequency of 1 kHz, merged into the straight line with a slope close to (–1) representing the CPE element in the case of the cell-free electrode which, at 1 Hz, measured 100 kΩ (**A**, **B**) and 40 kΩ (**C**). Using the HSE layout, the PDMS masks were replaced by cylindrical buffer reservoirs which were glued on the filter from both sides and made the second-generation prototype (compare **Fig. 17** on page 47) more leak-proof compared to the first one and no longer directly determined the centrosymmetrical active electrode area. The phase shift pertaining to the cell-free horse shoe-patterned filter membrane suspended between two buffer compartments closely resembled the ones on the impermeable Lexan® and the permeable filter membrane without any electrolyte beneath. Nevertheless, the cell layer growing on top of the filter again could not be detected due to the aforementioned problematic nature of the reverse side electrolyte impact. As long as the reverse side of the counter electrode was unavailable for the current e.g. due to the impermeable Lexan® substrate or the PDMS barrier directly below the porous filter membrane, the spectra of the cell-covered electrodes could

clearly be distinguished from the ones of the cell-free electrode. As soon as a second buffer compartment below the filter was available, the spectra of the cell-free and the cell-covered electrode became indistinguishable as in the REE layout. These observations made clear that on the one hand the area of the counter electrode on the underside needed to be completely insulated to prevent unwanted current pathways. The porosity of the working electrode on the other hand needed to be preserved in order to maintain the physiological environment and co-culture possibilities for the cells growing directly on the circular working electrode.

V.1.2.2   Insulation of the Counter Electrode

All of the preliminary experiments had undisputedly shown that an insulation of the reverse side of the counter electrode was necessary to guide the alternating current through the cell layer. A first approach towards the insulation of the counter electrode was made by applying a gel-like silicon glue on the reverse side of the filter membrane in all the area of the counter electrode. The general setup is depicted in **Fig. 17** on page 47. The lower (basolateral) compartment was left empty whereas the cells were inoculated according to the standard protocol in the upper (apical) compartment at a seeding density of $5 \cdot 10^5$ cells per cm^2. The frequency-dependent magnitude of impedance as well as the corresponding phase shift was determined before MDCK-I cell inoculation and again 24 h after and are shown in **Fig. 29**.

The only difference between the experimental setups was the application of the silicon glue on the reverse side of the filter in the area of the counter electrode. The effect however, could clearly be seen in the *Bode plots*. The impedance spectrum of the cell-free electrode on the left-hand side was similar to the one recorded on an impermeable substrate or on a permeable substrate placed on PDMS and exhibiting a bulk resistance of around 300 Ω. The horizontal line merged into the contribution of the CPE element at 1 kHz and yielded 100 kΩ at the lowest recorded frequency of 1 Hz (**Fig. 29A**). The spectrum of the cell-free electrode on the right-hand side showed similar values for the bulk resistance at high frequencies, but the CPE part was parallel-shifted one order of magnitude to higher frequencies (**Fig. 29B**). This way, the resistive and capacitive contributions joined at approximately 10 kHz instead of 1 kHz. Due to the different properties of the electrode-electrolyte interface following the insulation of the underside of the counter electrode, the sensitivity of the system was considerably reduced: due to the higher interface impedance, the capacitive properties of the cell layer could no longer be distinguished from the one of the electrode-electrolyte interface.

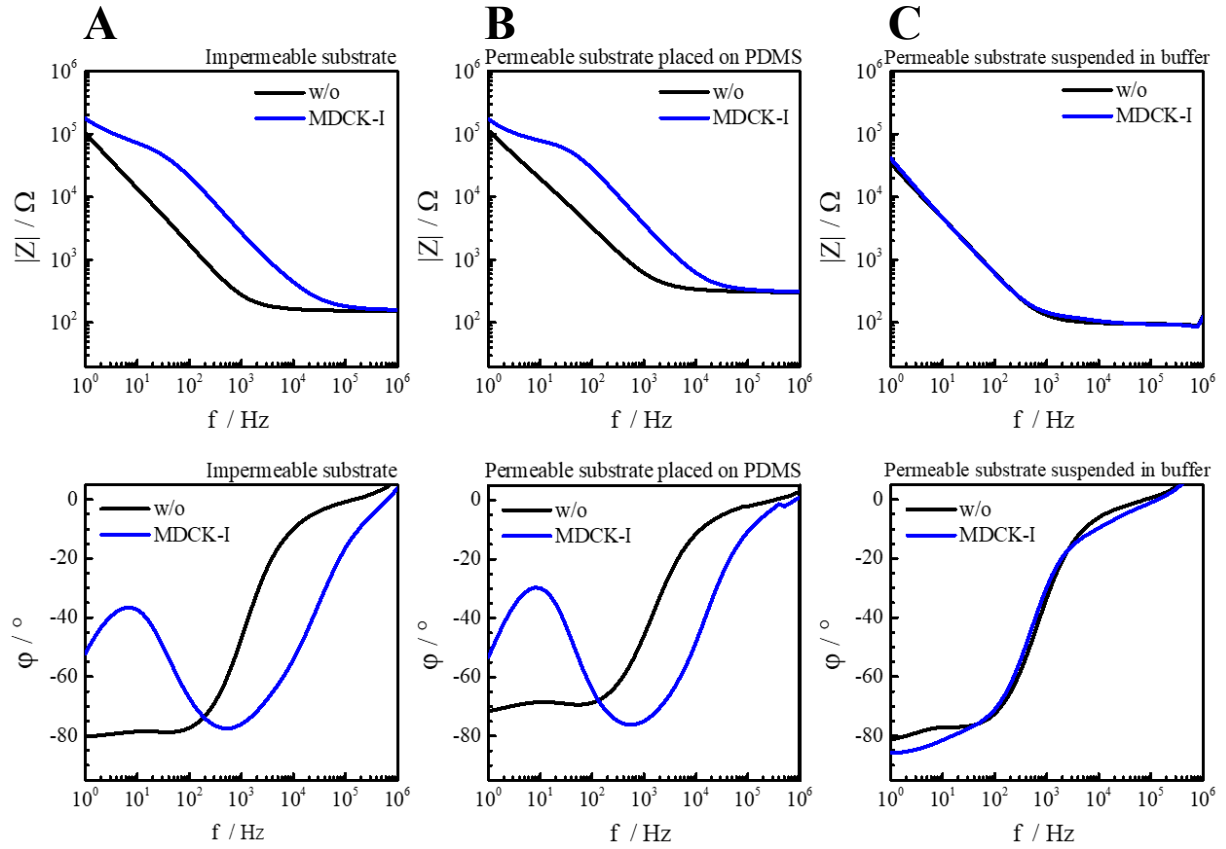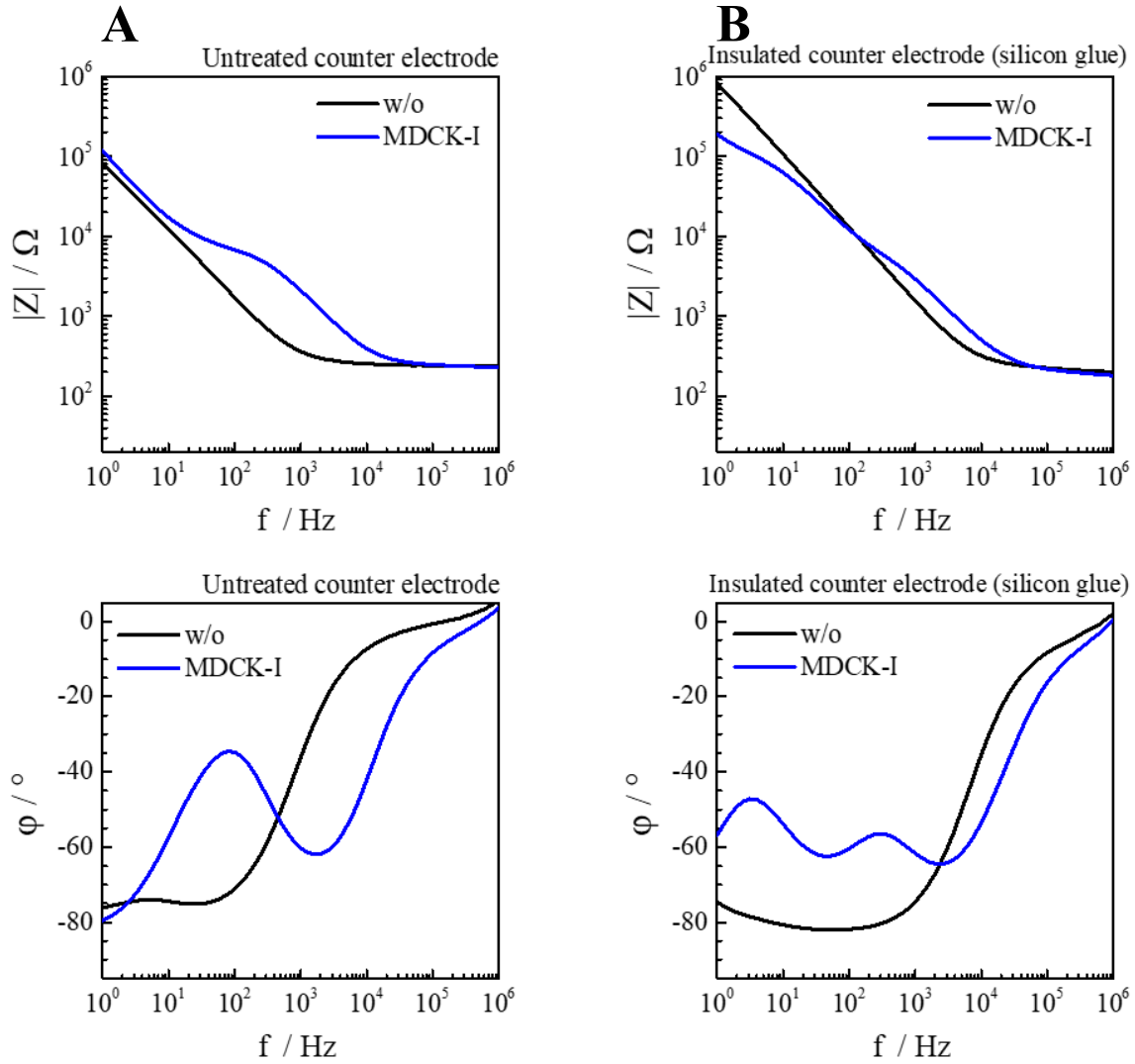**Fig. 29:** *Bode plots* of the horse shoe gold electrode layout (first layout, chapter IV.1.2.1.3) patterned on a permeable polycarbonate filter membrane. |Z|(f) is shown in the upper row with the corresponding φ(f) in the lower row. The basolateral compartment was left empty and the filter membrane was either completely untreated (**A**) or the reverse side of the counter electrode insulated with silicon glue (**B**). Spectra of the cell-free electrodes are color-coded **black** and spectra of a confluent MDCK-I cell layer are depicted in **blue**. T = 37 °C, 5 % CO_2.

The second characteristic feature was observed in the phase shift of the cell-covered insulated horse shoe gold electrode layout in **Fig. 29B**. The phase shift exhibited a second maximum at low frequencies indicating a resistive influence where the electrical behavior should normally be dominated by the near ideally capacitive electrode-electrolyte influence. The exact reason remained unclear although it is assumed that the flowable silicon glue completely soaked the filter membrane and thereby also covered parts of the counter electrode on the upper side which entailed (i) the parallel shift of the CPE element to higher frequencies as the available electrode area was reduced and (ii) the silicon layer could possibly have been partly loosened by the cells which would explain the lower impedance values at low frequencies with a confluent cell layer growing on top of the filter membrane (**Fig. 29B**, |Z|(f)).

Another approach to insulate the reverse side of the counter electrode was made with the help of a biocompatible and self-adhesive lamination foil (KN2120, Fraunhofer EMFT, Munich, DE) in the dimension of 14.4 mm in diameter with a central opening in a diameter of 500 μm which was positioned right beneath the circular working electrode. This way, the area of the working electrode was still permeable to small molecules and tracers and provided a physiological environment for the cells growing directly on it, whereas the entire area of the counter electrode was effectively sealed from below making the reverse side unavailable for the current. The amount of glue accounting for the self-adhesive properties of the lamination foil was not sufficient to wet the gold-coated side of the filter membrane and consequently did not change the properties of the electrode-electrolyte interface.

Fig. 30 shows the *Bode plots* for the cell-free electrode (**black**) and the cell-covered electrode (**red**) for which the setup is depicted in **Fig. 17** on page 47. The lamination foil was pinned to the reverse side of the polycarbonate filter membrane and the central opening was being positioned directly underneath the working electrode of the horse shoe electrode layout. The buffer compartments on both sides were completely filled. The frequency-dependent magnitude of impedance $|Z|(f)$ and corresponding phase shift $\varphi(f)$ are shown on the left-hand side (**A**) and the right-hand side (**B**), respectively.
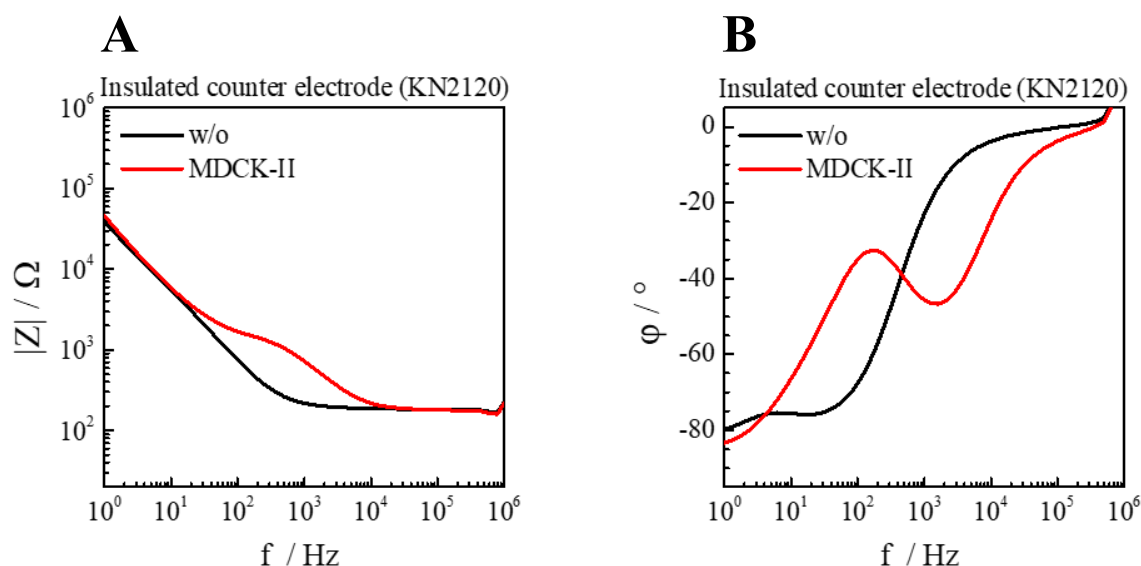
Fig. 30: *Bode plot* of the horse shoe gold electrode layout which was sputtered on a polycarbonate filter membrane suspended between two buffer compartments. The area of the counter electrode was insulated from below using the self-adhesive lamination foil (KN2120) with the central opening positioned directly beneath the working electrode. Impedance spectra $|Z|(f)$ are given on the left-hand side and the corresponding phase angle $\varphi(f)$ on the right-hand side. Spectra of the cell-free and the MDCK-II cell-covered electrode are depicted in **black** and **red**, respectively. Data was recorded at 37 °C and 5 % CO_2.

The impedance spectrum of the cell-free electrode in **Fig. 30A** closely resembled the ones from the previous chapters with the CPE element dominating the first two orders of magnitude of the frequency axis and the bulk resistance the last three orders of magnitude displaying constant impedance values of 180 Ω. The 45°-slanted line representing the electrode-electrolyte interface merged with the horizontal line at approximately 1 kHz. With a confluent MDCK-II cell layer growing on the upper side of the filter membrane, a cell contribution to the impedance spectrum was observable between 10 Hz and 50 kHz. Impedance values recorded for lower and higher frequencies overlapped with the cell-free ones. The dispersions of the electrode-electrolyte interface and the cell membranes were separated by one order of magnitude and exhibited nearly the same slope. The height of the plateau was 1500 Ω which roughly corresponded to an R_b value of 50 Ω·cm^2 with the area of the working electrode taken into account. This value compared well with the fitted results from the rectangular and equally-sized as well as the interdigitated finger electrode layout.

On the right-hand side in **Fig. 30B**, the corresponding phase angle is shown. In the phase spectrum of the cell-free electrode, values close to 0° were obtained at high frequencies and a value of –80° was determined at a frequency of 1 Hz. The steepest slope (inflection point) in the phase shift of the cell-free electrode occurred at 1 kHz corresponding to the same frequency at which the resistive and the capacitive elements of the cell-free electrode merged in the impedance spectrum. When a confluent MDCK-II cell layer was adherent on the electrode surface, a local minimum was observed at 1.5 kHz indicating the capacitive influence of the cell membranes and a local maximum emerged at 180 Hz corresponding to the resistive contributions of the cell-cell contacts as well as the cell-substrate contacts. At the low-frequency and high-frequency ends of the measured spectrum, the phase angle for the MDCK-II cell-covered electrodes again overlapped with the cell-free ones.

The insulation of the counter electrode with the self-adhesive lamination foil made it possible to obtain a clear cell-related signal despite the direct contact with a second, basolateral buffer compartment. This already paved the way for a potential stacking of multiple filter membranes equipped with the horse shoe electrode layout on one side where cells could grow on and the reverse side of the counter electrode being insulated by the lamination foil.

V.1.2.3 Three-Electrode Setup

The insulation of the counter electrode, which was discussed in the previous chapter, yielded the possibility of monitoring a cell layer growing on the apical side of a porous substrate dividing two buffer compartments. At the current state of the setup however, a second co-cultured cell layer growing on the basolateral side of the filter could only be monitored by reverting to the TER measurements where the bottom plate electrode would be measured against the working electrode of the horse shoe electrode layout on the filter. This would certainly have worked, although the idea of stacking multiple filters on top of each other would, at the same time, have been buried. Thus, an elegant alternative way was to use the already available lamination foil on the reverse side and by coating it with a 100-nm-thick gold layer, creating an additional counter electrode which, together with the still porous WE, could be used to monitor the co-cultured cell layer growing directly on the lamination foil and thereby allowing for the ECIS® principle to be applied. With this novel three-electrode setup, the two co-cultured cell layers on both sides of the permeable support could be measured sequentially by (i) measuring the working electrode against the coplanar counter electrode on the same side of the filter to detect morphological changes of the apical cell layer and (ii) the same working electrode could be measured against the gold-coated lamination foil pinned to the reverse side of the filter to observe cellular behavior of the cell layer on the basolateral side. Thus, the lamination foil with its central opening maintains the porous properties of the working electrode filter area. The following chapter will provide an overview of different geometries concerning the central hole in the lamination foil and the impact on the cell signal. The diameter of the hole in the lamination foil was chosen to be either larger, equal to or smaller than the diameter of the working electrode of the horse shoe layout. For all three cases, cells were seeded in one experiment exclusively on the apical side of the substrate to assess the impact on the frequency-dependent magnitude of impedance on both sides. In a complementary experiment cell inoculation was performed only on the basolateral side to see how that influenced the impedance spectra on both sides of the permeable support.

Diameter (hole) > diameter (WE)

For the first combination, the horse shoe electrode layout from **Fig. 12A** was employed which had also been used throughout the previous chapter and offered a 2-mm diameter of the working electrode. The diameter of the hole in the lamination foil was chosen to be 4 mm, thereby covering the underside of the counter electrode on the filter membrane completely and ending halfway between the working and the counter electrode.

Fig. 31 gives an overview of the resulting *Bode plots* when the apical and basolateral counter electrodes were measured against the one working electrode for cells having been seeded solely on the apical side (**A**) or the basolateral side (**B**).
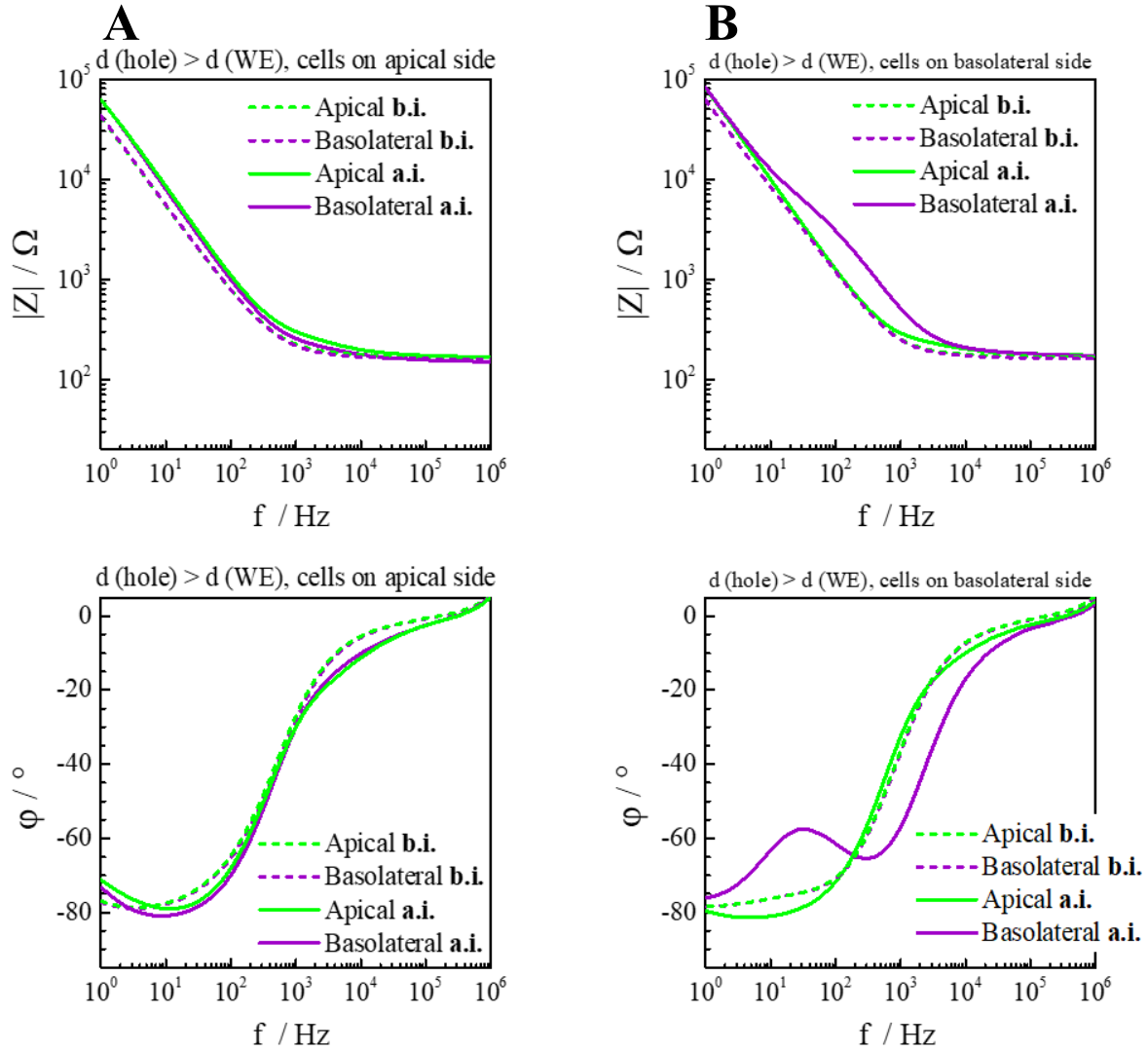
Fig. 31: *Bode plots* of the apical (**green**) and basolateral (**purple**) counter electrodes being measured against the one 2-mm working electrode after cells had been seeded solely on the apical side (**A**) or the basolateral side (**B**) and both reservoirs were completely filled. Dashed lines signify spectra recorded before cell inoculation (**b.i.**) and solid lines represent spectra recorded 48 h after MDCK-I cell inoculation (**a.i.**). Diameter of the hole in the lamination foil was 4 mm. Experiments were perfomed at T = 37 °C and 5 % CO_2.

The phase and impedance spectra for the cell-free electrode combinations in **Fig. 31** closely resembled the reference ones on the impermeable Lexan® substrate (**Fig. 28A**). The bulk resistance was determined to be around 200 Ω, merged into the contribution of the CPE at 1 kHz and yielded between 60 – 80 kΩ at the lowest recorded frequency of 1 Hz. Concentrating on the *Bode plot* on the left-hand side where MDCK-I cells (representing tight epithelial cells) had only been seeded on the apical side, no difference was observed between

the spectrum of cells growing on top of the filter or without a confluent cell monolayer. Once again, it seemed the current used the electrolyte in the basolateral compartment to reach the coplanar counter electrode. However, if MDCK-I cells were seeded only on the reverse side of the filter membrane and thus on the back side of the permeable WE as well as on the gold-coated lamination foil, they could be detected by using the WE of the HSE and the gold-coated lamination foil as counter electrode. The maximum in the phase spectrum indicated that time-dependent changes due to the cell layer should be followed at 30 Hz which was in accordance with previous measurements. In this case, the alternating current had no choice but to pass the basolateral cell layer to reach the other electrode. But considering that a cell monolayer on the apical side was not detectable, the geometry of the hole in the lamination foil being larger than the size of the working electrode was dismissed.

Diameter (hole) = diameter (WE)

The second combination again employed the HSE layout from **Fig. 12A** with its 2-mm diameter of the WE. This time, the hole in the lamination foil equally measured 2 mm in diameter so that only the area of the working electrode was not insulated with lamination foil from below. In analogy to **Fig. 31**, **Fig. 32** depicts the corresponding *Bode plots* when the apical and basolateral counter electrodes were measured against the one working electrode for MDCK-I cells having been seeded solely on the apical side (**A**) or the basolateral side (**B**).

Similar to the example before, problems arose when cells had been seeded on the apical side. The impedance and phase spectra clearly showed the presence of the MDCK-I cells on the apical side, but at the same time, the spectra also suggested a cell layer being present on the basolateral side which was not the case. Furthermore, when comparing the spectra of the cell-covered apical and basolateral electrode combinations, they were conspicuously identical. As to the reason, only presumptions could be made, but it seemed the alternating current first passed the apical cell layer before reaching the gold-coated lamination counter electrode. The assumed current pathways are schematically depicted in **Fig. 34** on page 81. In contrast to the apical cell seeding, an exclusive MDCK-II cell inoculation on the basolateral side yielded the expected spectrum of a cell-covered electrode only on the respective basolateral side while the coplanar apical electrode pair still portrayed a cell-free environment. The two facts that (i) the 2-mm hole in the lamination foil was produced with a hollow punch tool leaving the rim slightly uneven and that (ii) the exact positioning of the opening in the lamination foil beneath the working electrode had proven to be highly demanding, could have provided small loopholes for the current between the gold on the filter and the gold-coated lamination foil.

Thus, the current was able to flow in ways that had previously not been anticipated which in turn yielded the interdependent signals.

Fig. 32: *Bode plots* of the apical (green) and basolateral (purple) CEs being measured against the one 2-mm WE after cells had been seeded solely on the apical side (MDCK-I) (**A**) or the basolateral side (MDCK-II) (**B**) and both reservoirs were completely filled. Dashed lines signify spectra recorded before cell inoculation (**b.i.**) and solid lines represent spectra recorded 48 h after cell inoculation (**a.i.**). Diameter of the hole in the lamination foil was 2 mm and experiments were conducted at T = 37 °C and 5 % CO_2.

Diameter (hole) < diameter (WE)

For the last combination, the horse shoe electrode layout was changed to **Fig. 12C** exhibiting a 4-mm WE. The diameter of the hole in the lamination foil was adjusted to 3 mm which made the positioning easier and provided a larger area for the cells to establish a fully differentiated cell monolayer on the reverse side of the permeable WE. The hole in the lamination foil was cut with a high-precision desktop laser scriber which helped to generate smooth edges and thus to increase the contact area with the filter membrane at the perimeter.

Fig. 33 depicts the resulting spectra after MDCK-II cells had been seeded only on the apical side (**A**) or the basolateral side (**B**).
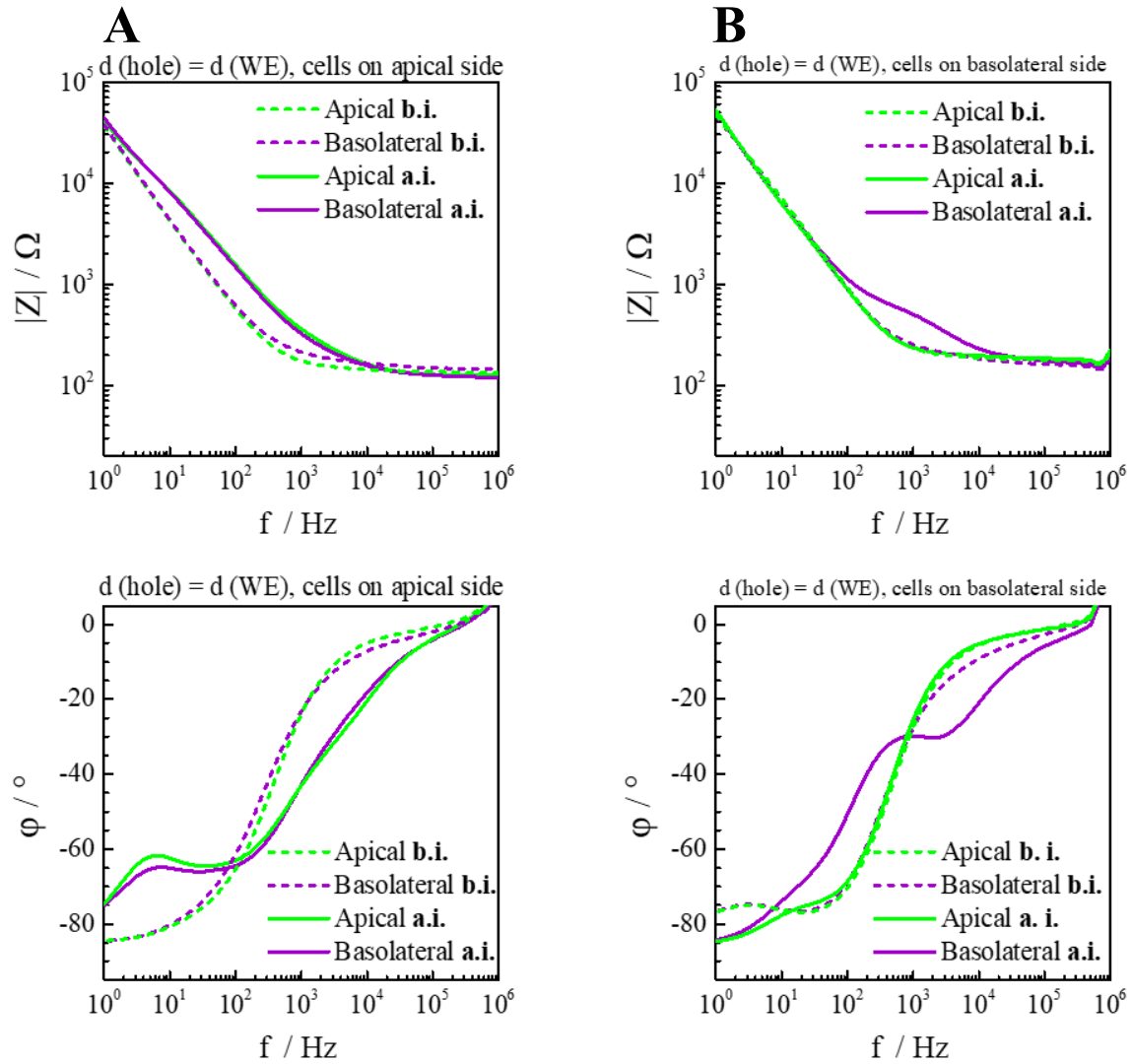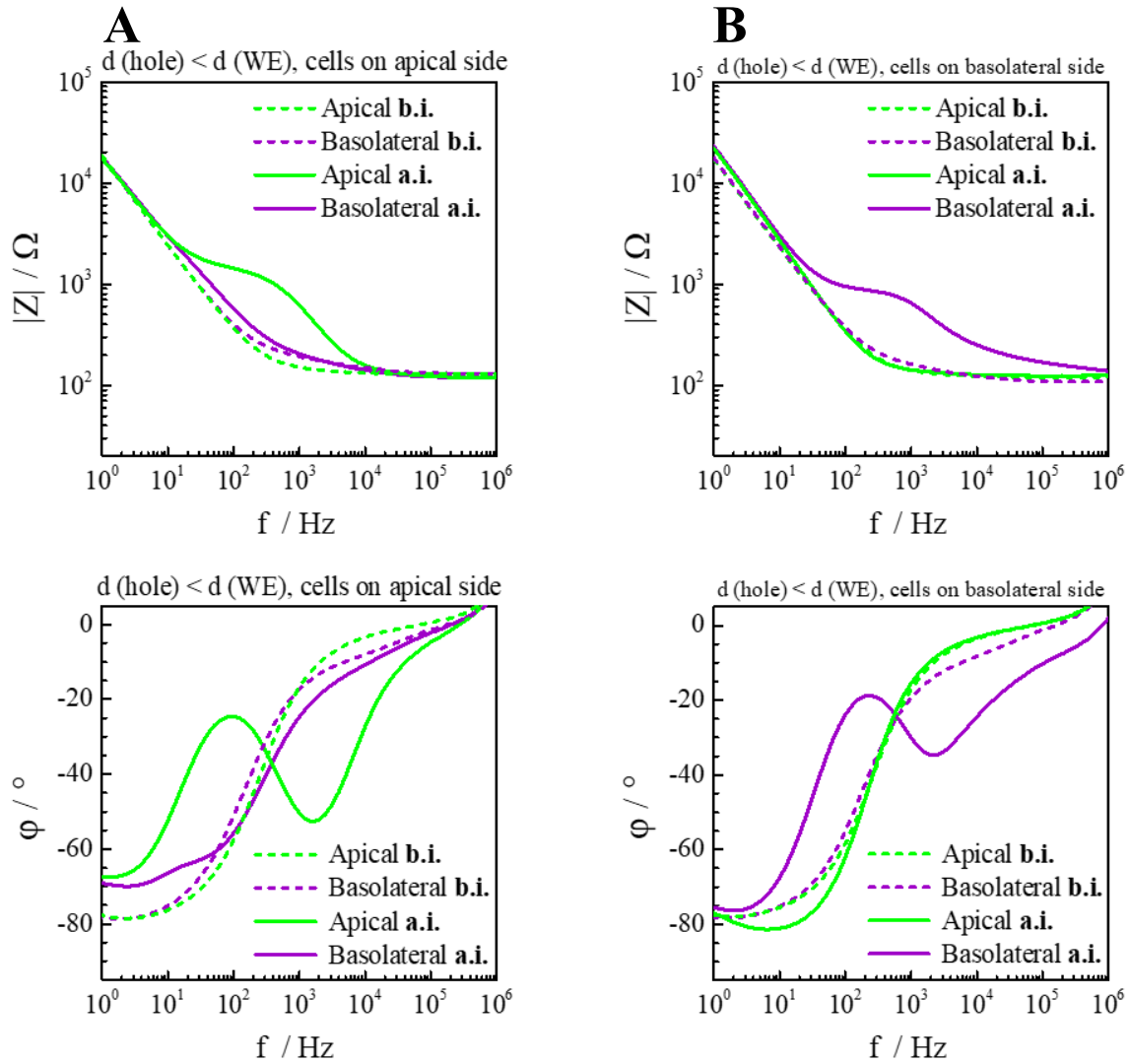

Fig. 33: *Bode plots* of the apical (green) and basolateral (purple) CEs being measured against the one 4-mm WE after MDCK-II cells had been seeded solely on the apical side (**A**) or the basolateral side (**B**) and both reservoirs were completely filled. Dashed lines signify spectra recorded before cell inoculation (**b.i.**) and solid lines represent spectra recorded 48 h after cell inoculation (**a.i.**). Diameter of the hole in the lamination foil was 3 mm. T = 37 °C, 5 % CO_2.

Both electrode combinations determined the bulk resistance to be approximately 150 Ω which was in accordance with the previous measurements. The interface impedance at 1 Hz was lower (20 kΩ) reflecting the larger area of the WE (12.53 mm^2) instead of the smaller area from the first layout (3.05 mm^2, compare **Fig. 32**). Apart from an additional, setup-related RC element (parallel connection of a resistor and capacitor connected in series to the bulk resistance and the CPE element) found between 1 kHz and 10 kHz for the basolateral CE combination, the spectra of the cell-free electrode combinations were very similar. The RC element was always seen in $|Z|_{cell-free}(f)$ for the basolateral electrode combination (dashed

purple line) and could either stem from the plate capacitor-like setup (lamination foil acting as insulating material between the two gold layers) or from the electrolyte and constriction resistance in the aperture of the lamination foil. Furthermore, the RC element was always seen if the gold-coated lamination foil was used as part of the electrical circuit, no matter if measured against the WE or the CE on the filter membrane and independent of the fact if the filter membrane in the area of the WE was intact or not. A detailed study thereof can be found in the supplementary information part (chapter IX.1). However, the overall influence was neglected as it was minimal compared to the change in the spectrum which was provoked even by a leaky, confluent NRK cell layer. With the diameter of the hole in the lamination foil being smaller than the one of the WE, it was possible to independently and individually detect cells growing on either side of the setup. **Fig. 34** schematically depicts the assumed current pathways for the different sizes of the hole in the lamination foil and cells either growing on the apical side (upper row) or the basolateral side (lower row).
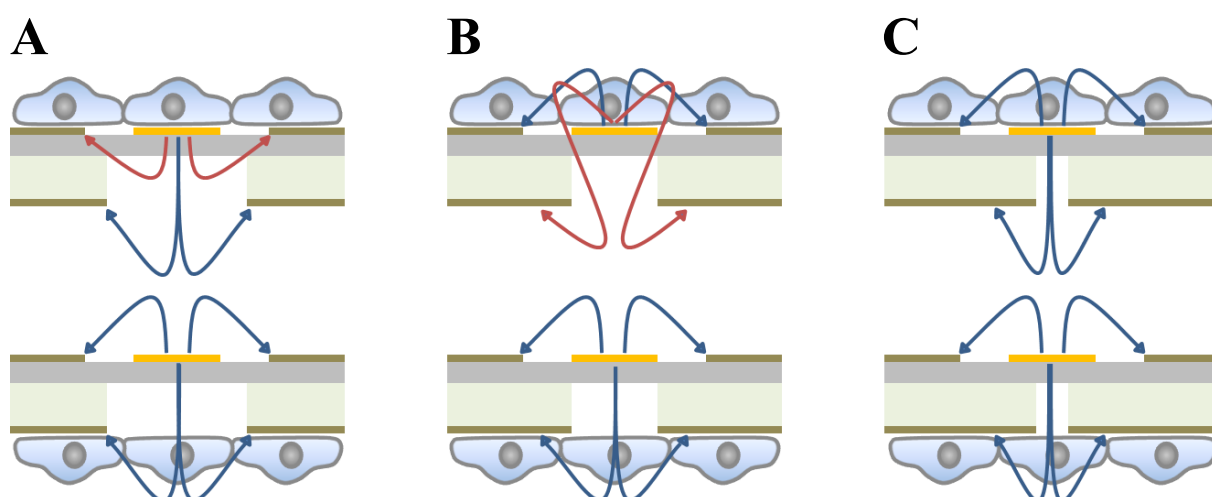
Fig. 34: Schematic depiction of the current pathway for different sizes of the hole in the lamination foil. (**A**) Diameter (hole) > diameter (**WE**), (**B**) diameter (hole) = diameter (**WE**), (**C**) diameter (hole) < diameter (**WE**). The filter membrane is color-coded grey and the lamination foil green. For the measurements unfavorable current pathways are depicted in red, successfully directed current pathways are marked blue.

In summary, the lack of a cell signal for a larger hole in the lamination foil compared to the size of the working electrode on the filter membrane again confirmed the problematic nature of the reverse side electrolyte current from chapter V.1.2.1. The equal sizing of the hole in the lamination foil and the working electrode proved to be highly complex regarding the precise positioning. Even a minimal misalignment led to a ghost cell signal on the basolateral side although cells had only been seeded on the apical side. Decreasing the hole in the lamination foil below the size of the working electrode finally enabled an individual addressing and unequivocal distinction between a cell layer growing on the apical and the basolateral side.

V.1.3   Stacking of Two Permeable Supports with Integrated Sensors

Successfully establishing the three-electrode setup to independently measure cell layers grown on either side of the filter membrane laid the groundwork for the stacking of more than two cell layers. In order to move from the proof-of-concept prototype (**Fig. 17**) to a stackable version, the plastic containers glued to both sides of the substrate had to be replaced by a stabilizing framework. This framework was required on the one hand to expose the entire area of the counter electrodes measuring 24 mm in diameter to the culture fluid, but on the other hand also to provide enough stabilization for a feasible and leak-proof cell seeding and secure handling of the permeable supports. A detailed description of the final production process is given in chapter IV.1.2.3. In cooperation with the workshops of the faculties of Biology and Chemistry, a cultivation chamber was designed, enabling the cultivation of cell monolayers on each side of the permeable support. As the feed lines of the one working and the two counter electrodes protruded from the cultivation chamber, they could be contacted while the permeable support was still jammed between the two half frames by magnetic flippers. **Fig. 35** depicts *Bode plots* stemming from two similarly manufactured permeable supports (F1 and F2) which were measured directly in the cultivation chambers (see **Fig. 18**) after MDCK-II cells had been cultivated solely on the back of F1 (CE on lamination foil) or the front of F2 (CE on filter membrane). The frequency-dependent magnitude of impedance is shown on the left-hand side (**A**) and the corresponding phase shift on the right-hand side (**B**). The spectra from the two filters have been plotted in the same graph for easier comparison.
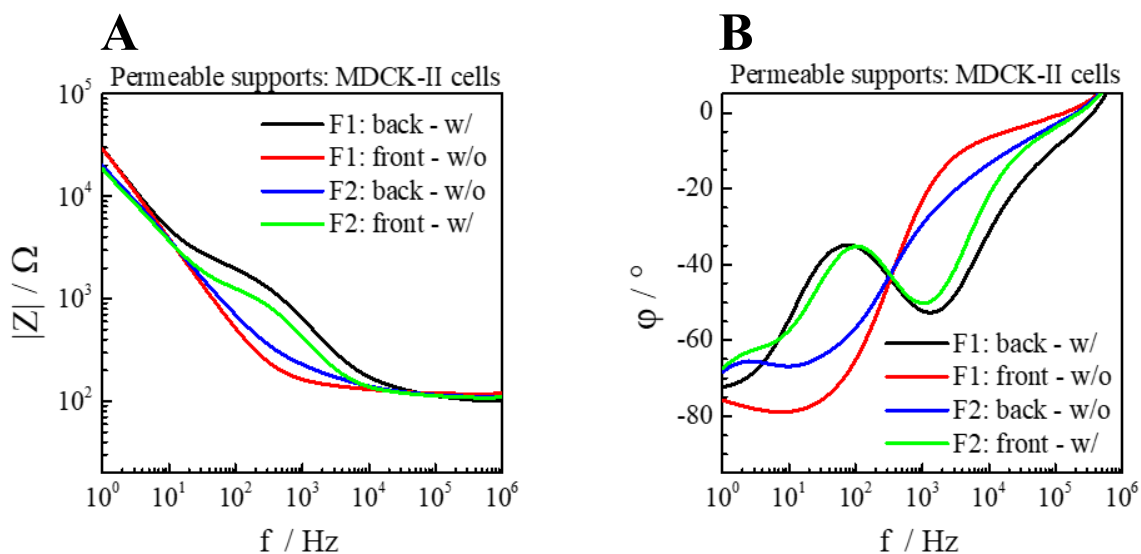

Fig. 35: Representative *Bode plots* from two individual permeable supports with a confluent MDCK-II cell layer growing on the back of the first permeable support (F1) or the front of the second permeable support (F2). Data was recorded 24 h after cell inoculation with the supports still installed in the culture medium-filled cultivation chambers at T = 37 °C and 5 % CO_2.

The bulk resistance at high frequencies was around 150 Ω and thus in accordance with the values from the prototype. The |Z| value at the lower frequency end of 1 Hz was around 30 kΩ as the HSE layout with the larger 12.53-mm^2 area of the WE was employed. It is worth noting that the slope of the CPE element in the impedance spectra, which is represented by the parameter n_{CPE}, was slightly differing from one permeable support to the next. Every permeable support was assembled by hand and the areas, where the stabilizing frames and the counter electrodes meet on both sides, were manually insulated with silicon glue to prevent culture medium from penetrating into the polycarbonate filter which, otherwise, could have led to a short-circuit. Thus, the electrode areas were roughly the same, but slight differences in the gold sputtering of the electrodes could have led to variations in the electrode porosity which affects the parameter n_{CPE} by varying amounts of gold and the resulting penetration depth[70]. The second characteristic feature was the seemingly different R_b and C_m values in a direct comparison of the resulting black and green spectrum. In both spectra, the resistive part of the cell influence was exhibited at 100 Hz as indicated by the corresponding maximum in the phase shift. The impedance values were 1255 Ω and 1955 Ω for the green and the black graph, respectively. However, this and the fact that the inflection point of the capacitive part of the cell influence were separated by 500 Ω was not an indication of different cell-related parameters but could be explained by the size of the active electrode area. For the front of the permeable support, the working electrode offered an active electrode area of 12.53 mm^2 whereas on the reverse side, the active electrode area was limited to 7.07 mm^2 due to the size of the hole in the lamination foil. The difference in the size of the active electrode area caused a parallel shift of the 45°-slanted line – representing the electrode-electrolyte interface – feigning higher C_m values for the cells growing on the front side of the permeable supports. Furthermore, the height of the plateau in the spectrum can only be used to directly compare R_b values if the active electrode area is kept constant. For the MDCK-II cells growing on the back of F1 (WE area of 7.07 mm^2), an R_b value of 39.8 $\Omega\cdot$cm^2 and a C_m value of 5.73 μF$\cdot$cm^{-2} were obtained by fitting the spectra and for the MDCK-II cells on the front of F2 (WE area of 12.53 mm^2), the R_b value was determined to be 55.0 $\Omega\cdot$cm^2 and the corresponding C_m value was 8.34 μF$\cdot$cm^{-2}. Although the C_m values were higher in comparison to literature data[67], the values for R_b and C_m were in the same range for the cells growing on different sides of the permeable supports. Thus, varying the WE area and setup under the same cell layer did not affect the e.g. R_b value, just the height of the plateau changed accordingly. The determination of the cell-related parameters will be further discussed in chapter V.3.1 as these were only representative single spectra which have not been measured in triplicates.

The final step in the development process of stacking two permeable supports was also made possible in cooperation with the workshops of the faculties of Biology and Chemistry. A measurement chamber was designed and constructed that could hold two permeable supports in a defined and reproducible distance from each other and at the same time provide culture medium for all four cell layers growing on each side of the two supports. A dimensioned drawing of the final measurement chamber is shown in **Fig. 19** on page 49. The *Bode plots* of two permeable supports, each with a confluent MDCK-I and MDCK-II cell layer on opposing sides are shown in **Fig. 36**.
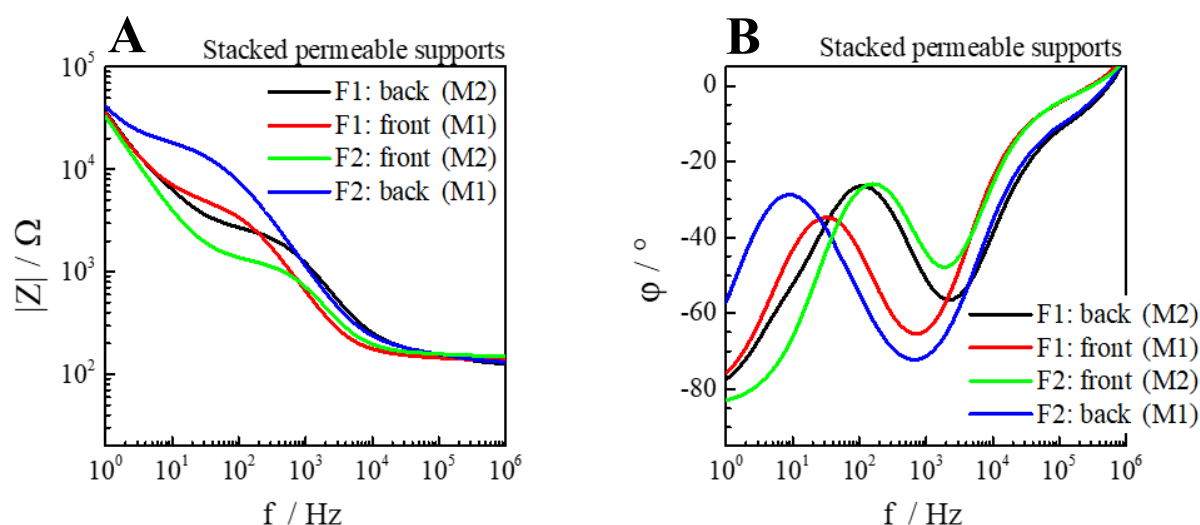
Fig. 36: *Bode plots* of two permeable supports stacked inside a measurement chamber. MDCK-I cells were cultivated on the front of F1 and on the back of F2 whereas MDCK-II cells were cultivated on the back of F1 and the front of F2. Representative spectra were recorded 24 h and 48 h after cell inoculation for M2 and M1 cells, respectively. T = 37 °C, 5 % CO_2.

For convenient electrical connection to the hardware, the permeable supports had to be stacked with the front sides facing each other, so that the MDCK-I cell layer on F1 was separated from the MDCK-II cell layer on F2 only by the culture medium in the middle compartment. In **Fig. 36A & B**, the impedance and phase spectra of two MDCK-I and two MDCK-II cell layers are shown, respectively. Similar to the measurement before, the cellular influence in the spectrum was shifted to higher frequencies for the smaller active electrode on the back of the permeable support in the same manner as the position of the resistive plateau was elevated. In all cases, when one compares the same electrode combinations on the two filters (black & blue or red & green), the very tight MDCK-I cell layer was always clearly distinguishable from the only moderately tight MDCK-II cell layer due to the significantly higher plateau position. To the best of our knowledge, with this setup we were the first ones being able to individually measure four cell layers which were brought into close physical proximity.

84

V.2   Permeable Support Characterization

A general material characterization of the final permeable supports was performed using stereo microscopy, scanning electron microscopy and energy-dispersive X-ray spectroscopy. Further characterization studies included optical and electrochemical diffusion studies.

V.2.1   Material Characterization

The porous polycarbonate filter membrane was optically intransparent and could therefore only be characterized optically via a stereo microscope and not via phase contrast microscopy. **Fig. 37** shows stereo microscopy images in different magnifications of the front side of a permeable support. The magnification increases from the upper left picture to the lower right.
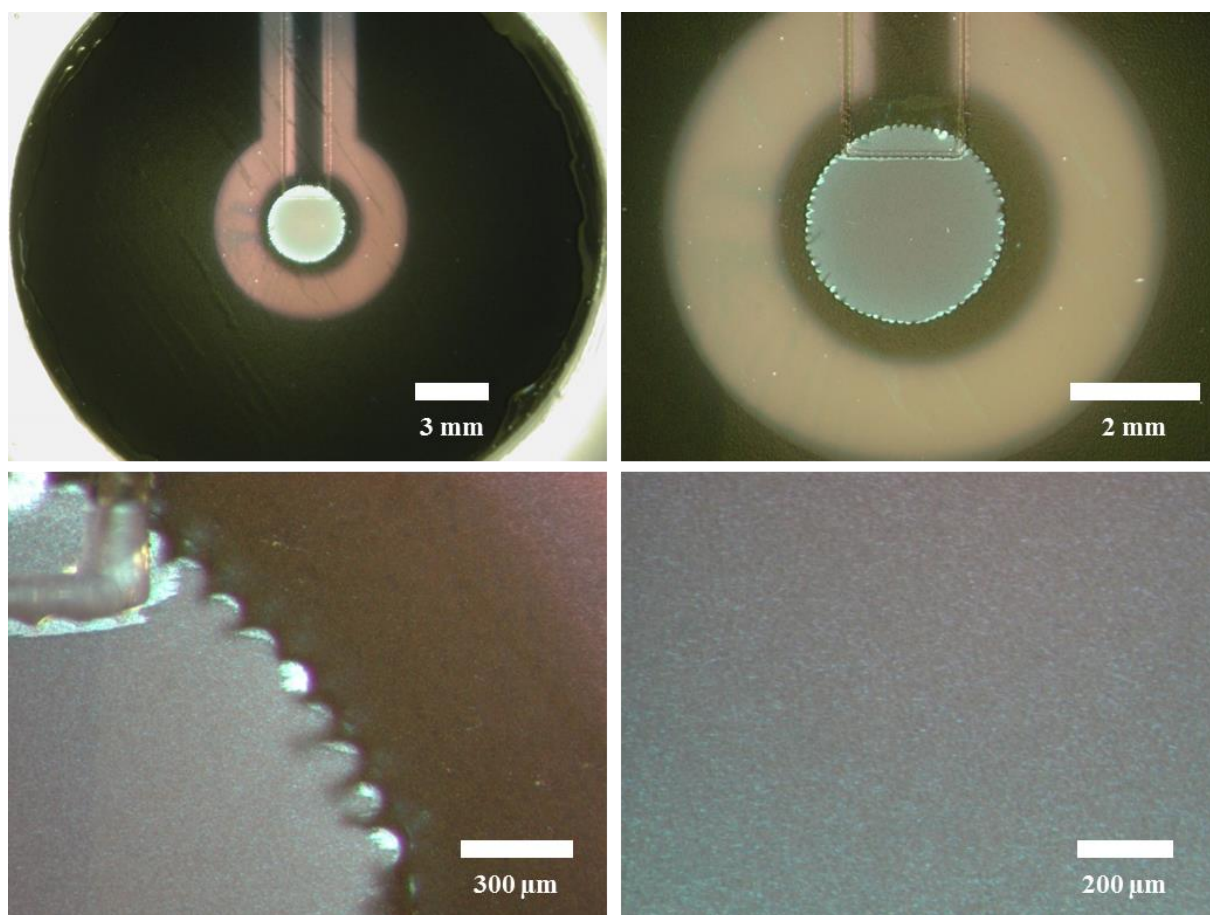
Fig. 37: Stereo microscopy images of the front side of a permeable support. The magnification increases from the upper left to the lower right picture.

The upper left picture confirmed that the only part of the permeable support not insulated by the lamination foil was the 3-mm center of the working electrode (light area). Focusing on the upper right picture, it is shown that (i) the gold-sputtered working electrode spanned the entire

hole in the lamination foil, (ii) the rim of the hole in the lamination foil was rugged due to the horizontal and vertical moving direction of the desktop laser scriber and (iii) the layer of self-adhesive glue on the lamination foil was thin enough not to spread across the filter area but was locally confined (light ring highlighting the perimeter of the hole in the lamination foil). The lower left picture also confirmed the local confinement of the glue as the polycarbonate filter touched by the glue turned impermeable but brighter. The lower right picture shows the porous structure of the pristine gold-covered polycarbonate structure.

The reverse side of the permeable support was characterized using scanning electron microscopy (SEM). **Fig. 38** depicts a permeable support prepared for the SEM process (**A**) where conductive tapes had been attached in order to prevent charging effects during the imaging process by providing grounding contact. The uneven border between the filter (left) and the lamination foil (right) is shown in the SEM image (**B**).

A   **B**
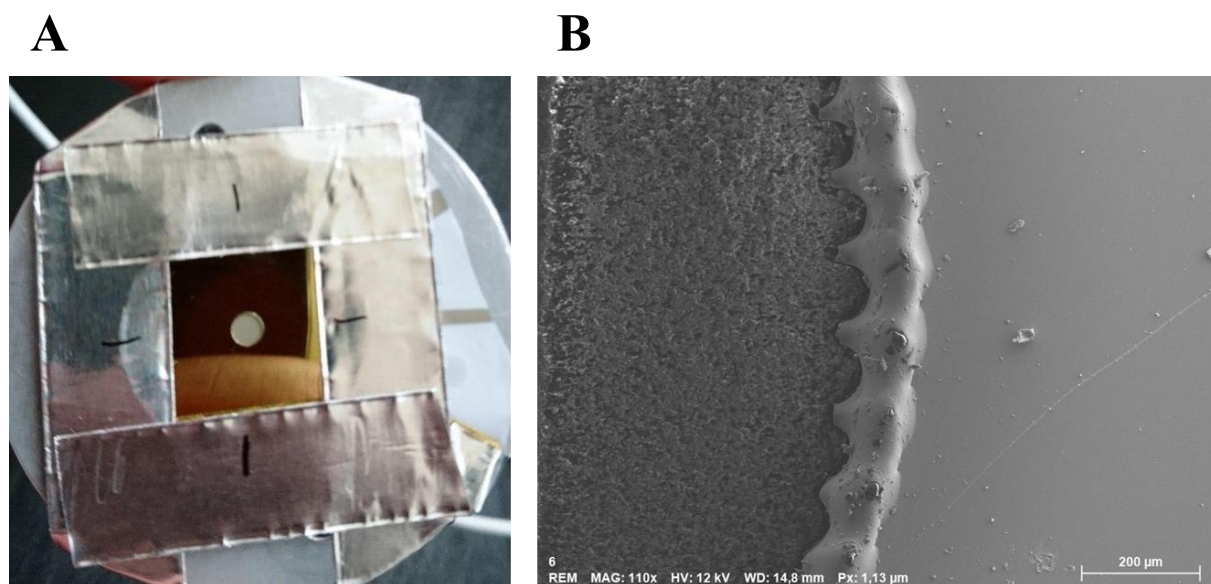
Fig. 38: (**A**) Picture of the reverse side of a permeable support being prepared for the SEM imaging process. The conductive tape was used to prevent charging effects by grounding the setup. (**B**) SEM picture of the rim lining the circular central opening in the gold-coated lamination foil. Scale bar is 200 µm and pictures were taken and provided by nanoAnalytics GmbH.

Fig. 38B is an overview SEM picture showing the rim of the hole in the lamination foil at a 110-fold magnification. The porous nature of the polycarbonate filter can be seen in the left-hand side of the image. The rugged rim of the hole in the lamination foil is due to the limited xy-resolution of the desktop laser-scriber as was described previously. During the cutting process, the material of the lamination foil is heated up and an embankment is formed which is shown in the center of the picture. The right-hand side of the picture depicts the smooth gold-coated surface of the lamination foil which was used as an additional CE.

86

High resolution SEM pictures with the corresponding EDX gold analysis have been performed on the back of the WE and are shown in **Fig. 39**. The left column depicts SEM pictures in different magnifications (4k-, 6k- and 13k-fold from first to third row) and the black spots correspond to the pores in the PC material. The right column shows the EDX analysis for gold in the same field of view. The red dots indicate the pores where gold was found.
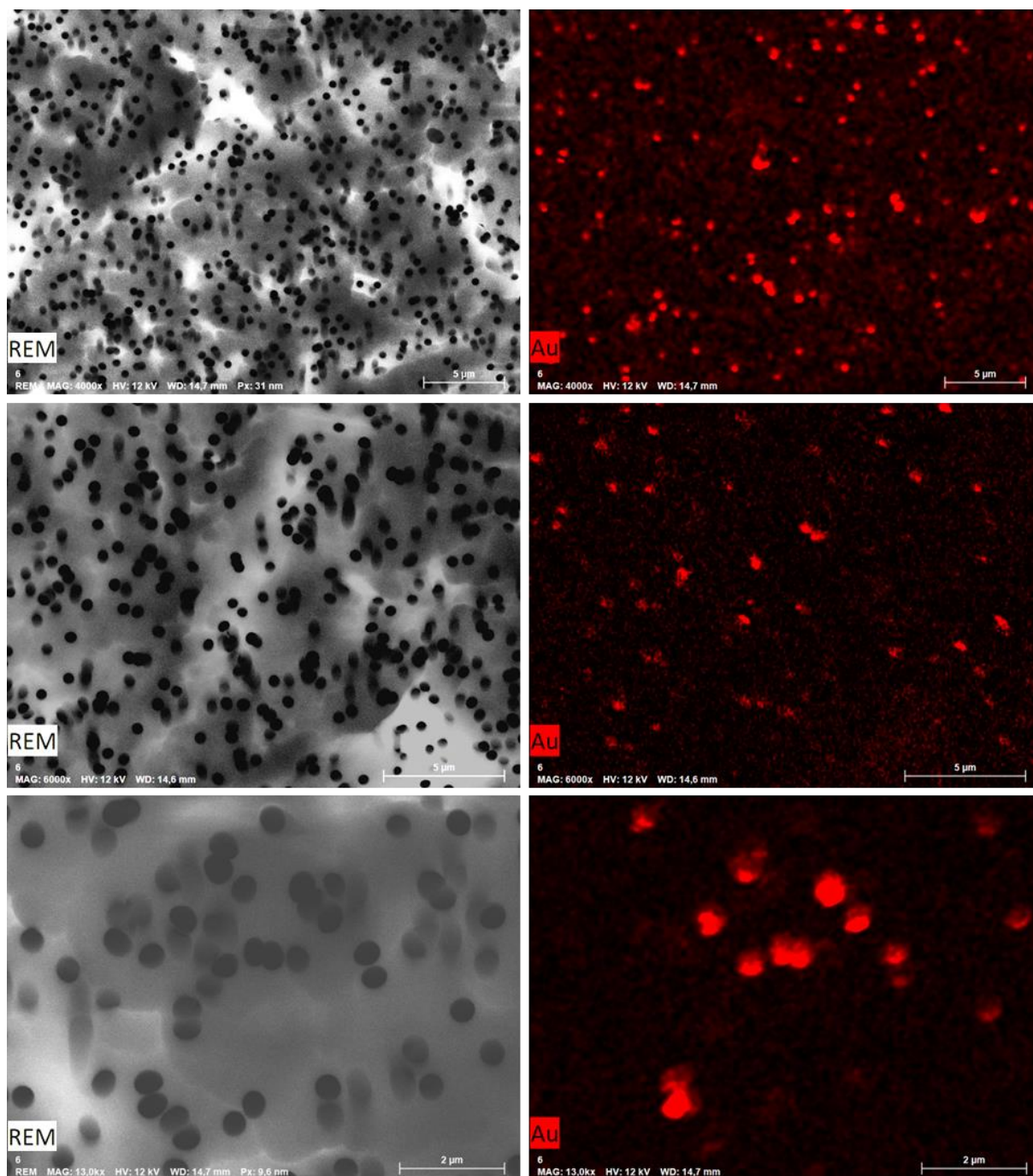
Fig. 39: Left-hand side: SEM pictures of the underside of the working electrode from the permeable support in different magnifications (4k-, 6k- and 13k-fold from top to bottom). The black dots indicate the pores in the filter (400 nm in diameter, one pore per μm^2). **Right-hand side**: Corresponding EDX pictures showing the amount of pores exhibiting the characteristic wavelength for gold (Au). Ratio of gold signals per total pore amount is 1:6. Scale bar is 5 μm for the first two rows and 2 μm for the last. Pictures were provided by nanoAnalytics GmbH.

The SEM picture with the largest magnification offered a 31.75 x 23.81 μm^2 field of view and 650 pores have been counted throughout this area. The exact number and position of the individual holes are shown in **Fig. 72** on page 173 in the supplementary information and yielded a pore density of 0.9 pores per μm^2 which was in good accordance with the declared 10^8 pores per cm^2 (1 pore per μm^2). With the EDX analysis, 110 gold spots had been counted in the same field of view resulting in a density of 0.15 gold spots per μm^2. On average, in every sixth pore, a gold signal was detected by the EDX analysis. The medium magnification showed 350 pores distributed across a field of view which was 21.17 x 15.88 μm^2 in size. This corresponded to a pore density of one pore per μm^2. The EDX analysis detected 50 gold spots in the same field of view which again corresponded to 0.15 gold spots per μm^2. Taking both densities into consideration, this amounted to a ratio of 1:7 for the detected gold spots with respect to the overall pore number. The highest magnification portrayed a field of view of 9.77 x 7.33 μm^2 in size and 65 pores had been counted throughout. The calculated pore density again was 0.9 pores per μm^2. In this field of view, 13 gold spots were counted, yielding a density of 0.18 gold spots per square micrometer and a ratio of gold spots to overall pores in the membrane of 1:5.

Comparing the three magnifications, the pore density was reproducible at the indicated number of one pore per μm^2 and the density of the gold spots found via the EDX analysis was equally reproducible around 0.16 gold spots per μm^2 for all magnifications. The only parameter fluctuating slightly was the number of gold spots with respect to the overall pore numbers in the same field of view. Taking all three results into consideration, an average ratio of 1:6 was found for the gold spots in proportion to the overall pore number.

V.2.2   Diffusion Studies

Apart from the optical characterization and the elemental EDX analysis, mass transport inside the measurement chamber was characterized optically by dye diffusion assays and electrochemically with the help of the diffusion of redox probes. In both cases, two permeable supports (compare chapter IV.1.2.3) were stacked inside the measurement chamber (compare chapter IV.1.2.4.3) and the three compartments filled with 5 mL of distilled water or PBS^{++} for the optical dye dilution assay and the redox probe-coupled assay, respectively.

V.2.2.1 Optical Dye Dilution Assay

A first impression of the mass transport inside the measurement chamber at room temperature was collected by an optical dye dilution assay. Therefore, two adjacent compartments of the three making up the measurement chamber were filled with distilled water (5 mL) and the last compartment was filled with a pink-colored solution of carbol fuchsin (5 mL, 0.2 % (w/v)). Pictures were taken in regular time intervals and exemplary ones are shown in **Fig. 40**.
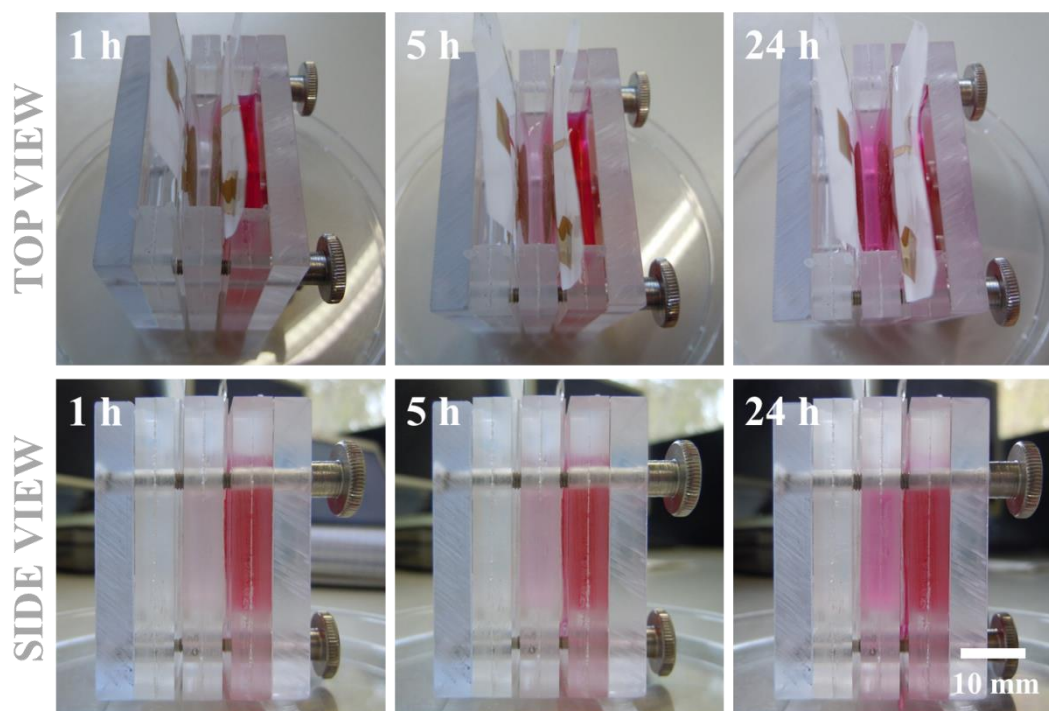
Fig. 40: Pictures of the measurement chamber holding two permeable supports after carbol fuchsin was added in the right compartment. In the upper row, the chamber is depicted in the top view and in the lower row, the chamber is shown from the side. The experiment was performed at room temperature and the scale bar is 10 mm.

Carbol fuchsin is a small water-soluble molecule with a molar mass of 351.9 g/mol which is similar to that of sucrose (342.30 g/mol). Over the course of 24 h, the intensely pink color in the right compartment continuously faded while it gradually became stronger in the middle compartment. The color in the left compartment in contrast did not change perceptibly. After one hour, a pink hue could be made out in the middle compartment, after 5 h the solution in the middle compartment became noticeably pink and after 24 h, the solution was pink-colored. The coloring in the right and the middle compartment was still not equal after 24 h. To estimate the required diffusion time from one permeable support through the 3-mm hole to the next, the *random walk model,* which was first mentioned in a short discussion in the journal *Nature* in 1905[71,72], was applied with sucrose serving as model analyte as the two molecules are almost equal in molar mass and the diffusion coefficient of sucrose is well

known. Equation (22) relates the one-directional mean squared displacement of a Brownian particle in its uncorrelated and unbiased form[73] with the diffusion coefficient and the elapsed time and (23) gives the closely related formula for the three-dimensional *random walk model*[74].

$$< x(t)^2 > = \int_{-\infty}^{\infty} x^2 \cdot dx \cdot P(x) = 2 \cdot D \cdot t \qquad (22)$$

$$< R(t)^2 > = 2 \cdot d \cdot D \cdot t \qquad (23)$$

The one-dimensional time-dependent displacement of the molecule is denoted $x(t)$ and the time-dependent three-dimensional mean square displacement is represented by $R(t)$; t is the time, D the diffusion coefficient, d the dimensionality of the system and $P(x)$ the probability distribution of the molecule. The diffusion coefficient for sucrose as solute in water at 25 °C is given as $5.2 \cdot 10^{-6}$ cm^2/s in literature[75]. With a distance of 7 mm separating the two permeable supports, equation (23) was solved for t and yielded 4.36 h for a sucrose molecule to diffuse all the way to the second permeable support. It must be taken into account however, that this is an estimate based on the isotropic model and thus, concentration gradients as well as the additional barrier in form of the gold-sputtered polycarbonate membrane have not been taken into account. In the experimental dye dilution assay, it took about 1.5 h to unequivocally discern the pink color in the middle compartment. The isotropic *random walk model* based on the Brownian motion merely yields the statistical amount of time needed for one molecule to travel a certain distance and the distance was chosen to be the full width of the middle chamber which was more than was needed to discern the pink coloring. In addition, in the optical dye dilution assay, the amount of carbol fuchsin was not quantitatively measured as sampling would have been required in regular time intervals. The taking of samples both in the donor compartment and the receiver compartment, and especially larger samples for a colorimetric readout, would inevitably alter the total volume and thus change the kinetics of the diffusion. Thus, in the next chapter, an experiment with a redox probe was performed where the presence of the probe could be detected electrochemically without the need of taking samples. With the ability to quantitatively determine the amount of a tracer molecule without repeated sampling, the relation between the diffusive flux and the initial concentration gradient can be investigated as is stated in Fick's first law[76] (compare eq. (24) on page 92).

V.2.2.2 Redox Probe Dilution Assay

For the redox probe dilution assay, a calibration curve was established first by adding 5 mL of an equimolar mixture of potassium ferrocyanide (368.35 g/mol) and potassium ferricyanide (329.24 g/mol) dissolved in PBS^{++} to all three compartments at 37 °C. Concentrations ranged from 0 mM to 1 mM in discrete 250 µM steps. With the redox species present in the bathing fluid, charge transfer occurs at the electrode-electrolyte interface at low frequencies[65] and thus, the associated magnitude of impedance was determined for the four electrode pairs on two permeable supports (F1 and F2) at 1 Hz and the reciprocal value – the admittance – plotted against the concentration (**Fig. 41A**). Thereafter, the ferro-/ferricyanide solution was added only to the F1-adjacent compartment in a concentration of 1 mM. The other two compartments were filled with PBS^{++} buffer to provide a suitable electrolyte solution for the electrochemical detection which was done at 1 Hz and at a 50-mV RMS voltage amplitude (0 V DC potential). **Fig. 41B** shows the time-dependent change of the magnitude of impedance and **Fig. 41C** the reciprocal magnitude of impedance plotted against the time. The initial slope $(0\,h \leq t \leq 10\,h)$ has been fitted linearly for the electrodes on F2.
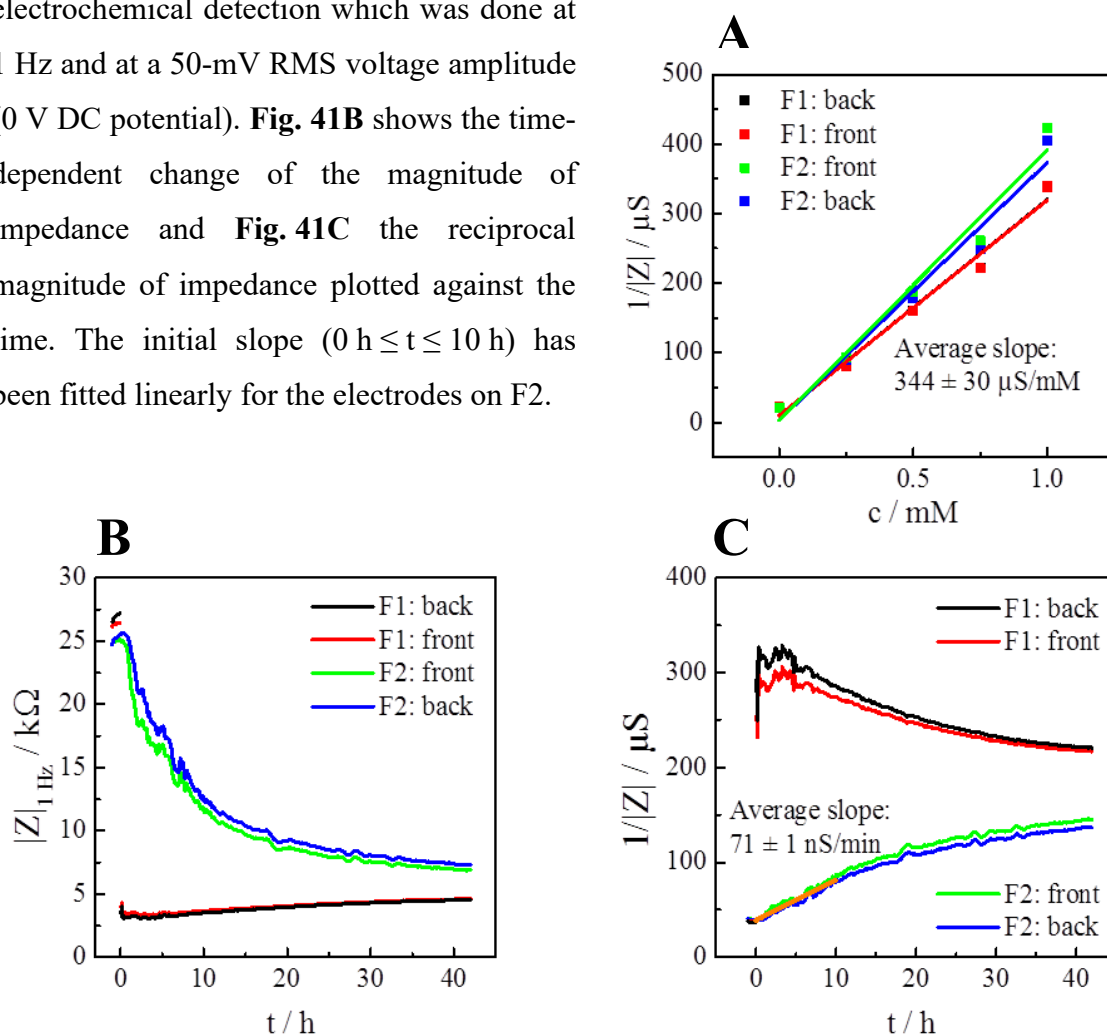
Fig. 41: (**A**) Calibration curve in a concentration range from $0 - 1$ mM in discrete 250 µM steps. All three compartments were filled with the same concentration of the equimolar ferrocyanide/ferricyanide solution. (**B**) Time-dependent magnitude of impedance at 1 Hz after 1 mM of the redox probe was applied only next to F1 at t = 0 h. (**C**) Reciprocal magnitude of impedance at 1 Hz plotted against the time. The initial increase detected for F2 was fitted linearly (orange line) between $0 - 10$ h and yielded a slope of (71 ± 1) nS/min. T = 37 °C.

Fig. 41A displays the dependency between the reciprocal magnitude of impedance and the available concentration and thus the amount of potassium ferrocyanide and potassium ferricyanide within the three 5-mL compartments. All four electrode combinations exhibited a linear relation with an average slope of (344 ± 30) µS/mM in the redox probe concentration range between 0 mM and 1 mM. The electrode combinations providing information from the back and front of the same permeable support (**black** & **red**, **green** & **blue**) exhibited a very similar time-dependent concentration profile which could be explained by the fact that the same working electrode was used to detect the redox probe. The only difference between the front and reverse side of the same permeable support in this cell-free experiment was the 10-µm thickness of the permeable polycarbonate filter membrane itself which was too thin to be distinguished by the two electrode combinations. The initial magnitude of impedance before the addition of the redox probe detected by the four electrode pairs was around 25 kΩ (**Fig. 41B**). Adding the redox probe in a concentration of 1 mM directly adjacent to F1 provoked an immediate drop to 4 kΩ in the case of both electrodes on F1 and a subsequent slow increase to 5 kΩ over the course of 40 h. The magnitude of impedance in the case of F2 initially continued to measure 25 kΩ before exponentially decreasing to around 7.5 kΩ after 40 h of measurement time (compare **Fig. 41B**). The change in the electrical admittance $(1/|Z|)$ over the same period of time is shown in **Fig. 41C** in order to correlate the electrochemically obtained signal with the amount of the redox probe via the calibration curve from **Fig. 41A**. The admittance at F1 initially was determined to be approximately 300 µS which then levelled off to 225 µS after 40 h. The post-addition value for the admittance at F2 was 35 µS which first increased steadily for the first 10 h and then the increase became slower until final values close to 150 µS were obtained after 40 h. A linear fitting of the initially steady increase during the first 10 h of measurement time for both sides of F2 yielded an average slope of (71 ± 1) nS/min. According to Fick's first law of diffusion (equation (24)), the diffusive flux *J* (representing the number of particles flowing through a unit area per unit time interval) is proportional to the concentration gradient $\frac{\partial c}{\partial x}$ with the diffusion coefficient *D* as the proportionality factor.

$$J = -D \cdot \frac{\partial c}{\partial x} \qquad (24)$$

This relation holds true as long as the concentration gradient and the diffusive flux remain constant which, in approximation, was true during the beginning of the measurement. From the experimental data, one could determine the initial diffusive flux *J* by dividing the slope from **Fig. 41C** by the slope of the calibration curve from **Fig. 41A** to correlate the change in

admittance to a change in concentration assuming that the concentration determined at F2 represents the concentration inside the entire volume between F1 and F2. Normalization with respect to the area of the 3-mm hole in the lamination foil yielded a diffusive flux of 242.57 pmol·cm^{-2}·s^{-1}. Together with an initial fixed concentration difference of 1 μmol·cm^{-3} and a literature value at 25 °C for the diffusion coefficient of the ferrocyanide/ferricyanide redox couple[77,78] of 8.96·10^{-6} cm^2·s^{-1}, the parameter $\partial \mathbf{x}$, for which the concentration gradient was still valid, was determined to be 369 μm behind the polycarbonate membrane. With the assumption of a linear temperature dependence of the diffusion coefficient between 25 °C and 37 °C, the diffusion coefficient for the ferrocyanide/ferricyanide redox couple at 37 °C was calculated by using the temperature dependence between 25 – 37 °C of the well-studied diffusion coefficients of dissolved oxygen in water[79,80], eventually yielding 1.2·10^{-5} cm^2·s^{-1} as diffusion coefficient for the redox probe couple at 37 °C. The higher diffusion coefficient slightly increased $\partial \mathbf{x}$ to 495 μm behind the polycarbonate filter membrane. At first glance, this distance seemed to be very short since the full diffusion length across the middle chamber measured 7 mm. However, due to the experimental determination of the slope in the beginning of the time-dependent admittance measurement, the initial concentration gradient of 1 mM was used for the calculation. This assumption only held true for a position in close proximity to the polycarbonate filter because otherwise dilution effects would have needed to be considered. Thus, the calculated length $\partial \mathbf{x}$ was limited to short diffusion distances using the experimental value for the flux, the diffusion coefficient for the redox couple at 37 °C and the initial concentration difference of 1 mM. Within this obtained distance of half a millimeter, the theoretical assumptions for the concentration gradient and the diffusion coefficient coincide with the experimentally determined flux.

The results from the redox probe dilution assay experiment shall in the following be verified using COMSOL Multiphysics® simulations which were performed by Linda Frank. Next to the validation of the experimentally determined values, the COMSOL Multiphysics® simulations offer the possibility of calculating time-dependent lateral concentration profiles instead of the time-dependent detection of the redox probes at only a fixed single electrode position. In the simulations, the lateral and time-dependent diffusion of the ferro-cyanide/ferricyanide redox couple was observed for the inner cross-sectional area of the measurement chamber (2.1 cm in depth, 3.4 cm in width) holding two permeable supports (F1 & F2) at the height of the center of the working electrode. The chamber cross section is schematically depicted in **Fig. 42**.
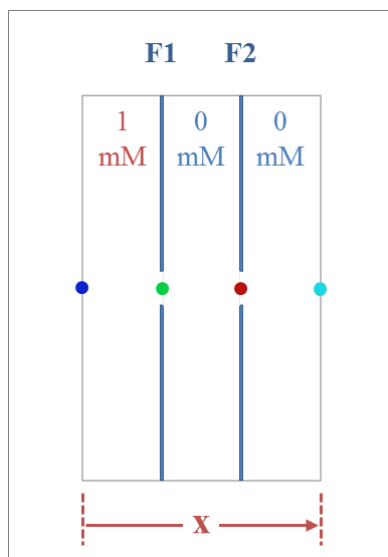
Fig. 42: Schematic depiction of the cross-sectional area of the measurement chamber holding two permeable supports (F1 & F2). The left compartment was filled with 1 mmol/L of $K_3[Fe(CN)_6]/K_4[Fe(CN)_6]$ at t = 0 h and the middle and right compartment were filled with PBS^{++}. The points of interest are color-coded.

The schematic depiction in **Fig. 42** shows that the diffusion is limited by the circular aperture in the lamination foil. Howard Berg in the book *Random Walks in Biology* describes the "diffusion through a circular aperture of radius s in a non-adsorbing barrier separating two semi-infinite media"[81].

$$I = 2Ds \cdot (C_2 - C_1) \tag{25}$$

In equation (25), **I** is the diffusion current, **D** the diffusion coefficient, **s** the radius of the circular aperture and C_1 and C_2 are the concentrations of the substance in question in the semi-infinite media. Semi-infinite is an approximation but as the two compartments exhibit a limited volume which is sufficiently larger compared to the dimensions of the circular aperture, the approximation is valid. In the beginning of the measurement at t = 0 h, $(C_2 - C_1)$ equaled 1 mM ($1 \cdot 10^{-6}$ mol·cm^{-3}), the radius (s) of the aperture is 0.15 cm, and the diffusion coefficient is $1.2 \cdot 10^{-5}$ cm^2·s^{-1}. These three values together result in a diffusion current of 3.6 pmol·s^{-1}, which, when compared to the experimentally measured diffusion current of 17.15 pmol·s^{-1}, is in the same range and only deviates by a factor of five.

In the COMSOL Multiphysics® simulations, four regions of interest were selected (colored dots in **Fig. 42**) for which the concentration of $K_3[Fe(CN)_6]/K_4[Fe(CN)_6]$ was calculated and plotted against the x-direction (**Fig. 43A**). In **Fig. 43B**, the total flux of the system was determined and plotted against the x-direction. **Fig. 43C** depicts the time-dependent change of the concentration and **Fig. 43D** shows an overlay with the experimental data from **Fig. 41C**.
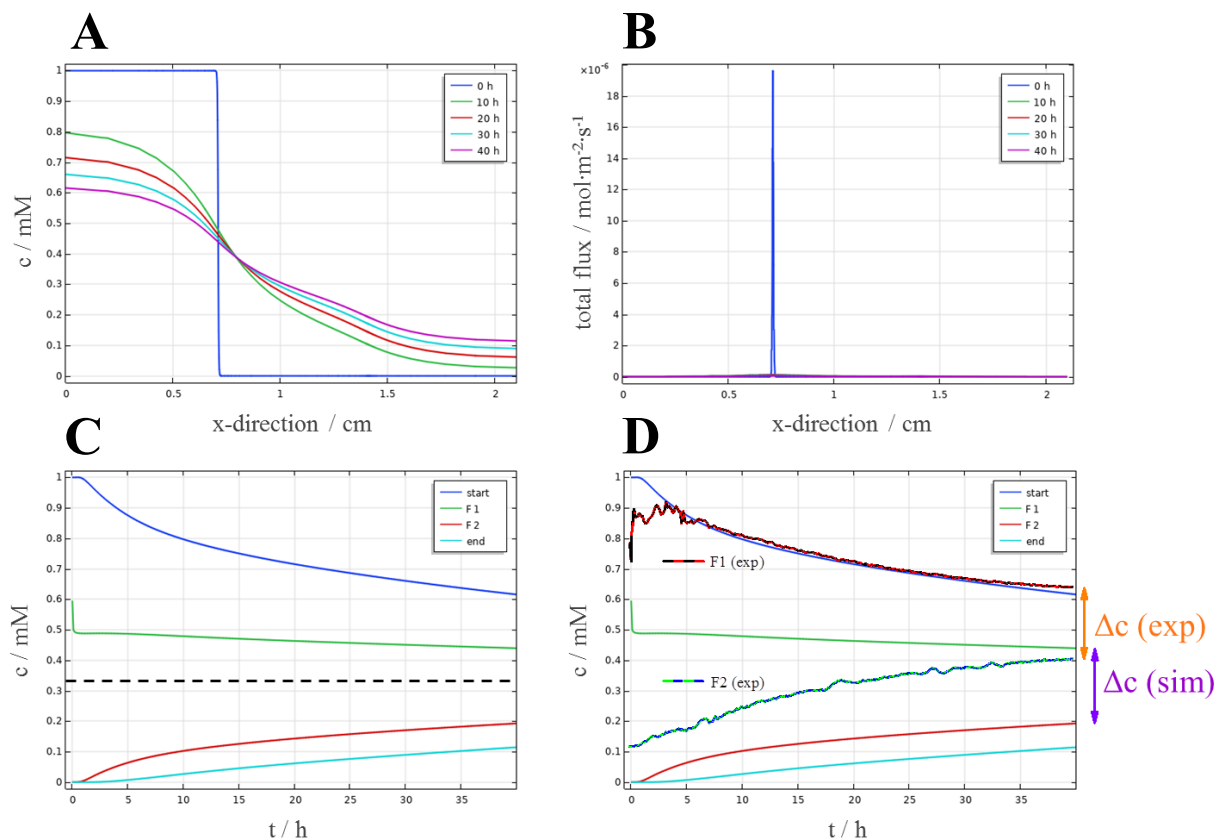
Fig. 43: COMSOL Multiphysics®-simulated diffusion processes at 37 °C after the addition of a 1 mM $K_3[Fe(CN)_6]/K_4[Fe(CN)_6]$ solution on the left-hand side of F1 ($x \leq 0.7$ cm). A diffusion coefficient of $1.2 \cdot 10^{-5}$ cm$^2 \cdot$s^{-1} was used for the calculations. (**A**) Space diagram at different preselected time points. (**B**) Total flux plotted against the x-direction (**C**) Time-dependent change of the concentration at four regions of interest (compare **Fig. 42**). The equilibration concentration is marked by the dashed black line. (**D**) Overlay of the simulated data from (**C**) with the experimental data from **Fig. 41C**. The differences in concentration after 40 h of measurement time are marked by the colored arrows.

The simulations confirmed much of the experimental data:

(i)   For the calculation of the diffusive flux from the experimental data, the initial concentration gradient of 1 mM was assumed to be constant which was only valid in the beginning of the measurement (**Fig. 43A**, 0 h). After the first 10 h of measurement time, the concentration gradient had already decreased to approximately 0.55 mM from the middle of the left compartment to the middle of the central compartment.

(ii)   The distance ∂x, in which the theoretical assumptions for the concentration gradient and the diffusion coefficient coincide with the experimentally determined flux, was calculated to be 495 μm which corresponded to a location in close proximity to the WE of F1. **Fig. 43B** depicts the simulated system's total flux, which was highest directly in the beginning at t = 0 h (322 pmol·cm^{-2}·s^{-1} vs an

experimentally determined value of 243 pmol·cm^{-2}·s^{-1}) and the contribution was greatest at the x-position of F1. From the simulated diagram, a value ∂x of 278 µm could be deduced which only deviated by a factor of 1.8 from the experimentally determined 495 µm.

(iii) The experimental concentration difference (Δc (exp)) between F1 and F2 amounted to 0.23 mM after 40 h of measurement time while the simulations yielded a difference (Δc (sim)) of 0.25 mM (compare the colored arrows in **Fig. 43D).** In both cases, no equilibrium was reached within 40 h but the concentrations at the end of the measurement were experimentally found to be higher than the simulations suggested.

Furthermore, the change of the ferrocyanide/ferricyanide concentration was visualized in color-coded heat maps in 10-h steps. The streamlined heat maps are depicted in **Fig. 44**. Dark red areas signify the original application concentration of c = 1 mM and the dark blue areas indicate the initial absence of ferrocyanide/ferricyanide and therefore a concentration of c = 0 mM. The first image (t = 0 h) described the state directly after the addition as the diffusion process started. The main flux happened at F1 where the left and middle compartments bordered on each other (compare **Fig. 43A**, F1 is positioned at x-direction = 0.7 cm and F2 at x-direction = 1.4 cm). The concentration of the ferrocyanide/ferricyanide solution after 10 h of measurement time had already fallen below 0.5 mM in the vicinity of F1, but a complete equilibration between all three compartments would still need a significant amount of time.
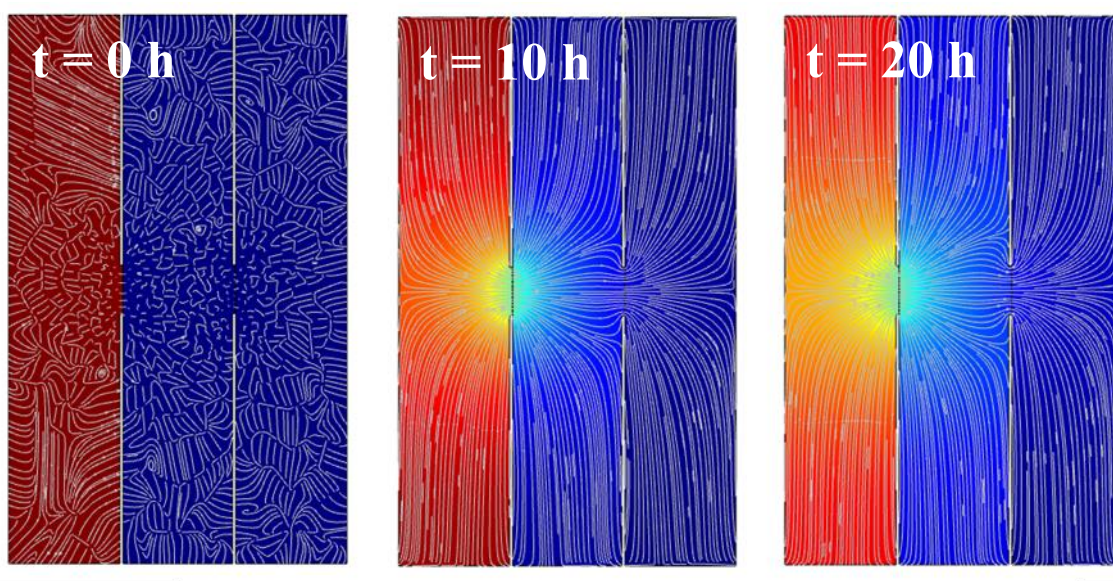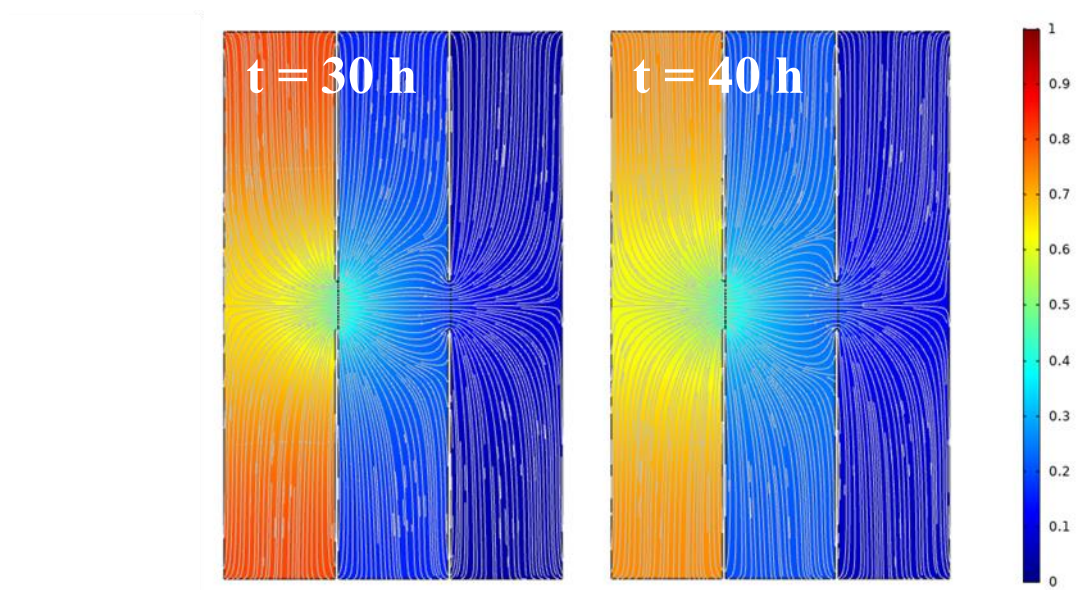
Fig. 44: Color-coded concentration profiles at different time points in the cross section of the measurement chamber. A solution of $K_3[Fe(CN)_6]/K_4[Fe(CN)_6]$ was added to the left compartment in a concentration of 1 mM at t = 0 h. The concentration changes were simulated for a physiological temperature of 37 °C with the COMSOL Multiphysics® *Chemical Engineering* module using a diffusion coefficient of $1.2 \cdot 10^{-5}$ $cm^2 \cdot s^{-1}$.

From the color-coded heat maps in **Fig. 44**, an averaged final bulk concentration after 40 h of equilibration time was determined in each of the three compartments. The simulated equilibration time was chosen to be similar to the experimental time span. Thus, an averaged concentration of 0.6 mM was found in the left compartment, a concentration of 0.3 mM on average was observed for the middle compartment and the right compartment exhibited a bulk concentration of around 0.1 mM. The simulations confirmed much of the experimental data and they also clearly showed that the concentration in the right compartment did not change much within the 40 h of measurement time. In order to achieve a complete balancing of the concentrations in all three compartments, longer measurement times or shorter diffusion ways would have been needed.

V.3   Impedance-Based Proof-of-Concept Measurements

In order to validate the novel measurement setup, frequency-resolved spectra of different cell lines were recorded and compared to data gained with either commercial or otherwise established setups. Furthermore, time-resolved response profiles were collected upon stimulation with various substances. In all cases, standard ECIS® experiments performed in parallel served as reference. For a better visualization, the cartoon in **Fig. 45** depicts the arrangement of the permeable supports within the measurement chamber and color-codes the ensuing position of the individual cell layers in the tissue model.
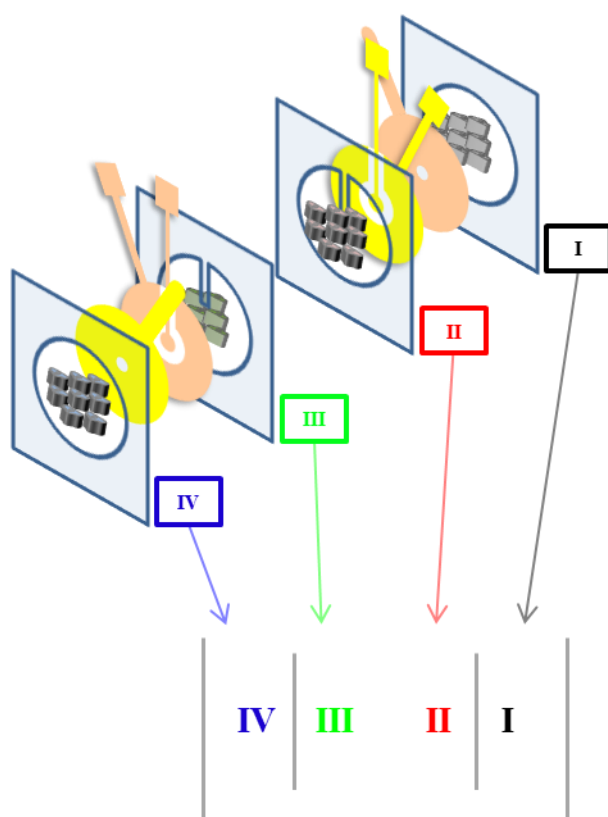
Fig. 45: Schematic drawing of two permeable supports stacked in the measurement chamber with the front sides facing each other. From right to left, the cell layers were assigned numbers I – IV (upper half). A minimalistic depiction of the measurement chamber with the supports and the color-coded numbers representing the cell layers is shown in the lower half.

To connect to the hardware, the front sides of the permeable supports had to face each other when stacked inside the measurement chamber. This means that cell layers **II** and **III** adhered directly on the entire area of the gold-coated side of the filter membrane (WE & CE), whereas cell layers **I** and **IV** grew on the reverse side of the PC membrane with the 3-mm hole in the gold-coated lamination foil exposing the underside of the WE. The difference in the active electrode areas was taken into account in the determination of the ECIS® parameters.

V.3.1 Frequency-Resolved Analysis of Different Cell Types

For the frequency-resolved proof-of-concept measurements, the three model cell lines varying in the tightness of cell-cell contacts were grown to confluence on the two permeable supports. The supports were stacked inside the measurement chamber and subsequently impedance spectra were collected and analyzed by quantifying the ECIS® parameters α, R_b and C_m. The three cell lines were chosen to be MDCK-I cells (an epithelial cell line forming tight barriers), MDCK-II cells (epithelial cells forming moderately tight cell barriers) and NRK cells (epithelial-like cell line exhibiting leaky barrier properties). The frequency range was chosen to span the entire region from 1 Hz to 1 MHz at a fixed AC voltage of 50 mV RMS.

V.3.1.1 Normal Rat Kidney Cells

The first cell type to be used as proof-of-concept was NRK. NRK cells are generally known to exhibit rather leaky cell barrier properties which consequently results in a smaller contribution to the overall impedimetric signal compared to cell lines with stronger barrier properties. NRK cells were cultivated on both sides of one permeable support in the cultivation chamber (compare IV.1.2.4.2) and afterwards transferred into the measurement chamber (see IV.1.2.4.3) in which the spectra were collected. Reference spectra were obtained by cultivating NRK cells on the bottom of the wells of the IDE sensor array (IV.1.2.2) without the filter inserts suspended in the wells. **Fig. 46** depicts *Bode plots* of the two confluent NRK cell layers growing on either side of the permeable support (**A**) and of a confluent NRK cell layer growing on top of the interdigitated sensor electrodes of the IDE sensor array (**B**).
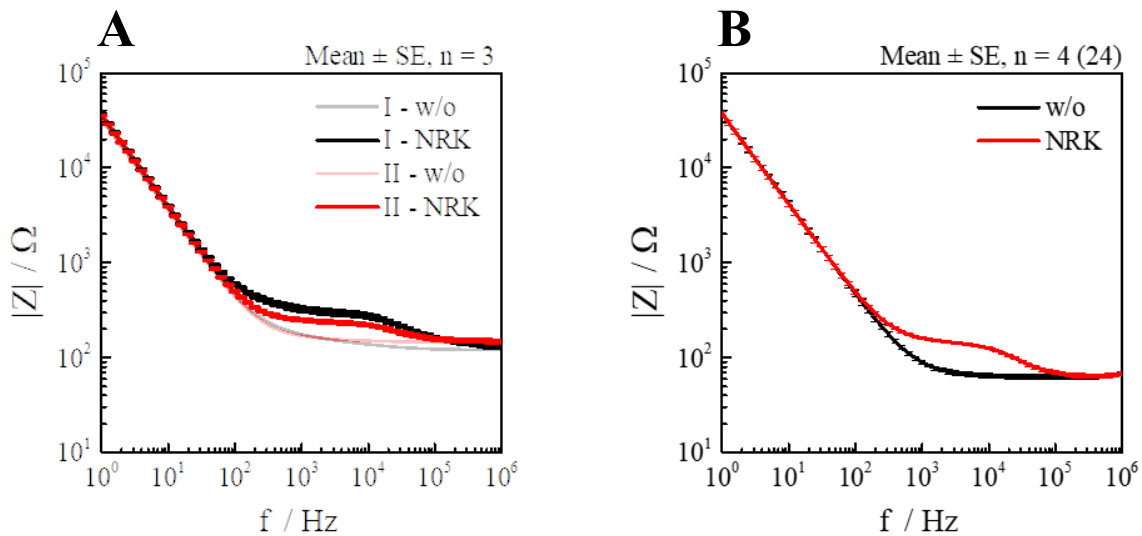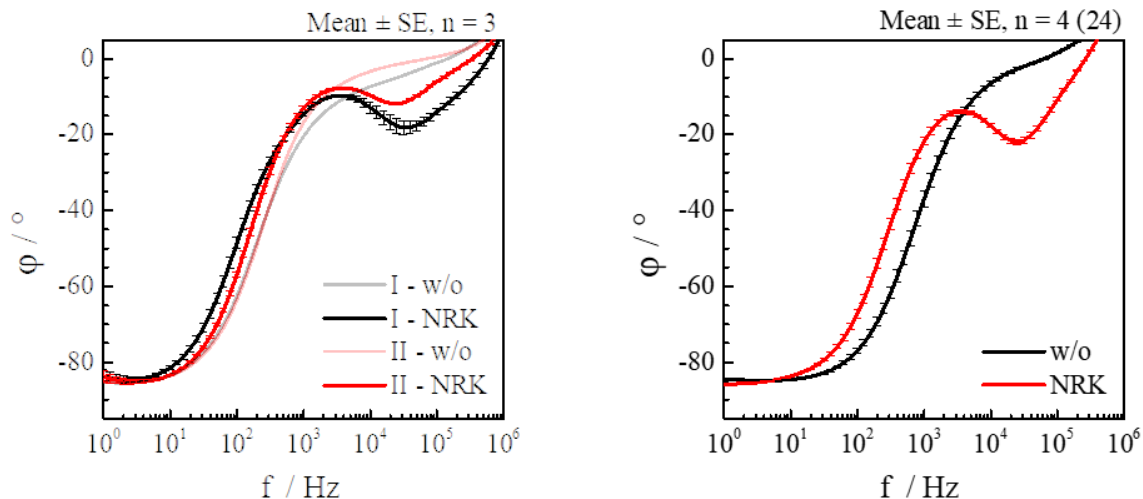
Fig. 46: (**A**) *Bode plot* of two confluent NRK cell layers growing on either side of one permeable support measured in the measurement chamber. (**B**) Reference *Bode plot* of NRK cells growing on the interdigitated sensor electrode layout pertaining to the IDE sensor array. Spectra were collected 48 h after cell inoculation at T = 37 °C and 5 % CO_2.

The magnitude of impedance in **Fig. 46** was very similar for (**A**) and (**B**). In the case of the spectra of the cell-free electrodes at low frequencies, the electrode-electrolyte interface caused impedance values of 35 kΩ at 1 Hz which, in the log-log presentation, were falling linearly until the contribution of the CPE element was surpassed by the contribution of the electrolyte. The value for R_{bulk} was between 130 Ω and 150 Ω for the two sides of the permeable support and approximately 70 Ω in the case of the IDE sensor array. With a confluent NRK cell layer growing directly on the electrodes, the cell influence was seen in the frequency range between 10^2 Hz and 10^5 Hz exhibiting a frequency-independent resistive part at the lower frequency end (~300 Ω for the two sides of the permeable support and 140 Ω in the case of the IDE sensor array) and a frequency-dependent, capacitive part with the inflection point at 40 kHz. The overall shape of this cell influence was also relatively similar in the two different setups. Notable, however, was the difference between the two electrodes on the front and reverse side of the permeable support. The cell-related plateaus at 4 kHz differed by 40 Ω which could be attributed to the difference in the active working electrode area as the cells growing on the front side covered the entire area of the 4-mm-diameter WE and the active electrode area for the cells growing on the reverse side was limited by the hole in the lamination foil (d = 3 mm). The difference in the electrode area was taken into account during the determination of the ECIS®-related parameters. The corresponding phase shift of the two measurement setups were also very similar, with a shift of –85° indicating mostly capacitive contributions at low frequencies and the lack of a phase shift at high frequencies indicating a solely resistive influence (**Fig. 46**). In both cases, the values of the phase shift turned positive at very high frequencies indicating a parasitic inductive contribution which probably stemmed

100

from the wiring and the measurement setup itself. At such high frequencies however, the cell influence was negligible which rendered these parasitic elements irrelevant for the determination of the ECIS® parameters. The spectra from **Fig. 46A** & **B** were fitted and the parameters extracted as described in chapter III.1.2 and the results are summarized in **Tab. 9**.

Tab. 9: ECIS® parameters R_b, α, C_m and R_{bulk} extracted from **Fig. 46A** & **B** via ECIS® model fitting for a confluent NRK cell layer growing on both sides of one permeable support and on the bottom of the IDE sensor array (mean ± SE, n ≥ 3).

	$R_b / \Omega \cdot cm^2$	$\alpha / \Omega^{0.5} \cdot cm$	$C_m / \mu F \cdot cm^{-2}$	R_{bulk} / Ω
I (NRK, Fig. 43A)	9 ± 1	7.8 ± 0.6	0.8 ± 0.1	133 ± 3
II (NRK, Fig 43A)	8.5 ± 0.7	5 ± 1	1.19 ± 0.04	150 ± 9
NRK (Fig.43B)	6.33 ± 0.04	4.08 ± 0.08	2.18 ± 0.01	65 ± 3
Literature value (NRK)[67]	9.3 ± 0.8	7.9 ± 0.3	1.20 ± 0.08	n.a.

The values for the resistance between the cells (R_b), the impedance from the cell-adhesion sites (α) and the membrane capacitance (C_m) for the two setups listed in **Tab. 9** compared well with the data presented in literature, with the only exception of a slightly higher C_m value which was found for **Fig. 46B**. The parameter values shall be discussed in chapter V.3.1.3.

V.3.1.2 *Madin-Darby Canine Kidney Cells*

The other two cell types complementing the selection for the proof-of-concept were two subtypes of the epithelial MDCK parent cell line. MDCK-I are forming extremely tight barriers with TER values exceeding 4000 $\Omega \cdot cm^2$, whereas MDCK-II cells are exhibiting TER values of > 300 $\Omega \cdot cm^2$ and are therefore classified as moderately dense[64]. In the resulting impedance and phase spectra of the cell-covered electrodes, clear differences should therefore be observable with respect to the height of the plateau reflecting the resistance between the cells as well as the corresponding frequency position of the maximum in the phase shift. The two different cell lines were cultivated one after the other on both sides of two permeable supports in cultivation chambers (see IV.1.2.4.2) and afterwards stacked in one measurement chamber (IV.1.2.4.3) according to **Fig. 45**. Reference spectra were obtained by cultivating MDCK-I and MDCK-II cells in commercially available 8W10E ECIS® arrays. **Fig. 47** depicts *Bode plots* of the four confluent MDCK cell layers growing on each side of the two permeable supports (**A**) and also of confluent monolayers of the two MDCK subtypes measured in the commercial 8W10E ECIS® arrays (Applied BioPhysics, Inc.) (**B**).

Every spectrum from each of the three independent measurements was fitted, the parameters extracted as described in chapter III.1.2 and the averaged results are summarized in **Tab. 10**.
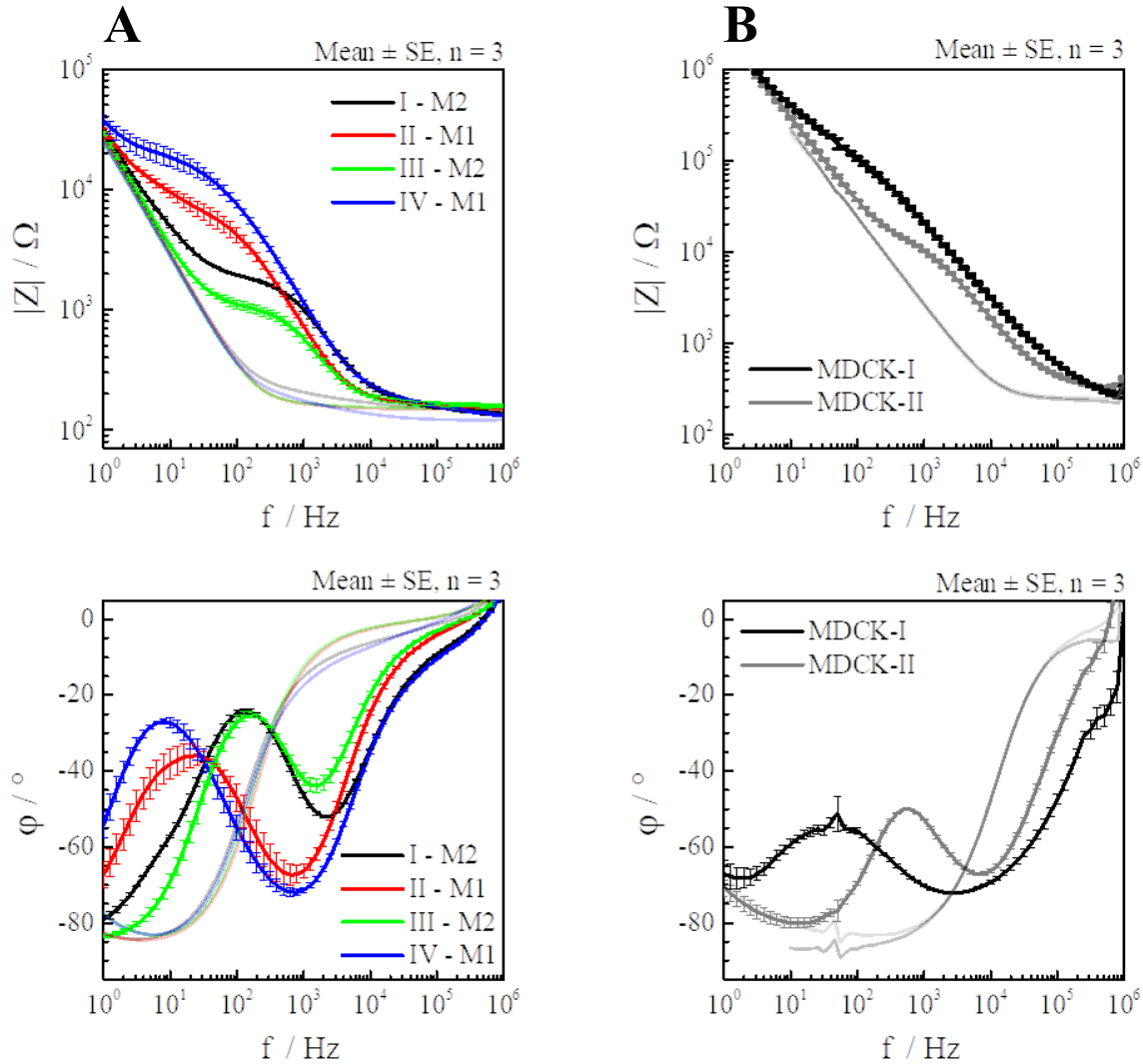
Fig. 47: (**A**) *Bode plots* of two permeable supports, each with an MDCK-I (M1) and an MDCK-II (M2) cell layer cultivated on the front and back of the same support. The two permeable supports were stacked in the measurement chamber. (**B**) Reference *Bode plots* of the two MDCK subtypes measured in commercial 8W10E ECIS® arrays. Spectra of the corresponding cell-free electrodes are included in a transparent form of the same color. Data was recorded 48 h after cell inoculation for M1 and 24 h after cell seeding for M2 at T = 37 °C and 5 % CO_2.

The electrode-electrolyte interface of the two permeable supports was almost identical in its A_{CPE} ($1\cdot10^{-4}$ µF·s$^{(n-1)}$·cm^{-2} and $4.9\cdot10^{-5}$ µF·s$^{(n-1)}$·cm^{-2} for back and front, respectively) and n_{CPE} values (0.86 and 0.96 for back and front, respectively) and thereby the CPE contribution of the first permeable support (**Fig. 47A**, transparent **black** & **red**) coincided with the one from the second permeable support (transparent **green** & **blue**). Thus, |Z| measured 25 kΩ for both cell-free permeable supports at the lowest frequency of 1 Hz. The CPE contribution decreased linearly up to 100 Hz before it merged into the horizontal contribution of R_{bulk} ending in 130 Ω for the reverse side of the supports (transparent **black** & **blue**) and 150 Ω for the front

102

side (transparent **red** & **green**). The cell-related influence was observed at frequencies below 10 kHz with the resistive part entailing a plateau value of 1.8 kΩ (160 Hz), 7.5 kΩ (20 Hz), 1.0 kΩ (160 Hz) and 18.4 kΩ (10 Hz) for cell layers **I** through **IV** with the corresponding local maximum in the phase shift (**Fig. 47A**). The cell membrane-related capacitive influence in the impedance spectrum overlapped in all cases for the two cell layers being measured by the same electrode combinations (**black**/**blue** and **red**/**green**).

The cell-free impedance spectra of the commercial 8W10E arrays revealed approximately the same bulk resistance of 200 Ω (**Fig. 47B,** transparent **grey** and **black**). Owing to the significantly smaller combined area of the working electrodes (0.49 mm^2), the slanted line of the CPE was shifted parallel to higher frequencies yielding 2.4 MΩ at 1 Hz. This in turn signified that the cell influence was also to be observed at higher frequencies (10^1 Hz – 10^5 Hz). The local maxima in the phase shift at 50 Hz and 500 Hz for MDCK-I and MDCK-II, respectively, indicated the strongest resistive influence of the cell-cell contacts, forming the plateau at values of 153 kΩ and 14 kΩ for MDCK-I and MDCK-II, respectively.

Tab. 10 summarizes the ECIS® parameters which were extracted from the spectra in **Fig. 47A** and also gives the literature values for MDCK-I and MDCK-II cells.

Tab. 10: Fitted ECIS® parameters R_b, α, C_m and R_{bulk} for confluent MDCK-I and MDCK-II cell layers growing on opposing sides of two permeable supports stacked in a measurement chamber (mean ± SE, n ≥ 3).

	R_b / Ω·cm^2	α / Ω$^{0.5}$·cm	C_m / µF·cm^{-2}	R_{bulk} / Ω
I (MDCK-II)	47 ± 3	15 ± 1	3.31 ± 0.04	156 ± 2
II (MDCK-I)	776 ± 101	80 ± 5	3.4 ± 0.1	154 ± 9
III (MDCK-II)	69 ± 6	13.5 ± 0.3	3.4 ± 0.2	163 ± 11
IV (MDCK-I)	573 ± 59	57 ± 7	4.9 ± 0.5	159 ± 10
Literature value (MDCK-II)[67]	88 ± 4	16 ± 0.6	3.03 ± 0.03	n.a.
Literature value (MDCK-I)[67]	2870 ± 240	117 ± 3	1.91 ±0.07	n.a.

The values for the same cell type generally were in good accordance; however it was notable that the R_b values seemed to be lower when measured on the reverse side of the permeable support. Compared to the literature value, R_b values extracted from the spectra of the MDCK-I cell layers were 76 % lower than the given value of 2870 Ω·cm^2 which shall be discussed in detail in the next chapter. The focus shall also be placed on the interpretation of the C_m value, which in parts also deviated from the ones stated in literature.

V.3.1.3 Comparison & Discussion

The spectra in **Fig. 47A** revealed two unexpected characteristics: the first one is seen in the phase spectra of the permeable supports at low frequencies. The phase shift of the two permeable supports at 1 Hz differed by almost ten degrees. Other measurements have shown that the parameter n_{CPE} also sometimes slightly varied which caused a different slope of the slanted CPE-line in the impedance spectra. This was probably due to the manual assembly of the permeable supports and could certainly be improved by an automated production process. The second eye-catching aspect was the additional RC element appearing between 10^3 Hz and 10^5 Hz in the impedance and phase spectra of the cell-free reverse side of the permeable supports (transparent **black** & **blue**, difference of 30 Ω). Beyond this frequency range, the spectra stemming from both sides of the supports perfectly matched each other. This effect was even more pronounced if the two counter electrodes (gold-coated filter membrane on the front side and gold-coated lamination foil glued to the back) were measured against each other (compare **Fig. 71** in the supplementary information, colors **pink** & **green**). Here, the difference between R_{bulk} and the other frequency-independent stretch in the mid-frequency region was approximately 80 Ω which indicated that an RC element had been formed. In order to answer the question whether the capacitance resulting from the plate capacitor setup or the combined resistances of the electrolyte resistance and the constriction resistance in the cylindrically-shaped aperture of the lamination foil were responsible for the additional RC element observed in the impedance magnitude spectra, the contributions of these parameters are calculated in the following:

The two counter electrodes on the filter membrane and on the lamination foil could potentially serve as conducting plates which were separated by a non-conductive layer (dielectric) as the 190-μm-thick lamination foil was only coated with gold on the underside and the rest of the polymer material formed a dielectric which means that a plate capacitor had effectively been formed. The capacitance of this plate capacitor (considering the areas of the CEs on both sides) is estimated by equation (26):

$$C_{plate\ capacitor} \ = \ \varepsilon_0 \cdot \varepsilon_r \cdot \frac{A}{d} \qquad\qquad (26)$$

C$_{plate\ capacitor}$ is the capacitance of the plate capacitor, **ε$_0$** is the electric constant, **ε$_r$** the relative permittivity, **A** is the overlap area between the two plates and **d** is the distance between the plates. With $\varepsilon_0 = 8.854 \cdot 10^{-14}$ F·cm^{-1}, $\varepsilon_r = 2$, A = 3.01 cm^2 and d = 0.02 cm, a capacitance of 26.7 pF is obtained. This very small capacitance is an indication for the fact that rather the

combination of the electrolyte resistance and the constriction resistance in the cylindrically-shaped aperture of the lamination foil were responsible for the additional RC element in the spectra of the reverse side of the permeable supports. According to equation (12), the resistance generally increases with the distance and decreases with a larger cross section. Based on this correlation, the value of the electrolyte resistance is calculated in equation (27) for the cylindrically-shaped aperture of the lamination foil which exhibits a diameter of 3 mm and a height of 200 μm (thickness of the lamination foil and the filter membrane) ($R_{electrolyte}$ for serum-containing cell culture medium in the bulk phase is 50 Ω·cm).

$$R_{electrolyte\ in\ aperture} = \frac{50\ \Omega cm \cdot 0.02\ cm}{0.0707\ cm^2} = 14.1\ \Omega \qquad (27)$$

In addition to the resistance of the electrolyte in the aperture, the constriction resistance $R_{constriction}$ needs to be taken into account. The constriction resistance is inversely proportional to the radius of the active electrode (~k/r) with k being a constant. For a commercially available 8W1E ECIS® array with an electrode radius of 125 μm, $R_{constriction,\ 8W1E}$ is known to be approximately 1000 Ω. With the known values for the constriction resistance and the radius of the electrode for an 8W1E array, the value of the constant k is determined to be 12.5 Ω·cm. The constriction resistance for the permeable support due to the aperture in the lamination foil is calculated in equation (28).

$$R_{constriction\ in\ aperture} = \frac{12.5\ \Omega \cdot cm}{0.15\ cm} = 83.3\ \Omega \qquad (28)$$

As the constriction resistance takes effect on the either side of the cylindrically-shaped aperture, the total resistance consists of $R_{electrolyte\ in\ aperture}$ and two times the $R_{constriction\ in\ aperture}$ and therefore yields 180 Ω. The experimental measurement in **Fig. 71** on page 172 yielded a difference of only 80 Ω which means that the calculated value above overestimates the actual effect, but it also shows that the additional RC element in the impedance magnitude spectrum is indeed caused by the combination of the restriction resistance and the electrolyte resistance in the aperture of the lamination foil because the experimentally determined value of 80 Ω and the estimated value of 180 Ω only deviate by a factor of 2.25.

Given enough permeable supports and time, one could measure a sufficiently large number and subtract the averaged results for the RC element from every measured spectrum. As this would have been a cost- and time-consuming process however, this technique was not applied in this work.

The cell line-specific and averaged parameter α, which yields information on the impedance from the cell adhesion sites, was determined to be in close agreement with the values from literature for NRK and MDCK-II (M2) cells and somewhat lower for MDCK-I (M1) cells. Values of (7 ± 2) $\Omega^{0.5}$·cm, (14 ± 1) $\Omega^{0.5}$·cm and (69 ± 14) $\Omega^{0.5}$·cm and were found for NRK, M2 and M1 cell layers, respectively, compared to (7.9 ± 0.3) $\Omega^{0.5}$·cm, (16 ± 0.6) $\Omega^{0.5}$·cm and (117 ± 3) $\Omega^{0.5}$·cm stated in literature[67]. One has to keep in mind however, that the literature values were determined on impermeable gold electrodes and especially in the case of highly barrier-forming M1 cells, the sensitivity of the ECIS® model decreases. Lo et al. (1999) calculated that larger pore sizes and increasing pore density in a permeable substrate decreases the additional resistance from the cell-substrate area[82] which could be due to more electrolyte underneath the cells.

The impedance spectra of the three cell lines mostly differed in the height of the plateau, representing the resistance between the cells. The R_b values were determined as (9 ± 1) Ω·cm^2 (NRK), (101 ± 28) Ω·cm^2 (M2) and (653 ± 124) Ω·cm^2 (M1) compared to literature values of (9.3 ± 0.8) Ω·cm^2 (NRK), (88 ± 4) Ω·cm^2 (M2) and (2870 ± 240) Ω·cm^2 (M1)[67]. NRK cells generally lack occludins and claudins, both tight junction proteins[83], which are ubiquitous in both strains of MDCK cells and explain the leaky barrier properties resulting in lower R_b values. M1 and M2 not only differ in their morphological appearance as M1 cells normally appear to be small and flat whereas M2 cells exhibit a larger and taller morphology, but there are also differences in the composition of their junctional proteins to be observed. In addition to claudin-1, claudin-4, occludin and ZO-1 which are present in both strains, M2 cells also express the tight junction protein claudin-2 which is pore-forming and facilitates the diffusion of cations across the intercellular pathway[64,66]. Furthermore, in contrast to M2 cells, a higher amount of the transmembrane protein E-cadherin is found in M1 cells which promotes cell-cell adhesion in animals and furthermore gap junctions are established in M1 cells, which normally is not the case in the other strain[84]. These differences in the tight junction compositions imply varying R_b values which could be seen in the spectra in **Fig. 47A**. In addition, the different cell types could unequivocally be distinguished according to the impedance and phase spectra. Especially in the case of the M1 cells, the determined R_b values did not reach literature values, but only 24 % thereof. Once again it must be taken into account that the reference R_b value was determined for cells growing on commercial impermeable substrates with no co-cultured M2 cell line on the other side of the filter. Comparable measurements can be found in the dissertation of Kathrin Hajek (PhD thesis Kathrin Hayek, 2016) where it was shown that the TER values of mono-cultured M1 in Transwell® filters were significantly

higher $(2975 \pm 129)\ \Omega \cdot cm^2$ than if M2 cells had been co-cultured on the underside of the filter insert $(2091 \pm 319)\ \Omega \cdot cm^2$. The reason behind this phenomenon still is part of an ongoing speculation: whether the enhanced expression of claudin-2 in the presence of M2 cells causes the lower TER values or the two cell layers compete for the necessary Ca^{2+} ions to establish the barrier function or if entirely other factors are responsible for the deviation in the TER values is still unknown and would make an interesting research topic.

The last parameter, the membrane capacitance C_m, was determined to be $(1.0 \pm 0.2)\ \mu F \cdot cm^{-2}$ for NRK cells, $(3.4 \pm 0.2)\ \mu F \cdot cm^{-2}$ for M2 cells and $(4.2 \pm 0.9)\ \mu F \cdot cm^{-2}$ in the case of M1 cells on the permeable supports compared to literature values $(1.20 \pm 0.08)\ \mu F \cdot cm^{-2}$ (NRK), $(3.03 \pm 0.03)\ \mu F \cdot cm^{-2}$ (M2) and $(1.91 \pm 0.07)\ \mu F \cdot cm^{-2}$ (M1). The only deviation from the literature value significantly exceeding the error margin was the one for the M1 cells. Due to the differences in the active electrode size ($12.53\ mm^2$ for the front side and $7.07\ mm^2$ for the reverse side), a direct visual comparison of the spectra was difficult but these differences were taken into account in the determination of the C_m value in **Tab. 10**. A larger C_m value for M1 cells than for M2 cells was also recently published by Urban et al. (2020) where the three barrier-forming cell lines NRK, M1 and M2 were cultured in Transwell® filter inserts and the TER value as well as the capacitance of the entire cell layer C_{cl} were impedimetrically determined via the *cellZscope* (nanoAnalytics, Münster, DE) in an integral approach using a bottom and a dipping electrode made of stainless steel. In the publication, higher C_{cl} values of $(1.91 \pm 0.06)\ \mu F \cdot cm^{-2}$ and only $(1.37 \pm 0.09)\ \mu F \cdot cm^{-2}$ were found for M1 and M2 cells, respectively[65]. A single flat cell membrane without microvilli or other convolutions is widely accepted to yield a membrane capacitance of $1\ \mu F \cdot cm^{-2}$ [85]. As the capacitance of the entire cell layer including the apical and the basolateral plasma membrane is calculated in a reciprocal way according to equation (11), a value of $0.5\ \mu F \cdot cm^{-2}$ is obtained for the capacitance of the entire cell layer C_{cl}. Higher values indicate a larger plasma membrane surface area and thereby the formation of e.g. microvilli. Considering that M1 cells exhibited the highest C_m value of $(4.2 \pm 0.9)\ \mu F \cdot cm^{-2}$ in this work and equally the highest C_{cl} value of $(1.91 \pm 0.06)\ \mu F \cdot cm^{-2}$ when cultivated on permeable Transwell® filter inserts in the publication by Urban et al., the two results were in favorable agreement with each other. The literature values given in **Tab. 10** were obtained by growing cells on planar but impermeable gold electrodes and can therefore not be compared unreservedly. Cell differentiation might well be different when cultured on permeable or impermeable substrates[86] and furthermore, the co-culture of different cell types is another factor to consider when the cell-related parameters are directly compared.

V.3.2   Time-Resolved Cell Response Profiles

In order to validate the functionality, sensitivity and long-term stability of the permeable supports, multiple time-resolved proof-of concept measurements have been performed with the final permeable supports. The different approaches included adhesion measurements of the two MDCK strains, experiments with reduced conductivity in the presence of confluent cell monolayers as well as the addition of two distinct model substances. The model substances were chosen to be (i) *cytochalasin D* which specifically and reversibly impairs the dynamics of the actin cytoskeleton of the cells and (ii) *tert-Butyl hydroperoxide* which acts as an irreversible oxidizing agent. All of the experiments in this chapter have been performed with MDCK-I and MDCK-II cells to investigate the influence of cell-cell contact tightness and were also simultaneously conducted in commercial 8W10E ECIS® arrays for comparison. For all of the following measurements, both the time-dependent impedance and capacitance signals are shown. As explained in chapter III.1.2 the impedance data at lower frequencies provides information on the electrical tightness of the cell-cell contacts and thus on the barrier properties of the cell layer and from the corresponding capacitance at higher frequencies, the degree of cell-coverage of the electrode surface can be deduced. Thus, a high impedance in combination with a low capacitance is observed for confluent cell monolayers; low imped-ance and equally low capacitance values are observed when cells have adhered to the surface of the electrode but not established cell-cell contacts and a low impedance at simultaneously high capacitance values indicate an empty electrode without the presence of living cells.

V.3.2.1   Adhesion Studies with Madin-Darby Canine Kidney Cells

V.3.2.1.1 Adhesion on Impermeable ECIS® Electrodes

For a comparison of the MDCK adhesion profiles on permeable and impermeable substrates, the adhesion of MDCK-I and MDCK-II cells in two 8W10E ECIS® arrays was impedimetrically observed for 50 h (cell inoculation at $t = 0$ h). **Fig. 48A** shows the time-dependent absolute magnitude of impedance at a frequency of 4 kHz which is equally representative for cell spreading and the subsequent barrier formation. In **Fig. 48B**, the time-dependent absolute capacitance at the most sensitive frequency of 10 kHz is shown. The adhesion signal of MDCK-I cells is color-coded **black** and the signal obtained for MDCK-II cells is color-coded **grey**.

Fig. 48: Time courses of impedance magnitude at 4 kHz (**A**) and capacitance at 10 kHz (**B**) for MDCK-I and MDCK-II cells seeded on commercial 8W10E ECIS® arrays. Seeding density was $5 \cdot 10^5$ cells/cm² in culture medium and the measurement conducted in a standard cell incubator at 37 °C and 5 % CO_2. For clarity reasons, only 50 error bars are shown.

Preceding cell inoculation, the cell-free magnitude of impedance at 4 kHz was constantly displaying a value between 800 – 850 Ω from –5 h to 0 h in **Fig. 48A**. After the cell seeding, the magnitude of impedance steeply increased to 5 kΩ within 5 h in the case of MDCK-I cells and to 5.4 kΩ within 9 h of measurement time for MDCK-II cells. The 3.5-h time delay between MDCK-I and MDCK-II started to form early after cell inoculation where the initial steep increase in impedance slowed down after 1 h in the case of the MDCK-II cells only to pick up speed again after approximately 4 h. After having reached a local maximum, the magnitude of impedance receded by 14 % in both cases. Following a period of a constant impedance values, the impedance reflecting the MDCK-I cells started to increase again after 20 h to reach final values of 6.4 kΩ whereas the impedance corresponding to MDCK-II cells was constant for almost 20 h before declining another 10 % to reach final values around 4.3 kΩ.

The corresponding capacitance of the cell-free electrode in **Fig. 48B** measured 52 nF before rapidly dropping to 7.2 nF after 4.7 h (MDCK-I) and 9.1 h (MDCK-II). The initial drop to 35 nF was identical for both cell types before the declining rate became slower for the MDCK-II cells. Final capacitance values (9 nF) were reached soon after the initial capacitance decrease for MDCK-II cells whereas the MDCK-I capacitance time course displayed 9 nF for about 12 h following the initial descent before decreasing further to a final value of 6.9 nF.

V.3.2.1.2 Adhesion on Permeable Filter Supports

Similar to the chapter before, the adhesion of MDCK-I and MDCK-II cells was observed; this time grown on the permeable supports. As cell adhesion and the establishment of a confluent cell monolayer can only occur in the horizontal orientation, the process was performed and monitored in two cultivation chambers simultaneously (see IV.1.2.4.2) for 50 h. MDCK-I cells were the first to be seeded on the front side of the first permeable support (**red**) and the reverse side of the second permeable support (**blue**) at $t = 0$ h as this cell type needs more time to fully develop the barrier functionality[66]. 24 h into the measurement, MDCK-II cells were seeded on the so far cell-free sides (**black** and **green**) of the permeable supports according to the protocol given in IV.2.5. **Fig. 49** shows the time-dependent absolute magnitude of impedance at 200 Hz (**A**) and the time-dependent absolute capacitance at 10 kHz (**B**).
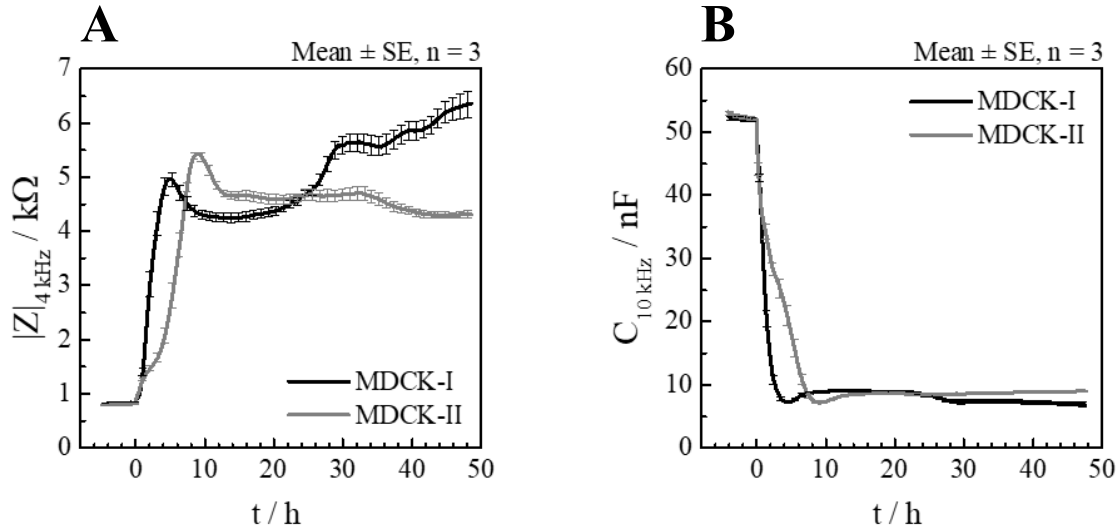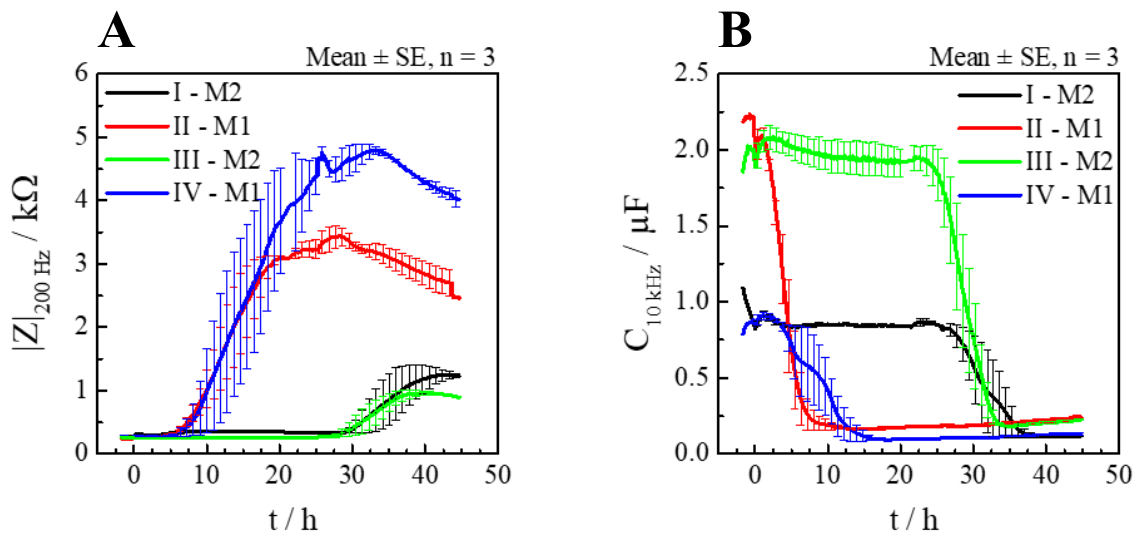

Fig. 49: Time courses of impedance magnitude at 200 Hz (**A**) and capacitance at 10 kHz (**B**) for MDCK-I and MDCK-II cells seeded on two permeable supports. MDCK-I cells were seeded on the front side of F1 (**II**) and the reverse side of F2 (**IV**) at $t = 0$ h and after 24 h, the supports were turned upside down and MDCK-II cells seeded on the other side (**I** on F1 & **III** on F2). Seeding density was $5 \cdot 10^5$ cells/cm^2 in culture medium and the measurement conducted in a standard cell incubator at 37 °C and 5 % CO_2. For clarity reasons, only 50 error bars are shown per time course.

The magnitude of impedance for the cell-free electrodes was stable at 280 Ω during baseline recording for all four electrode combinations. After MDCK-I cell inoculation at $t = 0$ h, the impedance of **II** and **IV** continued to measure 300 Ω for 5 h before first increasing steeply to 3.0 kΩ in the case of **II** and 4.0 kΩ in the case of **IV** before slowly rising further to 3.4 kΩ at 28 h (**II**) and 4.8 kΩ at 33 h (**IV**). After having reached these maximum values, the impedance leveled off to final values of 2.5 kΩ and 4.0 kΩ for **II** and **IV**, respectively. The impedance

for **I** and **III** remained at initial values around 300 Ω during the MDCK-I cell adhesion on the other side of the permeable support which provides proof of the independent signals from each side of the support. When the MDCK-II cells were seeded at t = 24 h, five more hours passed before the impedance started to increase to 1.0 kΩ in the case of **III** and 1.2 kΩ in the case of **I**.

The corresponding capacitance values in contrast already revealed different starting values. While the capacitance of the front side of the permeable supports measured between 1.9 µF (**III**) and 2.2 µF (**II**), the capacitance for the reverse side of the permeable supports yielded lower values of around 0.9 µF (**I** & **IV**). After MDCK-I cell seeding, the respective signals dropped to one tenth of the initial values over the course of 10 h (**II**) and 15 h (**IV**) with the latter exhibiting a two-step adhesion process as the decrease of capacitance appeared to slow down from 5 h to 10 h. Like the impedance, the capacitance of **I** and **III** also remained at initial values for 28 h before equally dropping to one tenth of the original values (0.1 µF for **I** and 0.2 µF for **III**). The two-step adhesion process could also be observed in the time course of capacitance for the reverse side of the first permeable support (**I** on F1) which suggested this to be setup-related rather than cell type-specific as the adhesion profiles of **II** and **III** did not display the additional shoulder in the capacitance time courses.

V.3.2.1.3 Comparison & Discussion

Apart from the different capacitance starting values with respect to the front and reverse side of the permeable supports, the most notable differences were the following: (i) the shape of the adhesion profile of MDCK-I cells deviated from the one observed on the impermeable ECIS® substrates where a second increase in impedance was observed after about 30 h (see **Fig. 48A**), (ii) the two-step capacitance decrease for cells growing on the reverse side of the permeable support seemed to be setup-related for the permeable substrate whereas a similar form could exclusively be observed in the case of MDCK-II adhesion on ECIS® arrays (compare **Fig. 48B**), (iii) according to the capacitance, the adhesion process generally seemed to take longer on the permeable supports (8 h in the case of MDCK-I cells) compared to the impermeable ECIS® arrays (4 h for MDCK-I cells) and (iv) the formation of a confluent cell monolayer took longer on the reverse side of the permeable support than on the front side (compare **Fig. 49B**: 8 h for the front side and 15 h for the reverse side until a confluent MDCK-I cell layer was established after cell inoculation at t = 0 h). The magnitude of

impedance favorably reflected the information obtained from the frequency-resolved spectra from the last chapter where, due to the differently sized active area of the working electrodes, the values for the same cell layer were higher on the reverse side of the permeable supports. Comparing the adhesion on the front of the permeable supports (**II** & **III**) with respect to their capacitance adhesion profile, it took approximately 2.5 h longer for the MDCK-II cells to adhere. This time delay was also observed in the ECIS® control experiments. On the reverse side, neither a time delay nor differences in the adhesion profile between MDCK-I (**IV**) and MDCK-II (**I**) were observed. In both cases, the time interval between cell inoculation and final capacitance values amounted to approximately 15 h which is significantly longer compared to impermeable substrates (5 h and 10 h for MDCK-I and MDCK-II, respectively) and the capacitance profiles in that time interval for **I** and **IV** were very similar for both cell types by displaying the same shoulder. This however, could be attributed to the lamination foil which poses a 150-µm-step for the cells to grow over in order to form a diffusion barrier. A comparison with literature data is not possible as a similar setup has not yet been published. In summary, the performed adhesion experiments not only enabled a clear distinction between moderately tight and very tight barrier-forming epithelial cells, they also further confirmed that an independent readout of the two cell lines growing on both sides of the permeable support was feasible. Further developmental work and an automated production process could possibly lead to an increasing convergence of the impedance and capacitance values stemming from the cell-covered electrodes on each side of the support by (i) extending the size of the hole in the lamination foil in order to obtain similar active working electrode sizes and (ii) using a thinner lamination foil for the additional counter electrode on the reverse side in order to minimize the size of the step and thus to align the working electrode on the filter membrane and the counter electrode on the lamination foil in a more coplanar fashion.

V.3.2.2 Influence of the Buffer Conductivity on the Cell Signal

A second time-resolved measurement to prove the independent readout of the two sides of the permeable supports was performed in which the culture medium of the two MDCK subtypes was replaced with an isoosmolar buffer exhibiting only half the conductivity of the culture medium (sucrose-supplemented mixture of L-15 medium and distilled H_2O). The experiment was simultaneously performed with confluent MDCK cell layers grown on two permeable supports and MDCK cells seeded in commercially available 8W10E ECIS® arrays. The formulation of this buffer is given in chapter IV.2.7 and the values determined for the osmolality and conductivity are summarized in **Tab. 7** on page 61.

V.3.2.2.1 Impermeable ECIS® Electrodes

MDCK-I and MDCK-II cells were grown to confluence in 8W10E ECIS® arrays and the morphological response to the addition of a culture medium with the same osmolality but only half the conductivity ($\sigma = 50\,\%$) was monitored. In half of the wells, standard L-15 buffer ($\sigma = 100\,\%$) served as control. The normalized time courses of impedance are depicted in **Fig. 50A** and the corresponding normalized time courses of capacitance in **Fig. 50B**. The color code was aligned with V.3.2.2.2 for easier comparison.
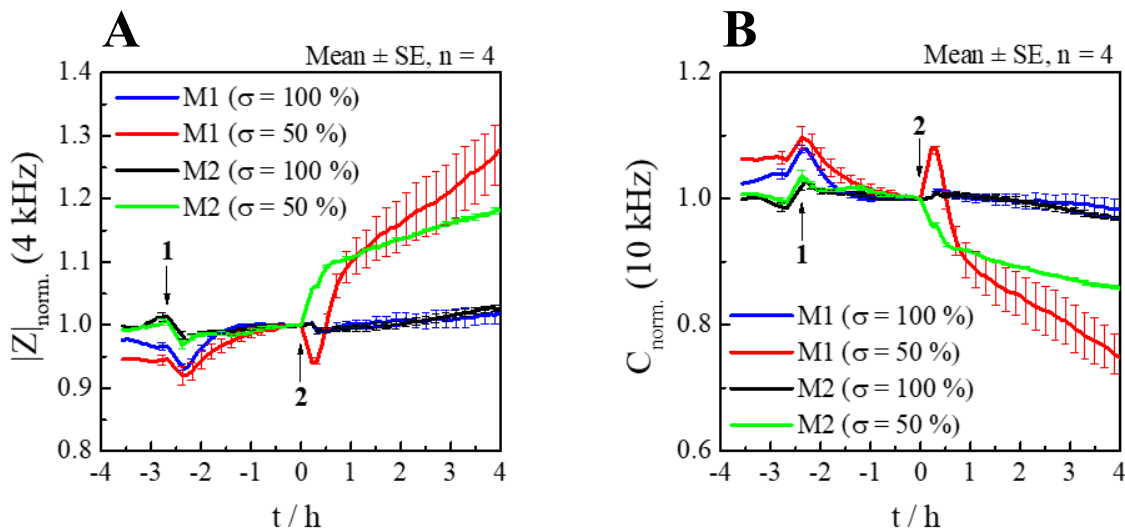
Fig. 50: Time courses of norm. impedance magnitude at 4 kHz (**A**) and norm. capacitance at 10 kHz (**B**) during the exposure of MDCK cells to either normal L-15 buffer ($\sigma = 15.68$ mS/cm, 100 %) or an isoosmolar buffer exhibiting only half the conductivity ($\sigma = 7.79$ mS/cm, 50 %) in 8W10E ECIS® arrays. The culture medium was exchanged against L-15 in all wells at point (**1**) and the L-15 again aspirated in half the wells and replaced with the semi-conductive buffer at point (**2**). Experiments were performed in a standard cell culture incubator at 37 °C and 0 % CO_2. Only 30 error bars are shown for reasons of clarity. The absolute values before normalization can be found in **Tab. 11** on page 176.

In the first hour of measurement time, a stable normalized impedance signal between 0.94 and 1.02 was observed (**Fig. 50**, left-hand side) with corresponding normalized capacitance values between 0.98 and 1.06 (**Fig. 50**, right-hand side) for cells under the influence of culture medium. At time point **1**, the culture medium in all wells was replaced with L-15 medium which, in the time courses, was observed as a 3 – 4 % dip and peak in the impedance and capacitance, respectively. In the ensuing 2.5 h, the signals reached stable values of one (t = 0 h, point of normalization). Following the replacement of the L-15 buffer with the semi-conductive one in half of the wells (t = 0 h, time point **2**), the impedance and capacitance of the control wells (**M2** & **M1**) did not change by more than 3 %, yielding final normalized impedance values of 1.02 and 0.98 for the normalized capacitance. In the wells where the buffer conductivity was halved (**M1** & **M2**), the normalized impedance for the MDCK-II cells (**M2**) increased sharply by 10 % during the first half hour and continued to rise for the last 3.5 h to reach final values of 1.18. The corresponding capacitance time courses confirmed these observations as the capacitance rapidly dropped to 0.92 within the first half hour and continued to decrease to a value of 0.86 during the rest of the measurement. A different reaction was observed for the MDCK-I cells (**M1**) as the normalized impedance initially decreased by 6 % which was followed by a subsequent steep increase surpassing the MDCK-II level after 1 h and reaching final values of 1.28 after 4 h of measurement time. The capacitance of the MDCK-I cells initially increased by as much as 8 % before rapidly dropping to MDCK-II levels after 1 h and decreasing further to 0.75 after 4 h of measurement time.

V.3.2.2.2 Permeable Filter Supports

A total of two MDCK-I cell layers and two MDCK-II cell layers were first cultivated on two permeable supports using the cultivation chamber described in chapter IV.1.2.4.2 and subsequently stacked in one measurement chamber (compare IV.1.2.4.3) according to the arrangement shown in **Fig. 45**. All three compartments of the measurement chamber were filled with L-15 medium. At time point t = 0 h, the L-15 buffer in the middle compartment was aspirated, a single spectrum of each of the four electrode combinations was recorded and subsequently the middle compartment was filled with the buffer exhibiting the lower conductivity. The normalized time courses of the impedance magnitude at 200 Hz are shown in **Fig. 51A** and the corresponding normalized time courses of capacitance at 10 kHz in **Fig. 51B**. The color code from **Fig. 45** was upheld and also used in the ECIS® reference measurement for better comparison.
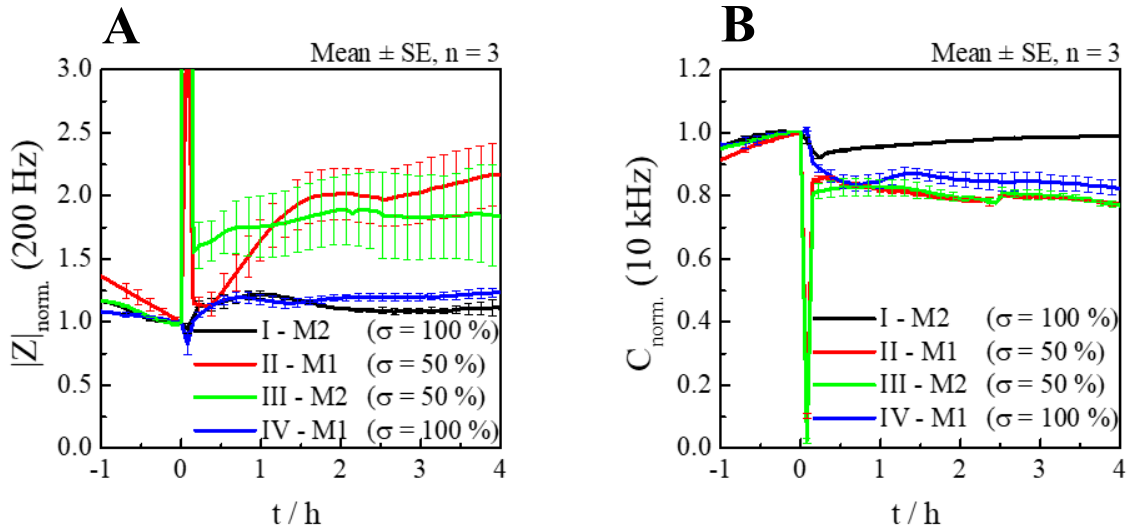
Fig. 51: Time courses of normalized impedance magnitude (**A**) and capacitance (**B**) of confluent MDCK cell layers growing on permeable supports being exposed to either L-15 buffer (σ = 15.68 mS/cm (100 %), side compartments) or an isoosmolar buffer exhibiting only half the conductivity (σ = 7.79 mS/cm (50 %), middle compartment). The L-15 buffer was replaced with the semi-conductive buffer at time point t = 0 h. Experiments were performed in a standard cell culture incubator at 37 °C and 0 % CO_2. For reasons of clarity, only 30 error bars are shown and the absolute values before normalization are listed in **Tab. 11** on page 176.

The normalized impedance magnitude leading up to t = 0 h was relatively stable in a range between 1.08 and 1.36 with the corresponding normalized capacitance measuring from 0.92 to 0.96. The aspiration of the middle compartment electrolyte led to a jump in the impedance magnitude in the case of the adjacent electrode combinations to values of 3.7 (**II**) and even 16.5 (**III**) while the impedance magnitude signal from the reverse sides of the two permeable supports directed towards the side compartments slightly dipped (0.95 and 0.83 for **I** and **IV**). Looking at the corresponding normalized capacitance, the values instantly decreased to minimal values of 0.1 (**II**) and 0.02 (**III**) whereas no significant change for **I** and **IV** was detected. As soon as the empty compartment was refilled with the semi-conductive buffer, the impedance magnitude values stemming from the MDCK-I cell layer measured 1.15 (**II**) and the MDCK-II cell layer yielded 1.55 (**III**) whereas the outward facing cell layers returned to pre-aspiration values of 1.0. The normalized capacitance also increased again to 0.85 (**II**) and 0.81 (**III**) while the signal for **I** and **IV** was still constant. During the further course of the measurement, the impedance magnitude signal of **III** steadily rose to 1.84 while the time course of normalized impedance in the case of **II** initially dipped slightly before steeply increasing for 1 h and thereafter continuing to rise to final values of 2.17 after 4 h. In comparison, the normalized impedance magnitude of **I** and **IV** was constant, reaching final values of 1.11 and 1.24 for **I** and **IV**, respectively. When comparing the post-addition normalized capacitance time courses, the response and even the final values of **II** and **III** were

very similar (0.77). However, striking differences occured between the outward-facing cell layers as the signal of **I**, after an initial 8 % dip, returned to an original value of 0.99 and the signal stemming from **IV** – although being constant during the process of aspirating the L-15 medium and the subsequent replacement – decreased to capacitance values of 0.85 within half an hour which, at that time, could not be distinguished from **II** and **III**. Thereafter, a slight decrease of the normalized capacitance of **IV** was observed, yielding a final value of 0.82.

V.3.2.2.3 Comparison & Discussion

The primary goal of proving the independent readout of two cell layers growing on each side of the permeable support was clearly accomplished. The high impedance and low capacitance values, which were recorded while the middle compartment was empty, only occurred for electrode combinations **II** and **III** due to the lack of the electrolyte while the signals for **I** and **IV** did not change significantly. Furthermore, when comparing the signals of cell layers **II** and **III** upon the stimulation with the isoosmolar but less conductive buffer, the signals favorably compared with the results from the ECIS® experiments: the change in impedance obtained for the MDCK-II cells was instantaneous and nearly constant for the rest of the measurement, whereas the MDCK-I cell impedance signal was constant at first on the permeable supports and initially even decreased on the ECIS® arrays before steeply increasing in both cases to end up at values higher than the MDCK-II signal. As already mentioned in chapter V.3.1.3, the composition of the junctional proteins varies between MDCK-I and MDCK-II cells. In addition to the proteins claudin-1, claudin-4, occludin and ZO-1, which are present in both strains, MDCK-II cells also express the tight junction protein claudin-2 which is pore-forming and facilitates the diffusion of cations across the intercellular pathway[66]. This could be one possible explanation for the rapid increase but thereafter constant impedance signal of MDCK-II cells following the addition of the semi-conductive buffer. Ions from the still higher ionic concentration in the inter- and subcellular spaces could diffuse into the less conductive buffer to re-establish an equilibrium. This means that the cell-specific ECIS® parameters would quickly adapt new values and from there on remain constant in the case of MDCK-II cells as the resistances of the electrolyte in the intercellular gaps and in the bulk solution align. In contrast to that, MDCK-I cells do not express the pore-forming claudin-2 protein which signifies that the shortage of conductive ions increases the resistance of the cell-cell contacts whereas the resistance from the cell adhesion sites as well as the membrane capacitance should remain largely unaffected.

116

As the magnitude of impedance in **Fig. 51A** is composed of all these contributions, the data set was used to extract the time-dependent changes of the individual ECIS® parameters R_b, α and C_m which are shown in **Fig. 52**.
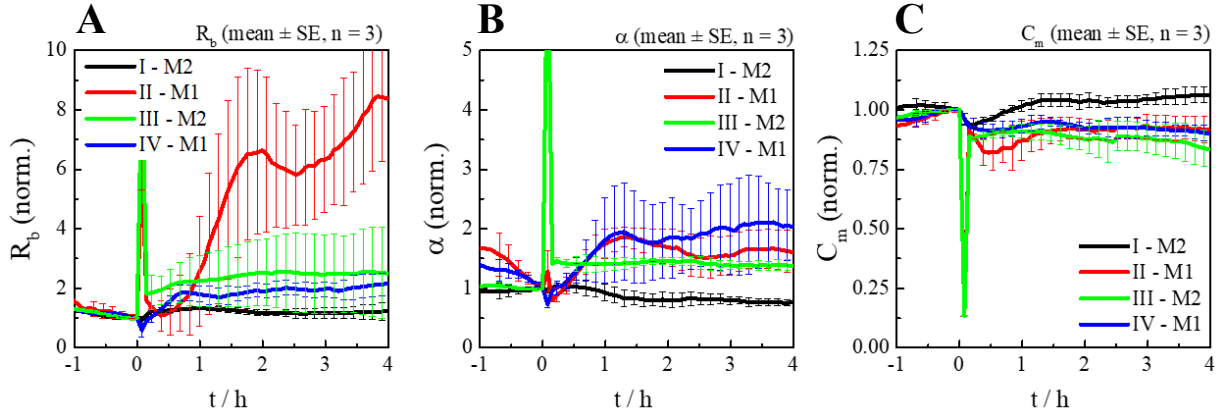
Fig. 52: Time-dependent change of the ECIS® parameters R_b (**A**), α (**B**) and C_m (**C**) extracted from the experiments with reduced conductivity using two permeable supports stacked in a measurement chamber (**Fig. 51**). The parameters were normalized with respect to the last value before the aspiration of the L-15 medium in the middle compartment. Only 30 error bars are shown for clarity. The absolute values for R_b, α and C_m before normalization can be found in **Tab. 11** on page 176.

Fig. 52 depicts the normalized time courses of R_b, α and C_m and by comparing the change of the three parameters with each other, it was confirmed that the one changing most was R_b. This observation reflected the aforementioned considerations. The R_b value for the MDCK-I cell layer (**II**) in direct contact to the semi-conductive buffer was stable at first but after half an hour increased steeply and the overall increase amounted to 700 % after the full 4 h of measurement time. In contrast to that did the corresponding parameter alpha only increase by 60 %. This indicated that indeed no ion exchange occured across the cell-cell contacts in the case of MDCK-I cells and thus, the resistance from the cell adhesion sites was mostly constant whereas the resistance between the cells was augmented due to less available ions. In contrast to that, the R_b and α value of the MDCK-II cell layer (**III**) both exhibited similar characteristics: after the semi-conductive buffer was added, the values instantly increased and thereafter remained constant for the rest of the measurement. The total increase for both parameters was 150 % and 40 % for R_b and α, respectively, which was significantly lower compared to the MDCK-I cells (**II**) and indicated that equilibrium was reached after a short amount of time. Another observation supporting the assumed differences in cationic diffusion across the intercellular spaces was the response of the cell layers on the reverse sides of the permeable supports. The ECIS® parameters of the MDCK-II cell layer (**I**) did not change at all since it was shielded by the barrier-forming MDCK-I cell layer (**II**) on the other side of F1.

In contrast to that, the MDCK-I cell layer (**IV**) on the reverse side of F2 seemed to react to the stimulation by a 100-% increase of the parameters R_b and α although an MDCK-II cell layer (**III**) was located in between. This could be explained by the fact that the cations, which were still present in initial concentrations in the filter pores and the cell-adhesion sites, were able to diffuse through the cell-cell contacts of the MDCK-II cell layer (**III**) into the middle compartment causing the increase of R_b and α for **IV**. The exact ways in which MDCK-I cells with their many tight junctions adapt to buffer ion deprivation when at the same time the osmolality is unchanging, still need to be investigated further.

V.3.2.3   *Exposure to Cytochalasin D*

An observation of morphological changes was performed following the addition of the mycotoxin cytochalasin D (CytD). CytD is a mold-produced and cell-permeable alkaloid known to effectively inhibit the polymerization of actin. The inhibition occurs due to the disruption of the actin filaments and thus, the p53-dependent pathway is activated which stalls the cell cycle at the G1-S transition[87]. In the presence of living cells, the substance rapidly binds to the F-actin and prevents the polymerization of the respective monomers which leads to a breakdown of the barrier-function; however, the process is reversible when the compound is washed out as was demonstrated in the preliminary work by Kathrin Hajek in 2016. The overall functionality and accurate quantification of the cellular response with the permeable support-based three-dimensional tissue model was again validated by comparing the cell reaction following the addition of cytochalasin D to cells grown in commercially available 8W10E ECIS® arrays as well as in the IDE sensor arrays with suspendable Transwell® filter inserts (IV.1.2.2) on which an additional cell layer could be cultivated.

V.3.2.3.1 Cells on Impermeable ECIS® Electrodes

Time-resolved response profiles of MDCK-I and MDCK-II cells grown to confluence on 8W10E ECIS® arrays are shown in **Fig. 53**. **A & C** depict the normalized time courses of impedance magnitude and capacitance for MDCK-I cells and **B & D** for MDCK-II cells after the addition of cytochalasin D in a concentration range from $0 - 5$ µM. Seven different cytochalasin D concentrations were tested as well as a control solution containing no CytD but dimethyl sulfoxide corresponding to the amount present in the highest CytD concentration.

118
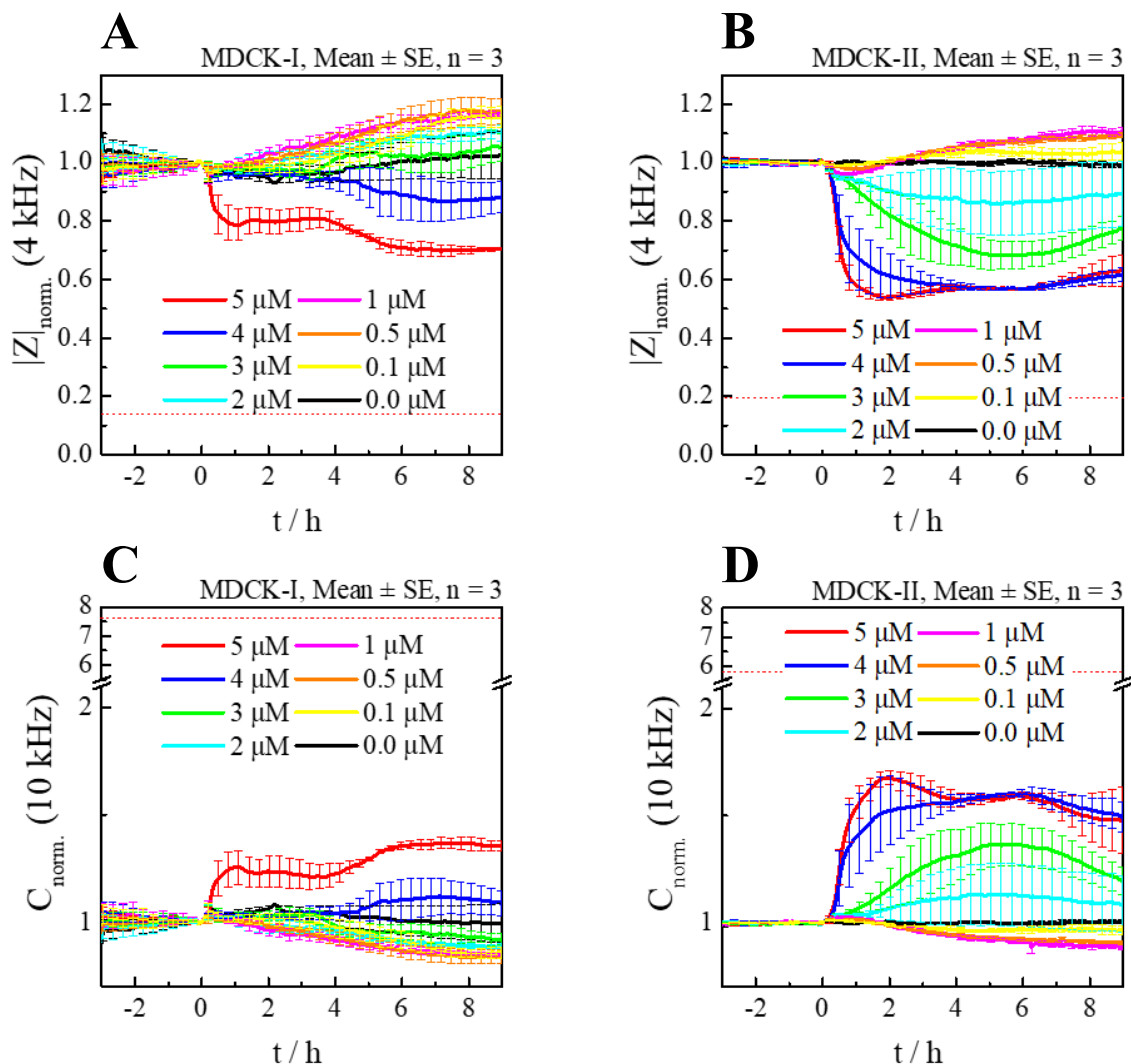
Fig. 53: Cytochalasin D added to confluent MDCK-I (**A**, **C**) and MDCK-II (**B**, **D**) cell layers grown on commercially available 8W10E ECIS® arrays in a concentration range of 0 – 5 µM. In the 0 µM control, dimethyl sulfoxide (DMSO) was added in a concentration comparable to 5 µM cytochalasin D. (**A**, **B**) depict time courses of impedance magnitude and (**C**, **D**) time courses of capacitance which were normalized with respect to the last data point before the addition of the compound (t = 0 h). Experiments were conducted in cell culture medium at 37 °C and 5 % CO_2. The red dotted line corresponds to the value of the cell-free electrode (absolute value of the cell-free electrode divided by the absolute value of the cell-covered electrode at the sampling frequency). For reasons of clarity, only 40 error bars are shown and the absolute values before normalization can be found in **Tab. 11** on page 176.

The CytD compound was added at t = 0 h with the signal leading up to that point fluctuating only slightly. The addition of the toxin to MDCK-I cells (**Fig. 53A**) showed an instantaneous effect only for the highest concentration (5 µM) where the normalized impedance dropped to 0.8 and remained constant for 4 h before decreasing further to final values of 0.7. The second-highest concentration (4 µM), in contrast, did not seem to have any effect within the first 4.5 h of measurement time before the impedance slightly decreased to 0.87. The signal of the cells treated with the control solution was very stable and only increased by 2 % during the entire

measurement. Cytochalasin D concentrations in the range of 0.1 μM to 3 μM however, elicited impedance increases between 5 % and 18 %. This phenomenon of a positive effect in the presence of a stressor in a non-toxic concentration (sub-EC$_{50}$) is a well-known and highly controversially discussed one called hormesis[88]. The cells respond to low concentrations of a toxin by a change of their morphology which in turn increases the impedance signal. Even at the most toxic concentration, the value of the cell-free electrode (0.14, dotted red line) was not reached meaning that the cells remained adhered to the electrode and only the cell-cell contacts seemed to be affected. The time courses of normalized capacitance (**Fig. 53C**) confirmed these findings as the capacitance only moderately increased for the highest concentration (5 μM) to 1.25 after 70 min and further to 1.35 after 6 h. The second-highest concentration (4 μM) remained constant for 4.5 h before increasing to final values of 1.12. A cell-free electrode would have revealed a normalized capacitance value of 7.6 (indicated by the red dotted line) which was not nearly reached, and consequently the electrode was still fully covered by individual cells without cell-cell contacts. Cytochalasin D concentrations lower than 4 μM collectively fell between 8 % and 16 % over the course of the measurement.

The $|Z|_{norm.}(t)$ signal of MDCK-II cells monitored at 4 kHz (**Fig. 53B**) changed more after the treatment with cytochalasin D as the addition of the highest concentration (5 μM) at t = 0 h provoked a rapid drop to a value of 0.54 after 2 h with a subsequent slight recuperation to 0.63 after the full 9 h of measurement time. The second-highest concentration (4 μM) did not decrease as much in the beginning but showed similar final values after 9 h. In contrast to the MDCK-I response, the MDCK-II cells reacted to concentrations of 3 μM and 2 μM with impedance decreases by 32 % and 14 %, respectively, before reaching final values of 0.78 and 0.89. The impedance of the control cells (0.0 μM) only fluctuated by 1 % and the signals for concentrations of 1 μM, 0.5 μM and 0.1 μM eventually increased between 1 % and 10 %. All in all, MDCK-II cells showed a strictly concentration-dependent behavior with an inversion point around 1 μM because at that concentration, the signal initially decreased but afterwards increased until the end of the measurement. The time courses of normalized capacitance (**Fig. 53D**) also favorably compared with the impedance results for the MDCK-II cells. The two highest concentrations (5 μM and 4 μM) rose by 50 % over the course of the measurement with the higher concentration reaching a peak value of 1.68 after 2 h. The capacitance of cells treated with a concentration of 3 μM steadily increased up to t = 5 h, reaching a maximum value of around 1.36 before continuously declining to a final value of 1.2. Incubation with 2 μM of cytochalasin D provoked a 10 % increase in the normalized capacitance after 4 h which thereafter did not change until the end of the measurement. The

120

cells without any cytochalasin D contact exhibited no change in capacitance over the entire course of the measurement and the signals for the concentrations from 0.1 µM, over 0.5 µM to 1 µM fell 5 %, 9 % and 11 %, respectively. Akin to the measurement with MDCK-I cells, the value of the cell-free electrode was not reached as a capacitance increase of 700 % would have been needed. This meant that the electrodes were still covered by viable MDCK-II cells which had temporarily lost their barrier function but remained attached to the gold surface.

V.3.2.3.2 Cells on Permeable Transwell® Filter Inserts

The effect of cytochalasin D on MDCK cells with an additional cell barrier was investigated using the IDE sensor array from chapter IV.1.2.2. The sensor cells which were seeded on the bottom of the well, and thus being adherent directly on the IDF electrodes, were MDCK-II cells. This setup constitutes a co-culture model of two cell layers in which one serves as a biological barrier without establishing physical contact. Thus, a cell-free Transwell® filter was compared to NRK, MDCK-II and MDCK-I cells seeded in the inserts. At t = 0 h, cytochalasin D was added to the apical compartment yielding a final concentration of 5 µM. Time courses of norm. impedance magnitude and capacitance are shown in **Fig. 54A** and **Fig. 54B**.
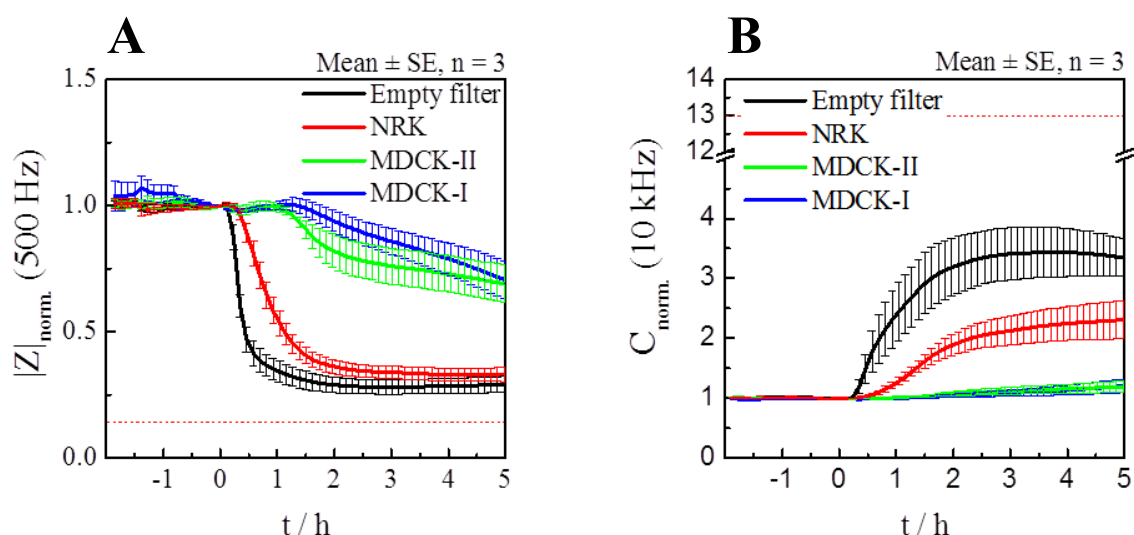
Fig. 54: Cytochalasin D was added to the apical compartments of the IDE sensor arrays in a final concentration of 5 µM at t = 0 h. Confluent cell layers of NRK cells (**red**), MDCK-II cells (**green**), MDCK-I cells (**blue**) were grown on Transwell® filter inserts and empty filters (**black**) served as control. The sensor cells growing directly on the IDF electrode layout were MDCK-II cells in all cases. Time courses of normalized impedance (**A**) and normalized capacitance (**B**) are shown. Experiments were conducted in culture medium at 37 °C and 5 % CO_2. The red dotted line corresponds to the value of the cell-free electrode (absolute value of the cell-free electrode divided by the absolute value of the cell-covered electrode at the most sensitive frequency) and only 40 error bars are depicted for reasons of clarity. Absolute values before normalization are given in **Tab. 11** on page 176.

The impedance and capacitance signals were normalized with respect to the last data point before the addition of cytochalasin D at $t = 0$ h. Directly after the addition of the substance, the sensor cells below the empty filter inserts (**Empty filter**) responded by a steep drop in impedance to 40 % of the initial value within the first 30 min of measurement time. The decrease thereafter continued, albeit at a lower rate to reach a minimum value of 0.28 after 2 h and a final value of 0.29 after the full 5 h of measurement time. The sensor cells growing beneath a confluent NRK cell layer (**NRK**) responded by exhibiting a similar response profile which was delayed by approximately 15 min and with the initial slope being less steep. Final values were also reached after 2 h (0.36) which thereafter remained constant. MDCK-II-shielded sensor cells (**MDCK-II**) needed 1 h for the initial response in which the impedance decreased to 0.8. The impedance then continued to drift lower ending up at a value of 0.7. If MDCK-I cells were used instead of MDCK-II cells as barrier cells (**MDCK-I**), 1 h and 20 min passed before the impedance started to decrease continuously to reach a final value of 0.7 after 5 h.

The time courses of normalized capacitance revealed only minimal changes if the two MDCK cell types were used as barrier cells (total change of 20 % for MDCK-I and 19 % for MDCK-II). In contrast to that, if the epithelial-like NRK cell line was employed as a diffusion barrier, the normalized capacitance started to rise above the initial level after 30 min and continued to rise for the remaining 4 h, reaching a normalized capacitance of 2.3 at the end of the measurement (implying a 130-% increase). When the filter inserts were left cell-free, an increase in the capacitance could be observed already 15 min after the addition of CytD and values of 3.2 were reached already after 2 h of measurement time which, over the course of the measurement, further increased to 3.4. However, even below the cell-free filter insert, the capacitance only reached about one quarter of the value representing the cell-free electrode.

V.3.2.3.3 Cells on Stacked Permeable Filter Supports

In this chapter, the effect of cytochalasin D was investigated if added to one side compartment of the measurement chamber holding two permeable filter supports, each with a confluent MDCK-I and MDCK-II cell layer on opposing sides. The permeable supports and cell layers were arranged according to **Fig. 45**. The fungal toxin was added at $t = 0$ h to the right-hand compartment, establishing a direct contact to cell layer (**I**). **Fig. 55A** shows the time courses of normalized impedance magnitude and **Fig. 55B** the corresponding normalized capacitance.
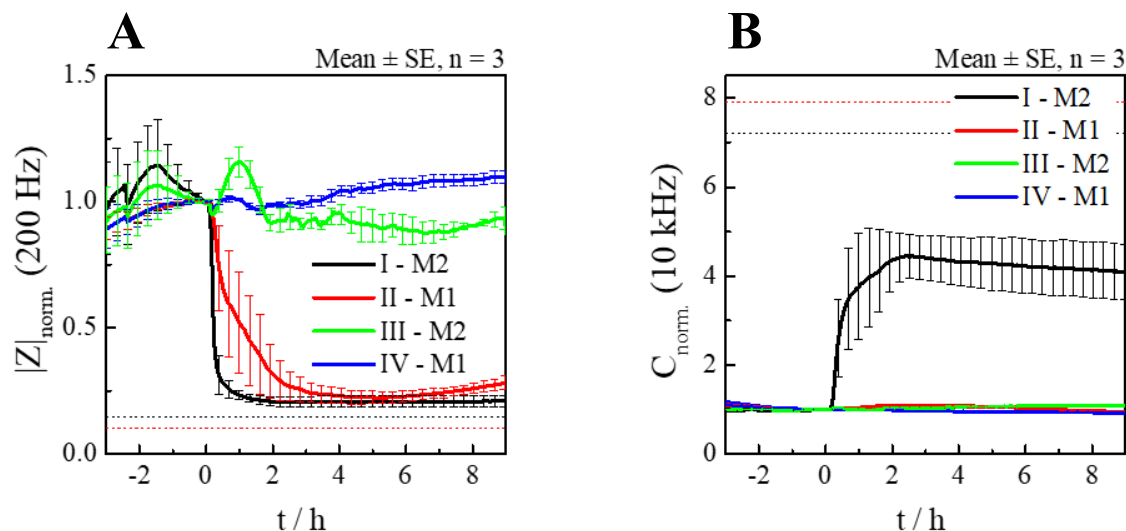
Fig. 55: Cytochalasin D added to the right compartment of the measurement chamber next to (**I**) to yield a concentration of 5 µM at t = 0 h. Four MDCK cell layers were grown to confluence on two permeable supports and arranged in the measurement chamber according to **Fig. 45**. (**A**) depicts the time courses of impedance magnitude and (**B**) the time courses of capacitance which were both normalized with respect to the last data point before the addition of the compound. Experiments were conducted in cell culture medium at 37 °C and 5 % CO_2. The red and black dotted lines correspond to the values of the cell-free electrodes (absolute value of the cell-free electrode divided by the absolute value of the same cell-covered electrode at the most sensitive frequency). Only 40 error bars are shown for reasons of clarity and the absolute values before normalization can be found in **Tab. 11** on page 176.

The MDCK-II cell layer in immediate contact to the location of the addition (**I**) was the first to respond with a drastic drop of the impedance signal as can be seen in **Fig. 55A**. Within 30 min of measurement time, the impedance dropped below 30 % of the pre-addition value. A final, constant normalized impedance value of 0.2 was established after 2 h. The MDCK-I cell layer on the other side of the permeable support (**II**) followed suit with an initial time delay of 10 min to reach 80 % of the pre-addition values and the time delay increased to 1 h before the impedance had decreased by 50 %. The lowest values were detected after 4 h (0.23) before the signal began to slightly recuperate, eventually reaching a value of 0.28. The impedance signal of the MDCK-II cell layer on the adjacent permeable support (**III**) first dipped by 5 % before rapidly increasing by 16 %, reaching a local maximum after 1 h. In the next hour, the signal decreased to 0.9 and thereafter remained constant with more fluctuation compared to the other cell layers. The MDCK-I cell layer which was located farthest from the site of addition (**IV**) continued its slight upward trend throughout the measurement, with the impedance rising by 10 % in total.

Fig. 55B depicts the corresponding time courses of the normalized capacitance. The overall capacitance for cell layers **II**, **III** and **IV** remained mostly constant. Changes were most pronounced for cell layer **II** for which maximum values (an 8 % increase) were observed from 2 h to 4 h before the capacitance leveled off to reach final values of 0.95. The capacitance of cell layers **III** and **IV** steadily increased and decreased by 8 %, respectively, over the course of the measurement. The only cells to reveal a significant signal change in response to the CytD addition was cell layer **I** where the capacitance started to soar up 10 min after the addition. A maximum value of 4.4 was attained after 2 h and the signal only slightly retreated to 4.1 after the complete measurement time. Nevertheless, only about half the capacitance value of the cell-free electrode (black dotted line) was obtained for cell layer **I** indicating that the electrode surface was still fully covered with cells but that the cell-cell contacts had been opened in analogy to the 2-step decrease of C(t) during cell seeding with adhesion being the first step and the subsequent spreading and formation of cell-cell contacts the second one. The impedance also indicated a complete breakdown of the barrier functionality.

V.3.2.3.4 Comparison & Discussion

The three experimental setups, including the commercially available ECIS® arrays, the IDF electrode layout with suspendable filter inserts and the tissue model with the stacked permeable supports, were chosen to establish a reliable response profile upon the stimulation with cytochalasin D. The ECIS® measurement hereby served as the reference measurement to find a concentration that on the one hand was not sufficiently toxic to kill the cells, but on the other hand toxic enough to provoke a measurable impedance signal. Furthermore, the response profiles for the two MDCK subtypes could be established; albeit only on an impermeable substrate. The IDE sensor array served as bridge between the impermeable ECIS® arrays and the permeable supports. The IDF electrode structure, on which the sensor cells could adhere, was also patterned on an impermeable substrate, but the added substance first had to diffuse across a biological barrier in a 1-mm distance to reach the sensor cells. Thus, the model encompassed a total of two cell layers which received a CytD stimulation in different concentrations due to dilution effects and the cell type-dependent binding of CytD by the barrier cell layer in the filter inserts. Due to the different barrier properties of the cell lines in question, a more delayed sensor cell response was anticipated for increasing barrier tightness. The highest concentration from the ECIS® experiments was chosen as working concentration and the anticipated delay of the sensor cell response could not only be observed

but strictly correlated with the barrier tightness of the cell type in the filter insert. These findings were then compared to the cell signal of four cell layers grown to all sides of two permeable supports. Identical time-resolved response profiles were seen in the measurement setup with the stacked permeable supports, and furthermore a short time delay could be observed between the cell layers growing on opposing sides of the same permeable support. This means that with the novel measurement setup, it could be proven that the cell response profile upon the stimulation with cytochalasin D is similar between impermeable and permeable substrates, that a co-culture and simultaneous monitoring of cells on each side of such a permeable support is feasible and multiple permeable supports could be stacked inside a measurement chamber with the possibility of individually addressing every single cell layer.

The effect of cytochalasin D on living cells with the three different measurement methods brought to light similarities as well as differences. The similarities included (i) an instant decrease in impedance following the addition of CytD in sufficiently high concentrations and (ii) a corresponding capacitance increase signifying a breakdown of the barrier property but an otherwise intact cell monolayer. The fact that the same application concentration (5 µM) appeared to have a substantially stronger effect for cells growing on permeable substrates could be due to the chosen mid-frequency ECIS® monitoring frequency of 4 kHz as it does not exclusively represent the effect on the cell-cell contacts which would be visible at lower frequencies. This specific monitoring frequency was chosen in agreement with the adhesion measurement to encompass paracellular as well as transcellular contributions. Nevertheless, the normalized capacitance at the most sensitive frequency of 10 kHz also indicated that M2 cells seemed to be more susceptible to CytD as lower concentrations were sufficient to provoke a measurable cell signal. The IDE sensor array measurements (**Fig. 54**) showed that the sensor cells' reaction was dependent on the type of the barrier cells which were suspended in the filter inserts above. If no barrier cells were present, the sensor cells' reaction occurred earlier and if a barrier cell layer was present, the time delay of the sensor cell reaction depended on the tightness and supposedly the amount of actin of the barrier. NRK cells as a leaky model initially delayed the sensor cells' response by only 15 min whereas M2 cells as moderately tight epithelial cells provided protection for 1 h and the tight epithelial M1 cells prevented a sensor cell signal for 1 h and 20 min. Interestingly did the capacitance of the sensor cells not change at all if MDCK cells were used as barrier cells. The experiments with the stacked MDCK cell layers (**Fig. 55**) confirmed this discovery as only the capacitance of the M2 cell layer (**I**) in the direct vicinity of the addition site increased in the wake of the CytD addition whereas the M1 cell layer (**II**) did not show any change of the capacitance although

the impedance significantly decreased. Also did the impedance signal for cell layer (**II**) start to rise again during the measurement which can be explained by the ongoing dilution of the local CytD concentration in the proximity of the first permeable support and the fact that the CytD effect is known to be reversible by a washout process as was demonstrated on multiple occasions in literature[89]. Moreover, a retardation of approximately 10 min could be observed of cell layer (**II**) in comparison to cell layer (**I**) as was also found by Hajek et al. (2017) in a similar measurement setup[90]. The M2 cell layer (**III**) and the M1 cell layer (**IV**) on the next permeable support did not show any CytD-dependent signal change which could be due either to the 7-mm distance between the two permeable supports resulting in prolonged diffusion times or the fact that CytD was added next to (**I**), meaning that there were two cell layers (**I**, **II**) separating the location of the addition from the second permeable support and thus two possibilities for the added CytD to bind to the F-actin. Considering that MDCK cell layers had previously in this work been shown to provide effective protection, the amount of CytD reaching cell layer (**III**) was apparently insufficient to cause a measurable signal change.

V.3.2.4   *Exposure to tert-Butyl Hydroperoxide*

The distinct cell response to the addition of tert-butyl hydroperoxide (tBHP) was investigated on impermeable ECIS® substrates and with the help of the IDE sensor array and its additional cell barriers as well as with two cell-covered permeable supports stacked in the measurement chamber. The substance tBHP is a tertiary hydroperoxide exhibiting strong oxidizing properties. Oxidative stress is known to be a key factor in the development of chronic diseases[91]. Reactive oxygen species (ROS) in low concentrations are common in cells and can be disposed of, but if oxidizing compounds, e.g. tBHP are added in higher concentrations, the decomposition causes oxidative stress including lipid peroxidation and DNA damage resulting in general cell damage and apoptosis[92]. Similar to the previous chapter, the cellular response upon stimulation with the oxidizing substance tBHP was compared between the different measurement setups. Thus, the time-dependent response profile upon stimulation with the oxidizing compound was recorded with the commercially available 8W10E ECIS® arrays serving as impermeable substrate, with the help of the IDE sensor array with barrier filter inserts (IV.1.2.2) with which an additional barrier cell layer could be suspended above the sensor cells as well as with the 3D tissue model. The response profiles of this irreversibly oxidizing compound were again compared in detail with each other and constituted another proof-of-concept measurement for the functionality of the novel 3D tissue model.

126

V.3.2.4.1 Cells on Impermeable ECIS® Electrodes

The cell reaction of MDCK-I and MDCK-II cells upon stimulation with different concentrations of the oxidizing compound tBHP was investigated on 8W10E ECIS® arrays and the time-resolved normalized impedance magnitude and capacitance data is shown in **Fig. 56A & B** and **Fig. 56C & D**, respectively. The concentration range for tBHP was chosen to be between 0 – 1 mM. Seven different tert-butyl hydroperoxide concentrations were tested as well as a control solution containing only cell culture medium.
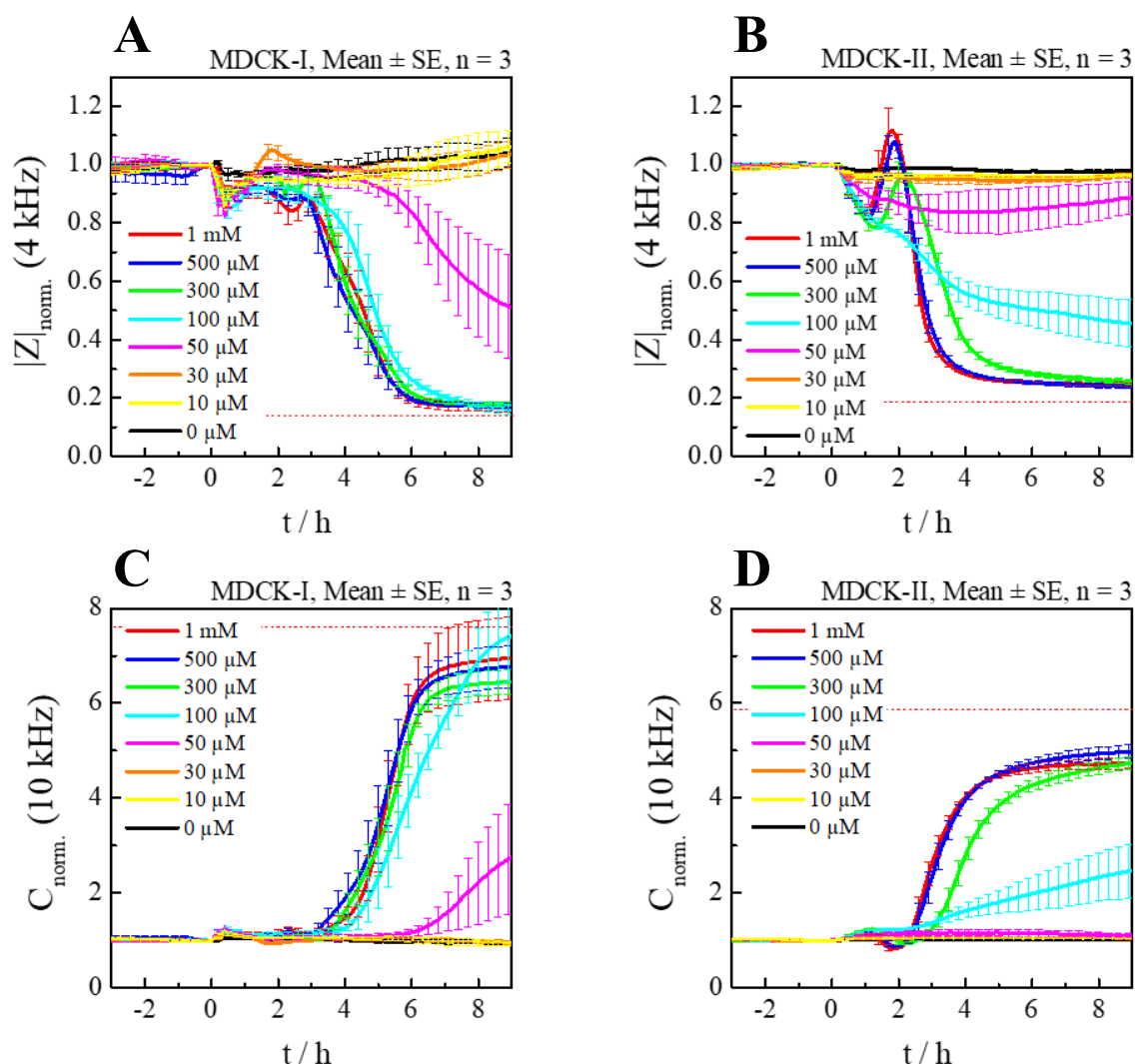
Fig. 56: Tert-butyl hydroperoxide added to confluent MDCK-I (**A**, **C**) and MDCK-II (**B**, **D**) cell layers grown on commercially available 8W10E ECIS® arrays in a concentration range from 0 – 1 mM. (**A & B**) depict time courses of impedance magnitude and (**C & D**) time courses of capacitance which were normalized with respect to the last data point before the addition of the compound (t = 0 h). Experiments were conducted in cell culture medium at 37 °C and 5 % CO_2. The red dotted line corresponds to the value of the cell-free electrode (absolute value of the cell-free electrode divided by the absolute value of the cell-covered electrode at the most sensitive frequency) and only 40 error bars are shown for clarity. The absolute values before normalization are presented in **Tab. 11** on page 176.

The data in **Fig. 56** was normalized with respect to the last value before the addition of tBHP at t = 0 h. The normalized impedance for the MDCK-I cells leading up to the point of addition was highly stable in all wells (**Fig. 56A**). In the aftermath of the addition, the impedance dipped for all wells between 18 % (100 µM) and just 3 % (0 µM). After 1.5 h, the impedance reached pre-addition levels in the case of the cells which did not come into contact with tBHP (0 µM) and the two lowest concentrations (10 µM and 30 µM) and thereafter only fluctuated slightly in a range of 4 %. After the first dip, the next-higher concentration (50 µM) exhibited normal impedance values for three hours before the signal started to decrease towards 0.51 at the end of the measurement. Increasing the concentration further to 100 µM entailed a 2-h-earlier impedance decrease with a correspondingly lower final value of 0.16. The three highest concentrations (300 µM, 500 µM and 1 mM) revealed very similar response profiles with the initial 30-min dip, a two-step recuperation up to 3 h of measurement time, a subsequent steep decrease to 0.2 until t = 6 h and thereafter a steadily continuing decline to approximately 0.16 which resembled the impedance value of the cell-free electrode. The MDCK-II cell response in general was similar with a few exceptions (compare **Fig. 56B**). The control cell signal (0 µM) was constant over the entire course of the measurement in a very narrow range of 3 %. This range was slightly higher at 4 % for the lowest concentration (10 µM) and further increased to 6 % for the next-higher concentration (30 µM). Increasing the amount of tBHP further to 50 µM entailed a steady decline of the impedance signal to 0.83 over the course of 4 h before a slight regeneration started to form so that a final value of 0.89 was obtained. 100 µM of tBHP provoked a two-step subsiding of the measured signal with the steepest slopes found 50 min and 173 min after the addition. Eventually, a normalized impedance of 0.45 was measured after 9 h. A tBHP concentration of 300 µM caused the impedance signal to dip to 0.78 at t = 80 min and a subsequent increase up to 0.96 could be observed. From there on, the impedance steeply declined for 2 h before levelling off and reaching a final value of 0.26 after 9 h. The time-dependent signal for the two highest concentrations (500 µM and 1 mM) exhibited similar characteristics: the signals both dipped around 17 % before rising 8 % and 12 % above the pre-addition level in the case of 500 µM and 1 mM, respectively. This local maximum was then followed by a steep decrease in impedance so that within one hour, the signal had dropped below 50 %. Then, the decrease became slower to yield final impedance values of 0.24 for both concentrations.

The corresponding normalized capacitance signals of MDCK-I cells collectively increased by 20 % as a reaction to the addition of tBHP but the signal was otherwise highly stable for the duration of 3 h before the capacitance started to shoot up for concentrations from 100 µM to

1 mM. Final values of 6.44, 6.76, 6.95 and 7.42 were obtained for 300 µM, 500 µM, 1 mM and 100 µM, respectively. The capacitance following the addition of a concentration of 50 µM only started to increase after 6 h of measurement time and revealed a final value of 2.76. On the contrary, no capacitance increase could be observed for the control conditions (0 µM) and the two lowest tBHP concentrations (10 µM and 30 µM). The capacitance value of the cell-free electrode is indicated by the red dotted line at 7.6, which was almost reached when the highest concentrations of the oxidizing substance were added. The normalized capacitance signal for MDCK-II cells was constant under control conditions (0 µM), and the lowest two concentrations (10 µM and 30 µM). A concentration of 50 µM provoked a minor increase of 16 % which was thereafter stable throughout the measurement. The signal for the next-higher concentration of 100 µM rose by 20 % in the first hour which was followed by a 1-h constant signal before the impedance again started to linearly rise to 2.46. Further increasing the amount of tBHP to 300 µM entailed a small dip in the capacitance at t = 2 h before the signal sigmoidally increased to 4.73. In the case of the two highest concentrations (500 µM and 1 mM), the dip was more pronounced (a brief 14-% decrease) and also observed 20 min earlier. The curve also resembled a sigmoidal increase with the steepest part 50 min closer to the point of addition. Eventually, capacitance values of 4.73 were obtained for 1 mM and even 4.98 for 500 µM which corresponds to almost 85 % of the cell-free capacitance value. These high capacitance values stood in stark contrast to the ECIS® measurement with cytochalasin D where the capacitance indicated that the vast majority of cells was still adherent on the electrode surface.

V.3.2.4.2 Cells on Permeable Transwell® Filter Inserts

A comparison of the cell response upon tert-butyl hydroperoxide stimulation was performed using the IDE sensor array from chapter IV.1.2.2 where an additional barrier cell layer could be suspended in the wells. The sensor cells growing on the bottom of the wells directly on the IDF electrode layout were MDCK-II cells and the barrier properties of the cell layer growing in the Transwell® filter inserts was varied between empty filter inserts, an NRK cell layer, an M2 cell layer and an M1 cell layer. At t = 0 h, tBHP was added to the apical compartment in a concentration of 2 mM as the second-highest concentration from the ECIS® experiments (500 µM) yielded no significant cell reaction but corresponds to the dilution of the 2 mM solution applied here (compare **Fig. 73** in the supplementary information). The resulting time courses of normalized impedance magnitude and capacitance are shown in **Fig. 57A & B**.
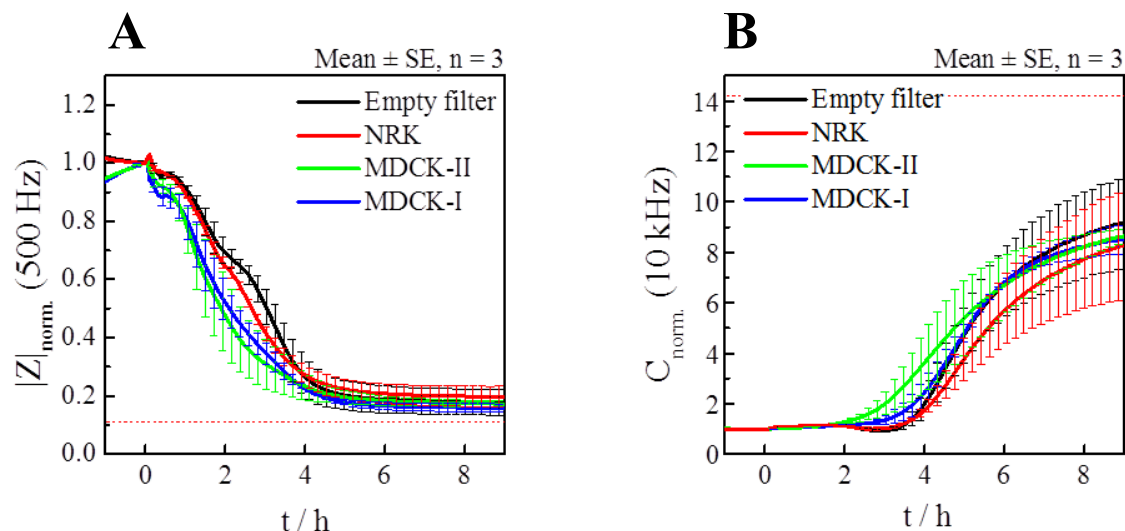
Fig. 57: Tert-butyl hydroperoxide was added to the apical compartments of the IDE sensor arrays in a final concentration of 2 mM. The filter inserts were equipped with confluent cell layers of NRK cells (**red**), MDCK-II cells (**green**), MDCK-I cells (**blue**) and empty filters (**black**) served as control. Sensor cells growing directly on the IDF electrode layout were MDCK-II cells in all cases. Time courses of normalized impedance magnitude (**A**) and normalized capacitance (**B**) are shown. Experiments were conducted in cell culture medium at 37 °C and 5 % CO_2. The red dotted line corresponds to the value of the cell-free electrode (absolute value of the cell-free electrode divided by the absolute value of the cell-covered electrode at the most sensitive frequency); absolute values before normalization are given in **Tab. 11** on page 176 and only 40 error bars are depicted for clarity.

In the one hour leading up to the addition of the oxidizing reagent tBHP, the signal of the MDCK-II sensor cells growing beneath MDCK barrier cells (**MDCK-II** & **MDCK-I**) increased by 6 % whereas the signal of the MDCK-II sensor cells growing beneath empty Transwell® filters (**Empty filter**) or NRK-cell covered filter inserts (**NRK**) slightly decreased by 2 %. Following the addition at t = 0 h, the signal for the MDCK barrier filters decreased in a two-step manner; subsequent to the initial 20-min impedance drop, a short plateau phase of 20 min was observed before the decrease continued, reaching final impedance magnitude values of 0.16 after 6 h of measurement time. In the case of the MDCK-II sensor cells growing beneath an empty or NRK cell-covered filter, a three-step impedance decrease was revealed. In addition to the 20-min drop and 20-min plateau phase, the steep decrease slowed down between 2 h and 2.5 h only to pick up speed again and final |Z|norm. values were equally reached after 6 h. The most pronounced difference within the two- or three-step decline was the 1-h time delay to reach 50 % of the pre-addition normalized impedance level.

The changes in the normalized capacitance were less blatant in the first 2 h of the measurement as the normalized capacitance collectively rose by 12 %. Thereafter, a sigmoidal increase in the normalized capacitance occurred in all four cases yielding final values between 8.3 (**red**) and 9.2 (**black**). The MDCK-shielded sensor cells exhibited identical values of 8.6

130

after 9 h of measurement time. However, differences were observed in the time point of the first increase. The **MDCK-II** signal started to rise after 2 h, the **MDCK-I** signal after 3 h and the **Empty filter** and the **NRK** signals first showed a small dip before following suit. All in all, there were no significant differences to be observed in the normalized capacitance by changing the barrier cell type growing in the filter inserts which were suspended above the sensor cells. Furthermore, the normalized capacitance increased only to about 65 % of the cell-free value, which was less than in the ECIS® control experiment.

V.3.2.4.3 Cells on Stacked Permeable Filter Supports

Complementary to the effect of cytochalasin D described in the previous chapters, the effect of the oxidizing substance tert-butyl hydroperoxide was investigated if added to one side compartment of the measurement chamber holding two permeable filter supports, each with a confluent MDCK-I and MDCK-II cell layer on opposing sides. The permeable supports and cell layers were arranged according to **Fig. 45** on page 98. The oxidizing reagent was added at $t = 0$ h to the right-hand compartment, establishing a direct contact to cell layer (**I**). **Fig. 58A** shows $|Z|_{norm.}$ for a frequency of 200 Hz and **Fig. 58B** the corresponding $C_{norm.}$ at 10 kHz.
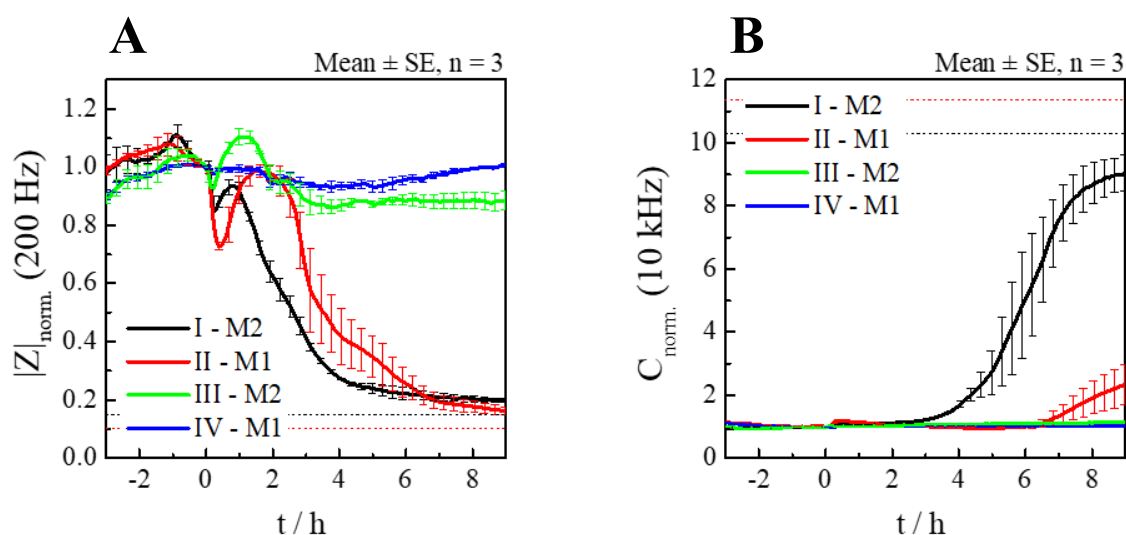
Fig. 58: Tert-butyl hydroperoxide added to the right compartment of the measurement chamber next to (**I**) to yield a final concentration of 500 µM. Four MDCK cell layers were grown to confluence on two permeable supports and arranged in the measurement chamber according to **Fig. 45**. (**A**) depicts the time courses of impedance magnitude and (**B**) the time courses of capacitance normalized with respect to the last data point before the addition of the compound at $t = 0$ h. Experiments were conducted in cell culture medium at 37 °C and 5 % CO_2. The red dotted line corresponds to the values of the cell-free electrode ($|Z|_{cell-free}/|Z|_{cell-covered}$ or $C_{cell-free}/C_{cell-covered}$ at the most sensitive frequency). Data prior to normalization is given in **Tab. 11** on page 176 and only 40 error bars are shown.

In the first 15 min after tBHP was added next to the MDCK-II cell layer (**I**), the normalized impedance decreased by 15 % before a recovery occurred during 30 min in which the normalized impedance again rose to 0.93 (compare **Fig. 58A**). Then, from 1 h to 4 h, a steep decline was observed in which the impedance fell to 0.27. A continuous but slower decline followed so that a normalized impedance of 0.2 was obtained after 9 h of measurement time. The MDCK-I cell layer (**II**) on the opposite side of the same permeable support was the next to respond also with an initial dip (27 %) and a subsequent recovery which took longer (90 min) and reached pre-addition levels again. It then took 1.5 h to reach 50 % of the original impedance and further 3 h to get down to 20 %. From there on, the impedance continued to drift lower until a value of 0.16 was eventually reached. The MDCK-II cell layer on the adjacent permeable support (**III**) also exhibited an 8-% dip in the beginning and in the following, the impedance rose 10 % above the initial value before decreasing to 0.86 where the signal remained constant for the rest of the measurement. The MDCK-I cell layer farthest away from the location of the addition (**IV**) showed no tBHP-related signal change and only fluctuated by 6 % over the course of the measurement.

Similar to the previous chapter, the normalized capacitance increased by 17 % for cell layers (**I**) and (**II**) closest to the location of the addition and it took around 3 h in the case of (**I**) before the capacitance sigmoidally increased to reach final values of 9 which equals approximately 90 % of the value of the cell-free electrode. Cell layer (**II**) on the opposite side of the permeable support exhibited no significant increase of capacitance for 6.5 h before a linear rise to 2.3 was detected. The signal of the cell layers (**III**) and (**IV**) on the second permeable support however, were stable at a normalized value close to 1 throughout the entire measurement with cell layer (**III**) exhibiting only minimally lower values.

V.3.2.4.4 Comparison & Discussion

The morphological change upon stimulation with the oxidizing reagent tert-butyl hydro-peroxide was very different from the cytochalasin D response profile. If the ECIS® measurement (**Fig. 56**) is assumed as the "gold standard", it took around 6 h for MDCK-I cells to reach final impedance values after the addition of tBHP and only 4 h in the case of MDCK-II sensor cells. Moreover, a first dip in the impedance and a subsequent recuperation of initial values occurred for both cell types before the impedance irrevocably began to fall. This dip and recuperation was more pronounced for MDCK-II cells. The corresponding

capacitance equally started to increase 2 h later in the case of MDCK-I cells but for both strains almost reached the level of a cell-free electrode over the course of the measurement. Judging from the impedance data, an EC_{50} value around 100 µM could be roughly estimated for MDCK-II cells, which was in good agreement with a 2015 toxicity investigation by Dr. Michael Lemberger, who determined an EC_{50} value of (168 ± 13) µM for the same cell type with the help of a carbon dots live/dead assay in his PhD thesis. In the experiments with the IDE sensor arrays (**Fig. 57**) MDCK-II cells were employed as sensor cells. Here, the same response profile was observed where final values were reached after 4 h. Missing, however, was the pronounced first dip and subsequent recuperation of initial impedance values. These characteristic features could solely be read into the less steep negative slope after 1 h. On the other hand, in contrast to the ECIS® measurement, the MDCK-II sensor cells had not been in direct contact with the added tBHP. The substance first needed to pass the filter and diffuse to the bottom of the well where it could oxidize e.g. the culture medium proteins on the way. Due to the oxidizing nature of tBHP, the different barrier property strength of NRK, MDCK-II and MDCK-I cells did not appear to have much influence on the time until the substance arrived at the bottom of the well. In the first experiment conducted with the IDE sensor arrays (compare **Fig. 73** in the supplementary information), an application concentration of 500 µM was chosen because this amount yielded the highest capacitance values for the MDCK-II cells in the ECIS® experiments. Owing to the threefold larger basolateral compartment, only one fourth of the 500-µM concentration would theoretically have been able to reach the sensor cell layer which amounted to a maximum concentration of 125 µM after establishing an equilibrium between the apical and the basolateral compartment. The actual concentration much likely was even lower because the tBHP concentration in the basolateral compartment depends on the diffusion process from the apical to the basolateral compartment and part of the oxidizing compound would already react with the barrier cell layer on the way. This, in turn, means that the EC_{50} value for MDCK-II cells probably was not reached at all and could explain why no considerable cell reaction was observed. In the second IDE sensor array measurement, the concentration was increased fourfold so that after the inevitable dilution step, a maximum of 500 µM could reach the sensor cell layer which, on the other hand, meant that the barrier cell layer was exposed to 2 mM of tBHP. This might be one part of the reason why there was no significant retardation to be observed. The other part could be that higher concentrations of tBHP induce oxidative stress and eventually apoptosis in living cells regardless of the barrier properties. Nevertheless, the order of response was counterintuitive as the sensor cells growing beneath the tight epithelial cells were the first to

respond and the ones growing beneath an empty filter insert the last. The reason for this phenomenon might be attributed to the formation of reactive oxygen species (ROS) and toxic metabolites in the additional cell barrier. The degradation of tBHP in living cells can be achieved according to two main pathways: (i) using the heme-containing enzyme cytochrome P450 or (ii) the enzyme glutathione peroxidase[93]. Byproducts from the first pathway include alkoxyl and peroxyl radicals causing lipid peroxidation and the formation of reactive aldehyde species[94]. The second pathway consists in the two-electron reduction of tBHP to the tertiary alcohol and can lead to a depletion of glutathione[95]. The formation of these reactive species from both pathways and the oxidizing potential of tBHP itself could explain the counterintuitive order of response by the sensor cells. However, the extent of these differences was moderate and the two experiments with 500 µM and 2 mM clearly showed that a concentration below the EC_{50} value of this oxidizing substance is tolerable for the cells and a concentration above the EC_{50} value is highly toxic, regardless of the biological barrier. The aforementioned experiments were complemented with the results from the stacked permeable supports with confluent MDCK cell layers (**Fig. 58**). The oxidizing reagent tBHP was added to the right-hand compartment next to cell layer (**I**) which – together with cell layer (**II**) – was the first to respond. In the initial dip, no time delay between the two cell layers could be observed; however, the following recuperation and subsequent decrease in impedance was much faster for the MDCK-II cells as was already observed in the ECIS® measurements. Judging by the time final impedance values were reached, cell layers (**I**) and (**II**) could clearly be distinguished from each other by the 2-h time lapse. The distinction was even clearer when taking into account that an additional cell barrier did not alter the response time. The cell layers (**III**) and (**IV**) on the adjacent permeable support again did not show a response within the time frame of the measurement which was probably due to the large diffusion distance and the limited stability of tBHP in the presence of culture medium proteins[96]. Another interesting observation was the corresponding change of the capacitance. The capacitance of the MDCK-II cell layer (**I**) started to increase after approximately 4 h which was rather observed for MDCK-I cells in the ECIS® experiments. However, a direct comparison was difficult as the cell response often varies with the porosity of the substrate. The capacitance of the MDCK-I cell layer (**II**) growing on the opposite side of the same permeable support was stable even for 6 h before increasing twofold before the measurement was stopped, which in the corresponding ECIS® experiment, would resemble a concentration of 50 µM in the response time and the overall effect. If this specific response profile was caused by the reactive oxygen species which were formed in the MDCK-II cell layer or because the cell

134

response was divergent because of the different substrate porosity remains to be elucidated. In summary, a response-profile was obtained by the three-dimensional tissue model which in kinetics and shape closely resembled the ECIS® "gold standard". A time delay was observed between the MDCK-II cell layer in direct contact with the tBHP and the MDCK-I cell layer on the opposite side of the permeable support. It is the subject of a continuing research whether this time delay was caused solely by the difference in cell type or due to the different factors, e.g. diffusion of tBHP across the porous substrate and the additional cell barrier in between.

V.3.3   Evaluation of the Measurement Setup

The development of the construction set tissue model yielded a fully functional way of monitoring the presence of living cells on each side of two permeable supports. Four confluent cell layers were successfully grown to the front and reverse sides with the possibility of extending the concept further to more cell layers. A comparison of the frequency-resolved spectra for different cell types allowed for an unequivocal distinction between the cell lines according to the characteristic shape of the *Bode plots*. Due to the coplanar electrode layout, the long-established ECIS® model could be applied which yielded cell type-related parameters that compared well with the ones found in literature. Furthermore, time-resolved cell response profiles confirmed (i) the possibility of an independent readout of every single cell layer and (ii) the experimental access to characteristic cell response profiles upon stimulation with selected stimuli. Thus, the kinetics of the cell response to the addition of cytochalasin D and tert-butyl hydroperoxide not only resembled the ones obtained in ECIS® control measurements, but were also confirmed in an independent control measurement using the *cellZscope2* (compare **Fig. 74** in the supplementary information) in which the transepithelial electrical resistance (TER) of the two MDCK strains was measured during the addition of CytD and tBHP. The device determines the TER value of a cell layer grown in Transwell® filter inserts which is sandwiched between a stainless steel bottom electrode and a stainless steel dipping electrode. In addition to the TER value – which yields information on the barrier properties – the *cellZscope2* also calculates the cell layer capacitance (C_{cl}) which describes the serial connection of the apical and the basolateral cell membrane and therefore the capacitance of the entire cell layer. The two model substances were added in the same concentrations which were also used for experiments using stacked

permeable supports (5 µM for CytD and 500 µM for tBHP). The substances were added to the apical compartment of MDCK-II-equipped Transwell® filter inserts and to the basolateral compartment if the inserts were supporting MDCK-I cells. This way, a direct addition to the culture medium surrounding MDCK-II cells was achieved as was also the case in the measurement chamber holding the two permeable supports. In the case of MDCK-I cells, the addition of the model substances to the basolateral compartment mimicked the conditions in the measurement chamber where diffusion through the polycarbonate membrane needed to occur in order to reach the cell layer. The measurement in **Fig. 74** shows the normalized TER (**A**) as well as the normalized C_{cl} (**B**) and confirmed the main observations from the experiments with the novel three-dimensional tissue model:

(i)   The cell reaction in the presence of CytD occurred faster than in the presence of tBHP; it lacked the interim recuperation but yielded similar final impedance values for the cell layer (**I**).

(ii)   The total change in capacitance was significantly larger after tBHP was added compared to the CytD-induced capacitance change. This suggested that in the presence of CytD, a cell layer was still present on the porous support and only the cell-cell contacts had been affected, whereas in the presence of tBHP, the cells had been killed and left the electrode surface cell-free.

(iii)   The concentrations of the two model substances – CytD and tBHP – were not high enough to trigger a cell reaction of the cell layers on the second permeable support. The distance between the two permeable supports would need to be shorter in order to obtain a cell signal due to shorter diffusion times and limited diffusion effects.

The comparison of the four experimental setups – ECIS® arrays, IDE sensor arrays, Transwell® filter inserts in the *cellZscope* and the novel three-dimensional tissue model – have shown that the response profiles for MDCK cells upon the direct stimulation with cytochalasin D and tert-butyl hydroperoxide were similar on impermeable and porous substrates alike. However, differences occurred if an additional barrier cell layer was located in between the location of the sensor cells and the position the model analyte was added. The main differences were observed in the delayed response profiles as well as a lower signal change of the capacitance. This arrangement with an additional barrier cell layer was only possible using the IDE sensor arrays and the stacked permeable supports with the latter additionally offering the clear advantage of the simultaneous monitoring of the barrier cell layer.

Thus, the three-dimensional tissue model using the stacked permeable supports in the measurement chamber combined all the positive individual aspects of the multiple measurement techniques:

(i)   the application possibility of the ECIS$^®$ model due to the coplanar electrode layout,

(ii)   a porous substrate for physiological cell (co)culture,

(iii)   the possibility of simultaneously monitoring the barrier cell layers,

(iv)   adjustable distances between the permeable supports due to the interchangeable parts of the measurement chamber,

(v)   the potential to incorporate more than two permeable supports.

All this proved that the stackable permeable supports help to provide interesting insights into the response of multiple cell layers to the addition of certain drugs and constitute a valuable measurement tool as neither of the other measurement techniques and setups is able to individually quantify the reaction of more than one cell layer.

V.3.4   Outlook

This three-dimensional construction set tissue model has been proven to constitute a valuable tool for investigating the individual responses of multiple stacked cell layers. So far however, none of the model substances provoked a cell response of the cell layers growing on the next permeable support within the nine hours of measurement time. In the current experimental setup, the distance between the two permeable supports was set to 7 mm due to the dimensions of the U-shaped measurement chamber segments. In future investigations this distance should therefore ideally be reduced to 1 mm to avoid a lack of response due to prolonged diffusion distances and consequently diffusion times. Furthermore, additional time-dependent cell response monitorings with multiple cell layers of only one cell type could shed some light on the unanswered questions from the previous chapter: this way a lower signal amplitude and a longer delay in the initial reaction are to be expected for cell layers which are placed further way from the location of the addition and thus deeper inside the tissue model. Decreasing concentrations due to dilution and the protection of the barrier cell layers in between could then clearly be separated from dissimilarities due to cell type differences.

The cell types tested within the scope of this thesis so far were limited to two epithelial and one epithelial-like cell type. The variety of cell types could be expanded to include not only epithelial, but also endothelial and muscle or nerve cells. This way, a general co-culture cell characterization according to adhesion, proliferation, migration and micromotion studies could be performed. Apart from the general cell characterization, this novel tissue model could also help to discover potential side effects of Covid-19 drugs like remdesivir, tocilizumab or dexamethasone which cannot be observed in conventional preclinical *in vitro* testing as they possibly emerge due to metabolic products of the drugs. Thus, the first cell layers could consist of epithelial lung cells which are affected most by the disease and for the deeper cell layers, heart cells would be a suitable model as heart problems are a frequent complication with SARS-CoV-2 medication. This way, a minimalistic body on a chip could be created as the first permeable support would hold the lung cells and the second permeable support would carry the heart cells. The culture medium in between the two permeable supports would then mimic the bloodstream with the dissolved degradation products of the SARS-CoV-2 drugs.

In the objectives part, a flow chamber holding multiple permeable supports was envisioned. This could be achieved with the current measurement chamber by drilling an inlet and an outlet into the side walls of each U-shaped segment. A flow of medium could this way be applied in all of the compartments or just in selected ones to ensure constant concentrations of a substance of interest. The cultivation chamber could similarly be modified to hold one permeable support in a horizontal orientation in order to apply a stream of gas or smoke and thus to limit the exposition to one of the compartments and to confine the vapors in an enclosed space. This way the toxicity of cigarette smoke or exhaust fumes could be investigated using the present model with only minimal changes.

Further down the road and beyond this project, the sensoric elements used for impedimetric sensing could also be complemented with sensors for detecting oxygen consumption, extracellular acidification and many more.

V.4 Laser-Scribed Graphene (LSG) as an Alternative Electrode Material

Parts of this chapter were adapted from the publication "Laser-scribed graphene (LSG) as new electrode material for impedance-based cellular assays" by P. Pütz, A. Behrent, A.J. Bäumner and J. Wegener as published 2020 in Sensors and Actuators B: Chemical.

In the time-resolved, non-invasive and label-free ECIS® technology (III.1.2), thin coplanar gold electrodes have been the "gold standard" for more than 30 years. This standard electrode material appeals with excellent biocompatibility, facile and rapid lithographic electrode patterning and high conductivity. Since the inception of ECIS®, it has become established to describe the interface impedance between the gold electrode and the electrolyte by a constant phase element (CPE) to account for the non-ideality of the capacitive behavior when immersed in cell culture medium or other physiological buffers[97]. The corresponding interface capacitance of planar gold electrodes ranges between 10 µF and 20 µF according to literature[98] and is therefore significantly lower than expected due to the rapid but stable chemisorption of the amino acid cysteine to the gold surface. The monomolecular cysteine layer comes with multiple advantages: (i) it increases the hydrophilicity of gold, (ii) it ensures rapid and reproducible cell adhesion and (iii) it leads to stable and consistent interface impedance. However, there is the other side of the equation for using gold as electrode material. As previously described in chapter III.1.2 and shown in **Fig. 4**, the interface impedance of the electrode is fixed and largely determines the sensitivity of the measurement setup as it is connected in series to the cells. Consequently, as long as gold is used as electrode material, the electrode-electrolyte interface is inevitably exhibiting a high interface impedance and a correspondingly low interface capacitance. At any given frequency the cell contribution to the overall signal can be increased by lowering the impedance of the electrode itself. Ever since ECIS® was invented, substitutes for gold as electrode material have been investigated. Reported alternative electrode materials range from precious metals like palladium[99], titanium[100] and platinum[101] over optically transparent indium-tin oxide[102] to conducting polymers[103]. Advantages of these materials include high optical transparency and therefore they are ideally suited for microscopic studies or the compatibility with printing processes which enables rapid prototyping. But so far the electrical properties of the alternative electrode materials did not outperform gold as the standard material and oftentimes the interface impedance was even higher than the one for gold.

In this context a promising alternative electrode material was investigated which is called laser-scribed graphene (LSG) and in literature it is also sometimes denoted as laser-induced graphene (LIG)[104,105]. LSG, as the name already implies, is a graphene-like material which can be generated by laser-induced carbonization of the commercially available precursor material Kapton®. There exists a variety of portable laser cutting platforms which allow for comfortable, convenient and accurate electrode generation directly in the lab. LSG appears to be perfectly suited for cell monitoring, as it exhibits significantly lower interface impedance compared to gold. Moreover, LSG fulfills another prerequisite to be able to compete with gold as electrode material namely the compatibility with roll-to-roll mass production[105].

V.4.1   Material Characterization

The novel electrode material LSG was characterized by scanning electron microscopy (**Fig. 59**), attenuated total reflection Fourier transform infrared spectroscopy (**Fig. 60A**) as well as Raman spectroscopy (**Fig. 60B**). Additionally, a cyclic voltammogram was recorded with LSG serving as working and counter electrode material and potassium ferrocyanide as redox probe (**Fig. 60C**).
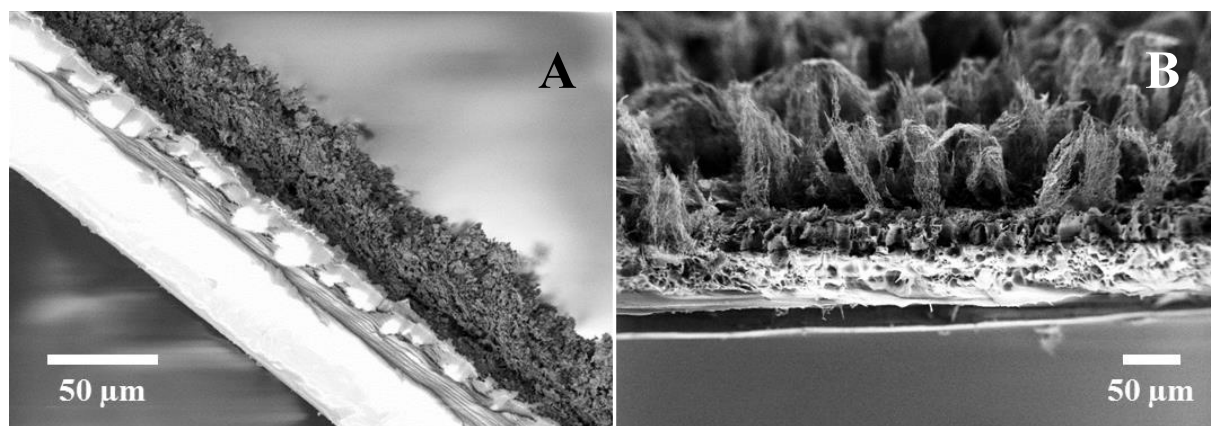

Fig. 59: Cross sectional scanning electron microscopy images of LSG electrodes on their Kapton® base substrate. (**A**) shows an overview image from which a 50-µm height of the carbonized layer can be estimated (1000x magnification) and (**B**) shows a high resolution picture of the foam-like LSG surface topography that is facing the electrolyte solution when used in electrochemical experiments (500x magnification). Pictures were recorded by Dr. Marcel Simsek under the supervision of Prof. Antje Bäumner. Scale bars depict 50 µm.

Surface carbonization of the polyimide Kapton® precursor foil by laser irradiation yielded conductive LSG films in a height of approximately 50 µm with their characteristic, foam-like topography as shown in the SEM micrographs (**Fig. 59**). This rough surface topography is

well-known and the structural basis for the potential use of LSG as in-plane micro-supercapacitors[104]. It has been the reason to consider LSG as electrode material for cell-based biosensing as this topography may overcome the limits of gold and other materials with respect to interface capacitance. Pioneering work has been contributed by others who optimized engraving results and corresponding LSG surface topography with respect to experimental settings during laser-induced carbonization[106,107].
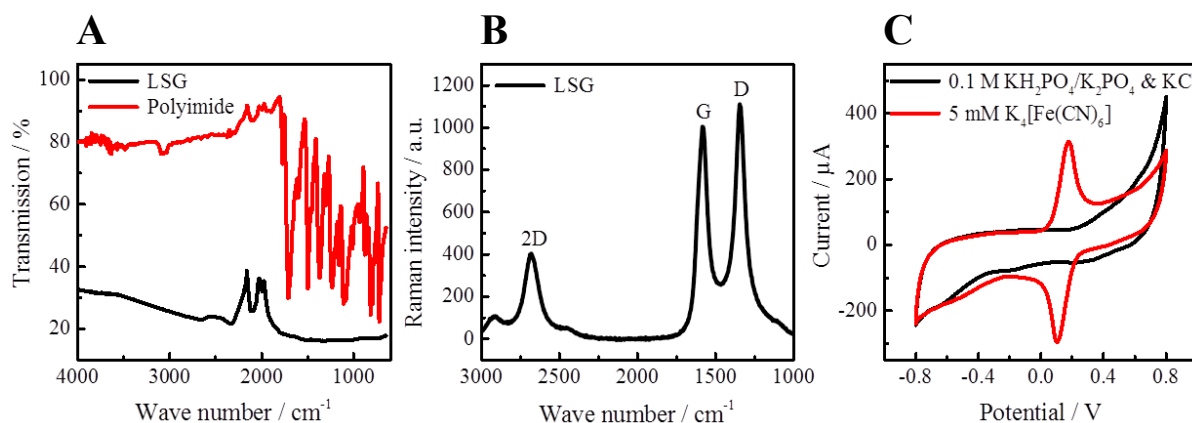

Fig. 60: (**A**) ATR Fourier transform infrared spectrum of the precursor material Kapton® and the carbonized graphene. The typical polyimide fingerprint pattern between 600 – 1800 cm^{-1} disappears after the carbonization process. (**B**) Raman spectrum of the LSG material. Intensity ratio of the 2D- and G-peak indicates multilayers of graphene, the D-peak reveals defects and distortions within the sp^2-carbon lattice. (**C**) Cyclic voltammogram of potassium ferrocyanide using a three-electrode measurement setup with the working and counter electrode made from LSG and an Ag/AgCl reference electrode. Peak potential separation is 75.5 mV. Measurements have been performed by Arne Behrent under the supervision of Prof. A. Bäumner.

Attenuated total reflection Fourier transform infrared spectroscopy (ATR-FTIR) of the LSG films (**Fig. 60A**) revealed the complete loss of the polyimide fingerprint bands at wave-numbers below 1800 cm^{-1} which were clearly present when the untreated polyimide films had been studied the same way. Accordingly, most of the transparent polyimide has been transformed to the black LSG in the areas exposed to the carbonizing laser beam.

The Raman spectrum (**Fig. 60B**) showed three major peaks (2D, G, D) as it has been described by others for LSG[105]. The co-presence of the G and the 2D-peak indicated the formation of multiple graphene layers. Amorphous or glassy carbon would not have shown the 2D Raman peak. However, the higher intensity of the G-peak relative to the intensity of the 2D peak in combination with the presence of the D-peak (indicator for defects or bent sp^2-carbons) characterized the LSG after the laser-induced carbonization as multi-layer, foamy graphene with a significant amount of defects. Other authors have described similar characteristics for LSG[104].

142

The general suitability of LSG as electrode material in aqueous solution was tested with a 3-electrode cyclic voltammetry measurement (**Fig. 60C**). The working and counter electrodes were made from LSG and an Ag/AgCl reference electrode was used. A KH_2PO_4/K_2HPO_4 (0.1 M) / KCl (0.1 M) buffer at pH 7.4 was measured with and without $K_4[Fe(CN)_6]$ (5 mM) as redox marker. The cyclic voltammogram yielded a separation of the anodic and cathodic peak potential of 75.5 mV. This low peak-to-peak separation of the ferrocyanide/ferricyanide redox couple on the LSG electrode material (at a scan rate of 100 mV/s) indicated easy electron transfer.

The sheet resistance of the LSG films was determined by four-probe conductance measurements to be $10 - 15$ Ω/square compared to 1 Ω/square for gold-films as used in this thesis. This plays an important role for the lead resistance of the electrodes and will be discussed in detail in the next chapter.

Cell staining experiments were conducted to investigate the compatibility of LSG electrodes for cell growth on their surfaces. Cell adhesion and proliferation on the electrode surface naturally is an unconditional prerequisite for the use of LSG as transducer in cell-based assays. LSG surfaces have been characterized before as non-adhesive for *bacterial* cells and not supportive for *bacterial* cell growth[108]. This phenomenon was readily explained by entrapment and confinement of *bacterial* cells in the porous structure of LSG and the incompatibility of hydrophilic surfaces to promote *bacterial* cell adhesion. It is noteworthy that animal cells are too large to enter the porous LSG network and require hydrophilic surfaces for cell adhesion. The presence of confluent cell layers on the LSG electrodes was verified by staining the actin cytoskeleton and the cell nuclei (**Fig. 61A & B**) as well as a viability cell staining with subsequent z-stack CLSM imaging (**Fig. 61C**).
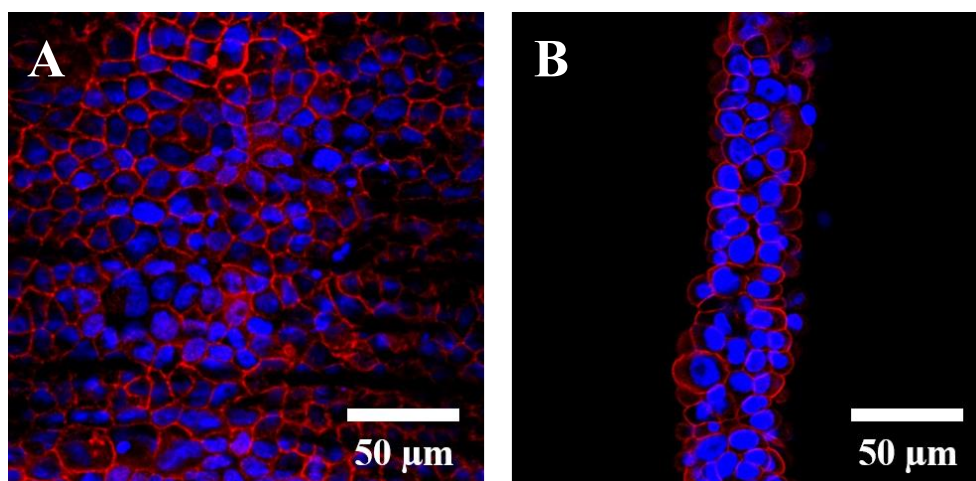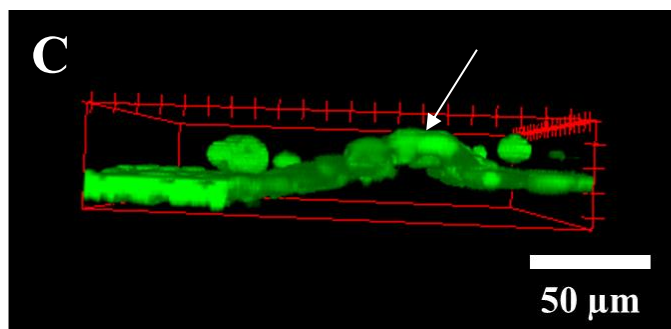
Fig. 61: CLSM images of living cells growing on LSG electrodes. (**A**) Phalloidin- and DAPI-stained MDCK-II cells growing centrally on an LSG electrode, (**B**) phalloidin- and DAPI-stained MDCK-II cells growing on the approx. 10-µm elevated edge of the LSG electrode and (**C**) z-stack of a Calcein-AM-stained MDCK-II cell monolayer with the LSG electrode on the left-hand side, the elevated edge of the electrode in the middle (indicated by the white arrow) and the polyimide precursor material on the right-hand side. Scale bar depicts 50 micrometers.

The microscopic analysis of the actin belt (**Fig. 61A**) with respect to the expression of a barrier-forming phenotype did not reveal significant differences once the cell monolayers were complete but confirmed excellent biocompatibility for LSG. The CLSM images also revealed a height profile of the LSG electrodes with elevated edges (compare **Fig. 61B**, where the focal plane was set to the highest point of the elevated edge), which is probably due to the thermic processes during laser scribing. The focal plane, at which **Fig. 61B** was recorded, is marked by the white arrow in the z-stack shown in **Fig. 61C**. This z-stack provides further proof that the LSG electrode and the polyimide precursor material exhibit excellent biocompatibility as MDCK-II cells were seeded to confluence on an area encompassing the LSG electrode with the elevated edge as well as the uncarbonized Kapton$^®$ membrane next to it. The confluent MDCK-II cell layer was subsequently stained with a Calcein-AM/Ethidium-HD viability staining according to chapter IV.2.6 and exclusively green fluorescence was detected, indicating only living cells. Furthermore, **Fig. 61C** shows that the surface level of the Kapton$^®$ membrane (right-hand side) is about 10 µm higher than the one of the LSG electrode (left-hand side). The reason for this is that during the LSG generation process, the precursor material is pyrolized and the initial presence of oxygen and nitrogen atoms is significantly reduced. However, the height profile including the approximately 10-µm central elevation is irrelevant for the electrochemical electrode performance and the cells attach and proliferate on all parts of the LSG electrode as well as on the Kapton$^®$ membrane as was proven by the continuous green layer of living cells spanning the entire field of view.

V.4.2   Impedance-Based Comparison between Gold and LSG

A side-by-side comparison between gold and LSG as thin-film electrodes was performed to analyze the suitability of LSG film electrodes for impedimetric monitoring of adherent animal cells with respect to the reference material gold. Therefore, the rectangular and equally-sized electrode layout from chapter IV.1.2.1.1 was generated from both materials (**Fig. 62**). The gold was sputter-coated onto Lexan® as substrate material (**A**) using a metal mask and LSG electrodes were generated from the polyimide foil Kapton® by laser carbonization (**B**). A PDMS chamber (dashed white line) was glued on the arrays to define a cell culture dish (straight white line marks the inner dimensions of the cell culture dish).
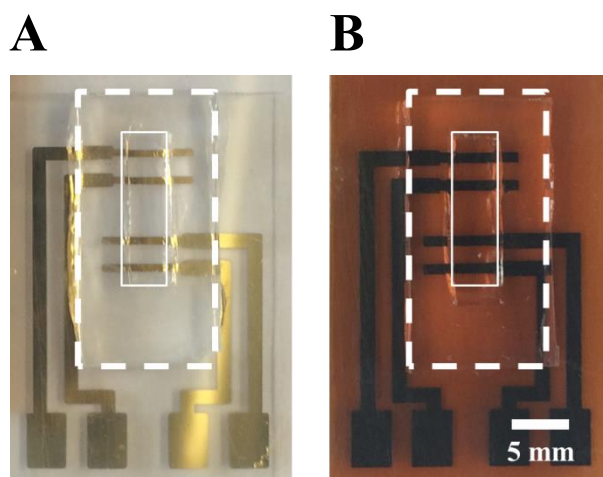

Fig. 62: Gold-films on Lexan® (**A**) and LSG on Kapton® (**B**) patterned to give the same layout of rectangular and equally-sized electrodes (compare IV.1.2.1.1). The dashed white line indicates the position of the PDMS block with a central opening (straight line) that was used to form a cell culture dish. The electrodes were connected to the impedance analyzer using the four contact pads outside the PDMS block. Scale bar depicts 5 mm.

Fig. 63A overlays the frequency-dependent electrochemical impedance magnitude |Z|(f) of cell-free electrodes prepared from LSG or gold in exactly the same electrode layout (compare **Fig. 62A** showing thin-film gold electrodes patterned on Lexan® and **Fig. 62B** LSG electrodes generated by carbonizing the Kapton® material) when immersed in cell culture medium exhibiting physiological salinity. **Fig. 63B** compares the corresponding frequency-dependent phase angle φ(f) of both electrode materials. The frequency-dependent magnitude of impedance and the corresponding phase angle are color-coded **black** for the LSG electrodes and **gold** in the case of the gold electrodes.
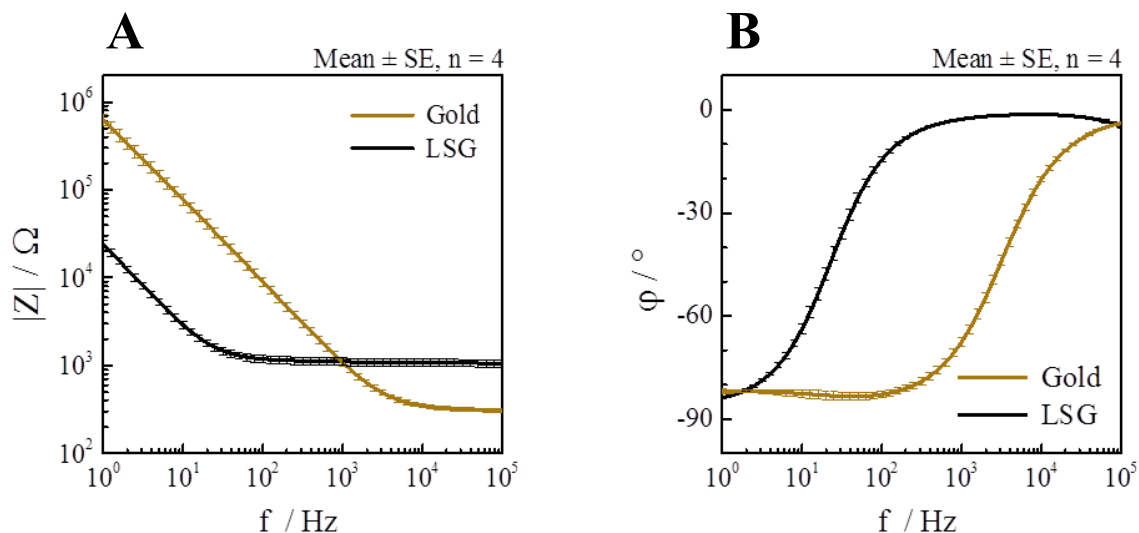
Fig. 63: (**A**) Typical impedance magnitude spectra |Z|(f) of the cell-free electrodes made from gold (**gold**) and LSG (**black**) in the rectangular and equally-sized electrode layout (chapter IV.1.2.1.1) submerged in cell culture medium. (**B**) Corresponding frequency-dependent phase angle φ(f) for the same two electrodes bathed in cell culture medium. Spectra were recorded at a temperature of 37 °C and 5 % CO_2.

Both materials in **Fig. 63A** produced the same type of impedance magnitude spectrum with a constant magnitude of impedance |Z|(f) at high frequencies and a linear decline with a slope close to (–1) for low frequencies in log-log presentation. This typical electrochemical behavior for almost ideally polarizable electrodes immersed in physiological media or buffers was shown by gold and LSG alike. LSG electrodes in principle behaved like the gold-films but the impedance magnitude spectra were shifted along the frequency and impedance axes. Specifically, at high frequencies the impedance magnitude for LSG (1100 Ω) was higher than for gold (300 Ω). This higher bulk resistance was due to the higher resistance of the LSG leads compared to gold since the bulk electrolyte was identical in both experiments. In other experiments, the higher lead resistance was significantly reduced by metallization of the leads outside of the measurement well with silver paint (compare **Fig. 75** in the supplementary information). More interestingly, the impedance magnitude spectra for LSG were shifted to lower frequencies compared to gold electrodes. Accordingly, the interface impedance of LSG electrodes was significantly smaller at any individual frequency compared to gold electrodes due to the enormous topographic surface enlargement of the LSG films. The dispersion that comes with the almost capacitive behavior of the electrode-electrolyte interface was shifted to significantly lower frequencies which can be translated into an increase in the *apparent* interface capacitance (compare CPE contribution in chapter III.1.2). For the gold electrodes an average *apparent* interface capacitance of $(18 \pm 5)\ \mu F/cm^2$ at f = 1 Hz was determined whereas the same data transformation returned a capacitance of almost $(450 \pm 80)\ \mu F/cm^2$ for

LSG. The term "apparent" acknowledges the non-ideal capacitive behavior discussed in chapter III.1.2. This 25-times larger interface capacitance for LSG confirmed that it was a potentially very attractive electrode material for impedance-based cellular assays and cell manipulation as it provided the low interface impedance and consequently high interface capacitance that otherwise limited the use and sensitivity of other electrode materials. This phenomenon was confirmed by the frequency-dependent phase angle $\varphi(f)$ of both materials (**Fig. 63B**) as at high frequencies, a shift close to 0° was measured and at low frequencies, the shift was approximately –85° (especially in the case of LSG, the phase angle began to slightly decrease again from $10^4 - 10^5$ Hz indicating parasitic capacitive behavior towards the highest frequencies). The steepest slopes in the phase angle correspond with the point in the impedance spectrum where the CPE element and the bulk resistance merge. This point oftentimes is close to the most sensitive frequency and in the case of LSG it was shifted two orders of magnitude to lower frequencies compared to the reference material gold.

The following two chapters will provide detailed proof-of-concept measurements with the LSG and gold electrodes from **Fig. 62** serving as electrode material in cell-based assays using MDCK-I and MDCK-II cells.

V.4.2.1 Frequency-Resolved Cell Analysis

In the following, moderately tight epithelial cells (MDCK-II) and very tight epithelial cells (MDCK-I) were seeded on gold and LSG electrodes in the exact same layout (dimensions are given in chapter IV.1.2.1.1 and photographs of the final electrode layout using LSG and gold as electrode material are shown in **Fig. 62**) in order to compare the frequency-dependent impedance magnitude spectra $|Z|(f)$, the normalized impedance magnitude spectra $|Z|_{norm.}(f)$, the phase angle $\varphi(f)$ and the capacitance spectra $C(f)$ with confluent MDCK cell layers growing on the surface. **Fig. 64** shows the aforementioned frequency-resolved spectra for a confluent MDCK-II cell layer on LSG electrodes (**black**) and gold electrodes (**gold**). The corresponding spectra of the same cell-free electrodes are color-coded (grey) for the LSG electrodes and (yellow) for the gold electrodes.
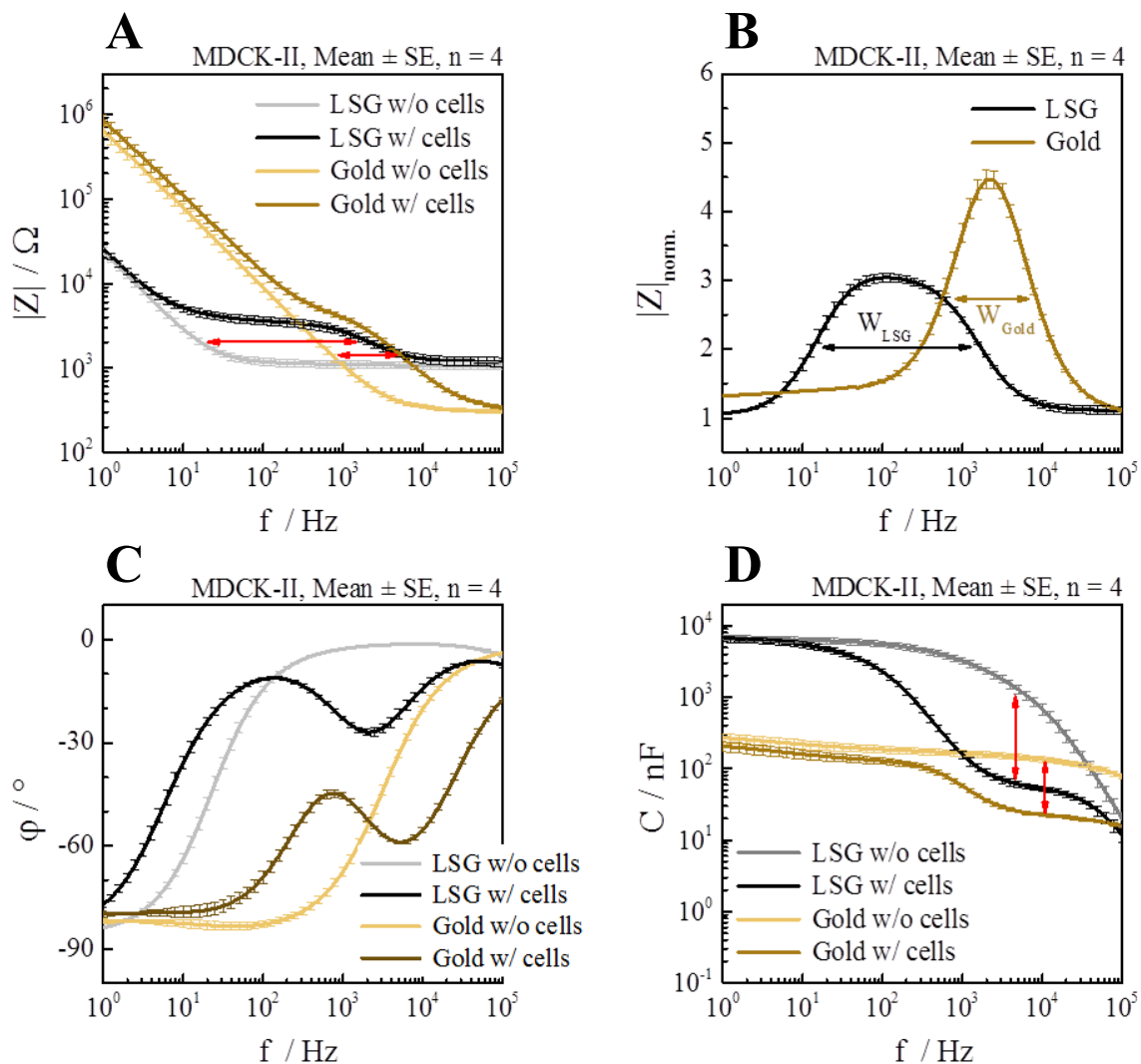
Fig. 64: (**A**) Impedance magnitude spectra |Z|(f) of the cell-free gold and LSG electrodes in comparison to the corresponding spectra with a confluent MDCK-II cell monolayer adherently grown on the electrode surface. The red arrows highlight the distance between the electrode and cell dispersion. (**B**) The impedance magnitude spectra were normalized by dividing the impedance of the cell-covered electrode by the impedance of the cell-free electrode for each frequency. The width of the bell-shaped curves indicates the frequency window available for impedance-based cell monitoring. (**C**) Frequency-dependent phase angle φ(f) for cell-free and MDCK-II cell-covered gold and LSG electrodes. (**D**) Capacitance spectra C(f) for cell-free gold and LSG electrodes in comparison to the MDCK-II cell-covered ones. The red arrows indicate the difference between the frequency-independent contribution of the CPE and the cell layer. Data was recorded 96 h after cell inoculation at T = 37 °C and 5 % CO_2.

The presence of the MDCK-II cells on both electrode materials induced a second dispersion at higher frequencies than was obtained for the electrode-electrolyte interface (**Fig. 64A**). This dispersion is due to the capacitance of the cell membranes and even without quantitative analysis it was obvious that the cell and electrode dispersion were closer together for gold electrodes in comparison to LSG. Those regions of the spectra between electrode and cell membrane dispersion represent the impedance of the cell-electrode junction as well as the impedance of the cell-cell contacts. It is therefore the most important frequency region to

monitor cell-based assays. This region was significantly broader for LSG as electrode material as indicated by the red arrows and furthermore visualized when the *normalized* impedance was calculated from (**A**) and plotted against the frequency (**Fig. 64B**). Here the impedance of the cell-covered electrode at any given frequency was divided by that of the cell-free electrode at the same frequency. Since the spectra overlapped at the high and low frequency end, the frequency dependence of the normalized impedance was bell-shaped. The bandwidth W of the curves (full width at half maximum) was approximately one order of magnitude for gold but two orders of magnitude for LSG. The bandwidth W is a direct measure for the frequency range that is useful for monitoring cell-based assays. Since (i) the sensitivity of the measurement for one given cell type correlates with the *area under the curve (AUC)* of the normalized impedance, and (ii) the AUC is proportional to the bandwidth W, this increase in bandwidth is indicative for an increase in measurement sensitivity. The fact that the spectrum for gold electrodes peaks at higher values than the spectrum for LSG electrodes is largely due to the higher lead resistance of the LSG material. The reduction of the resistance of the feed lines by metallization outside of the measurement chamber (**Fig. 75** in the supplementary information) and the use of smaller electrode areas will in general shift the peak of the normalized impedance to larger values and make the measurement even more sensitive. **Fig. 64C** shows the phase spectra φ(f) for both electrode materials with and without the confluent MDCK-II cell layer attached to the electrode surface. The emerging local minima and maxima in the spectra of the cell-covered electrodes corresponded to the capacitive influences of the cell membranes and the resistive influences of the cell-cell contacts and the cell-substrate contacts, respectively. Although the minima were only separated by a factor of two in their frequency position (2.5 kHz for LSG and 5 kHz for gold), the maxima were almost one order of magnitude apart and even without quantitative analysis, it was obvious that the peak below the maximum in the case of LSG was broader which underlined the significantly broader measurement range for this electrode material. The capacitance spectra C(f) for the cell-free and cell-covered LSG and gold electrodes are given in **Fig. 64D** and the difference is marked by the red arrows. The frequency-independent CPE contribution at low frequencies was observed as an only minimally slanted horizontal line (highlighting the near-ideal capacitive properties) and an influence of a parasitic parallel capacitance at high frequencies was observed for LSG in the falling values. From the C(f), the vast difference in the interface capacitance was seen directly at the lowest frequencies. At 1 Hz, the capacitance value for gold was 270 nF and for LSG a value of 6775 nF was determined. The ratio of the capacitances at 1 Hz of the cell-free LSG electrode to the cell-free gold electrode was almost exactly 25.

Fig. 65 shows the frequency-dependent impedance magnitude spectra |Z|(f) (**A**), the normalized impedance magnitude spectra |Z|norm.(f) (**B**), the phase angle φ(f) (**C**) and the capacitance spectra C(f) (**D**) for a confluent MDCK-I cell layer on LSG electrodes (**black**) and gold electrodes (**gold**). The corresponding spectra of the same cell-free electrodes are color-coded (**grey**) for the LSG electrodes and (**yellow**) for the gold electrodes.
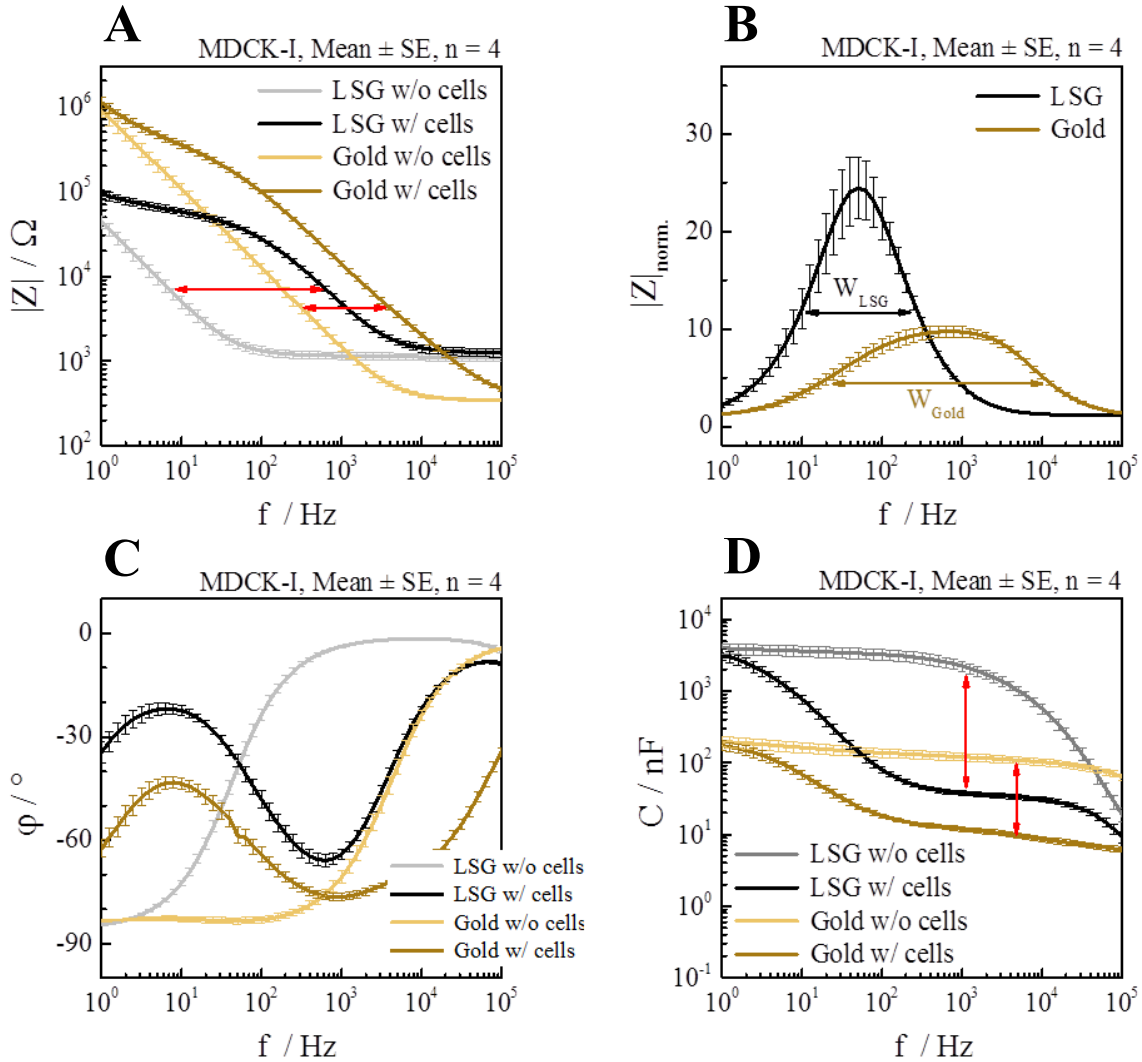
Fig. 65: (**A**) Comparison of the impedance spectra |Z|(f) of cell-free gold and LSG electrodes and the same electrodes with a confluent MDCK-I cell monolayer grown on the electrode surface. The red arrows highlight the distance between the electrode and cell dispersion. (**B**) Normalized frequency-dependent magnitude of impedance obtained by dividing the impedance magnitude of the cell-covered electrode by the impedance magnitude of the cell-free electrode for each frequency. The frequency window available for impedance-based cell monitoring is indicated by the width of the bell-shaped curves. (**C**) Comparison of the frequency-dependent phase angle φ(f) for cell-free and MDCK-I cell-covered gold and LSG electrodes. (**D**) Capacitance spectra C(f) are shown for cell-free and MDCK-I cell-covered gold and LSG electrodes. The red arrows indicate the difference between the frequency-independent contribution of the CPE and the cell layer. Data was recorded 96 h after cell inoculation at T = 37 °C and 5 % CO_2.

The presence of a confluent MDCK-I cell layer with extremely tight cell-cell contacts highlights the considerations from before. The frequency-dependent impedance spectra |Z|(f) are shown in **Fig. 65A** and the separation of the electrode-electrolyte interface and the cell membrane capacitance again is approximately one order of magnitude for the gold electrode and two orders of magnitude for the LSG electrodes as indicated by the red arrows. The spectra from (**A**) were normalized with respect to the spectrum of the cell-free electrode and afterwards plotted against the frequency in **Fig. 65B**. From this normalized representation, it became obvious that the regions of the spectra between electrode and cell membrane dispersion were so close together in the case of the gold electrode (indicated by the red arrows in the impedance magnitude spectra) that over a broad frequency range (200 – 2000 Hz) the normalized impedance magnitude value was limited to approximately nine. In the case of the LSG electrode, the dispersions were separated so much that a perfectly Gaussian-like normalized impedance magnitude spectrum was obtained with a maximum value of 24.4 at a frequency of 50 Hz. Thus, the sensitivity for the tight epithelial MDCK-I cells was almost three times higher for LSG in comparison to gold. The phase angle φ(f) (**Fig. 65C**) confirmed the ample separation of the electrode and cell membrane dispersion in the case of LSG as the local minimum in the phase spectrum of the cell-covered LSG electrode (cell membrane contribution) was found around 1 kHz and the constantly low phase shift for the cell-free LSG electrode (electrode-electrolyte interface) below 5 Hz. This could be translated into a separation of more than two orders of magnitude. For the gold electrode, this separation only amounted to one order of magnitude. The capacitance spectra C(f) in **Fig. 65D** indicated a twentyfold higher interface capacitance for the LSG electrode compared to the gold electrode and also reflected the larger difference between the cell-free and the cell-covered LSG electrodes in comparison to the gold one (the difference between the capacitive contribution of the CPE element and the cell layer is marked by the red arrows).

V.4.2.2   Time-Resolved Cell Analysis

The strength of impedance-based cell monitoring is the ability to follow the cell behavior continuously and to extract dynamic aspects of their behavior. Therefore, the time needed to establish a confluent cell monolayer on both electrode materials was observed for MDCK-I (M1) and MDCK-II (M2) cells in the full frequency range from 1 Hz to 1 MHz. The resulting 3D plots representing the frequency- and time-dependent magnitude of impedance |Z|(f, t) are given in **Fig. 66** for the moderately tight M2 cells and in **Fig. 67** for the tight M1 cells.
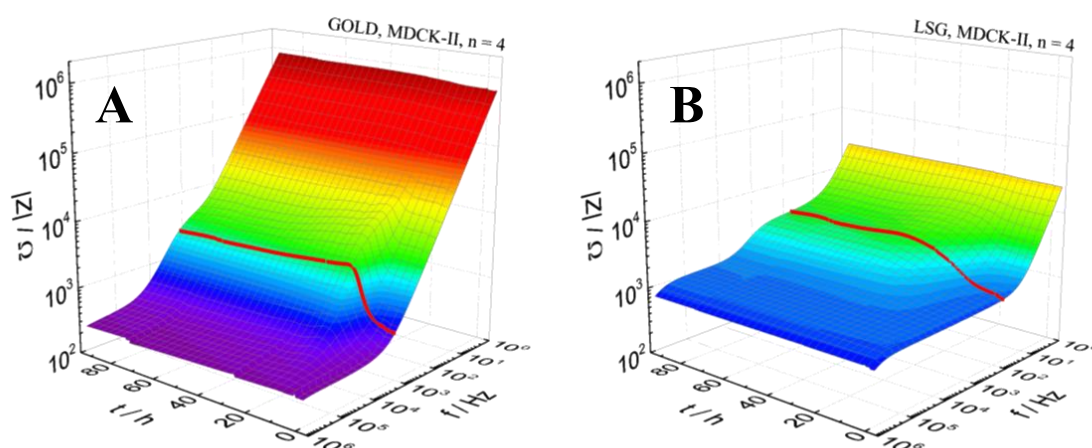
Fig. 66: Time- and frequency-dependent impedance magnitude during the attachment, spreading and differentiation of initially suspended M2 cells on gold electrodes (**A**) and LSG electrodes (**B**). The mean absolute magnitude of impedance from four measurements is shown without the standard error and the time courses at the most sensitive frequencies are marked in red (2 kHz and 100 Hz for gold and LSG, respectively). Seeding density was $5 \cdot 10^5$ c/cm^2 in culture medium and the measurement conducted in a standard cell incubator at 37 °C and 5 % CO_2. Cells were supplemented with fresh culture medium 24 h and 72 h after inoculation (t = 0 h).

Cell inoculation was performed at t = 0 h at which point the spectrum of a still cell-free electrode was obtained with a bulk resistance of 300 Ω in the case of the gold electrodes (**A**) and 1100 Ω for the LSG electrodes (**B**). The CPE contribution at 1 Hz was significantly higher for gold (0.6 MΩ) compared to LSG (24 kΩ) as was already discussed in the previous chapter. In the direct comparison, the significantly larger frequency range in which the cell signal could be monitored on LSG compared to gold became obvious. This fact also demonstrated that the most sensitive frequencies differed between the two materials with f_{sens} = 2 kHz for the gold electrodes and f_{sens} = 100 Hz for the LSG electrodes. The time-dependent adhesion profile at the most sensitive frequencies exhibited a very similar shape by first reaching a maximum value in the impedance signal before decreasing again and stabilizing after approximately three days of adhesion time. However, the time needed to form a complete and mature M2 cell monolayer (initial maximum in the impedance signal) required 16 h on gold-film electrodes compared to 40 h on the LSG electrodes (the time courses at the most sensitive frequencies for both materials are highlighted in red). Thus, cell layer formation was significantly retarded on LSG. The longer times needed to establish a confluent cell monolayer were probably due to the large and rough surface area of LSG. The foam-like structure likely made it harder for the cells to adhere and establish the cell-cell contacts[109]. However, the R_b values quantifying the tightness of cell-cell contacts were similar for M2 cells with (34 ± 6) Ω·cm^2 on gold and (27 ± 6) Ω·cm^2 on LSG. The assumption that the rough surface topography influences the time needed to establish a fully differentiated cell

monolayer could also be reinforced by the parallel adhesion, spreading and differentiation process of M1 cells on the LSG and the gold material which is shown in **Fig. 67**.
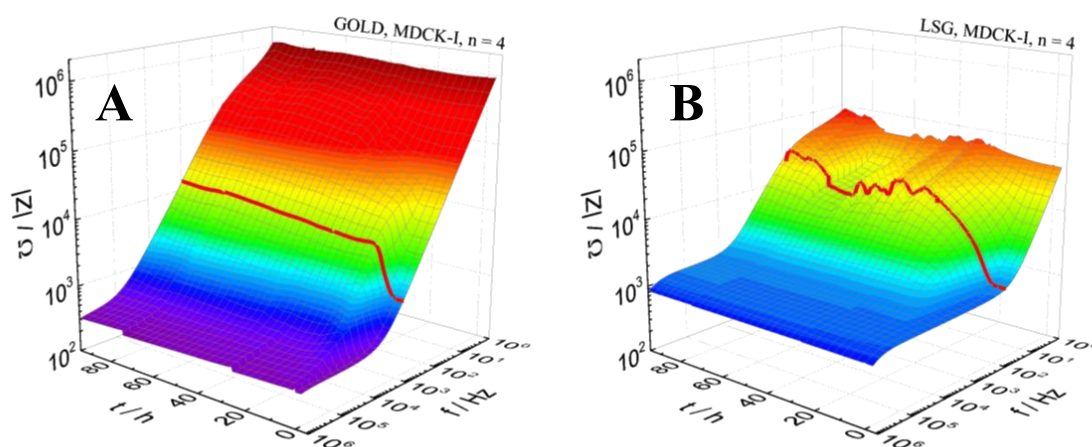

Fig. 67: Time- and frequency-dependent impedance magnitude during M1 cell attachment, spreading and differentiation on gold electrodes (**A**) and LSG electrodes (**B**). The averaged absolute magnitude of impedance from four measurements is shown without the standard error and the time courses at the most sensitive frequencies are marked in red (1 kHz and 80 Hz for gold and LSG, respectively). Seeding density was $5 \cdot 10^5$ c/cm^2 in culture medium which was exchanged 24 h and 72 h after inoculation (t = 0 h). The measurement was conducted in a standard cell incubator at 37 °C and 5 % CO_2.

The spectra of the cell-free electrodes at t = 0 h in **Fig. 67** were similar to the ones from the previous measurement (compare **Fig. 66**). The 3D surface plots confirm the observations from before that the frequency region between the dispersion of the electrode-electrolyte interface and the one of the cells is smaller for the gold electrodes (**A**) in comparison to the LSG electrodes (**B**). In contrast to the M2 cell adhesion, the time needed to form a complete and mature M1 cell monolayer took approximately 35 h on the gold electrodes, which is in good agreement with the adhesion measurements of M1 cells on 8W10E ECIS® arrays (compare chapter V.3.2.1.1). In the case of the LSG electrodes, the determination of a clear time point for the establishment of a mature M1 cell layer was difficult as the impedance signal was highly fluctuating. These fluctuations were much stronger during M1 cell adhesion compared to M2 cell adhesion. Presumably, the reason for the dynamic movement of the cells lay in the rough topography which challenged the cells with respect to making specific contacts to the electrode surface or aligning relative to each other to form cell-cell junctions. For M1 cells with their higher cell-cell contact expression rate, this rough surface proved to be even more challenging. In contrast to the experiments with M2 cells, the R_b values for M1 cells were deviating from each other on the different electrode materials. An R_b value of only (396 ± 97) $\Omega \cdot cm^2$ was determined for M1 cells on LSG after 96 h of adhesion time and a significantly larger value of (1765 ± 497) $\Omega \cdot cm^2$ for M1 cells after 96 h of adhesion time on

the gold electrode. Microscopic analysis of the actin belt (compare **Fig. 61**) and in-depth impedance analysis with respect to the expression of a barrier-forming phenotype did not reveal significant differences once the cell monolayers were complete, apart from the substantial difference in the R_b values for M1 cells. The parameter α, yielding information on the cell-substrate contacts, was also similar in the case of M2 cells at $(9 \pm 1)\,\Omega^{0.5}{\cdot}cm$ and $(7 \pm 2)\,\Omega^{0.5}{\cdot}cm$ for the materials LSG and gold, respectively, and correspondingly higher for M1 cells on gold at $(93 \pm 8)\,\Omega^{0.5}{\cdot}cm$ compared to M1 cells on LSG at $(56 \pm 11)\,\Omega^{0.5}{\cdot}cm$. C_m values were always twice as high on LSG at $(6.4 \pm 0.4)\,\mu F{\cdot}cm^{-2}$ (M1) and $(8 \pm 1)\,\mu F{\cdot}cm^{-2}$ (M2) compared to $(3.02 \pm 0.01)\,\mu F{\cdot}cm^{-2}$ (M1) and $(4.0 \pm 0.4)\,\mu F{\cdot}cm^{-2}$ (M2) on gold. Thus, different cell behavior on the two materials was largely limited to the dynamics of the cell layer formation and only in the case of the very tight cells affected the final phenotype.

V.4.3   LSG as Bipolar Electrodes in Cell-Based Assays

Apart from the interesting properties of laser-scribed graphene with respect to the large surface area, the material is a promising candidate for another field of application: bipolar electrodes. Bipolar electrodes were established by Christian Götz during his PhD thesis under the supervision of Prof. Dr. Joachim Wegener and have been patented. The principle is the following: instead of using two individual coplanar electrodes, the anode and the cathode are connected via a high-resistance connecting line providing a single but bipolar electrode. The conductive electrode connection needs to exhibit sufficiently high resistance in order to prevent the formation of short circuits. The application of an AC voltage entails a potential gradient along the length of the electrode and a coupling of the electrical current with the electrolyte (see **Fig. 68C**). As the potential gradually decreases along the length of the electrode, this feature is highly advantageous in the electroporation and wounding process of living cells growing on the electrodes. In a conventional coplanar two-electrode electroporation/wounding setup, the optimization of the parameters, e.g. number of pulses and pulse duration and amplitude is a time-consuming process which can be substantially shortened by using bipolar electrodes as, due to the potential gradient, the amplitude dependence can be tested at once. Christian Götz performed extensive studies during his PhD thesis with respect to the minimization of the width W of the line-shaped bipolar electrode, the maximization of the electrode length and a general characterization of the bipolar electrodes including a comparison with ECIS® electrodes. Initially, very thin gold films in a thickness of 20 nm were used as material for the line-shaped bipolar electrodes but were later substituted by

154

transparent indium tin oxide (ITO) due to the approximately fourfold higher material resistance in the same layout. The appeal of using LSG as electrode material in bipolar electrodes lies in (i) the high intrinsic resistance which in conventional impedance spectroscopy was attempted to be reduced by metallization of the leads, (ii) the advantage of rapid prototyping as the preparation steps PVD and photolithography are replaced by comfortable laser scribing, (iii) the possibility to generate finer and more reproducible electrode structures due to limited precision of the photolithography wet etching process below 500 μm and (iv) significantly lower costs and less waste production because of the efficient carbonization of the precursor material polyimide. In this thesis, the applicability of LSG as electrode material in bipolar electrodes was investigated and a dimensioned drawing of the electrode layout is shown in **Fig. 68A**. A zoom-in of the topmost part of the line-shaped bipolar electrode is depicted in **Fig. 68B**. The distance between the two contact pads and consequently also between the high-resistance connection was always set to 1 mm and the width of the line-shaped bipolar electrode was varied. The working principle is shown in **Fig. 68C**.
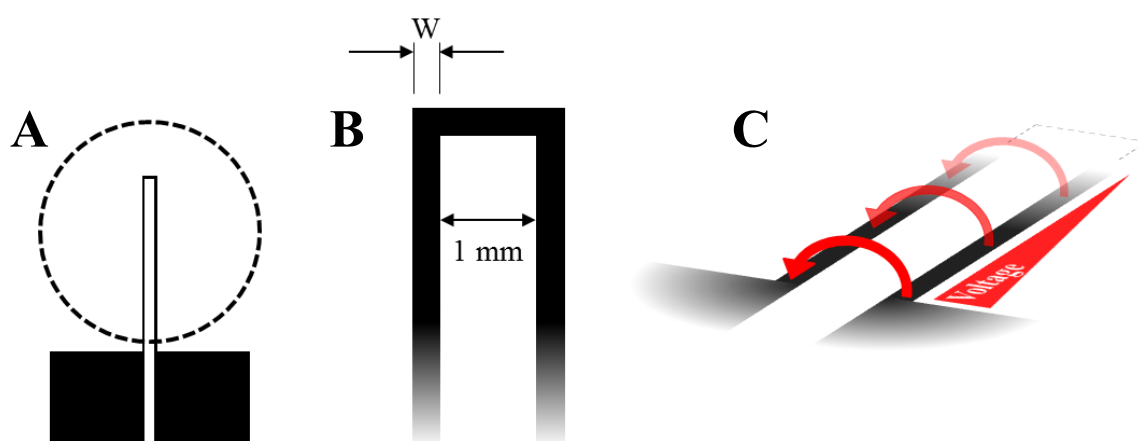

Fig. 68: Overview of bipolar electrodes: (**A**) shows a dimensioned drawing of a bipolar electrode where two contact pads are connected via a 300-μm-thick high-resistance conduction line. The dashed line indicates a glass ring serving as cell culture dish. (**B**) Depiction of a zoom-in of the topmost part of the electrode. The distance between the two contact pads was set to 1 mm and the width W of the bipolar electrode was systematically varied. (**C**) Working principle of a bipolar electrode: due to the high-resistance bipolar electrode, the application of an AC voltage entails a potential gradient along the electrode and, if the resistance is chosen high enough, a current flow across the electrolyte (red arrows) which decreases along the path.

The spectra for the MDCK cell-covered bipolar electrode layout from **Fig. 68A** with differing width W of the bipolar electrode were simulated with a LabVIEW^TM software written by Prof. Dr. Wegener (University of Regensburg) to determine the optimal layout geometry (see chapter V.4.3.1). The resulting best geometry was then employed to detect the presence of a confluent cell monolayer of MDCK-I and MDCK-II cells (compare chapter V.4.3.2).

V.4.3.1   Influence of Electrode Geometry on the Impedance Spectrum

The simulation of the MDCK cell-covered bipolar electrode layout was performed with the LabVIEW[TM] software ECIS-simulation-2017-V2-0. The cell-related parameters were chosen as published by Reiss et al. (2015)[67] for MDCK-I and MDCK-II cells. In order to get an idea about the parameter $R_{||}$ – which is the resistance of the bare thin-film electrode connected in parallel to the CPE element and the bulk resistance – the bipolar electrode layout from **Fig. 68A** was scribed for five different line widths from 200 μm to 2 mm. The five layouts were measured in absence of cells and the experimental data from the measurement of the cell-free electrodes (see **Fig. 76** in the supplementary information) were afterwards used to simulate the cell-covered bipolar LSG electrodes. The resulting simulated impedance spectra $|Z|$(f) are shown in **Fig. 69A-E**. The spectra in **Fig. 69F** were included as simulated reference spectra for MDCK cells growing on LSG in the unipolar REE layout from chapter V.4.2.
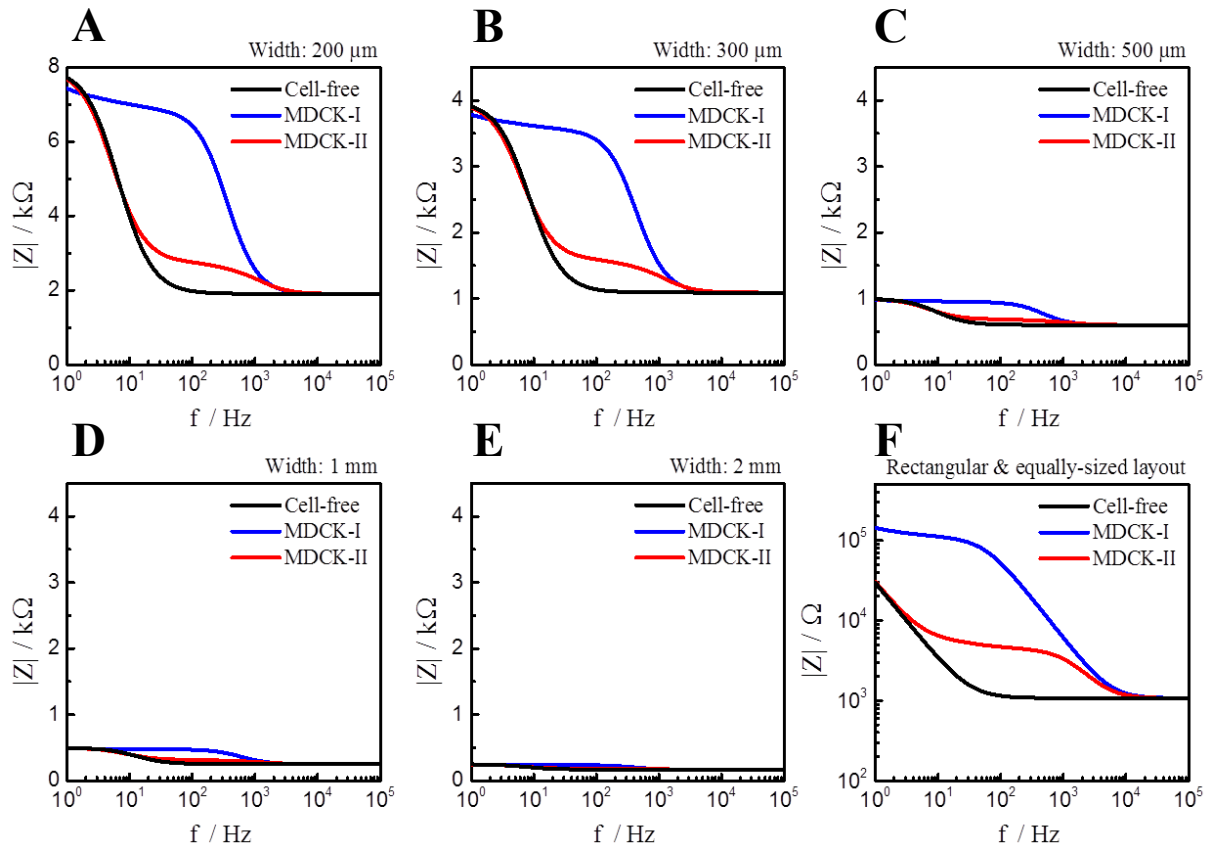
Fig. 69: Simulation of bipolar LSG electrodes with different electrode widths in semi-log presentation. The distance between the two electrode fingers was set to 1 mm in (**A-E**) and the CPE parameters were A_{CPE} = 5·10^{-5} F·s$^{(n-1)}$·cm^{-2} & n_{CPE} = 0.95. Cell parameters for M1 cells: R_b = 2870 Ω·cm^2, α = 117 Ω$^{0.5}$·cm, C_m = 1.91 μF·cm^2 and for M2 cells: R_b = 88 Ω·cm^2, α = 16 Ω$^{0.5}$·cm, C_m = 3.03 μF·cm^2. Variable parameters were (**A**) W = 200 μm, $R_{||}$ = 8 kΩ, R_{bulk} = 2.5 kΩ, (**B**) W = 300 μm, $R_{||}$ = 4 kΩ, R_{bulk} = 1.5 kΩ (**C**) W = 500 μm, $R_{||}$ = 1 kΩ, R_{bulk} = 1.5 kΩ (**D**) W = 1 mm, $R_{||}$ = 0.5 kΩ, R_{bulk} = 500 Ω and (**E**) W = 2 mm, $R_{||}$ = 0.25 kΩ, R_{bulk} = 500 Ω. (**F**) Is the reference LSG unipolar electrode in the REE layout (log-log plot).

The active electrode area in the simulations was taken as the complete area of the line-shaped bipolar electrodes which was exposed to the culture medium inside the 23-mm glas ring. The simulated spectra of the cell-free bipolar electrodes showed the clear trend that a broader bipolar electrode width W significantly reduced the parallel resistance $R_\parallel$ due to the larger cross sectional area (compare equation (12)). The bulk resistance was also aligned with the data from **Fig. 76** to match the experimental data and therefore decreased with increasing width W. Otherwise, the spectra of the cell-free electrodes showed the similar characteristics of a frequency-independent resistive influence at the lowest frequency followed by the dominating capacitive contribution of the electrode-electrolyte interface with the steepest slope around 10 Hz. If the frequency was increased further, the spectra were again dominated by a resistive contribution (R_{bulk}) which formed the horizontal line above 100 Hz. In **Fig. 69F** the unipolar rectangular & equally-sized LSG electrode layout was simulated in the *Bode plot*-typical log-log presentation. This one clearly deviated from the other spectra in the low-frequency range because it lacked the parallel resistance due to the two individual electrodes. The spectra in **Fig. 69A-E** highlight the importance of the width W of the line-shaped bipolar electrode. If the width was 500 µm (**C**), the parallel resistance was reduced to 1 kΩ and for a bulk resistance of 600 Ω, the maximum signal change due to the presence of living cells amounted to 400 Ω. At a width of 1 mm, the maximum signal change was limited to 250 Ω and at 2 mm to less than 100 Ω. Thus, the optimal line width on the one hand lay below 500 µm but on the other hand could not be chosen indefinitely small as this would have driven the parallel resistance up to such large values that, in effect, a two-electrode setup would have been created and the special features of the bipolar electrodes would have been lost. In a direct comparison of **Fig. 69A & B**, it was shown that the simulated spectra of the cell-covered electrodes compared very well with each other. The MDCK-II cell sensitivity ($Z_{cell-covered}/Z_{cell-free}$) was slightly higher for the 300-µm width (1.40) compared to the 200-µm width (1.39). The sensitivity for the detection of MDCK-I cells in contrast was higher for the 200-µm width (3.25) if set side by side to the 300-µm width (2.98). Taking into consideration that MDCK-I cells are among the most tight epithelial cells yielding the highest TER values which most other cell lines do not reach, the 300-µm line-shaped bipolar electrode width was chosen as the most promising bipolar electrode layout in view of the fact that the sensitivity for the monitoring of commonly used cell lines with lower TER values like *normal rat kidney* (NRK), *human embryonic kidney* (HEK) or *Chinese hamster ovary* (CHO) cells would be larger if measured on the 300-µm layout. In addition, the handling of the 300-µm line width was easier as very thin LSG lines are prone to breaking or peeling off the substrate surface.

V.4.3.2   Bode Plots of Cell-Covered Bipolar Electrodes

In order to confirm the simulated spectra of cell-covered bipolar electrodes with experimental evidence, the bipolar electrode layout from **Fig. 68A** in a width of 300 μm was equipped with a 23-mm glass ring which was glued onto the substrate and served as a cell culture dish for the seeding of MDCK-I and MDCK-II cells according to chapter IV.2.4. Impedance and phase spectra were recorded before cell inoculation as well as 24 h, 48 h and 72 h after cell seeding. The resulting *Bode plots* are shown in **Fig. 70A & C** for MDCK-II cells and in **B & D** for MDCK-I cells.
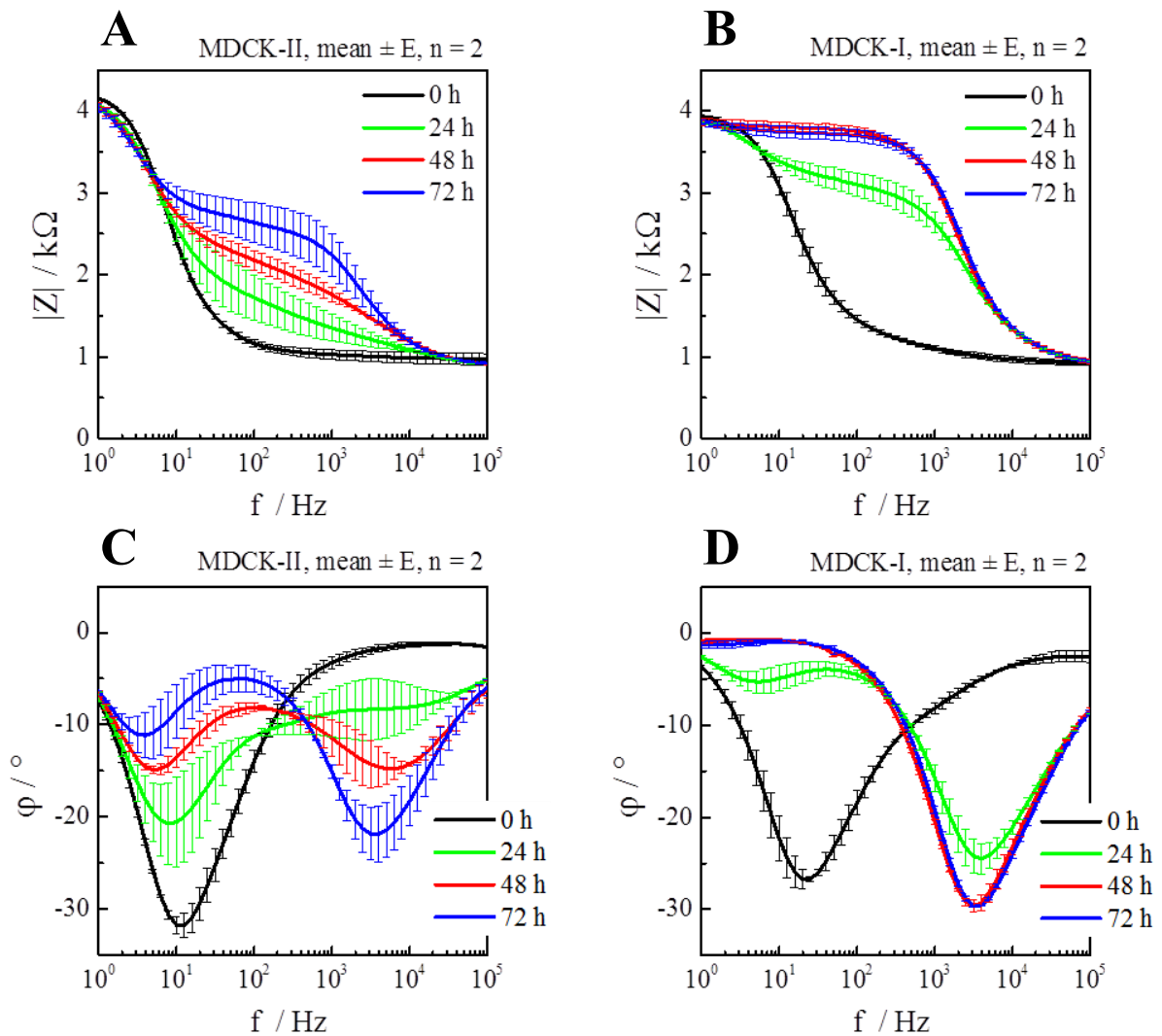
Fig. 70: *Bode plots* for bipolar LSG electrodes during the adhesion, spreading and differentiation of MDCK-II cells (**A & C**) and MDCK-I cells (**B & D**) in a semi-logarithmic presentation. The magnitude of impedance |Z|(f) is shown in the upper row (**A, B**) and the corresponding phase angle φ(f) in the lower row (**C, D**). Seeding density was $5 \cdot 10^5$ c/cm^2 in culture medium, the measurement conducted in a standard cell incubator at 37 °C and 5 % CO_2 and spectra were recorded every 24 h for three days. E depicts the maximum spread between the data points from the two independent measurements.

The cell-free impedance spectra in **Fig. 70A & B** closely resembled the simulated ones with a bulk resistance around 1 kΩ above 100 Hz, the dominating CPE element at frequencies lower than 100 Hz where the slanted line was capped by the parallel resistance at the lowest frequencies. The phase angle in the lower row corroborated with the findings as a phase shift close to zero was found at high and low frequencies indicating purely resistive behavior of the bulk resistance and the parallel resistance, respectively. At 10 Hz, a minimum around –30° was obtained for the cell-free electrode which could be attributed to the capacitive influence of the electrode-electrolyte interface. The value of –30° indicated that the behavior was not purely capacitive which could be explained by the parallel connection of the parallel resistance to the serially connected CPE and R_{bulk}.

Comparing the impedance magnitude spectra of the bipolar electrode with a fully differentiated cell layer of MDCK-II cells (**Fig. 70A**) and MDCK-I cells (**Fig. 70B**), the two cell types could clearly be distinguished from each other with respect to the impedance values in the range from 10 – 1000 Hz. MDCK-I cells yielded a value of 3.7 kΩ at 100 Hz as was to be expected from the simulated data (compare **Fig. 69B**, **MDCK-I**) and the MDCK-II cells produced an impedance value of 2.6 kΩ at the same frequency which exceeded sensitivity expectations by 1000 Ω (**Fig. 69B**, **MDCK-II**). As to the reason why the simulated and the experimental data deviated from each other, it has to be taken into account that the cell-related parameters were chosen to reflect literature ones for the ECIS® model which requires a small working electrode and a significantly larger counter electrode. The smaller working electrode in the ECIS® layout then dominates the overall interface impedance which is not given in the bipolar setup which means that the model yields incorrect results for the bipolar electrodes. In the case of the MDCK-I cells, the highest possible impedance signal was obtained, as the parallel resistance also limited the cell-related signal to its intrinsic value. The experimental results also fit well with the results from the impedance-based cell analysis using the rectangular & equally-sized LSG electrodes from the previous chapter. The electrode- and the cell-related dispersion were again separated by at least two orders of magnitude (compare **Fig. 70** for the bipolar version and chapter V.4.2.1 for the two-electrode setup). This could, especially in the case of the bipolar electrodes, be seen in the phase angle minima for the cell-free electrode (**0 h**) and for the same electrode with a confluent and fully differentiated cell layer (**72 h**) as the minima corresponded exclusively to the electrode-electrolyte interface in the case of the cell-free electrode and the capacitive influence of the cell membranes in the case of the cell-covered electrode.

The strict separation of the two capacitive contributions could thus far only be achieved using LSG as electrode material as the other established electrode materials gold and ITO exhibit significantly higher *apparent* interface impedances due to their material-specific properties.

V.4.4   Conclusion & Outlook

Laser-scribed graphene may serve as an alternative electrode material to interface adherent living cells and to monitor their behavior by impedance measurements. Due to the foam-like electrode structure, the interface capacitance is a lot higher compared to the standard material gold. This high interface capacitance allows for a better separation of the electrode- and cell-related dispersion so that impedance-based monitoring of cell behavior becomes possible even for highly polarized epithelia with exceptionally high membrane capacitances. This low interface impedance is also advantageous for other approaches to electrochemically monitor or manipulate adherent cells like, for instance, reversible or irreversible *in situ* electroporation. The process of electroporation can even be simplified further by using LSG as bipolar electrode material because a constant potential gradient is established along the length of the bipolar electrode and renders the time-consuming optimization of the electroporation parameter voltage or current amplitude superfluous. Thus, only the puls duration and frequency need to be optimized and each combination automatically yields the corresponding amplitude range along the bipolar electrode. Especially when fine electrode structures are required, the generation of LSG offers the clear advantage of high precision yet reproducible and comfortable laser-scribing with which structures of 200 µm and below can be achieved while simultaneously saving material and chemicals which, in contrast, are needed in the photolithography wet etching process. Given that the electrode topography is easily tunable by alternating the laser parameters, tailor-made electrode materials are readily available. Since the production of LSG is cost- and time efficient as well as biocompatible with mass production techniques, the stage is set for a broad use of this material in impedance-based cellular assays.

VI   SUMMARY

The preclinical testing of active substances is routinely performed first on living cells *in vitro* and later on, tests are done on living animals. There still exists a wide-ranging gap between two-dimensional cell monolayers *in vitro* and animal models as a complex organism. Existing three-dimensional tissue models either do not yield time-dependent information on the cell reaction or only provide an integral response of the entire tissue. Thus, the aim of this work was the development of a three-dimensional *in vitro* model of mammalian tissue with integrated thin film electrodes as required for a time-resolved impedimetric readout of the individual cell layers. The concept was built upon preliminary studies and knowledge which had already been acquired in the lab for analyzing two cell layers on opposing sides of a permeable polymer substrate. In this thesis, this basic concept was adapted to a more flexible architecture that allows studying a variable number of cell layers in close proximity to each other, mimicking 3D tissue. Therefore, three different electrode layouts – (i) two rectangular, equally-sized electrodes, (ii) an interdigitated finger electrode layout and (iii) a small centrosymmetrical working electrode in combination with a significantly larger counter electrode – were compared to each other and their compatibility with respect to the project requirements was investigated. The distinction of different adherently growing cell types on the electrode layouts was unambiguously possible according to the recorded impedance and phase spectra. Furthermore, the extraction of cell-specific ECIS® parameters from the impedance spectra yielded anticipated parameter values compatible with the available literature. Advantages of the first layout lay in the field of *rapid prototyping* because of the material-efficient and geometrically simple layout. The second, interdigitating finger electrode layout, was able to provide a more representative integral signal of the entire cell population due to the larger active electrode area. The last electrode layout with the centrosymmetrical working electrode was the only one allowing for an effective counter electrode insulation which proved to be crucial in the development process. The reproducible generation of a one-sided gold-film electrode layout on a permeable polymer membrane was subsequently optimized with regard to sputter conditions, the material stability of the substrate polymer and the homogeneity of the gold coating. Test measurements with selected cell lines were performed on membranes with electrodes prepared on the cell-facing side only, after a cell cultivation-suitable receptacle had been established on each side to define the growth area as well as a reproducible way of connecting the electrodes to the hardware. During these measurements the impact of the backside electrolyte current became obvious which provided

an alternative current pathway bypassing the confluent cell layer grown to the front side. Thus, the cell layer became invisible to the impedance measurements. Due to the backside electrolyte impact, an efficient insulation of the counter electrode on the reverse side was indispensable and could eventually be achieved by using a self-adhesive lamination foil. The insulation was confined to the area of the counter electrode by drilling a central opening in the lamination foil in order to maintain the permeability of the working electrode. After coating the lamination foil with a thin gold layer similar to the permeable polymer membrane, the lamination foil could be used as an additional counter electrode for the detection of living cells on the reverse side of the polymer membrane. This way, the very same working electrode could be used to detect cells on the front- and reverse side by sequentially contacting it first against the counter electrode on the filter and afterwards against the gold-coated lamination foil, respectively. An extensive investigation of a suitable dimension of the hole in the insulating lamination foil eventually allowed for an individual and independent addressing of the cell layers growing on both sides of the filter membrane and thus also to a successful transfer of the three-electrode setup to a stackable system of multiple permeable supports. The establishment of a functional and reproducible cell cultivation process on both sides of the permeable support was achieved with the help of specially designed cultivation chambers and a corresponding measurement chamber in which two of the final cell-covered permeable supports could be stacked next to each other. Mass transport within the measurement chamber alone was documented by a cell-free optical dye dilution assay as well as the impedimetric detection of a redox probe. The results thereof, including the experimentally determined total flux from the diffusion studies, were confirmed via simulations using the *finite element method*. Furthermore, frequency- and time-resolved proof-of-concept studies with epithelial cells exhibiting cell-type specific barrier properties have not only shown that an individual monitoring of each of the four cell layers is possible; distinct measurements with reduced buffer conductivity and the addition of model substances e.g. cytochalasin D and tert-butyl hydroperoxide also provoked specific response profiles validated by independent ECIS® measurements on impermeable substrates and *zellZscope* measurements with permeable filter inserts.

In summary, the novel measurement system is capable of mimicking a three-dimensional tissue model by providing a physiological environment for each cell with neighboring cells in all three dimensions. At the same time, each single cell layer can be monitored individually, non-invasively and in a time-resolved manner by using this new biotechnological hybrid. The chamber material was chosen to consist of tempered polycarbonate which is extremely robust

and therefore not only reusable but also suitable for frequent ethanol-sterilization. Due to the separate cultivation and measurement of the cells on the permeable supports, these steps can be performed in parallel. Thus, cell proliferation, adhesion and spreading processes can be directly monitored in the cultivation chambers and experiments with multiple permeable supports stacked next to each other – which all have confluent cell monolayers grown to each side – can be performed in the measurement chambers. Moreover, thanks to the modular setup of the measurement chamber, the number of permeable supports which are stacked therein, can be scaled up easily and the process is equally suited for all cell types as long as they grow adherently. This way, data of a cell reaction upon the reversible or irreversible external stimulation can be collected in a real-time and non-invasive manner and diffusion processes across multiple layers of tissue become accessible with the direct information from each layer. Last but not least, different cell types can be combined to yield organ-on-a-chip approaches in order to test the effectiveness or side effects of active substances.

Parallel to the development of the novel three-dimensional measurement setup, the new and promising electrode material *laser-scribed graphene* (LSG) was investigated with respect to the applicability as an alternative electrode material in cell-based assays. Thus, the LSG material was compared to the established gold standard by frequency- and time-resolved impedance data. Due to the rough topography and consequently large surface of LSG, a 25-fold higher interface capacitance was found for the same electrode geometry compared to gold which allowed for a better separation of the electrode- and cell-specific dispersions in the impedance spectrum. Because of this significantly higher membrane capacitance it is assumed that, in contrast to gold electrodes, it would still be possible to detect the presence of cell types with extraordinarily high membrane capacitances. An excellent biocompatibility of the LSG material was proven according to fluorescence cell stainings with subsequent microscopic evaluation as well as extensive investigations via impedance spectroscopy.

VII   ZUSAMMENFASSUNG

Die präklinische Testphase von Wirkstoffen wird routinemäßig zuerst an lebenden Zellen *in vitro* und später an lebenden Versuchstieren durchgeführt. Der Schritt von zweidimensionalen Zellmonolagen *in vitro* hin zu lebenden Versuchstieren als einem komplexen Organismus ist weiterhin sehr groß, da bestehende dreidimensionale Gewebemodelle entweder keine zeitaufgelöste Informationen über die Zellreaktionen liefern können, oder aber nur ein integrales Signal des gesamten Gewebemodells. Deswegen war das Ziel der vorliegenden Arbeit die vollständige Entwicklung eines dreidimensionalen *in vitro* Gewebe-Modells, welches Dünnfilmelektroden für die impedanzbasierte Auslesung bereits von vorne herein beinhaltet. Das Konzept baute auf bereits erworbenen Kenntnissen und vorbereitenden Studien innerhalb des Arbeitskreises auf, anhand derer es möglich war, zwei Zelllagen auf beiden Seiten einer permeablen Polymermembran zu analysieren. In dieser Arbeit wurde das grundlegende Konzept weiterentwickelt und an einen flexibleren Aufbau angepasst, wodurch eine variable Anzahl von Zelllagen zu einem 3D Gewebemodell zusammengesetzt werden können. Dazu wurden zuerst drei verschiedene Elektrodenlayouts – (i) zwei rechteckige, gleich große Elektroden sowie (ii) interdigitierende Elektrodenfinger und (iii) eine kleine, zentrosymmetrische Arbeitselektrode in Kombination mit einer deutlich größeren Gegenelektrode – miteinander verglichen und auf deren Kompatibilität in Hinblick auf das Projektziel untersucht. Die Unterscheidung von verschiedenen Zelltypen, welche adhärent auf den verschiedenen Elektrodenlayouts wuchsen, war anhand der Impedanz- und Phasen-spektren auf allen Elektrodenlayouts zweifelsfrei möglich und auch die aus den Spektren bestimmten, zellspezifischen Parameter entsprachen in allen Fällen den Erwartungen und waren mit der einschlägigen Literatur kompatibel. Die Vorteile lagen im Falle des ersten Layouts im Bereich des *rapid prototypings*, da es sich um ein materialsparendes, geometrisch einfaches Layout handelte. Das zweite, interdigitierende Layout, ermöglichte es durch die vergleichsweise große Fläche, einen aussagekräftigeren Querschnitt der gesamten Zell-population zu erhalten und das dritte, zentrosymmetrische Layout bot als einziges die Möglichkeit einer effizienten Isolierung der Gegenelektrode, was sich im weiteren Verlauf als unabdingbar herauskristallisierte. Die reproduzierbare, einseitige Aufbringung des Elek-trodenlayouts auf eine permeable Polymermembran wurde anschließend im Hinblick auf geeignete Sputterbedingungen, Formstabilität des Trägerpolymers und Homogenität der Beschichtung optimiert. Testmessungen mit ausgesuchten Zelllinien wurden an den zellseitig mit Elektroden funktionalisierten Polymermembranen durchgeführt, nachdem eine zur

164

Kultivierung taugliche Berandung sowie eine reproduzierbare Kontaktierung an die Treiberelektronik etabliert wurden. Dabei trat das Problem des Rückseitenelektrolyten zu Tage, welcher einen alternativen Stromweg unter Umgehung der auf der Oberseite ange-wachsenen Zellschicht bot. Durch diesen alternativen Stromweg konnte die Zellschicht in der Impedanzmessung nicht detektiert werden und es stellte sich die eingangs erwähnte Isolierung der Gegenelektrode als notwendig heraus, welche letztendlich durch eine selbsthaftende Laminierungsfolie bewerkstelligt werden konnte. Dabei wurde nur die Fläche der Arbeits-elektrode ausgespart, um die Permeabilität an dieser Stelle zu gewährleisten. Nach vorangegangener Belegung der Laminierungsfolie mit ebenfalls einer dünnen Goldschicht und einer entsprechenden externen Kontaktierung, konnte die Laminierungsfolie als zusätzliche Gegenelektrode genutzt werden, um auf der Rückseite der Sensormembran kultivierte Zellen zu adressieren. Dazu wurde ein und dieselbe Arbeitselektrode sequentiell erst gegen die Gegenelektrode auf dem Filter und anschließend gegen die goldbelegte Laminierungsfolie auf der Unterseite geschaltet. Eine ausführliche Untersuchung der geeigneten Abmessungen der Lochgröße in der isolierenden Laminierungsfolie erlaubten eine individuelle und unabhängige Adressierung der beiden Zellschichten auf Ober- und Unterseite und dadurch auch eine Übertragung auf ein schichtbares System aus mehreren permeablen Trägersubstraten. Die Etablierung einer routinemäßigen Kultivierung der Zellen auf beiden Seiten der permeablen Trägersubstraten gelang mit Hilfe von speziell entwickelten Kultivierungskammern und einer Messkammer, in der zwei der finalen permeablen Trägersubstrate hintereinander geschichtet werden konnten. Die Funktionstüchtigkeit der Kammer alleine wurde anhand von zellfreien optischen Farbverdünnungsassays sowie der impedimetrischen Detektion von Redoxsonden bewiesen. Die Ergebnisse, inklusive der experimentell bestimmten Teilchenstromdichte aus den Diffusionsstudien, konnten mit Hilfe von Simulationen basierend auf der *Methode der finiten Elemente* bestätigt werden. Des Weiteren haben Proof-of-concept-Messungen mit verschieden dichten Epithelzelllinien anhand von frequenz- und zeitaufgelösten Experimenten nicht nur gezeigt, dass ein individuelles Monitoring jeder der vier Zellschichten in dem System möglich ist und verschiedene Zelltypen eindeutig voneinander unterscheidbar sind, sondern spezielle Messungen mit veränderten Leitfähigkeiten und der Zugabe von Modellsubstanzen Cytochalasin D und *tert*-Butylhydroperoxid zeigten spezifische Reaktionsprofile, welche durch unabhängige ECIS® Experimente auf impermeablen Substraten und *zellZscope* Messungen mit permeablen Filtereinsätzen bestätigt werden konnten.

Zusammenfassend ist das neu entwickelte System in der Lage, ein dreidimensionales Gewebemodell zu imitieren, da eine physiologische Umgebung durch Nachbarzellen in allen drei Dimensionen für jede einzelne Zelle gewährleistet wird. Gleichzeitig kann in dem neuartigen Setup aber auch jede einzelne Zellschicht individuell, zeitaufgelöst und nichtinvasiv adressiert werden. Durch die Verwendung von robustem, getempertem Polycarbonat als Kammermaterial sind sowohl Kultivierungs- als auch Messkammern wiederverwendbar und können beliebig oft mit Ethanol sterilisiert werden. Durch die zeitlich und räumlich getrennte Vorkultivierung und anschließende Messung der Zellen auf den permeablen Trägersubstraten können mehrere Messungen parallel durchgeführt werden. Daten können sowohl während der Adhäsions- oder Proliferationsphase in den horizontalen Kultivierungskammern, oder auch hintereinander geschichtet in Form von mehreren konfluenten Zelllagen in der vertikalen Messkammer erhoben werden. Des Weiteren ist die Anzahl der permeablen Trägersubstrate in der Messkammer durch den modularen Aufbau derselben beliebig erweiterbar und für alle adhärenten Zelltypen gleichermaßen geeignet. Dadurch können Zellreaktionen nicht nur in Echtzeit und nicht-invasiv im Hinblick auf externe Stimulierungen erhoben werden, sondern auch Diffusionsvorgänge über mehrere Gewebeschichten werden dadurch zugänglich. Nicht zuletzt können so auch verschiedene Zelltypen zu Organ-on-a-chip-Ansätzen kombiniert werden, um dort gezielt Wirkstoffforschung zu betreiben.

Parallel zur Entwicklung des neuen dreidimensionalen biotechnologischen Hybridsystems wurde das neuartige und vielversprechende Elektrodenmaterial *laser-scribed graphene* (LSG) auf dessen Eignung als alternatives Elektrodenmaterial für den Einsatz in zellbasierten Assays getestet und mit dem etablierten Referenzmaterial Gold verglichen. Es zeigte sich, dass LSG aufgrund der deutlich größeren Oberfläche bei gleichen Elektrodenabmessungen eine 25-fach größere Grenzflächenkapazität besitzt und dadurch die im Impedanzspektrum auftretenden elektroden- und zellspezifischen Dispersionen besser voneinander getrennt werden können. Gerade bei Zelltypen mit außergewöhnlich hohen Membrankapazitäten würde dies, im Gegensatz zu Gold, noch zu einer zweifelsfreien Detektion von Zellen auf der Elektrodenoberfläche führen. Die gute Biokompatibilität von LSG wurde anhand von Zellfärbungen mit anschließender mikroskopischer Überprüfung genauso bestätigt wie durch die Ergebnisse der Impedanzspektroskopie.

VIII   REFERENCES

[1]   DiMasi, J. A., Hansen, R. W. and Grabowski, H. G., **2003**. *J. Health Econ.* 22 (2), 151-185.

[2]   Griffith, L. G. and Swartz, M. A., **2006**. *Nat. Rev. Mol. Cell Biol.* 7 (3), 211-224.

[3]   Martignoni, M., Groothuis, G. M. and de Kanter, R., **2006**. *Expert Opin. Drug Metab. Toxicol.* 2 (6), 875-894.

[4]   Mazzoleni, G., Di Lorenzo, D. and Steimberg, N., **2009**. *Genes Nutr.* 4 (1), 13-22.

[5]   Yamada, K. M. and Cukierman, E., **2007**. *Cell* 130 (4), 601-610.

[6]   Ringer, S., **1882**. *J. Physiol.* 3 (5-6), 380-393.

[7]   Roux, W., **1888**. *Archiv Path. Anat. Physiol. Klin. Med.* 114 (2), 246-291.

[8]   Harrison, R. G., **1906**. *Proc. Soc. Exp. Biol. Med.* 4 (1), 140-143.

[9]   Newth, D., **1970**. *Nature* 225 (5231), 480-480.

[10]   Carrel, A., **1912**. *J. Exp. Med.* 15 (5), 516-528.

[11]   Carrel, A. and Burrows, M. T., **1911**. *J. Exp. Med.* 13 (3), 387-396.

[12]   Vertrees, R. A., Goodwin, T., Jordan, J. M. and Zwischenberger, J. B., **2008**. *Molecular Pathology Library* 1 150-165.

[13]   Rahbari, R., Sheahan, T., Modes, V., Collier, P., Macfarlane, C. and Badge, R. M., **2009**. *BioTechniques* 46 (4), 277-284.

[14]   Derda, R., Tang, S. K. Y., Laromaine, A., Mosadegh, B., Hong, E., Mwangi, M., Mammoto, A., Ingber, D. E. and Whitesides, G. M., **2011**. *PLOS ONE* 6 (5), e18940.

[15]   Simon, K. A., Park, K. M., Mosadegh, B., Subramaniam, A. B., Mazzeo, A. D., Ngo, P. M. and Whitesides, G. M., **2014**. *Biomaterials* 35 (1), 259-268.

[16]   Achilli, T.-M., Meyer, J. and Morgan, J. R., **2012**. *Expert Opin. Biol. Ther.* 12 (10), 1347-1360.

[17]   Kelm, J. M., Timmins, N. E., Brown, C. J., Fussenegger, M. and Nielsen, L. K., **2003**. *Biotechnol. Bioeng.* 83 (2), 173-180.

[18]   Metzger, W., Sossong, D., Bächle, A., Pütz, N., Wennemuth, G., Pohlemann, T. and Oberringer, M., **2011**. *Cytotherapy* 13 (8), 1000-1012.

[19]   Kunz-Schughart, L. A., Freyer, J. P., Hofstaedter, F. and Ebner, R., **2004**. *J. Biomol. Screen.* 9 (4), 273-285.

[20]   Bertuzzi, A., Fasano, A., Gandolfi, A. and Sinisgalli, C., **2010**. *J. Theor. Biol.* 262 (1), 142-150.

[21]   Hutmacher, D. W., **2000**. *Biomaterials* 21 (24), 2529-2543.

[22] Yang, S., Leong, K. F., Du, Z. and Chua, C. K., **2001**. *Tissue Eng.* 7 (6), 679-689.

[23] Kessler, M. W. and Grande, D. A., **2008**. *Organogenesis* 4 (1), 28-32.

[24] Agarwal, T., Subramanian, B. and Maiti, T. K., **2019**. *ACS Biomater. Sci. Eng.* 5 (9), 4167-4182.

[25] Rajab, T. K., O'Malley, T. J. and Tchantchaleishvili, V., **2020**. *Int. J. Artif. Organs* 44 (10), 1031-1043.

[26] Murphy, S. V. and Atala, A., **2014**. *Nat. Biotechnol.* 32 (8), 773-785.

[27] Lee, G. Y., Kenny, P. A., Lee, E. H. and Bissell, M. J., **2007**. *Nat. Methods* 4 (4), 359-365.

[28] Vikram Singh, A., Hasan Dad Ansari, M., Wang, S., Laux, P., Luch, A., Kumar, A., Patil, R. and Nussberger, S., **2019**. *Appl. Sci.* 9 (4), 811.

[29] Preethi, G. U., Joseph, M. M., Unnikrishnan, B. S., Shiji, R. and Sreelekha, T. T., **2015**. *Int. J. Nano Res.* 2 (2), 1-9.

[30] Elliott, N. T. and Yuan, F., **2011**. *J. Pharm. Sci.* 100 (1), 59-74.

[31] Edmondson, R., Broglie, J. J., Adcock, A. F. and Yang, L., **2014**. *Assay Drug Dev. Technol.* 12 (4), 207-218.

[32] Sung, J. H., Srinivasan, B., Esch, M. B., McLamb, W. T., Bernabini, C., Shuler, M. L. and Hickman, J. J., **2014**. *Exp. Biol. Med.* 239 (9), 1225-1239.

[33] Huh, D., Hamilton, G. A. and Ingber, D. E., **2011**. *Trends Cell Biol.* 21 (12), 745-754.

[34] Riss, T. L., Moravec, R. A., Niles, A. L., Duellman, S., Benink, H. A., Worzella, T. J. and Minor, L., **2016**. *Assay Guid. Man.* 1-34.

[35] Single, A., Beetham, H., Telford, B. J., Guilford, P. and Chen, A., **2015**. *J. Biomol. Screen.* 20 (10), 1286-1293.

[36] Dmitriev, R. I., Borisov, S. M., Kondrashina, A. V., Pakan, J. M., Anilkumar, U., Prehn, J. H., Zhdanov, A. V., McDermott, K. W., Klimant, I. and Papkovsky, D. B., **2015**. *Cell. Mol. Life Sci.* 72 (2), 367-381.

[37] Costa, E., Silva, D., Moreira, A. and Correia, I., **2019**. *Biotechnol. Bioeng.* 116 (10), 2742-2763.

[38] Richardson, D. S. and Lichtman, J. W., **2015**. *Cell* 162 (2), 246-257.

[39] Sanford, L. and Palmer, A., **2017**. *Chapter One - Recent Advances in Development of Genetically Encoded Fluorescent Sensors*, Academic Press, 1-49.

[40] Thielecke, H., Mack, A. and Robitzki, A., **2001**. *Biosens. Bioelectron.* 16 (4), 261-269.

[41] Thielecke, H., Mack, A. and Robitzki, A., **2001**. *Fresenius J. Analyt. Chem.* 369 (1), 23-29.

[42] Kloß, D., Fischer, M., Rothermel, A., Simon, J. C. and Robitzki, A. A., **2008**. *Lab Chip* 8 (6), 879-884.

[43] Jeong, K., Turek, J. J. and Nolte, D. D., **2007**. *Appl. Opt.* 46 (22), 4999-5008.

[44] Langehanenberg, P., Bally, G. v. and Kemper, B., **2010**. *J. Mod. Opt.* 57 (9), 709-717.

[45] Murphy, K. C., Hung, B. P., Browne-Bourne, S., Zhou, D., Yeung, J., Genetos, D. C. and Leach, J. K., **2017**. *J. R. Soc. Interface* 14 (127), 20160851.

[46] Wilson, L. B., **1905**. *J. Am. Med. Assoc.* XLV (23), 1737-1737.

[47] Tokuyasu, K., **1980**. *Hist. J.* 12 (4), 381-403.

[48] Stoeckli, M., Chaurand, P., Hallahan, D. E. and Caprioli, R. M., **2001**. *Nat. Med.* 7 (4), 493-496.

[49] Walenta, S., Schroeder, T. and Mueller-Klieser, W., **2002**. *Biomol. Eng.* 18 (6), 249-262.

[50] McKinnon, K. M., **2018**. *Curr. Protoc. Immunol.* 120 5.1.1-5.1.11.

[51] Giaever, I. and Keese, C. R., **1984**. *Proc. Natl. Acad. Sci. U.S.A.* 81 (12), 3761-3764.

[52] Giaever, I. and Keese, C. R., **1991**. *Proc. Natl. Acad. Sci. U.S.A.* 88 (17), 7896-7900.

[53] Giaever, I. and Keese, C. R., **1993**. *Nature* 366 (6455), 591-592.

[54] Pajkossy, T., **1994**. *J. Electroanal. Chem.* 364 (1), 111-125.

[55] Tolansky, S. and Burch, C. R., **1967**. *Biogr. Mem. Fellows R. Soc.* 13 392-402.

[56] Zernike, F., **1942**. *Physica* 9 (7), 686-698.

[57] Kwon, K.-C., Lim, Y.-T., Kim, N., Yoo, K.-H., Jong-Myeon, H. and Gi-Chang, P., **2010**. *EURASIP J. Image Video Process.* 2010 1-6.

[58] Lakowicz, J. R., **1999**. *Fluorophores*, Springer US, Boston, MA. 63-93.

[59] De Broglie, L., **1939**. *Licht und Materie*, H. Goverts Verlag, Hamburg.

[60] Vernon-Parry, K., **2000**. *III-Vs Review* 13 (4), 40-44.

[61] Everhart, T. E. and Thornley, R. F. M., **1960**. *J. Sci. Instrum.* 37 (7), 246-248.

[62] Puetz, P., Behrent, A., Baeumner, A. and Wegener, J., **2020**. *Sens. Actuator B Chem.* 321 128443.

[63] Kaur, G. and Dufour, J. M., **2012**. *Spermatogenesis* 2 (1), 1-5.

[64] Dukes, J. D., Whitley, P. and Chalmers, A. D., **2011**. *BMC Cell Biol.* 12 43-43.

[65] Urban, F., Hajek, K., Naber, T., Anczykowski, B., Schäfer, M. and Wegener, J., **2020**. *Sci. Rep.* 10 (1), 7373.

[66] Furuse, M., Furuse, K., Sasaki, H. and Tsukita, S., **2001**. *J. Cell Biol.* 153 (2), 263-272.

[67] Reiss, B. and Wegener, J., **2015**. *2015 37th Annual International Conference of the IEEE Engineering in Medicine and Biology Society (EMBC)* 7079-7082.

[68] Wan, W., Zhang, S., Ge, L., Li, Q., Fang, X., Yuan, Q., Zhong, W., Ouyang, J. and Xing, M., **2015**. *Int. J. Nanomedicine* 10 1273-1290.

[69] Ramiah Rajasekaran, P., Chapin, A. A., Quan, D. N., Herberholz, J., Bentley, W. E. and Ghodssi, R., **2020**. *Microsyst. Nanoeng.* 6 (1), 1-12.

[70] Norlin, A., Pan, J. and Leygraf, C., **2004**. *J. Electrochem. Soc.* 152 (2), J7.

[71] Pearson, K., **1905**. *Nature* 72 (1867), 342-342.

[72] Rayleigh, L., **1905**. *Nature* 72 (1866), 318-318.

[73] Codling, E. A., Plank, M. J. and Benhamou, S., **2008**. *J. R. Soc. Interface* 5 (25), 813-834.

[74] Li, S. and Gao, X.-L., **2013**. Pan Stanford, Singapore. 940.

[75] Stewart, P. S., **2003**. *J. Bacteriol.* 185 (5), 1485-1491.

[76] Fick, A., **1855**. *Lond. Edinb. Dubl. Phil. Mag.* 10 (63), 30-39.

[77] Alemu, H., Khoabane, N. and Tseki, P., **2003**. *Bull. Chem. Soc. Ethiop.* 17 (1), 95-106.

[78] Ernst, H. and Knoll, M., **2001**. *Anal. Chim. Acta* 449 129-134.

[79] Haynes, W. M., **2014**. *CRC handbook of chemistry and physics*, 95. CRC press, Boca Raton.

[80] Mamchaoui, K. and Saumon, G., **2000**. *Am. J. Physiol. Lung Cell Mol. Physiol.* 278 (4), 858-863.

[81] Berg, H. C., **2018**. *Random walks in biology*, Princeton University Press, Princeton University Press.

[82] Lo, C.-M., Keese, C. R. and Giaever, I., **1999**. *Exp. Cell Res.* 250 (2), 576-580.

[83] Mitic, L. L., Schneeberger, E. E., Fanning, A. S. and Anderson, J. M., **1999**. *J. Cell Biol.* 146 (3), 683-693.

[84] Collares-Buzato, C. B., Jepson, M. A., McEwan, G. T. A., Hirst, B. H. and Simmons, N. L., **1998**. *Cell Tissue Res.* 291 (2), 267-276.

[85] Adrian, R. H., **1980**. *The Capacity of Cell Membranes: Gating Current Measurements*, Springer US, Boston, MA. 49-55.

[86] Chung, H. H., Mireles, M., Kwarta, B. J. and Gaborski, T. R., **2018**. *Lab Chip* 18 (12), 1671-1689.

[87] May, J. A., Ratan, H., Glenn, J. R., Losche, W., Spangenberg, P. and Heptinstall, S., **1998**. *Platelets* 9 (3-4), 227-232.

[88] Calabrese, E. J., **2009**. *Environ. Health Perspect.* 117 (9), 1339-1343.

[89] Stevenson, B. R. and Begg, D. A., **1994**. *J. Cell Sci.* 107 (Pt 3) 367-75.

[90] Hajek, K. and Wegener, J., **2017**. *Exp. Cell Res.* 351 (1), 121-126.

[91] Kehrer, J. P., **1993**. *Crit. Rev. Toxicol.* 23 (1), 21-48.

[92] Goya, L., Martín, M. Á., Ramos, S., Mateos, R. and Bravo, L., **2009**. *Curr. Nutr. Food Sci.* 5 (1), 56-64.

[93] Hix, S., Kadiiska, M. B., Mason, R. P. and Augusto, O., **2000**. *Chem. Res. Toxicol.* 13 (10), 1056-1064.

[94] Davies, M. J., **1989**. *Biochem. J.* 257 (2), 603-606.

[95] Kučera, O., Endlicher, R., Roušar, T., Lotková, H., Garnol, T., Drahota, Z. and Červinková, Z., **2014**. *Oxid. Med. Cell Longev.* 2014 1-12.

[96] Gad, S. E., **2005**. *Hydroperoxide, tert-Butyl*, Elsevier, New York. 554-555.

[97] Wegener, J., Zink, S., Rösen, P. and Galla, H. J., **1999**. *Pflugers Arch.* 437 (6), 925-934.

[98] Wegener, J., Sieber, M. and Galla, H.-J., **1996**. *J. Biochem. Biophys. Meth.* 32 (3), 151-170.

[99] Brischwein, M., Grothe, H., Otto, A. M., Stepper, C., Weyh, T. and Wolf, B., **2004**. *Chem. Sens. Biosens.* 2 159-180.

[100] Zhang, F., Lin, L.-X., Wang, G.-W., Hu, R., Lin, C.-J. and Chen, Y., **2012**. *Electrochim. Acta* 85 152-161.

[101] Soon, C., Foong, M., Ahmad, M., Zin, R. and Thong, K., **2015**. *Sens. Transducers* 187 113-119.

[102] Martinez, J., Montalibet, A., McAdams, E., Faivre, M. and Ferrigno, R., **2017**. *Conf. Proc. IEEE Eng. Med. Biol. Soc.* 813-816.

[103] Karimullah, A. S., Cumming, D. R., Riehle, M. and Gadegaard, N., **2013**. *Sens. Actuator B Chem.* 176 667-674.

[104] Lin, J., Peng, Z., Liu, Y., Ruiz-Zepeda, F., Ye, R., Samuel, E. L., Yacaman, M. J., Yakobson, B. I. and Tour, J. M., **2014**. *Nat. Commun.* 5 5417.

[105] Ye, R., James, D. K. and Tour, J. M., **2018**. *Acc. Chem. Res.* 51 (7), 1609-1620.

[106] Duy, L. X., Peng, Z., Li, Y., Zhang, J., Ji, Y. and Tour, J. M., **2018**. *Carbon* 126 472-479.

[107] Tiliakos, A., Ceaus, C., Iordache, S. M., Vasile, E. and Stamatin, I., **2016**. *J. Anal. Appl. Pyrolysis* 121 275-286.

[108] Singh, S. P., Li, Y., Be'er, A., Oren, Y., Tour, J. M. and Arnusch, C. J., **2017**. *ACS Appl. Mater. Interfaces* 9 (21), 18238-18247.

[109] Ranella, A., Barberoglou, M., Bakogianni, S., Fotakis, C. and Stratakis, E., **2010**. *Acta Biomater.* 6 (7), 2711-2720.
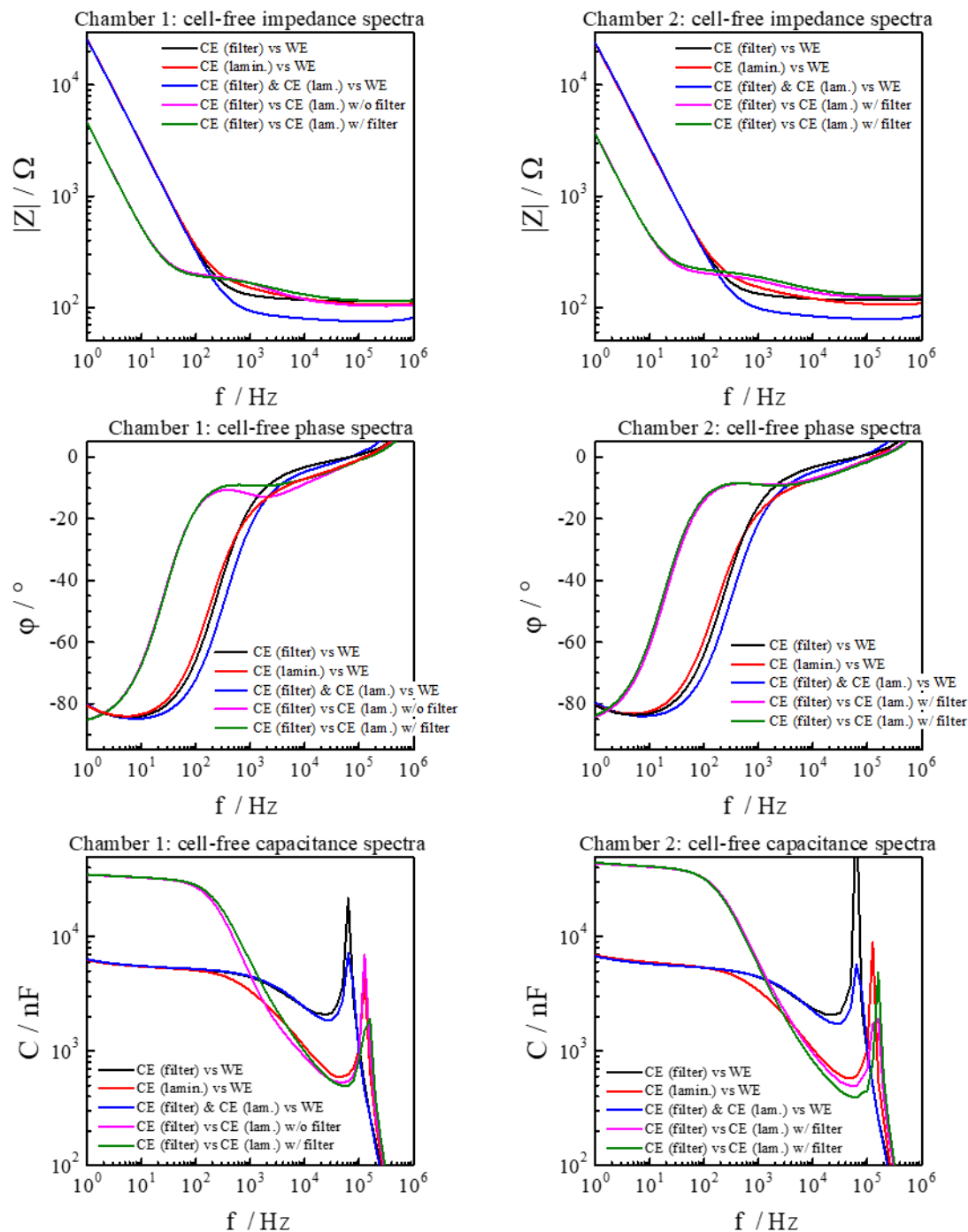
IX APPENDIX

IX.1 Supplementary Information

Fig. 71: Different electrode combinations using the three electrodes present in the prototype chamber from **Fig. 17**. The WE was either measured against the CE on the same side of the filter (**black**), the CE on the reverse side of the filter (**red**) or both CEs connected in parallel (**blue**). A measurement of both CEs against each other is depicted in **green** and the same measurement was performed where the polycarbonate membrane had been removed only in chamber 1 (**pink**). Measurement was performed in PBS^{++} at T = 37 °C and 0 % CO_2.
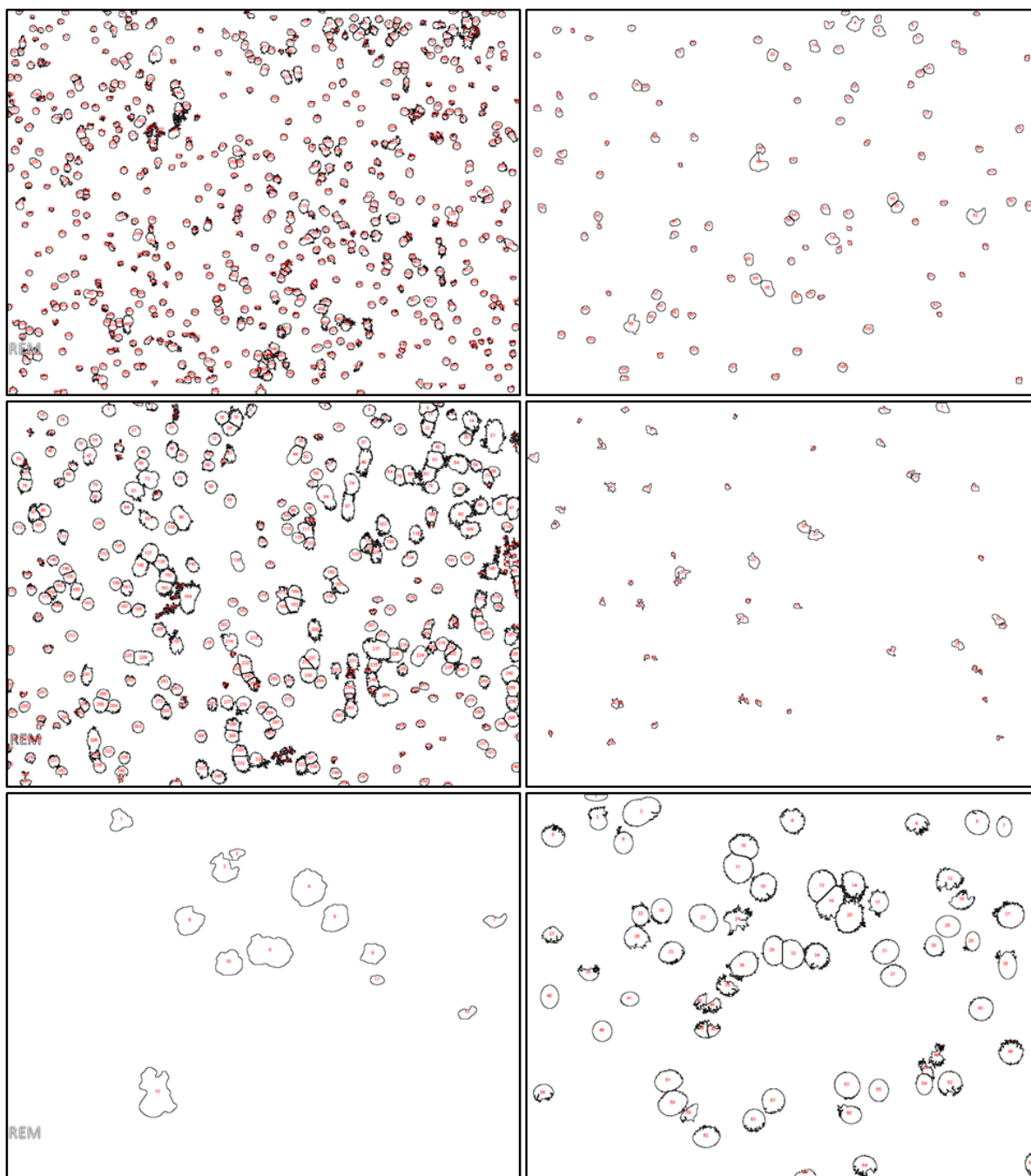
Fig. 72: Left-hand side: counted signals for the determination of the pore density in the SEM pictures of the underside of the working electrode from the permeable support in different magnifications. **Right-hand side**: corresponding EDX signals pictures indicating the amount of pores exhibiting the characteristic wavelength for gold. Ratio of gold signals per channels is 1:6. Magnification is 4000, 6000 and 13000-fold from first to third row. Pictures were taken and provided by nanoAnalytics GmbH.
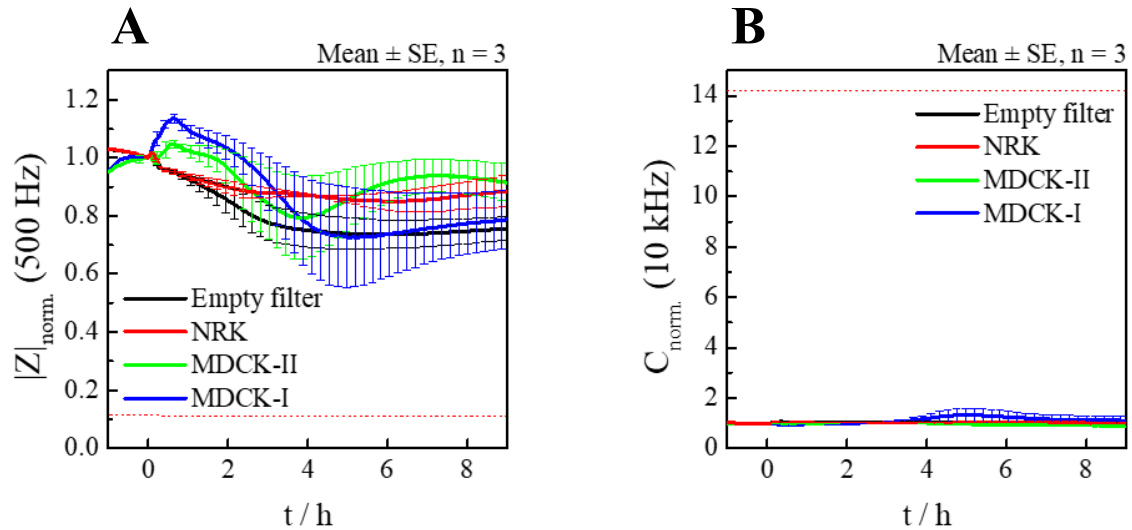
Fig. 73: Tert-butyl hydroperoxide was added to the apical compartments of the IDE sensor arrays a final concentration of 500 µM. The filter inserts were equipped with confluent cell layers of NRK cells (**red**), MDCK-II cells (**green**), MDCK-I cells (**blue**) and empty filters (**black**) served as control. Sensor cells growing directly on the IDF electrode layout were MDCK-II cells in all cases. Time courses of normalized impedance (**A**) and normalized capacitance (**B**) are shown. Time courses were normalized with respect to the last data point before the addition. Experiments were conducted in full medium at 37 °C and 5 % CO_2. The red dotted line corresponds to the value of the cell-free electrode and only 40 error bars are depicted. Data prior to normalization is given in **Tab. 11**.
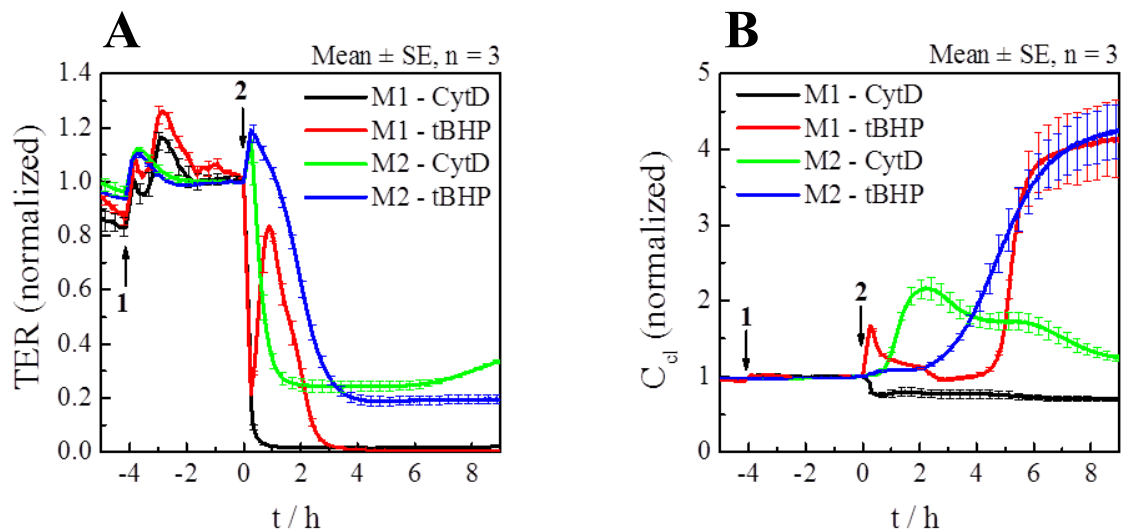

Fig. 74: Time courses of fitted and normalized transepithelial electrical resistance (TER, **A**) and cell layer capacitance (C_{cl}, **B**) from a measurement performed with the *cellZscope2* (nanoAnalytics, Münster, DE) using six MDCK-I cell-covered, six MDCK-II cell-covered and two cell-free Transwell® filter inserts. A medium control addition (containing 1 ‰ DMSO in the case of CytD) was performed at time point (**1**) in all wells and at time point (**2**) CytD (5 µM, **black** & **green**) and tBHP (500 µM, **red** & **blue**) were added to the apical and baso-lateral compartments in the case of MDCK-II (**green** & **blue**) and MDCK-I (**red** & **black**), respectively to mimic the addition process in the measurement chamber. The measurement was conducted in cell culture medium at 37 °C and 5 % CO_2. Absolute values used for normalization (with respect to the last data point before the addition) are given in **Tab. 11**.
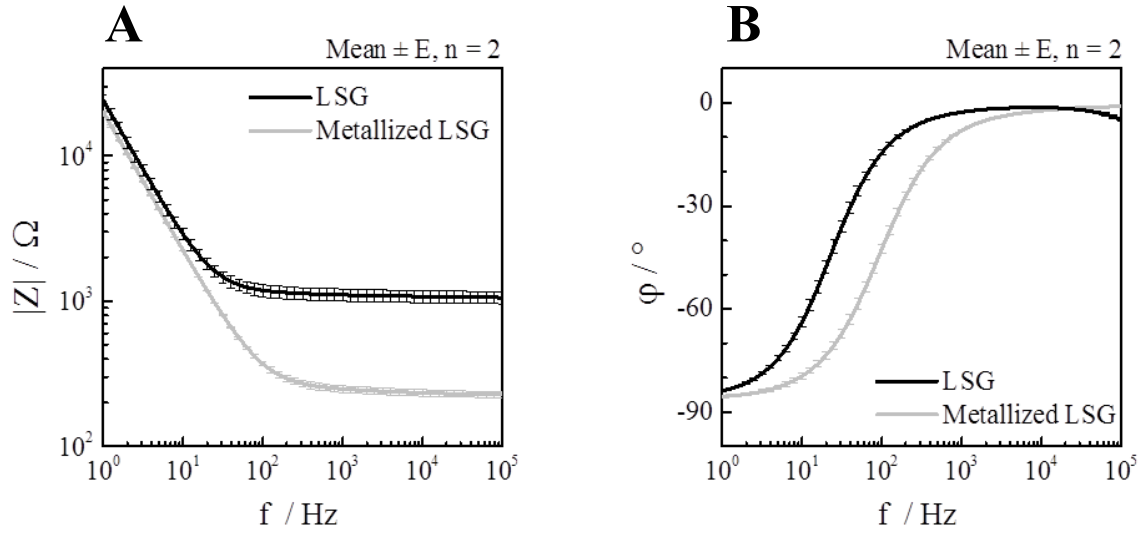
174

Fig. 75: Comparison of the impedance (**A**) and phase spectra (**B**) of untreated LSG electrodes (**black**) and the same electrode layout with the leads outside of the measurement metallized with silver paint (**grey**) when immersed in cell culture medium. E depicts the maximum spread between the data points from the two independent measurements. T = 37 °C, 5 % CO_2.
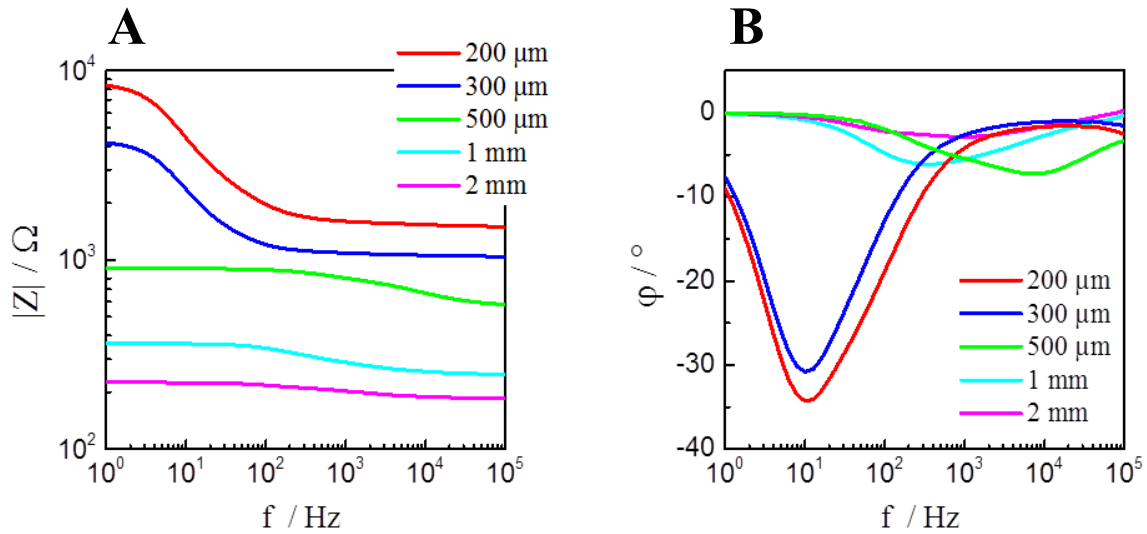

Fig. 76: *Bode plots* of bipolar LSG electrodes with differing width W of the high-resistance conduction line connecting the anode and the cathode. The geometry of the layout can be seen in **Fig. 68A**. The measurement was conducted in cell culture medium at 37 °C and 5 % CO_2 and representative single spectra are shown.

Absolute values for normalized time courses of impedance and capacitance

Tab. 11: Raw data (mean ± SE, n ≥ 3) of the time-dependent impedance and capacitance measurements which have been depicted in their normalized form. The values represent the ones with respect to which the measurements were normalized to.

# Figure	Condition	Impedance / Ω	Capacitance / F
Fig. 50	M1 (σ = 100 %)	5398 ± 132	7.0E-09 ± 2E-10
	M1 (σ = 50 %)	5454 ± 97	6.9E-09 ± 1E-10
	M2 (σ = 100 %)	4142 ± 57	9.1E-09 ± 1E-10
	M2 (σ = 50 %)	4231 ± 58	8.9E-09 ± 1E-10
Fig. 51	I – M2 (σ = 100 %)	1659 ± 138	1.26E-07 ± 4E-09
	II – M1 (σ = 50 %)	1541 ± 207	2.22E-07 ± 5E-09
	III – M2 (σ = 50 %)	1042 ± 169	2.5E-07 ± 1E-08
	IV – M1 (σ = 100 %)	4118 ± 139	1.24E-07 ± 4E-09
Fig. 52	I – M2 (σ = 100 %)	R_b: (68 ± 11) $\Omega \cdot cm^2$, α: (23.4 ± 0.5) $\Omega^{0.5} \cdot cm$, C_m: (3.67 ± 0.07) $\mu F \cdot cm^{-2}$	
	II – M1 (σ = 50 %)	R_b: (81 ± 10) $\Omega \cdot cm^2$, α: (50 ± 8) $\Omega^{0.5} \cdot cm$, C_m: (3.7 ± 0.3) $\mu F \cdot cm^{-2}$	
	III – M2 (σ = 50 %)	R_b: (84 ± 23) $\Omega \cdot cm^2$, α: (18.3 ± 0.6) $\Omega^{0.5} \cdot cm$, C_m: (4.0 ± 0.1) $\mu F \cdot cm^{-2}$	
	IV – M1 (σ = 100 %)	R_b: (464 ± 45) $\Omega \cdot cm^2$, α: (41 ± 7) $\Omega^{0.5} \cdot cm$, C_m: (4.5 ± 0.2) $\mu F \cdot cm^{-2}$	
Fig. 53	5 μM (MDCK-I)	5858 ± 1054	7E-09 ± 1E-09
	5 μM (MDCK-II)	4174 ± 135	9.0E-09 ± 3E-10
	4 μM (MDCK-I)	5509 ± 758	7E-09 ± 1E-09
	4 μM (MDCK-II)	4200 ± 147	9.0E-09 ± 3E-10
	3 μM (MDCK-I)	5758 ± 790	6.7E-09 ± 9E-10
	3 μM (MDCK-II)	4028 ± 85	9.3E-09 ± 2E-10
	2 μM (MDCK-I)	5484 ± 942	7E-09 ± 1E-09
	2 μM (MDCK-II)	4236 ± 36	8.86E-09 ± 7E-11
	1 μM (MDCK-I)	5317 ± 808	7E-09 ± 1E-09
	1 μM (MDCK-II)	4240 ± 68	8.9E-09 ± 2E-10
	0.5 μM (MDCK-I)	4906 ± 491	7.8E-09 ± 8E-10
	0.5 μM (MDCK-II)	4124 ± 56	9.1E-09 ± 1E-10
	0.1 μM (MDCK-I)	5644 ± 740	6.8E-09 ± 9E-10
	0.1 μM (MDCK-II)	3990 ± 51	9.4E-09 ± 1E-10
	0.0 μM (MDCK-I)	5230 ± 688	7.3E-09 ± 9E-10
	0.0 μM (MDCK-II)	3968 ± 54	9.4E-09 ± 1E-10
Fig. 54	Empty filter	751 ± 99	2.3E-07 ± 2E-08
	NRK	725 ± 74	2.3E-07 ± 1E-08
	MDCK-II	778 ± 96	2.2E-07 ± 2E-08
	MDCK-I	779 ± 98	2.1E-07 ± 1E-08

Fig. 55	I – M2	2188 ± 231	1.07E-07 ± 4E-09
	II – M1	3152 ± 118	1.86E-07 ± 5E-09
	III – M2	1272 ± 131	2.3E-07 ± 1E-08
	IV – M1	4394 ± 115	1.22E-07 ± 1E-09
Fig. 56	1 mM (MDCK-I)	5463 ± 582	6.9E-09 ± 8E-10
	1 mM (MDCK-II)	4126 ± 119	9.2E-09 ± 3E-10
	500 µM (MDCK-I)	5488 ± 278	6.8E-09 ± 4E-10
	500 µM (MDCK-II)	4272 ± 118	8.8E-09 ± 3E-10
	300 µM (MDCK-I)	5403 ± 185	6.9E-09 ± 2E-10
	300 µM (MDCK-II)	4242 ± 93	8.9E-09 ± 2E-10
	100 µM (MDCK-I)	5870 ± 638	6.4E-09 ± 7E-10
	100 µM (MDCK-II)	4220 ± 38	8.92E-09 ± 7E-11
	50 µM (MDCK-I)	5498 ± 391	6.8E-09 ± 5E-10
	50 µM (MDCK-II)	4283 ± 33	8.79E-09 ± 7E-11
	30 µM (MDCK-I)	5082 ± 206	7.4E-09 ± 3E-10
	30 µM (MDCK-II)	4132 ± 127	9.2E-09 ± 3E-10
	10 µM (MDCK-I)	5462 ± 83	6.8E-09 ± 1E-10
	10 µM (MDCK-II)	4212 ± 76	8.9E-09 ± 2E-10
	0 µM (MDCK-I)	5139 ± 360	7.4E-09 ± 6E-10
	0 µM (MDCK-II)	3956 ± 55	9.4E-09 ± 1E-10
Fig. 57	Empty filter	541 ± 16	2.9E-07 ± 1E-08
	NRK	579 ± 23	2.9E-07 ± 2E-08
	MDCK-II	732 ± 8	2.49E-07 ± 9E-09
	MDCK-I	569 ± 36	2.5E-07 ± 1E-08
Fig. 58	I – M2	1320 ± 428	2E-07 ± 1E-07
	II – M1	2759 ± 239	1.98E-07 ± 5E-09
	III – M2	999 ± 87	2.5E-07 ± 2E-08
	IV – M1	4592 ± 248	1.17E-07 ± 4E-09
Fig. 73	Empty filter	714 ± 54	2.48E-07 ± 3E-09
	NRK	686 ± 59	2.54E-07 ± 4E-09
	MDCK-II	723 ± 32	2.48E-07 ± 2E-09
	MDCK-I	782 ± 27	2.40E-07 ± 8E-09
Fig. 74	M1 – CytD	TER: $(3047 ± 34)$ $\Omega \cdot cm^2$, C_{cl}: $(1.87 ± 0.02)$ $\mu F \cdot cm^{-2}$	
	M1 – tBHP	TER: $(3112 ± 99)$ $\Omega \cdot cm^2$, C_{cl}: $(1.87 ± 0.02)$ $\mu F \cdot cm^{-2}$	
	M2 – CytD	TER: $(101 ± 5)$ $\Omega \cdot cm^2$, C_{cl}: $(1.87 ± 0.06)$ $\mu F \cdot cm^{-2}$	
	M2 – tBHP	TER: $(94.3 ± 0.3)$ $\Omega \cdot cm^2$, C_{cl}: $(2.01 ± 0.04)$ $\mu F \cdot cm^{-2}$	

IX.2 List of Abbreviations

A

α	Resistance from the cell adhesion sites
A	Area / Ampere
AC	Alternating current
A$_{CPE}$	Electrode-electrolyte interface parameter
a.i.	After cell inoculation

B

b.i.	Before cell inoculation

C

°C	Degree Celsius
c	Concentration
C	Capacitance
C$_{cl}$	Cell layer capacitance
C$_m$	Membrane capacitance
CE	Counter electrode
CHO	Chinese hamster ovary
CLSM	Confocal laser scanning microscope
cm^2	Square centimeter
CO$_2$	Carbon dioxide
CPE	Constant phase element
CT	Computed tomography

D

DAPI	4',6-diamidino-2-phenylindole
DC	Direct current
dest.	distilled
DHM	Digital holographic microscopy
DMEM	Dulbecco's Modified Eagle Medium
DMSO	Dimethyl sulfoxide
DSMZ	Deutsche Sammlung von Mikroorganismen und Zellkulturen (German Collection of Microorganisms and Cell Cultures)

E

ECIS®	Electric cell-substrate impedance sensing
EDTA	Ethylenediaminetetraacetic acid
EDX	Energy-dispersive X-ray spectroscopy

F

f	Frequency
F	Farad
FACS	Fluorescence-activated cell sorting
FBS	Fetal bovine serum
Fig.	Figure
FRET	Förster resonance energy transfer

G

g	Gram

H

h	Hour
H_2O	Water
HEK	Human embryonic kidney
HEPES	2-[4-(2-hydroxyethyl)piperazin-1-yl]ethanesulfonic acid
HPDFO	High power density focusing optics
HSE	Horse shoe electrode
Hz	Hertz

I

I	Current
I_2/KI	Aqueous solution of iodine & potassium iodide
IDF	Interdigitated finger electrode

K

KCl	Potassium chloride
kg	Kilogram
KH_2PO_4	Potassium dihydrogen phosphate
kHz	Kilohertz
$k\Omega$	Kiloohm

L

L	Liter
L-15 medium	Leibovitz's medium
LSG	Laser-scribed graphene

M

μF	Microfarad
μg	Microgram
μL	Microliter
μm	Micrometer
m	Meter
MALDI	Matrix-assisted laser desorption/ionization mass spectrometry
MCTS	Multicellular tumor spheroids
MDCK-I/II (M1/M2)	Madin-Darby Canine Kidney
MEME	Minimum Essential Medium Eagle
MHz	Megahertz
min	Minute
MRI	Magnetic resonance imaging
mg	Milligram
mL	Milliliter
mm	Millimeter
mS	Millisiemens
mV	Millivolt

N

NA	Numerical aperture
NaCl	Sodium chloride
NADPH	Reduced form of nicotinamide adenine dinucleotide phosphate
Na_2HPO_4	Sodium hydrogen phosphate
NaOH	Sodium hydroxide
norm.	Normalized
n_{CPE}	Capacitor ideality parameter

NIR	Near-infrared radiation
NRK	Normal rat kidney

O

Ω	Ohm
Osmol	Quantity of osmotically active particles

P

PBS^{++}/PBS^{--}	Phosphate-buffered saline (with/without calcium & magnesium)
PDMS	Polydimethylsiloxane
PFA	Paraformaldehyde

R

R	Resistance
R_b	Resistance from the cell-cell contacts
R_{bulk}	Resistance of the electrolyte, constriction & feed lines
RC	Parallel coupling of a resistor and a capacitor
REE	Rectangular, equally-sized electrodes
RMS	Root mean square
rpm	Revolutions per minute
RT	Room temperature

S

s	Second
S	Siemens
SEM	Scanning electron microscopy

T

t	Time
T	Temperature
Tab.	Table
TER	Transepithelial electrical resistance
TPEF	Two-photon excitation microscopy
TRITC	Tetramethylrhodamine-isothiocyanate
Triton-X-100	2-[4-(2,4,4-trimethylpentan-2-yl)phenoxy]ethanol

U

U	Electric potential difference (voltage)

V

V	Volt
v/v	Volume concentration

W

w/v	Mass concentration
WE	Working electrode

Z

Z	Impedance

180

IX.3   Hardware & Consumables

<u>Hard- and Software</u>

A

Argon plasma cleaner PDC 32G-2	Harrick Plasma, New York, US
AutoCAD 2019	Autodesk, Inc., San Rafael, US
Autoclave DX-45	Systec GmbH, Nürnberg, DE

B

Bunsen burner for cell culture	IBS Tecnomara GmbH, Fernwald, DE
Bürker hemocytometer	Paul Marienfeld GmbH & Co. KG, Lauda-Königshofen, DE

C

Centrifuge Heraeus Multifuge 1S-R	Thermo Fisher Scientific Inc., Waltham, US
Cell culture incubator Heraeus Function Line BB15	Thermo Fisher Scientific Inc., Waltham, US
Cell Incubator CO2cell 190	MMM Group, Planegg, DE
cellZscope	nanoAnalytics GmbH, Münster, DE
CLSM Eclipse 90i	Nikon GmbH, Tokyo, JP
Conductivity meter Multi 720	WTW^{TM}, Weilheim, DE
CorelDRAW Graphics Suite 2017	Corel Corporation, Ottawa, CA

E

ECIS$^{®}$ impedance analyzer	Applied BioPhysics, Troy, US
ECIS$^{®}$ arrays 8W10E	Applied BioPhysics, Troy, US

F

Freezer (ultra-deep) B 30-85	Fryka-Kältetechnik GmbH, Esslingen am Neckar, DE

I

Isopropanol bath Mr. Frosty^{TM}	Thermo Fisher Scientific Inc., Waltham, US

L

LabVIEW^{TM} software	National Instruments, Austin, US
Laminar flow hood HERAsafe	Thermo Fisher Scientific Inc., Waltham, US
Laser cutting platform VLS2.30	Universal Laser Systems, Inc., Arizona, US
Liquid nitrogen tank German Cryo GC-BR2150 M	Jutta Ohst german-cryo GmbH, Jüchen, DE

M

Microscope (phase contrast) Nikon Diaphot	Nikon GmbH, Düsseldorf, DE
Microscope (CLSM) Nikon Eclipse 90i	Nikon GmbH, Düsseldorf, DE
Microscope (stereo) Nikon SMZ 1500 C-W10xB/22	Nikon GmbH, Düsseldorf, DE

O

OriginPro 2016	OriginLab Corp., Northampton, US
Oscillator SI-1260	Solartron Instruments, Farnborough, UK
Osmometer (cryoscopic) Osmomat030	Gonotec GmbH, Berlin, DE
Oven SLE 500	Memmert, Schwabach, DE

P

Powerpoint 2019	Microsoft Corp., Redmond, US
Printer (ink jet) SC-P600	Epson, Suwa, JP

S

Scales	Mettler-Toledo, Columbus, US
Spin coater WS-650-23B	Laurell Technologies Corp., North Wales, US
Sputter coater SCD 050	Bal-Tec AG, Balzers, LI

U

UV exposure unit BEL14017	ISEL Germany AG, Eichenzell, DE

V

Vacuum unit DCU	Pfeiffer Vaccuum GmbH, Asslar, DE

W

Waterbath TW12	Julabo GmbH, Seelbach, DE

Consumables

B

Blu Tack	Bostik, Inc., Milwaukee, US

C

Carbol fuchsin	Sigma Aldrich, St. Louis, US
Cell culture flasks T-25	Greiner Bio-One, Kremsmünster, AT (Sarstedt, Nümbrecht, DE)
Cell culture plate 12-well	Corning Inc., New York, US
Cryo vials	Techno Plastic Products AG, Trasadingen, CH
Cysteine	Sigma Aldrich, St. Louis, US
Cytochalasin D	Cayman Chemical Company, Ann Arbor, US

D

DAPI	Sigma Aldrich, St. Louis, US
DMSO	Carl Roth GmbH & Co KG, Karlsruhe, DE
DMEM	Sigma Aldrich, St. Louis, US

E

EDTA	Sigma Aldrich, St. Louis, US

F

Falcon® Tubes (15 mL, 50 mL)	Sarstedt AG & Co. KG, Nümbrecht, DE
FBS	Sigma Aldrich, St. Louis, US
Ferrocyanide, ferricyanide	Merck, Darmstadt, DE
Fibronectin	Sigma Aldrich, St. Louis, US

H

HEPES	Carl Roth GmbH, Karlsruhe, DE

I

Ink jet films DinA4 X-10	Folex Coating GmbH, Cologne, DE

L

L-15 medium	Sigma Aldrich, St. Louis, US
Lamination foil KN2120	Fraunhofer EMFT, München, DE

M

MEME	Sigma Aldrich, St. Louis, US

P

Paraformaldehyde	Sigma Aldrich, St. Louis, US
PBS^{++}/PBS^{--}	Sigma Aldrich, St. Louis, US
PDMS Sylgard® 184	Dow Chemical Company, Midland, US
Penicillin/Streptomycin	Sigma Aldrich, St. Louis, US
Photoresist AZ® ECI3027	Microchemicals, Ulm, DE
Pipettes (2 mL, 5 ml, 10 mL, 25 mL)	Brand GmbH, Wertheim, DE
Pipette tips (10 µL, 200 µL, 1000 µL)	Sarstedt, Nümbrecht, DE
Polycarbonate filter HTTP09030	Merck Group, Darmstadt, DE
Polycarbonate substrate Lexan®	GE, München, DE
Polyimide substrate Kapton®	DuPont, Wilmington, US

S

Silicon glue	RS Components, Corby, UK
Syringe (5 mL, 10 mL, 20 mL)	Becton, Dickinson and Company, Franklin Lakes, US
Syringe filter (pore diameter 0.2 µm)	Techno Plastic Products AG, Trasadingen, CH

T

Tert-butyl hydroperoxide	Sigma Aldrich, St. Louis, US
Transwell® filter inserts	Corning Inc., New York, US
TRITC phalloidin	Sigma Aldrich, St. Louis, US
Triton-X-100	Sigma Aldrich, St. Louis, US
Trypsin 0.05/0.25 % (w/v)	Sigma Aldrich, St. Louis, US

IX.4   Publications

- Published: P. Puetz, A. Behrent, AJ. Baeumner, J. Wegener (**2020**): „Laser-scribed graphene (LSG) as new electrode material for impedance-based cellular assays", *Sens. Actuator B Chem.*, 321, 128443.

- Finished: P. Puetz, C. Goetz, A. Behrent, AJ. Baeumner, C. Kutter, J. Wegener (**2021**): „Impedimetric analysis and electric manipulation of adherent cells using a single bipolar electrode". Planned journal: *Scientific Reports*.

PIERRE PÜTZ

Personal Information

Name	Pierre Dominik Pütz
E-Mail	pierre.puetz@ur.de
Born	07-27-1990 in Ebersberg

Education

Since 2017
PhD student at the University of Regensburg
- PhD topic: "Impedimetric Monitoring of Three-Dimensional Tissue Models as a Construction Set"
- Financed by the Studienstiftung des deutschen Volkes
- In cooperation with the Fraunhofer Institution EMFT

October 2014 – September 2016
Chemistry studies (M.Sc.) at the University of Regensburg
- Master Thesis: "Carbon Dots: Sensors & Actuators for Living Cells" (Grade: 1.3)
- Graduation in M.Sc. Chemistry (Grade: 1.1)

October 2011 – July 2014
Chemistry studies (B.Sc.) at the University of Regensburg
- Bachelor Thesis: "Synthesis and Characterization of Carbon Dots for Applications in Living Cells and Bioanalytical Assays" (Grade: 1.0)
- Graduation in B.Sc. Chemistry (Grade: 2.1)

September 2001 – June 2010
Ludwig-Thoma Secondary School, Prien a. Chiemsee
- Advanced Courses: Mathematics & English
- Graduation: Allgemeine Hochschulreife (Grade: 1.7)

September 1997 – July 2001
Franziska-Hager Elementary School, Prien a. Chiemsee

Additional qualifications

Training courses: February 2016 - March 2016
„Frühjahrsschule Industrielle Analytische Chemie"
Gesellschaft Deutscher Chemiker, Universität Tübingen

April 2016 – May 2016
„Schulung studentischer Tutorinnen und Tutoren"
Zentrum für Hochschul- und Wissenschaftsdidaktik, UR

October 2019
„Insights Discovery Seminar"
Gerda Bensch – ITTB GmbH, Fraunhofer EMFT, München

September 2020
„Staatliche Fortbildungsveranstaltung Gentechnikrecht"
Institut für Medizinische Mikrobiologie und Hygiene, UR

Stays abroad: October 2010 - April 2011
English course at the Intensive English Academy
and internship at HUG Engineering AG
Palm Springs, California, United States

Foreign languages: **English** (advanced), **Spanish** (upper intermediate), **French** (intermediate), **Slovenian** (beginner)

IT skills: MS Office, macOS, OriginLab data evaluation, Audio- and video editing, technical AutoCAD drawings

Further interests

- **Music:**   15-year experience as piano teacher for kids
- **Sports:**   Since 2014 international artistic shows as "Duo Ingrávido"
- **Languages:**   Spanish- and French courses at the university
  Private Slovenian course
- **Travel:**   Preferred countries: Asia & Central America

References

- **Prof. Dr. Joachim Wegener** (University of Regensburg)
  E-Mail: joachim.wegener@ur.de, Telephone: +49/941 943-4546
- **Dr. Stefanie Michaelis** (Fraunhofer Institution EMFT)
  E-Mail: stefanie.michaelis@emft.fraunhofer.de, Telephone: +49/941 943-4048
- **Dr. Peter Antes** (Studienstiftung des deutschen Volkes)
  E-Mail: antes@studienstiftung.de, Telephone: +49/228 82096-286

IX.6   Acknowledgments

On a recreational note: thank you to all the acrobats and artists who helped me forget work-related worries when we were sweating in the gym. Acrobatics has always been a much-needed counterbalance to the (in parts) frustrating time spent in the lab.

From the bottom of my heart to all of you: THANK YOU <3

IX.7   Statutory Declaration

I hereby formally declare that I have written the submitted dissertation independently and without inadmissible outside support except for the quoted literature and other sources mentioned in this work. All of the literature and other sources which were employed either literally or in content during the preparation of this academic work have been clearly marked and are separately listed.

Further people were not involved in the content- or material-specific preparation of this dissertation. In particular, no paid services of a doctoral consultant or any other person have been enlisted. No one received perquisites, neither directly or indirectly, for any kind of work related to the submitted dissertation.

This work has not been submitted domestically or abroad in the same or similar form to another authority.

Ich erkläre hiermit an Eides statt, dass ich die vorliegende Arbeit ohne unzulässige Hilfe Dritter und ohne Benutzung anderer als die angegebenen Hilfsmittel angefertigt habe; die aus anderen Quellen direkt oder indirekt übernommenen Daten und Konzepte sind unter Angabe des Literaturzitats gekennzeichnet.

Weitere Personen waren an der inhaltlich-materiellen Herstellung der vorliegenden Arbeit nicht beteiligt. Insbesondere habe ich hierfür nicht die entgeltliche Hilfe eines Promotions-beraters oder anderer Personen in Anspruch genommen. Niemand hat von mir weder unmittelbar oder mittelbar geldwerte Leistungen für Arbeiten erhalten, die im Zusammenhang mit dem Inhalt der vorgelegten Dissertation stehen.

Die Arbeit wurde bisher weder im In- noch im Ausland in gleicher oder ähnlicher Form einer anderen Prüfungsbehörde vorgelegt.

Place / Date   **Pierre Dominik Pütz**